A Sheffield Hallam University thesis

ProQuest Number: 10694404

ProQuest 10694404

ProQuest LLC.
789 East Eisenhower Parkway
P.O. Box 1346
Ann Arbor, MI 48106 – 1346

THERMO-ANALYTICAL AND PHYSICO-CHEMICAL

CHARACTERISATION OF ORGANOCLAYS AND

POLYMER-CLAY NANOCOMPOSITES

ANDREW CUNNINGHAM

A thesis submitted in partial fulfilment of the requirements of

Sheffield Hallam University

for the degree of Doctor of Philosophy

July 2004

Declaration

The work described in this thesis was carried out by the author in the Materials Research Institute, Sheffield Hallam University, between October 2000 and July 2004. The author declares that this work has not been submitted for any other degree. The work is original except where acknowledged by reference.

Author:

Andrew Cunningham

Supervisor:

Professor Christopher Breen

Acknowledgements

To say thankyou is one thing, but to mean it is another. Likewise, gratitude is something that few people desire and yet those very same people deserve in abundance. It is therefore with true sincerity that the following acknowledgements are offered to each and every individual who has aided in the evolution of the work leading to the presentation of this thesis.

Many thanks go to Professor Chris Breen for his scientific input and continuous enthusiasm throughout these years and for maintaining a belief in my ability and dedication to "Push back the frontiers of science".

My gratitude also goes out to my scientific co-conspirator and general lab compendium Paul H, who when not going out for "fresh air" was easily distracted to assist in my investigation of the nano-universe. The fine art of synergy mastering is something that takes years to perfect and when someone fully understands the workings of this contraption they should write a comprehensive guide. Until then, my thanks go to Jeff for keeping the Synergiser active - I think i'm grateful for that? Thanks go to lads and lasses of the MRI who have shared in the fun and despair throughout the years, Damien, Leena, Jo, Jill, Aysen, Ben, Katie, Deeba and Fran. For technical assistance and advice, thanks must go to Mike Simmons, Chris, Neil, and Kev.

Many thanks are also reserved for my family and friends who have provided support in a range of guises. To Mum and Col, words could never express how sincerely grateful I am to you both. To Gran, now that i'm Dr Cunningham you can rely on me for medical advice. Last, but not least, all the love to my Lady Jo. Thanks for everything babes, from beginning to end you've always been the greatest friend and best refuge a Roy could have.

"In loving memory of Mr A. Cunningham"

Abstract

A variety of modified clay minerals have been screened to determine their effectiveness as agents for the production of polystyrene-clay nanocomposites. The n-alkylammonium and n-alkyltrimethylammonium surfactants employed to compatibilise the aluminosilicate layers of the minerals were shown to degrade through a series of stages and mechanisms to yield a hydrocarbon product mixture consisting of a homologous series of saturated and unsaturated hydrocarbons, also, the dehydrocyclisation (DHC) of fragmented alkyl chains was shown to lead to the production of various ring compounds which included substituted cycloalkenes, benzene and toluene.

The thermal stability of various cation exchanged modification treatments have been analysed. These organoclays have been characterised by XRD, TGA and TG-MS. The evolved gas analysis conducted by TG-MS was employed to identify which products were being thermally desorbed under thermal events previously seen when using TGA. In particular attention was paid to the activity of these materials with respect to the formation of linear, branched and cyclic aliphatics and aromatics from the feedstock surfactants.

Intra-series comparisons of different organoclays showed that as the alkyl chain length of the n-alkylammonium surfactants was increased the concentration of thermal desorption products at approximately 400 °C was also increased. However, characterisation of n-alkyltrimethylammonium exchanged MMT showed that the concentration of thermal desorption products at lower temperatures (approximately 250 °C) increased with alkyl chain length between C_n = 8 - 16. TG-MS analysis showed that this was mostly due to the DHC of alkyl fragments. These compounds appear to have been largely overlooked in related literature.

SWa-1, a clay containing greater concentrations of structural iron, showed higher T_{max} values for n-alkylammonium surfactant thermal desorption than similarly exchanged SAz-1. This may be evidence of a current theory that structural iron acts as a *radical trap*. This is thought to significantly reduce the catalytic activity of the clay's acid sites until higher temperatures.

The formulation of polystyrene-clay nanocomposites (PSCNs) by *in-situ* polymerisation led to various results pertaining to their thermal stability. The relative effectiveness of various initiator species for the production of the most thermally stable PSCNs was AIBN > BPO > SPS > APS >>AIBA. Lower radical initiator and organic modifier concentrations led to the production of PSCNs with higher thermal stability. The relative effectiveness of these various organoclays for the production of more thermally stable PSCNs was MCBP-C_n > C15A > C20A >> C10A. The preparation method was shown to be effective for producing exfoliated nanocomposites for up to 1 wt% of the various organoclays using AIBN and BPO as initiators. The MCBP-C_n PSCNs remained exfoliated up to 5 wt% , they also showed higher thermal stability when compared with the commercial products, which XRD results showed to remain stacked at organoclay loadings > 1 wt%.

A novel one-pot synthesis method for the production of PSCN, by the *in-situ* polymerisation of PS in the presence of decanamide (an uncharged surfactant) and Na-MMT, was shown to be successful. Whereas, other novel PSCN formulations incorporating N-vinylformamide and the amphoteric surfactant foamtaine SCAB were shown to be encouraging but have, so far, had limited success.

In contrast, the analysis of industrially produced unsaturated polyester-clay nanocomposites showed very little increase in the thermal stability of the material. Associated analyses indicated increased dimensional stability of the material, AFM analysis showed that imaging of the clay dispersal was possible by this macroscopic technique. Also, ATR-FTIR analysis of the UPR and UPCN, showed that although not exfoliated the silane modified-MMT had a good synergistic effect on the overall material by reducing the formation of combustion products.

The thermal stability and associated studies of kaolin-phenylphosphonic acid (KPPA) complexes was also conducted. PPA was shown to intercalate the kaolin crystal structure forming an expanded phase that exhibited remarkable thermal stability (T_{max} = 660 °C). ^{31}P MAS NMR of all the KPPA samples showed three peaks (at +1.2, -3.7 and -7.3 ppm) which represented PPA existing in three non-equivalent bonding states at the kaolin surface. The high thermal stability of these hybrid materials was evident from these studies. This research into the use of covalently bound intercalates in nanocomposite manufacture signifies the necessity for further research.

Table of Contents

List of Abbreviations

AFM	Atomic Force Microscopy
AIBA	2,2-azo-bis-isobutyramidine
AIBN	2,2 -azo-bis-isobutyronitrile
APS	Ammonium Persulphate
ATR-FTIR	Attenuated Total Reflectance Fourier Transform Infra-Red Spectroscopy
BPO	Benzyl Peroxide
BTX	Benzene, Toluene and Xylene
C10A	Bz-MMT, dimethyl hydrogenated tallowalkyl benzyl ammonium MMT
C15A	Ta15-MMT, dimethyl dihydrogenated tallowalkyl ammonium MMT
C20A	Ta20-MMT, dimethyl dihydrogenated tallowalkyl ammonium MMT
CEC	Cation Exchange Capacity
CTAB	Cetyltrimethylammonium Bromide
DMF	Dimethylformamide
DRIFTS	Diffuse Reflectance Infrared Fourier Transform Spectroscopy
DTAB	Dodecyltrimethylammonium Bromide
DTG	Differential Thermo-Gravimetry
EGA	Evolved Gas Analysis
ESEM	Environmental Scanning Electron Microscope
FTIR	Fourier Transform Infra-Red Spectroscopy
FS	Foamtaine SCAB
GPC	Gel Permeation Chromatography
HRR	Heat Release Rate
KPPA	Kaolin intercalated with Phenylphosphonic Acid
LDS	Lloyds post-cure
MCBP	Mineral Colloid British Pharmocopoeia
MMT	Montmorillonite
M_n	Number Average Molecular Weight
M_w	Weight Average Molecular Weight
MW	Molecular Weight
Na-MMT	Sodium Exchanged Montmorillonite
NanoLDS	Styrenated orthophthalic unsaturated polyester resin containing 4wt% silane modified MMT Clay, low temp. post cure
NanoSB	Styrenated orthophthalic unsaturated polyester resin containing 4wt% silane modified MMT Clay, high temp. post cure
NIST	National Institute of Science and Technology

NMF	*N*-methylformamide
NVF	*N*-vinylformamide
OPS	One-Pot Synthesis
OTAB	Octyltrimethylammonium Bromide
^{31}P NMR	Phosphorous-31 Nuclear Magnetic Resonance Spectroscopy
PCN	Polymer-Clay Nanocomposite
PDI	Polydispersity Index
PDMS	Polydimethylsiloxane
PMMA	Polymethylmethacrylate
PPA	Phenylphosphonic Acid
PS	Polystyrene
PSCN	Polystyrene-Clay Nanocomposite
Ra	Roughness Average
Rq (RMS)	Roughness Root Mean Squared
RT	Room Temperature
SAz-1	Ca-rich smectite
SB	Scott-Bader post-cure
S-MMT	Silane Modified Montmorillonite
SPS	Sodium Persulphate
Std LDS	Styrenated orthophthalic unsaturated polyester resin, low temp. post cure
Std SB	Styrenated orthophthalic unsaturated polyester resin, high temp. post cure
SWa-1	Fe-rich smectite
TCRL	Toyota Central Research Laboratories
TEM	Transmission Electron Microscopy
TGA	Thermo-Gravimetric Analysis
T_{max}	Temperature Maximum
TTAB	Tetradecyltrimethylammonium Bromide
UPCN	Unsaturated Polyester-Clay Nanocomposite
UPR	Unsaturated Polyester Resin
VDAC	Vinylbenzyldimethyldodecylammonium Chloride
XRD	X-Ray Diffraction
XRF	X-ray Fluorescence Spectrometry

1

Introduction to Clays, Polymers and Nanocomposite Materials

1.1 Introduction

1.1.1 Clays, Organoclays and Nanocomposite Materials

Nanotechnology has been widely recognised as one of the most promising directions of technological development for the 21st century. This new class of polymer system is currently the source of great interest within the plastics industry. These materials incorporate organically modified layered silicates, often referred to as *organoclays*, within a host matrix as low quantity (i.e. ≤ 5 wt%) fillers dispersed at the nanometre-level. This dispersion of clay platelets has led to the general description of this class of materials as polymer-clay 'nanocomposites' (PCN) [1-1].

Nanocomposites have shown substantial property improvements when compared to virgin polymers, properties which have shown improvements include:

i)   Mechanical properties e.g. strength, modulus and dimensional stability

ii)   Decreased permeability to gases, water and hydrocarbons

iii)   Thermal stability and heat distortion temperature (HDT)

iv)   Flame retardency and reduced smoke emissions

v)   Chemical resistance

vi)   Surface appearance

vii)   Electrical conductivity

viii) *Optical clarity in comparison to conventionally filled polymers*

Also, in the majority of cases, this enhanced material performance occurs without a significant increase in the density of the polymer, and without any reduction in the materials potential recyclability. In the field of materials science, the development and study of nanocomposite hybrid materials is a multi-disciplinary research activity which is generating both academic and industrial interest. Applications for PCNs have so-far been proposed for use in the materials, construction, aerospace, food-packaging sectors.

Current trends favour the use of fillers like metal-trihydrate/hydroxide and halogenated compounds to impart thermal stability/flame retardency; however, the use of these systems has definite environmental and safety concerns [1-2]. An example of the impracticality of these systems comes from the application of aluminium trihydrate (ATH) and magnesium hydroxide in wires and cables. This application requires loadings in excess of 60 wt% to achieve a suitable level of flame retardency, which leads to an inflexible product due to its higher density and can cause processing problems. Whereas, halogenated flame retardants are expensive and may release biologically harmful toxins into the environment under combustion conditions [1-3, 1-4]. Nanocomposites avoid the disadvantages of these traditional flame retardant systems.

Until recently the use of mineral based systems had not been considered for flame retardency, however, reports of the improved thermal stability of siloxane polymer-clay composites [1-5] and a polyimide-clay composite has generated new interest in the use of these mineral based systems [1-6].

Initial studies in this thesis concentrated on the thermal characterisation of a range of alkylammonium and alkyltrimethylammonium organoclays. This was followed by in-depth studies of polymer-clay nanocomposite (PCN) materials. These materials were formulated from their base components and the production processes which were used derived a large number of different quaternary ammonium exchanged montmorillonite (MMT) clay dispersed in polystyrene (PS) matrices and several novel formulations for PS-clay nanocomposites. Whereas, another study was centred on the dispersion of silane-modified MMT within unsaturated polyester matrices that were then subjected to different curing profiles. The objective behind the work in this thesis was to quantify and characterise the *increased thermal stability which these hybrid systems imparted on in-house manufactured* thermoplastic and thermoset materials, and then, relate any differences to the formulation criteria of the various organo-silicate dispersions.

1.1.2   The Commercial Market for Polymer-Clay Nanocomposites

Polymer-clay nanocomposite materials are value-added materials, that with further research and industrial foresight will be able to bring about a revolution in the plastics industry that would be beneficial to both the production industry (reduced costs, better processibility) and the consumer market (improved functionality, reduced cost, additive enhancement). Prospective market growth for the use of nanocomposite materials in various commercial sectors is shown in fig. 1.1.
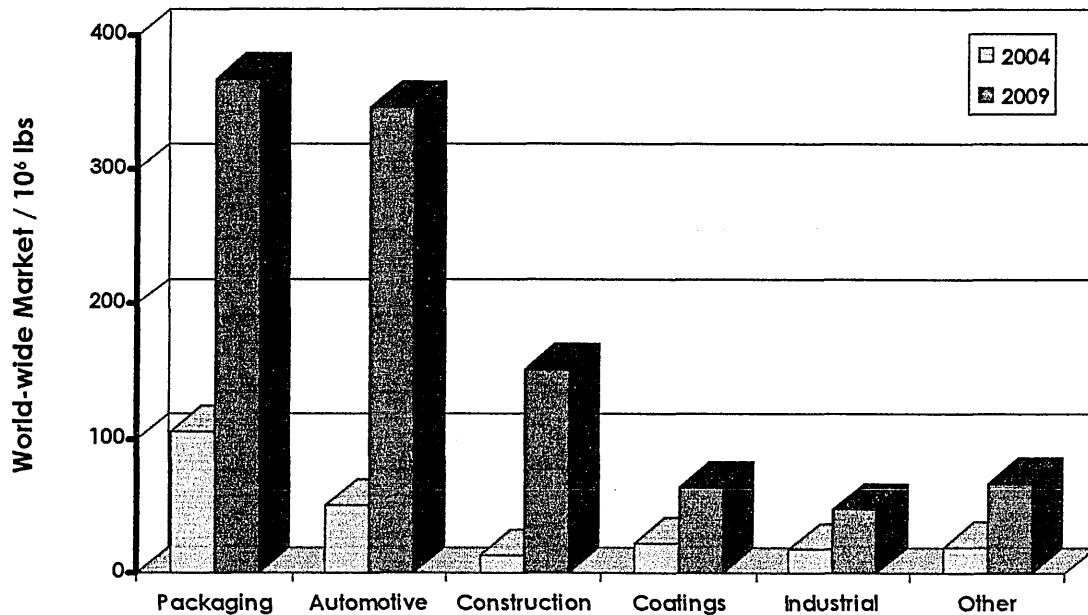
Figure 1.1   Global market analysis of the growth of nanocomposites in different commodity sectors, predicted to 2009 [1-7].

1.2   Classification of Minerals

Class	Subclass	Group	Subgroup

Silicates
- tectosilicates
  - silica — quartz
  - feldspars — alkali series / plagioclase series
- phyllosilicates
  - smectites
  - kaolinites
  - illites
  - chlorites

Table 1.1   The sub-division of the silicate class.

Clay is the common term for a number of fine-grained, soil materials that become 'plastic' when wet. Chemically, clays are hydrous aluminium silicates, ordinarily containing impurities, e.g., potassium, sodium, calcium, magnesium, or iron, in small amounts [1-8].

All minerals are divided into several classes, and the group which was the main focus for this research was the silicates. The silicates are divided into several sub-classes based on the types of linkages between the basic units of their structure (i.e. SiO_4 tetrahedra).

The sub-classes found in sedimentary rocks are the tectosilicates and the phyllosilicates [1-9, 1-10], see table 1.1. To understand the properties of phyllosilicates it is necessary to look at the individual structural components that give rise to their characteristic structure and properties.

1.2.1 Phyllosilicates (Clay Minerals)

1.2.1.1 *Clay Structure*

The basic structural feature of all minerals in this subclass are $SiO_4{}^{4-}$ tetrahedra linked by sharing three of the four oxygens, which form sheets (fig. 1.2) with a pseudo-hexagonal network (referred to as silica-tetrahedral sheets).

O and $\bigcirc$ = Oxygens   o and ● = Silicons
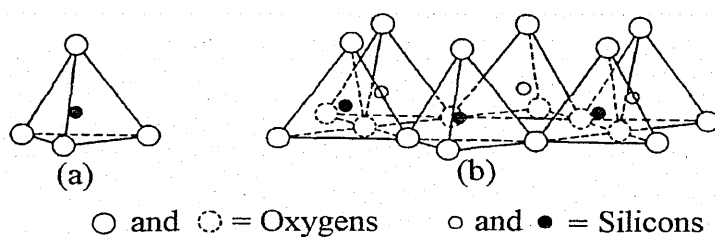
Figure 1.2 **Diagrammatic sketch of (a) single silica tetrahedron and (b) the sheet structure of silica tetrahedra arranged in a hexagonal arrangement.**

It can also be seen that the resulting layer structure (fig. 1.2) gives rise to a hole in its network of tetrahedra, this is referred to as a ditrigonal cavity. The oxygen atoms in the $SiO_4{}^{4-}$ sheets can be external groups (i.e. hydroxyl) or form part of the bonding to a second layer as described below.

This tetrahedral sheet is combined with other sheet-like groupings of cations (mainly Al, Mg and Fe) and co-ordinated with six oxygen and hydroxyl anions. This is referred to as the octahedral-layer since the anions are arranged around the cations in an octahedral arrangement. Anions are shared between adjacent octahedral groups which results in a planar network (fig. 1.3). These silica and octahedral sheets can be superimposed on each other. They may share oxygen atoms and thus become fused together in layers by chemical bonds between the two sheets.

(a)   (b)

$\bigcirc$ and $\{\cdot\}$ = Hydroxyls $\bullet$ Aluminums, Magnesiums, etc.
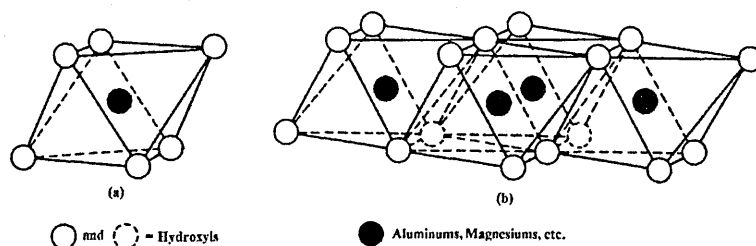
Figure 1.3   Diagrammatic sketches showing a single octahedral unit and the sheet structure of the octahedral units.

The ratio of tetrahedral to octahedral sheets and the type of cation in the sheets is the basis for the classification system used to assign clays to various groups. These sheet-like structures are represented in fig. 1.4. For example, when an SiO_4 and an $Al(OH)_6$ sheet are joined together, as shown in fig. 1.4a, the structure is designated a *1:1 layer arrangement* and is typical of minerals such as kaolinite.

Tetrahedral sheet

Octahedral sheet

(a)   (b)   (c)
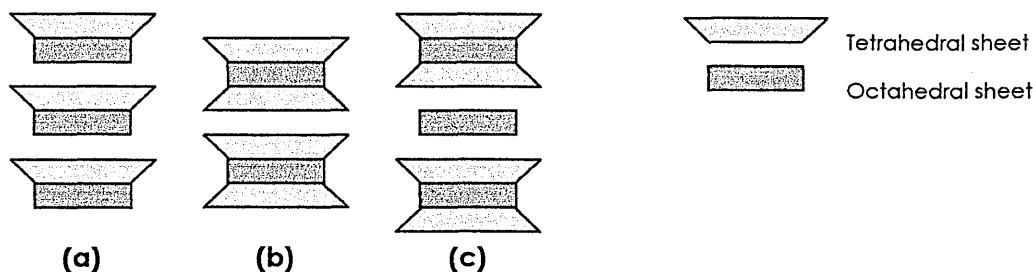
Figure 1.4   Clay layer arrangements, (a) 1:1, (b) 2:1 and (c) 2:1:1.

The octahedral layer may also join with a second silica tetrahedral layer and form a 2:1 layer silicate, this structure is designated as a *2:1 layer arrangement.* This occurrence is evident in smectites, pyrophyllite, talc, vermiculite, illite, mica and chlorite. It was this type

of clay (fig. 1.4b) which is of most interest, particularly the smectite group because of their ability to undergo cation exchange and swell in the presence of solvent.

In fig. 1.4c it can be seen that chlorite has an extra sheet and is characterised by a 2:1:1 layer structure. All these structures may be stacked up into successive layers. Clay minerals may also be subdivided into groups based on their octahedral layer type, an overview of the main clay mineral groups can be seen in table 1.2.

Layer type	Group	Di-/Trioctahedral	Subgroups	Species
1:1	Serpentines	trioctahedral	serpentines	chrysotile
	Kaolinites	dioctahedral	kaolins	kaolinite, dickite
2:1	Smectites	trioctahedral	saponites	saponite, hectorite
		dioctahedral	montmorillonites	montmorillonite, beidellite
	Micas	trioctahedral	trioct. mica	biotite
		dioctahedral	dioct. mica	muscovite

Table 1.2   Classification of clay minerals (1:1 and 2:1 layer arrangements) [1-11]

1.2.1.2   Clay Mineral Properties and Characteristics

1.2.1.2.1   Isomorphous Substitution
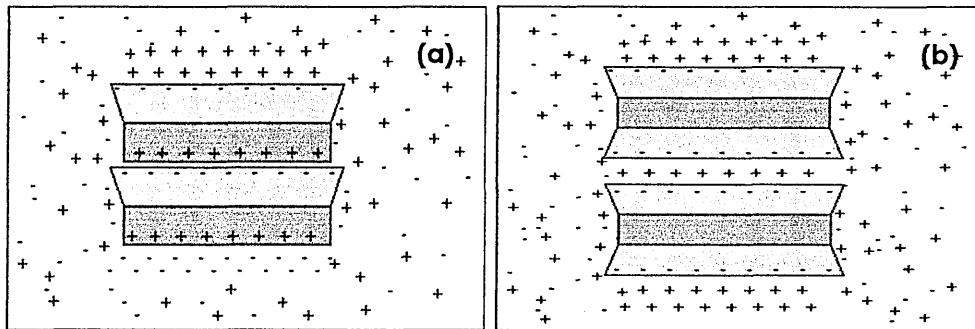
Figure 1.5   Schematic diagram for associated charge in (a) 1:1 structure and (b) 2:1 structure. Note that positive ions are attracted to the light-grey tetrahedral basal oxygen surface, whilst negative ions are attracted to the dark-grey octahedral hydroxyl surface. The case for low-charge 2:1 structures is notably different from 1:1 structures. In (b) the negative charge on the layer attracts cations to the gallery surfaces.

7

Isomorphous substitution is a modification process that occurs when the mineral is formed, usually when there is an excess of water present. Ions of a lower charge replace those of a higher charge in the different layers, i.e. Mg^{2+} substitutes Al^{3+} in the octahedral sheet or Al^{3+} substitutes Si^{4+} in the tetrahedral sheet, this results in an excess of electrons.

This generates a net negative charge which is satisfied by the adsorption of cations such as Na^+, Ca^{2+}, Mg^{2+} or K^+ which together with the presence of water leads to a charged aqueous environment between the clay layers. The sharing of these exchangeable cations bonds the clay layers together. These cations are termed the interlayer or exchange cations and may be readily exchanged in the laboratory for other cationic species.

The number of cations required to neutralise the negative charge on the layer is known as the cation exchange capacity (CEC) and is measured in milliequivalents (mEq) per 100 grams of clay. Different clays have different CECs, some of which are shown in table 1.3. These cations can be exchanged by other cations, this can be done by simply dispersing the clay in a solution of the desired cations that are common in clay minerals found in nature, e.g. Na^+, Ca^{2+}, Mg^{2+} or K^+ (fig. 1.5). Exchangeable cations can also be associated with the edges of silicate layers, where the structural ions have unsatisfied valences. These are often referred to as broken bonds. Approximately 20% of the CEC is associated with broken bonds and 80% is situated in the interlayer region.

Clay species	CEC Range (mEq/100g)
Kaolinite	1 - 15
Chlorite	< 10
Illite	10 - 40
Smectite	80 - 150
Vermiculite	120 - 200

Table 1.3   CEC of various clay species [1-11].

1.2.1.2.2 Swelling/Hydration of Clay
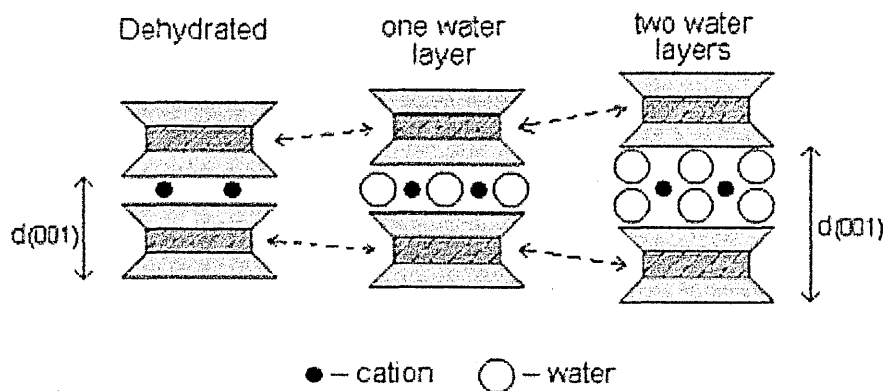
Figure 1.6   Swelling of clay (e.g. MMT),

The exchangeable cations are often hydrated and this water may be replaced by polar organic liquids. When water is adsorbed between the layers, the distance between the layers ($d_{(001)}$-spacing) increases. This is the result of a swelling of the clay layers and is represented in fig. 1.6. When an organic solvent is adsorbed between the layers it is referred to as intercalation. Another feature of clay's structure that has a direct bearing upon the chemistry of the complexes is the acidic nature of the clay surface [1-12]. The clay can show Bronsted and Lewis acidity with the structure governing the degree to which these occur. For example, Lewis acidity is more commonly associated with exposed Al^{3+} and Fe^{3+} at the edges of the clay sheets and can be increased by the thermal treatment of the clay. Similarly, the Bronsted acid characteristics are usually governed by the availability of water in the interlayer around the cations and are the result of the dissociation of water molecules in a hydration space between the cations. The degree to which this effect is seen depends on the nature of the substitution, i.e. whether it is mainly from the tetrahedral or octahedral sheet, and on water content, the lower the water content the higher the acidity. Bronsted acidity is also very dependent on the polarising power of the interlayer cation.

1.2.2　Clay Minerals of Particular Relevance to this Thesis

1.2.2.1　Montmorillonite (MMT)

The composition of montmorillonite (MMT) always deviates from the ideal formula, $Al_2Si_4O_{10}(OH)_2.xH_2O$, due to a relatively high amount of isomorphous substitution. An idealised structural formula for MMT is $Na_{0.3}(Al_{1.7}Mg_{0.3})Si_4O_{10}(OH)_2$. Fig. 1.7 shows the molecular structure of MMT, this model is the most widely accepted and was first proposed by Hofmann, Endel and Wilm [1-13] and modified by Magdefrau and Hofmann [1-14], and, Hendricks [1-15]. The other known model was proposed by Edelman and Favejee [1-16]. The outstanding feature of the montmorillonite structure is that water and polar molecules can easily enter between the layers. This is because the electrostatic bonding between the layers and exchangeable cations is weak and the chances of swelling or intercalation are excellent.
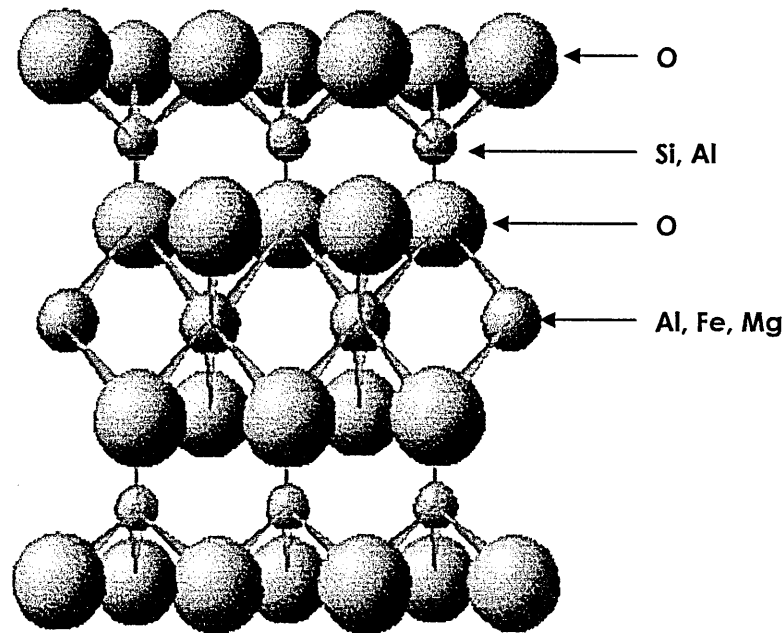
Figure 1.7　The 2:1 clay structure of montmorillonite (ball and stick model) [1-17].

1.2.2.2　Kaolinite

Kaolinite is the most common of four polymorphs, the others being dickite (rare), nacrite (rare) and halloysite (moderately common). Fig. 1.8 shows the molecular structure of

10

kaolinite, the ideal structural formula of kaolinite is $Al_2Si_2O_5(OH)_4$, although Fe, Ti, K and Mg may also be present.
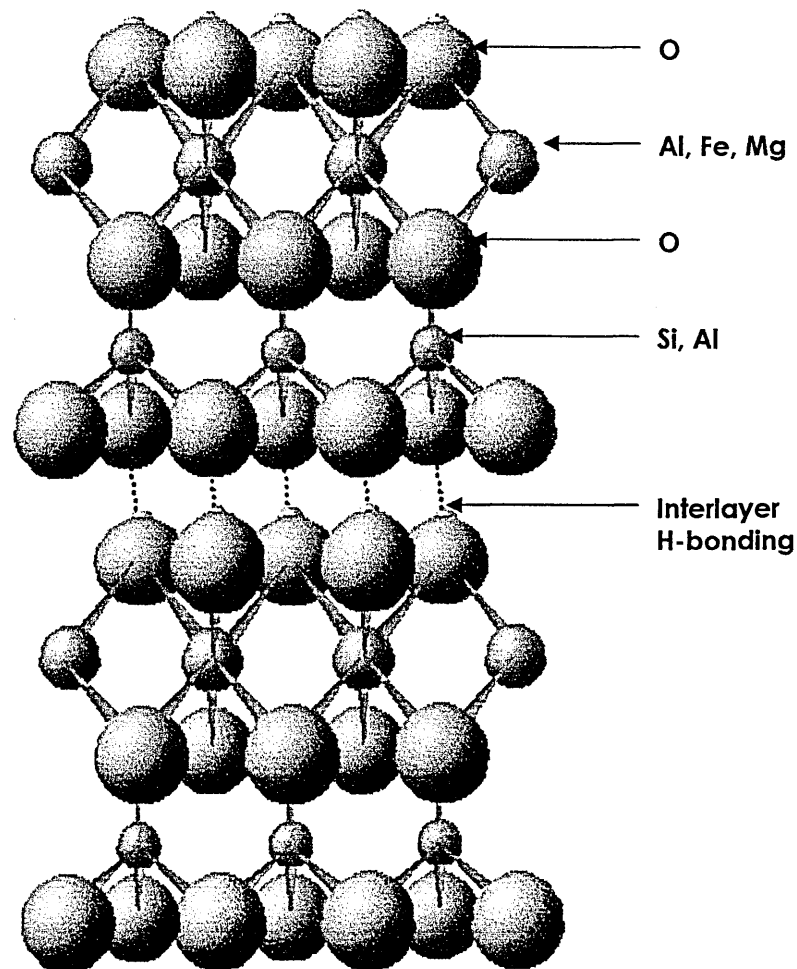
Figure 1.8   The 1:1 clay structure of kaolinite (ball and stick model) [1-18].

There is no charge (at most, a very weak one) on the lattice due to isomorphous substitution in kaolinite and thus no interlayer cations are present. If exchangeable cations are present these are usually associated with broken bonds at the crystal edges. The layers in kaolinite are held together by hydrogen-bonding and intercalation may occur if this bonding network can be entered into. A summary of the comparative physical properties of MMT and Kaolinite can be seen in table 1.4.

	MMT	Kaolinite
CEC	80-150	1-15
Particle size (microns)	0.1-2	0.5-5
Surface area BET - N_2 m^2 g^{-1}	30-80	15-25

Table 1.4   Summary of the properties of the clay minerals used [1-19].

1.3   Organic-Mineral Interactions

The interactions between minerals and organic molecules have been a source of interest to industry for a number of years. Some of the industrial sectors that are specifically interested by such interactions include: geological [1-20], oil exploration [1-21], pharmaceutical [1-22], waste treatment [1-23], plastics, catalysis [1-19], laundry powders [1-24], agricultural [1-25 – 1-27], among others. Most interest is associated with clay minerals because of their high reactivity. An example of this is the vital role that clay minerals may play in the control of hazardous organic molecules. Environmental problems associated with the presence and accumulation of pollutants/pesticides in soils as well as in surface and ground waters are becoming increasingly important. The bioremediation of hazardous materials (e.g. fuel contamination - BTX) may be achieved by adsorption of the organic pollutants by synthetic organoclays. The entrapment of these materials within the galleries of the clay can slow the migration of pollutants through soils and waterways, but this process may also be applied to change their decomposition activation energy [1-28, 1-29]. MMT may be used as a catalyst because of its intercalation and retention properties and this can be modified so that their catalytic behaviour can be tuned/manipulated [1-30, 1-31]. Haderlein & Schwarzenbach [1-32] studied the adsorption of a large number of nitroaromatic compounds on MMT, illite and kaolinite surfaces in order to predict their movement through soil systems. After studying the effects of environmental factors on the adsorption process, such as pH, they found these to be very important. Their experiments gave a fuller understanding to the interactions between nitroaromatic molecules and minerals [1-33, 1-34].

A second example is the addition of organoclays, as thixotropes in paints and as fillers in dye suspensions [1-35]. The latter can lead to changes in the colour of the dye due to π-interactions between the aromatic compounds and the oxygen plane of the clay, knowledge of these interactions is therefore vital. The adsorption behaviour of surfactants and polymers on MMT has also been studied [1-36] because mixtures of polymers, surfactants and clays may be used in treatment fluids for enhancing oil recovery.

Many techniques, which will be discussed later in this section, have been used to characterise organoclay mineral complexes and properties. The techniques which have been used may determine:

   a. whether adsorption complexes have been formed or whether the clay and organic material are present simply as a mechanical mixture,

   b. the type and strength of interactions between organic molecules and clay layers,

   c. the effect of the clay surface on the stability or degradation mechanism of the adsorbed organic.

1.3.1   Types of Organo-Mineral Interactions

Each type of clay mineral will interact with an organic molecule differently since each clay surface and its interlayer space have different types and populations of Bronsted and/or Lewis acidic and basic sites. The principal interactions observed between clays and organic molecules are of the acid-base type.

1.3.1.1   Typical Smectite and Organo-Molecular Interactions

The processes by which smectite clays interact with organic molecules are very complex. Lacher et al. [1-37 – 1-39] conducted a detailed study of the interactions occurring between different cationic exchanged MMTs and benzinine (i.e. a pesticide); the results showed that various types of interactions occurred. Other examples of complexes formed through organoclay interactions include; sulfolane adsorbed on cationic exchanged MMTs

[1-40], the interactions of alachlor (herbicide) with homoionic MMTs [1-41], and, the adsorption of atrazine on MMTs [1-42]. In addition to the five main types of interactions, described in table 1.5, it is possible for positively charged organic molecules to be exchanged with the inorganic cations in the gallery [1-43]. However, the number and variety of organic compounds which can acquire a positive charge is limited. Many such compounds (e.g. alkylammonium ions) contain nitrogen, of which the amines form the largest class.

A benefit of such cation-exchanges is that a fixed internal porosity is achieved since the pore size and shape depend on the alkylammonium ion. Harper & Purnell [1-44] used this fact to create a novel adsorbent system for organic vapour sampling which would overcome problems encountered by other adsorbent systems (e.g. activated carbon). Also, Barrer [1-45], has reviewed his own studies, lasting 40 years, on the behaviour of clay minerals (in particular smectites) and their derivatives as sorbents.

Cation-exchange with organic molecules may also occur indirectly. Ruiz-Conde *et al.* [1-46] studied the interaction of aqueous solutions of formamide, acetamide and propionamide with vermiculite. Vermiculite is similar in structure to MMT but a higher CEC. These situations showed that amides were hydrolysed to liberate NH_4^+.

There are a number of factors that govern the adsorption of organic molecules to smectites. Dashman & Stotzky [1-47] examined the effect of molecular weight and basicity on the adsorption and binding ability of amino acids to homoionic MMTs. It was found that these factors were not as important as the type of exchangeable cations in their adsorption.

14
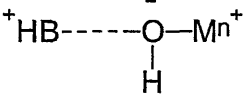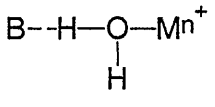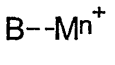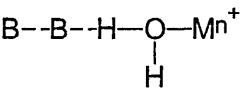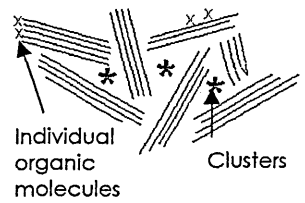
1.	**Protonation of Organic Molecules**
$^+HB\text{-----}\underset{\underset{H}{\vert}}{O}\text{---}Mn^+$ $^-$	Water coordinated to exchangeable metallic cations serves as a proton donor (Bronsted acid). Depending on the polarising power of the metal (Mn^+) and the basic strength of the organic molecule (B), the organic molecule may be protonated by accepting a proton from a water molecule, thus gaining a positive charge (1.).
2.	**Water Bridges**
$B\text{--}H\text{---}\underset{\underset{H}{\vert}}{O}\text{---}Mn^+$	The organic molecule may form a H-bond with the polar water molecule (2.), i.e. the water acts as a bridging molecule.
3.	**Lewis Acidity**
$B\text{--}Mn^+$	After thermal dehydration or at room temperature the exchangeable cations may serve as Lewis acids and adsorbed bases become co-ordinated directly to the cations. If M is an alkali metal cation, then the bond between it and B is mainly electrostatic, ion-dipole attraction.
4.	**Water Bridge Associations**
$B\text{--}B\text{--}H\text{---}\underset{\underset{H}{\vert}}{O}\text{---}Mn^+$	Organic molecules may also be associated to molecules of type 2. The presence of these depends greatly on the size of the molecule.
5.	**Other Associations**
Individual organic molecules Clusters	Organic molecules may also be associated with broken edges, external clay surfaces, with substitutions in the tetrahedral layer or clusters between stacks of clay layers.

Table 1.5   Possible organic-mineral interactions.

1.3.1.2   Factors Affecting the Adsorption of Organic Molecules onto Minerals

In addition to the previously mentioned properties of minerals and organic compounds that effect adsorption, table 1.6 gives a more comprehensive list of the properties of minerals and organic compounds that affect the adsorption process.

Surface Properties:	Organic Molecular Properties:
a. Surface configuration **b.** Exchangeable ions on surface **c.** Total surface area **d.** Interlayer spacing **e.** Surface Chemistry (O or OH) **f.** Particle size and crystallinity	**a.** Size **b.** Shape **c.** Flexibility **d.** Charge **e.** Polarity

Table 1.6   Surface and organo-molecular properties affecting adsorption.

In addition to these molecular factors, certain reaction conditions are also significant:

i)   Raising the temperature may disrupt the structure of the interacting liquid due to its greater thermal motion; this would increase the relative number of free molecules and the rate of intercalation.

ii)   Addition of water to the intercalating liquid, this would effect the extensive associated *structure of some pure liquids into smaller aggregates of molecules,* which in turn would increase the rate of intercalation. Too much water would result in the solvation of the intercalating molecules, which in turn, would result in *relatively few unsolvated molecules being available to intercalate, thus decreasing* the intercalation rate.

iii) ·   Reaction medium. For example the selectivity of adsorption of organic ammonium *ions to smectite clays can change depending on whether water or other solvents are used* [1-48]. Batouti *et al.* [1-49] showed that the rate of exchange of Cu^{2+} on Na-MMT clay was faster in acetonitrile than dimethylformamide.

There are no well-defined trends to determine whether an organic molecule will intercalate or how fast it will do so. For example, a large dipole moment will favour the formation of a complex, but a large dipole moment may cause extensive association ('complexing') in the liquid state and this will decrease the rate of intercalation.

1.3.1.3 Alkylammonium Exchanged Clays

The native metal exchange cations on clays can be replaced with different cations by simple ion exchange reactions. A variety of organic cations may be used in this regard to form organoclays [1-50].
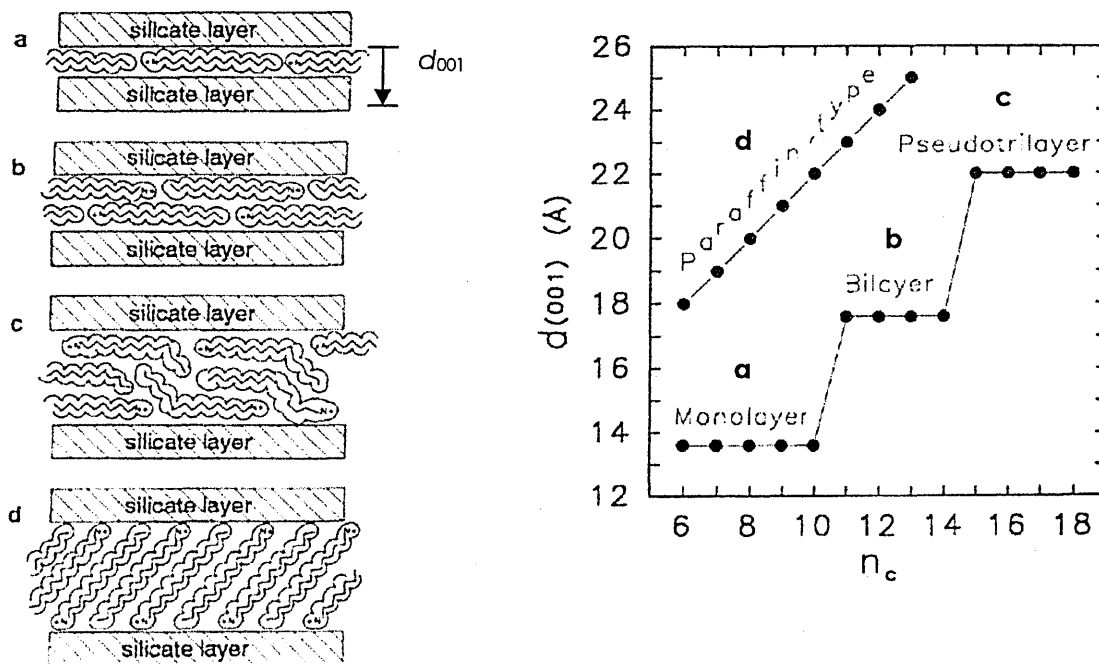
Figure 1.9 Idealised relationships between basal spacing and alkylammonium expansion [1-52, 1-53].

The substitution of organic cations for inorganic gallery cations dramatically alters the properties of a clay, the specific nature of the gallery spaces changing from hydrophilic to organophilic. This occurs because the heat of hydration of the organic cations are very low which do not attract water, and because of the substantial amount of organic carbon associated with the clay layers and interlayer [1-51]. Also, the intercalated organic cations pack in between the aluminosilicate layers resulting in greater interlayer spacing than would occur due to swelling in the presence of water.

The arrangement of organocations within the clay gallery can be indicated by the degree of interlayer expansion. Depending on an organocation's size (i.e. alkyl chain length) and

17

the layer charge of the mineral, the organocations may reside as monolayers, bilayers, pseudotrimolecular layers or paraffin complexes, which correspond to d_{001} spacings of approximately 13.5Å, 18.0Å, 21.5Å and 30.0Å. These types of interlayer alkylammonium complexes are illustrated in fig. 1.9.

1.3.1.4 Typical Kaolinite and Organic Molecule Interactions

There are fewer molecules that intercalate into kaolinites than smectites, types of compounds that are known to do so include:

a. inorganic salts [1-54]

b. organic salts [1-42, 1-55]

c. long chain fatty acids [1-56]

d. small and large highly polar organic molecules such as; urea, formamide, glycerol and benzidine [1-42, 1-54, 1-57]

Polar organic molecules do not intercalate into kaolinites as readily as with smectites because the strong H-bonding that exists between the kaolinite layers needs to be overcome. Some molecules intercalate directly into kaolinites from either a liquid or a concentrated aqueous solution, whilst others can only enter by means of an entraining agent (carrier), or by displacement of a previously intercalated compound [1-58]. The possible organic-clay interactions for kaolinites are not as varied as for smectites. The bonding between the clay and the organic molecules, involves the inner-surface-hydroxyls and sometimes the basal oxygens of the adjacent kaolinite surface. Some molecules that are known to intercalate and bond to the surface of kaolin are formamide, *N*-methylformamide, *N,N*-dimethylformamide and phosphonates.

Non-reacting guest compounds can be entrained between the layers by reactive guest molecules. *The basic principles of intercalation reactions have been highlighted by Lagaly* [1-59]. The reactive guest molecules enter the clay galleries and essentially break the H-

bonds between the hydroxyl groups and the adjacent siloxane layer which leads to an expansion of the kaolinite layers. H-bonds are then formed with either the oxygen surface of the siloxane layer, or more likely the hydrophilic hydroxyl surface of the gibbsite like layer. The possibility also exists that the molecule may also interact with the edges of the kaolinite. However, it is more difficult to intercalate non-polar organic molecules because the strong H-bonding between the kaolinite layers needs to be broken. Intercalation is strongly dependent on a variety of factors as highlighted by Olejnik *et al.* [1-60].

The following exchange factors may equally apply to swelling and non swelling minerals:

a.   *Dipole moment-molecular size balance.*

To achieve direct intercalation, the organic compound should be small and possess a large dipole moment. However, in general high polarity is associated with large molecules. These characteristics may act in opposition to each other.

b.   *Extent of association in the liquid or solid.*

The more 'free' solution molecules which are present, the faster the intercalation. It is suggested that at higher concentrations there is a larger proportion of molecules which are relatively free, i.e. not solvated by the solvent, compared to the situation in concentrations below 10 M.

c.   *Temperature.*

If the temperature of the liquid is raised, the greater thermal motion results in disruption of the structure.

d.   *Molecular dimensions.*

The size of the intercalating molecule is affected by the size and type of functional groups. The electron donating effect of methyl groups can enhance delocalisation of the charge in amides and increase the basicity of the carbonyl atom, resulting in a marked variation in the intercalation of species into the gallery. Therefore, the molecular size of a potential exchange molecule should be as small as possible for several reasons. Firstly, the most important adsorption sites are usually 'acid centres' which may be located in narrow pores

or in cavities which are only accessible through narrow channels. Secondly, the acid site, in particular aprotonic Lewis acid sites, may be exposed in an oxygen vacancy and therefore may be sterically hindered by neighbouring oxide ions. Thirdly, larger molecules may be aligned to one site and in turn be blocking other potential sites in close proximity.

e. *Orientation and packing of intercalated molecules.*

Olejnik et al. [1-60], *found that the difference between the minimum dimensions of non-expanded kaolinite and the d-spacing of a variety of complexes, suggested that there was considerable keying of the molecules into the kaolinite surface. Considering the lack of exchangeable cations in kaolinite and the absence of multi-layers in the gallery (as seen in montmorillonite complexes), it suggested that the polarity of kaolinite plays a much more important role in swelling behaviour than MMT. The gross molecular orientation of an intercalated compound can be determined by XRD (via the d-spacing).*

There is never more than a single layer of organic molecules taken up by kaolinite or halloysite, whereas MMT may intercalate up to three layers of organic molecules. Other sites at which organic interactions may occur would be broken edges, external clay surfaces or clusters between stacks of kaolinite layers. The main discriminating fact that differentiates between the intercalation of organic molecules into smectites and kaolinites is that the organic molecules are specifically aligned when in the gallery spaces of kaolinites.

1.3.1.5   Other Organo-Mineral Interactions

Illites are 2:1 layer phyllosilicates, but they have an adsorption capacity that is less than that of MMT, this is due to its non-expanding structure, which in turn confines organo-mineral interactions to the external crystal edges [1-61]. A study of the adsorption of a number of antibiotics (e.g. streptomycin) on several clay types showed that adsorption decreased in the order MMT > illite > kaolinite [1-62]. Another study compared the capacity of different clays to take up non-ionic herbicides and found adsorption to decrease in the same order

[1-63]. Grim *et al.* showed that illite reacted with organic ions up to its CEC. The ions were previously thought to be limited to the exterior surface of the illite particles, i.e. they did not replace the potassium cations between the silicate layers [1-63]. The adsorption of organic molecules to chlorite has not been investigated in much detail because its adsorption capacity is very small. It is believed that if adsorption does occur then it would be limited to external crystal edges [1-42].

1.4 Compatibilising Agents

In addition to the applications stated earlier, the main application of the surface modification applied in the following studies had the purpose of acting as a compatibilising agent. These agents compatibilised various clay minerals with the host polymer matrices of polystyrene and unsaturated polyester, which would lead to the formation of polymer-clay nanocomposites (PCNs).

Historically, the first compatibilising agent used to generate PCNs, were amino acids which were used in the synthesis of polyamide-6-(Nylon 6)-clay nanocomposites [1-64, 1-65]. The success of this material was due to the molecules acid function which had the ability to polymerise with ε-caprolactam monomers intercalated within the clay galleries. This intragallery polymerisation led to the delamination of the clay throughout the polymer matrix and a PCN was formed. Since then, a wide range of amino acids have been successfully intercalated between the layers of MMT [1-66].

N-Alkylammonium and quaternary alkylammonium cations have most commonly been reported as the compatibilising agents for more general PCN formulations. This is because they enter readily into cationic exchange with the inorganic cations situated between the layers of clays like MMT. However, other compatibilising agents have recently been used to produce PCNs which either participate in or initiate the polymerisation process. Ethylene-vinyl alcohol copolymers, have been shown to incorporate hydroxylated

quaternary alkylammonium cations; these improved the compatibility between the clay and the EVOH through the introduction of favourable hydroxyl group interactions. Some other suitable compatibilising agents for the synthesis of nanocomposites with a variety of host polymers are listed by Ogawa et al. [1-67].

In other attempts to produce PCNs, maleic anhydride grafted polypropylene has been shown to lead to the production of polypropylene-clay nanocomposites. Also, the use of aminomethyl-styrene [1-68] and living free-radical initiators [1-69] have been shown to have limited degrees of success in the formation of polystyrene-clay nanocomposites.

Silanes are another form of compatibilising agent which have been used in this regard, most particularly with thermoset resins. These molecules have shown the potential to covalently bond with the surface and edges of the clay layers through condensation reactions with the available hydroxyl groups on the clay surface.

1.4.1 *n*-Alkyl- / Quaternary Ammonium Exchanged Clays

Jordan (1949) [1-66] was the first to discover that organoclays could be dispersed in polar organic liquids, when long-chain alkylammonium ions were cation exchanged with MMT, these dispersions resulted in the formation of gels with a high liquid content. The compatibility of clay gallery spaces with various polymers can be accomplished by modifying the silicate surface with organocations via a cation exchange reaction [1-70]. The cationic head group of the alkylammonium molecule preferentially resides at the layer surface, while the aliphatic tail radiates along or away from the surface. The nature of the gallery space is altered by the presence of these aliphatic chains modifying it from its hydrophilic state to a hydrophobic/organophilic state. The organocations may also contain various functional groups, which could react with polymers and improve the adhesion between the clay platelets and a host matrix. Therefore, it is possible to obtain a

good dispersion of organoclays in organic solvents and increase the *d*-spacing of a swelling clay by increasing the chain length and/or the charge density of the clay [1-71].

The most widely used alkylammonium ions are produced when the amine function of primary alkylamines is protonated in an acidic medium. The basic formula of an alkylammonium cation is $CH_3-(CH_2)_{n-1}NH_3^+$, where *n* is between 1 and 18. It is interesting to note that the length of the ammonium ions has a strong impact on the resulting structure of nanocomposites. Alkylammonium ions based on secondary amines have also been *successfully used* [1-72].

Depending on the layer charge density of the clay, the alkylammonium ions adopt different structures between the clay layers (monolayers, bilayers, pseudo-trilayers, and paraffin type monolayers). In fig. 1.9, p. 17, the alkylammonium ions were shown to adopt a paraffin type structure (clay with high layer charge density) and the spacing between the clay layers increases by about 10 Å. Alkylammonium ions lower the surface energy of the clay so that organic species with different polarities can intercalate between the clay layers. *n*-Alkylammonium derivatives of smectites have been extensively studied and the results obtained are summarised in numerous publications (e.g. Grim [1.74], Theng [1.75], Lagaly [1.76], Jones [1.77], Newman [1.78], Favre [1.79] and Hackett [1.80]).

In the early 1990's, Lan & Pinnavaia used alkylammonium exchanged clays during a study *of the formation of epoxy resin-clay nanocomposites. Three types of Na-MMT were cation* exchanged with $CH_3(CH_2)_{n-1}NH_3^+$, where *n* = 7, 11, 18, which produced different results relative to the nature of the clay. XRD and composite testing showed that the synthesis of delaminated nanocomposites favoured exchange with alkylammonium cations with a chain length greater than C_n = 8 whereas alkylammonium cations with shorter chain lengths led to the formation of intercalated nanocomposites [1-70, 1-71]. This study was substantiated by Messersmith & Giannelis [1.73] who were concurrently conducting

23

research at Cornell University incorporating functionalised quaternary alkylammonium cations (i.e. $CH_3(CH_2)_{17}N^+CH_3(CH_2OH)_2$) in epoxy resin materials.

1.4.2 Silane Treated Clays

Silanes have been used in the synthesis of unsaturated polyester-clay nanocomposites. Silanol coupling agents are a family of organo-silicon monomers which can be characterised by the formula $R-SiX_3$, where R would be an organo-functional group attached to silicon in a hydrolytically stable manner and X would designate groups which would be converted to silanols upon hydrolysis. Silanol coupling agents interact with "receptive" inorganic surfaces forming tenacious bonds at the interface. These receptive inorganic surfaces are characterised by the presence of hydroxyl groups (OH) which would be principally attached to silicon and aluminium, which are particularly favourable for bonding with silanes. In a smectite, hydroxyl groups would be present on the gallery surfaces, and also, particularly on the edges. The silane coupling agents would first be hydrolysed to form a reactive silanols. These silanols would then H-bond to the hydroxyl groups present on the inorganic surface, before forming oxano bonds.

1.4.3 Thermal and Physical Analysis of Alkylammonium Exchanged Clays

In the years following the reports on Nylon-6 by Kojima and his co-workers at TCRD, a critical gap in the understanding of the behaviour of these nanocomposites has emerged. Most methods for fabricating PLS nanocomposites rely on very direct methods for achieving mixing, such as *in-situ* polymerisation or extrusion with high shear. Mixing the organoclay and monomer during polymerisation eases penetration of the clay galleries, but only works for systems where the polymerisation process is 'simple'.

1.4.3.1 Aluminosilicate Catalysis

The gallery surfaces of smectites, which are primarily composed of silicon and aluminium oxides, are covered by a layer of hydroxyls. This study is chiefly concerned with the

aluminosilicate surfaces showing acid character. On a surface which has been partially dehydroxylated by heating, both Bronsted (acids due to the presence of protons) and Lewis (acids which only liberate protons on reaction with water) acid sites would be expected to be present. Isomorphous substitution occurring in the silicon tetrahedral sheet, where Al^{3+} can proxy for Si^{4+}. If the Al^{3+} remained three co-ordinate, the neighbouring SiO_4^{4-} would carry an excess negative charge, which could be balanced by a proton in the form of a hydroxyl group. Such an aluminium atom would constitute a Lewis acid centre, which may react with the silanol group to form the Bronsted acid centre in the form of a proton. The proton could then catalyse hydrocarbon reactions that proceed by a carbonium ion mechanism [1-81].

1.4.3.1.1 Hofmann Degradation of Alkylammonium Surfactants

Ammonium salts (in this thesis primary and quaternary) may be converted to alkenes and ammonia by an elimination reaction, known as the Hofmann degradation reaction. In the case of *n*-alkylammonium cations, this reaction could be thermally driven, ammonia would be released as the temperature was increased. The hydrogen atoms on the alkyl chain's β-carbons would enter into nucleophilic substitution reactions (SN^2) with hydroxyl groups on the clay surface. This decomposition pathway would yield ammonia in the case of *n*-alkylammonium cations and tertiary methyl amino groups in the case of quaternary alkylamines, as well as alkenyl fragments and water.

In the case of organoclays, the proximity of the Lewis base sites (i.e. hydroxyl groups) and the basic aluminosilicate surface to the intercalated alkylammonium molecules would be conducive to enhancing (i.e. lowering the activation energy of) the Hoffmann degradation reaction. This has been shown by the lower onset temperature of the thermal desorption of alkylammonium cations in organoclays compared to their virgin state and increased alkene production. The presence of branched alkanes also implies that

secondary reactions, such as alkene addition, may occur between desorption products, which complicates a simple explanation of product generation.

1.4.3.1.2 Catalytic Cracking

The mechanisms for the reactions occurring during catalytic 'cracking' are quite well understood, and can be summarised as follows. Small concentrations of alkenes are formed by dehydrogenation of the linear hydrocarbon and these react with protons on the acid catalyst to give carbocations (carbonium ions). The stability of these ions is primary < secondary < tertiary; movement of a hydride ion (H^-) changes a primary into a secondary ion, while methyl group migration forms tertiary ions. Carbocations with long chain lengths are unstable with respect to short chain lengths, and carbon-carbon bonds are broken by β-scission to give an alkene and a primary carbocation. This and other unit steps are set out in table 1.7 [1-82, 1-83].

Dehydrogenation to alkene	$R_1CH_2\text{-}CH_2R_2 \rightarrow R_1CH=CHR_2 + H_2$
Formation of carbocation	$R_1CH=CHR_2 + H^+ \rightarrow R_1CH_2\text{-}C^+HR_2$
Methyl group migration	$CH_3\text{-}CH_2\text{-}C^+HR_6 \rightarrow C^+H_2\text{-}CH(CH_3)R_6 \rightarrow CH_3\text{-}C^+(CH_3)R_6$
Hydride transfer	$R_1CH_2\text{-}CHR_2 + R_3CH(CH_3)\text{-}CH_2R_4 \rightarrow$ $R_1CH_2\text{-}CH_2R_2 + R_3C^+(CH_3)\text{-}CH_2R_4$
β-scission	$R_3C(CH_3)\text{-}CH_2\text{-}CH_2R_5 \rightarrow R_3C(CH_3)=CH_2 + C^+H_2R_5$

Table 1.7   Reactions occurring during catalytic cracking.

The dominant side reactions which can occur are thought to be intramolecular chain transfer reactions, sometimes referred to as back-biting of the alkyl chain. This process could involve the abstraction of a backbone hydrogen by Lewis acid sites, or the donation of a hydrogen ion by Bronsted acid sites on a clay surface, both of which would result in the formation of a tertiary radical centre. This radical species would be capable of termination (i.e. through radical coupling/disproportionation), monomer addition and β-scission. The β-scission step would be the main cause of branched chain alkane formation (Table 1.7), causing the molecule to form an ion that would rearrange into a more stable

form. This may result in the formation of branched aliphatic species or various aromatic species [1-84].

More recent studies have concentrated on fundamental research like that within this thesis regarding the compatibility of organoclays with polymer-clay nanocomposite formulations. The products of thermal desorption have been the focus of several papers [1-85 - 1-87], the findings of which will be compared against the results of TG-MS analysis on *n*-alkylammonium and quaternary ammonium exchanged smectites in chapter 3.

1.4.3.1.3   Catalytic Reforming
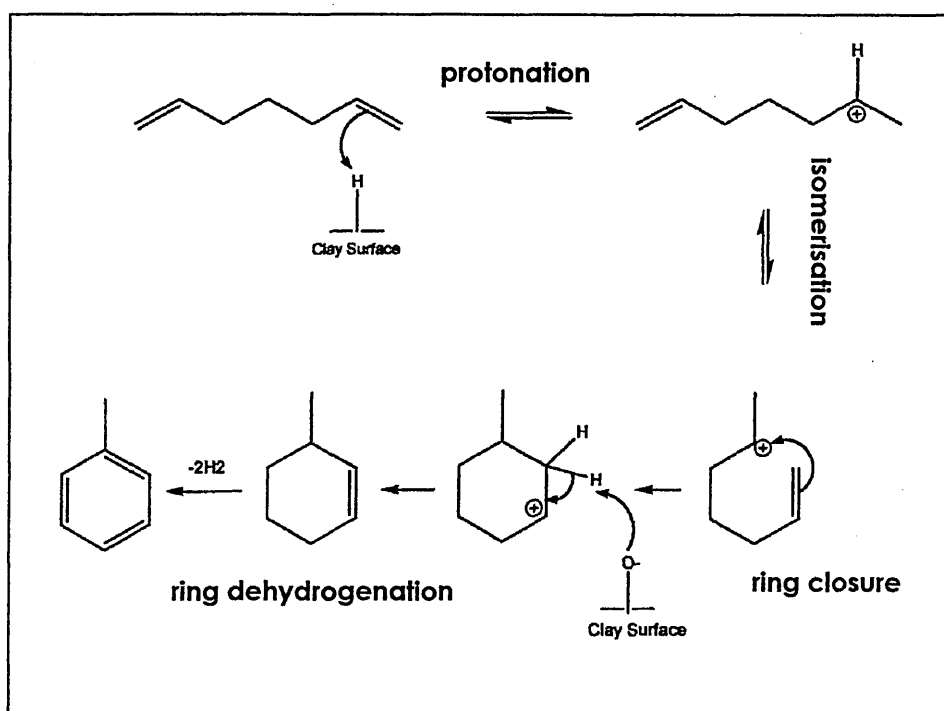
Figure 1.10   Dehydrocyclisation on an acidic clay surface [1-88].

The decomposition products that are formed (and which have subsequently been identified by TG-MS) are the following:

(i)   the dehydrocyclisation of *n*-alkanes to alicyclics, and hence to aromatics,

(ii)   dehydrogenation of alicyclic species to aromatics,

(iii)   ring enlargement of cyclopentane derivatives to cyclohexanes,

(iv)   isomerisation of n-alkanes to iso-alkanes.

All of these reactions lead to the formation of branched alkanes, ring compounds or aromatics species (fig. 1.10).

Alkanes and cycloalkanes undergo dehydrogenation to alkenes and hydrogen. The alkenes then migrate to acidic sites where they react to form carbocations and undergo either skeletal rearrangement, ring closure or ring enlargement. It can then lose a proton, becoming an alkene again, before being re-hydrogenated. This apparently complicated sequence of steps occurs with remarkable facility under these reaction conditions [1-88].

1.5   Polymers, Composites and Nanocomposite Principles

Polymer-clay nanocomposites (PCNs) are formed as the result of the hybridisation of organic polymers and specific clay minerals. More specifically, a PCN is a polymer that contains well dispersed nanometre sized (i.e. 10^{-9} m) clay particles.

1.5.1   Polymers

In contrast to the clay minerals industry, the polymer industry has been built with synthetic chemicals as its basis, although this has begun to change recently with the introduction of polylactic acid and other polymers derived from biomass [1-89 & 1-90]. Polymers have their origin in the 1930s when *polyvinyl chloride* (PVC ~ originally reported by Baumann, 1870) was the first of many thermoplastics to be commercially developed (by BASF). Following this work, Carothers [1-91] at Du Pont synthesised polyesters, neoprene and the first *polyamide - nylon 66* as a replacement for silk which was patented in 1935. A frenzy of development in the synthetic polymer industry followed, spurred on by the need for commodity independence in times of war.

Other notable polymers developed during this period were:

1935 - *polyethylene* (PE) by ICI.

1935 - *polymethylmethacrylate* (PMMA) by ICI, also goes by the tradenames acrylic and Perspex, its shatter-resistant properties were first applied to protective screens and aircraft canopies.

1937 - *polystyrene* (PS) by BASF, originally reported by Simon (1839) and again by Staudinger (1922), although it was not mass produced until 1937.

Since then, new polymers were introduced every few years including *polytetrafluoroethylene* (PTFE/Teflon), *polycarbonate* (PC), *polyethylene terephthalate* (PET), *polypropylene* (PP), *polyurethane* (PU) and *acetal* [1-92].

Other materials developed during the period 1935-1945 were *silicones*, widely used as water repellents and in heat resistant paints, *epoxy resins* for their excellent adhesion and chemical resistance properties and *polyester resins* which combined with glass fibre offered a structural material for boat and car bodies. Also, the large-scale production of artificial rubber developed rapidly, spurred on by a booming automobile industry, the military demands of WWII and the Japanese occupation of Eastern India. By 1930, two new forms of artificial rubber were developed, both based on the petroleum by-product butadiene (e.g. *acrylonitrile butadiene styrene* (ABS)). Because many of these polymers became malleable when heated, they became generically referred to as "plastics", a term taken from the Greek word "plastikos" meaning "to be moulded".

Plastics are classified as being of two basic types [1-93]:

I. *Thermoplastics* by definition are polymers which soften with heat. Example polymers are PMMA, PTFE, nylons, PC, PP, PE, PS, PVC, PET and others.

II. *Thermosets* or thermosetting plastics which harden with the application of heat. Heat is usually applied in the form of a chemical which generates heat in the liquid

plastic, causing it to become hard. Example polymers are unsaturated polyester (e.g. fibreglass resin), phenolic (e.g. bakelite) and epoxy resins (e.g. araldite).

1.5.2 Polymer Additives

From the time of their inception, polymers and polymer derivatives have been applied to an increasingly varied range of products and components that impinge on all areas of life. This is best seen in the food packaging industry where traditional glass, metal and paper have been, and continue to be, displaced by polymers. The automobile industry has also embraced polymers to reduce the weight of cars and improve manufacturing methods. However, polymers have certain limitations in both the food packaging and the automotive industries. In the packaging industry, for instance, certain foods (e.g. tomato products and beer) are sensitive to oxygen and cannot be stored in polymer containers because of the oxygen permeability of the polymer. In the automotive industry, low stiffness and tensile strength and the tendency to warp and creep under heat, load and pressure have limited the use of polymers in automotive applications.

Polymer composite materials have been developed since the 1950's to meet the requirements made of polymer materials. These plastics have been reinforced with respect to a specific failing through the incorporation of mineral fillers and fibres.

Generally, polymers have disadvantages including [1-94]:
- Poor stability in light, oxygen, air, flame, etc;
- Poor mechanical properties, i.e. hardness, stiffness, Young's modulus, rigidity, tensile strength, tear strength, fatigue strength, hysteresis loss, interlaminar fracture toughness, shear strength, complex modulus, storage modulus, loss modulus, etc;
- High heat generation under dynamic conditions;
- Easy crack initiation and crack propagation;

- Poor processing properties like complex viscosity, storage viscosity, loss viscosity, extrudate swell;
- High cost.

Due to the short-fall in desirable polymer properties mineral fillers, metals, and fibres have been added to thermoplastics and thermosets for decades to form composites. In terms of function these are classified into a large number of groups, of which the following are the most important [1-95]:

- Antioxidants (0.1-10 wt%), used to prevent the oxidation of the polymer in the presence of oxygen/air. E.g. acetone-diphenylamine-acetone-amine, 4,4'-dioctyldiphenylamine.

- Crosslinking agents (0.1-5 wt%), used to increase hardness, modulus, stiffness, tensile strength, fatigue strength, shear strength, abrasion resistance and reduce crack initiation/propagation. E.g. sulphur and hydrogen peroxide.

- Coupling agents (10 wt% of filler), provide good adhesion between filler and polymer. E.g. coating $CaCO_3$ with stearic acid to create a link between two active sites.

- Extenders (10-30 wt%), tolerated by the polymer up to a certain extent, to reduce the product cost. E.g. refinery oil and chlorinated wax.

- Fillers (30-150 wt%), generally used to increase bulk, modulus, stiffness, tensile strength, fatigue strength, shear strength, abrasion resistance and to reduce crack initiation/propagation, cost. E.g. carbon black, silica, clay, zinc oxide, fibre.

- Flame-retarders (0.1-5 wt%), used to reduce the polymer degradation against flame. E.g. antimony (III) oxide, aluminium trihydroxides, brominated and phosphorous based flame retardants.

- Peptisers (0.2-0.5 wt%), used to reduce M_w. E.g. Zn salt of pentachlorothiophenol.

Compared to their respective pure polymers and resins, composite materials show a number of improved properties. Thus, for structural applications, composites have become very popular and are sold in million tonne quantities [1-96]. These filled thermoplastics are sold in larger volumes than their virgin polymers and the volume of fillers sold is roughly equal to the volume of thermoplastic resin sold. From these quantities it has been shown that modified polymers already command a large market share of the plastics industry.

In recent years, advances made in synthetic techniques and the ability to readily characterise materials at the atomic level have led to an interest in nanometre-size materials. Nanometre-size plates, grains and fibres have a dramatically increased surface area and different chemistry when compared to traditional polymer additives. Nano-sized polymer additives have a very long tradition in the plastics industry. Carbon black/ acetylene black is produced by thermal decomposition of acetylene gas and known to have surface areas that are >1000 m^2/g, particle size <50 nm [1-97]. For many decades carbon black has been applied to the improvement of rubber. It reinforces the structure of rubber, improves wear and abrasion resistance in vehicle tyres. Carbon black is also used in plastics because it imparts UV protection, enhanced conductivity and structural reinforcement [1-98]. To put the relative quantities into perspective, hundreds of thousands of tons of carbon black are used every year for the production of vehicle tyres.

Clays have also been used as low cost fillers and extenders in polymers for many years. However, the advantages of using clays for more than just packing a polymer matrix have only become evident in recent years through the work of various research groups.

1.6 Polymer-Clay Nanocomposites

Nanocomposites are particle-filled polymers in which at least one dimension of the dispersed particles is in the nanometre range (10^{-9} m). Three types of nanocomposites can be distinguished:

i) **Isodimensional nanoparticles**, particles with three dimensions of nanometre scale, examples are spherical silica nanoparticles obtained by *in situ* sol-gel methods [1-99, 1-100] or by polymerisation promoted directly from their surface [1-101], but also can include semiconductor nanoclusters [1-102].

ii) **Nanotubes** (also referred to in the literature as whiskers), two dimensions are in the nanometre scale, forming an elongated *structure*. Examples are carbon nanotubes [1-103].

iii) **Sheets**, the third type of nanocomposite is characterised by one dimension in the nanometre range. The sheets range in thickness from one to a few nanometres and hundreds to thousands of nanometres long. This family of composites can be gathered under the name of polymer-layered crystal nanocomposites, and their study will constitute the later stages of this thesis. These materials are almost exclusively obtained by the intercalation of a *monomer or polymer inside the galleries of the layered host crystals*.

Amongst all the potential nanocomposite precursors, those based on clay and layered silicates have been more widely investigated probably because the starting materials are readily available and because their intercalation chemistry has been studied for many years [1-104 - 1-105]. Owing to the nanometre-size particles obtained by dispersion of the clay, these nanocomposites exhibit markedly improved mechanical, thermal, barrier, optical and physico-chemical properties when compared with the pure polymer or conventional (microscale) composites as first demonstrated by Kojima *et al.* [1-106] for nylon-clay nanocomposites.

1.6.1 Nanocomposite Structures

Depending on the nature of the components used (layered silicate, organic cation and polymer matrix) and the method of preparation, three main types of composites may be obtained (fig. 1.11):

i) **Phase separated composite** (fig. 1.11a) is formed when the polymer is unable to intercalate between the silicate sheets.

ii) **Intercalated structure** (fig. 1.11b) in which a single (and sometimes more than one) extended polymer chain is intercalated between the silicate layers resulting in a well ordered multi-layer morphology.

iii) **Exfoliated / delaminated structure** (fig. 1.11c) is produced when the silicate layers are completely and uniformly dispersed in a continuous polymer matrix.

Layered Silicate   Polymer

(a)   (b)   (c)

Phase separated   Intercalated   Exfoliated
(microcomposite)   (nanocomposite)   (nanocomposite)
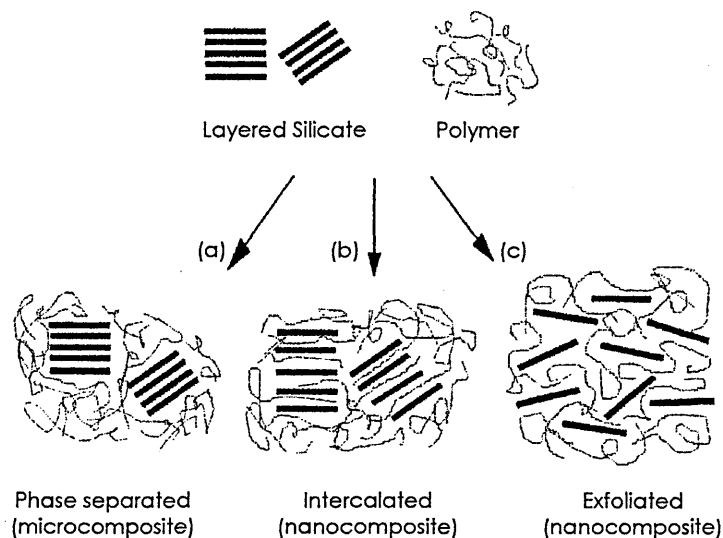
Figure 1.11   **Scheme of different types of composite arising from the interaction of layered silicates and polymers: (a) phase separated microcomposite; (b) intercalated nanocomposite and (c) exfoliated nanocomposite.**

XRD is used to identify intercalated structures, the intercalation of the polymer chains usually increases the interlayer spacing, in comparison with the spacing of the organoclay used (fig. 1.12), leading to a shift of the diffraction peak towards lower angles (the angle and d_{001} values are related through the Bragg equation (see Ch. 2, section 2.4.1)).

When exfoliated structures are achieved, no diffraction peaks are visible in the x-ray diffractograms, either because spacing between the layers is too large or because the nanocomposite no longer presents any ordering.
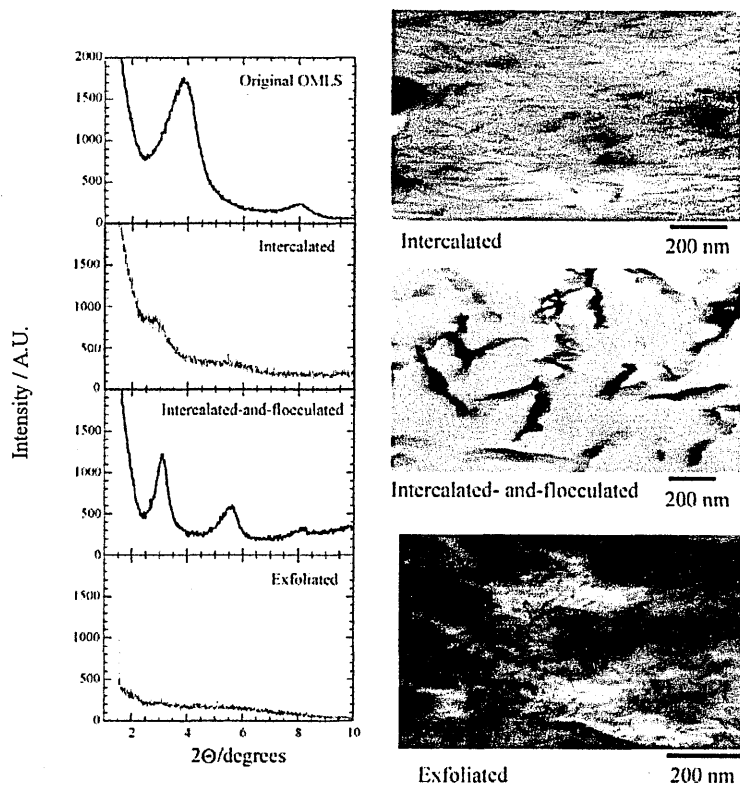
Figure 1.12 **XRD patterns and (b) TEM images for the different types of nanocomposites [1-107 - 1-109].**

Transmission electronic microscopy (TEM) may be used to demystify and characterise the nanocomposite morphology. Fig. 1.12 also shows the TEM micrographs obtained for an intercalated and an exfoliated PS nanocomposite. Besides these two well defined structures, other intermediate organisations can exist representing both.

1.6.2 Nanocomposite Preparation

Several strategies have been considered to prepare polymer-layered silicate nanocomposites. The three main processes are [1-110]:

i) *In-situ intercalative polymerisation.* The layered silicate is swollen in liquid monomer so that the polymer formation can occur in between the intercalated sheets. Polymerisation can be initiated by heat, radiation, diffusion of a suitable initiator or by fixation of an organic initiator inside the galleries before the monomer swelling step.

ii) *Melt intercalation.* The layered silicate is mixed with the polymer matrix in a molten state. Under these conditions, if the layer surfaces are sufficiently compatible with the polymer, the polymer would migrate into the interlayer space to form either an intercalated or an exfoliated nanocomposite.

iii) *Solvent adsorption.* The layered silicate is exfoliated into single layers using a solvent in which the polymer is soluble. The weak electrostatic forces that attract the silicate layers would be dispersed in an organic solvent. The polymer would then be adsorbed onto the delaminated sheets and when the solvent was evaporated (or the mixture precipitated), the silicate sheets would reassemble, sandwiching the polymer to form, in the best case, an ordered multi-layer structure. Nanocomposites are also obtained through emulsion polymerisation, under this process, where the layered silicate is dispersed in the aqueous phase.

1.6.3   Nanocomposite Property Enhancement

Blumstein [1-111] was the first to report the improved thermal stability of polymer layered silicates in the literature. PMMA was blended with MMT, with the clay forming the larger portion of the mixture. PMMA synthesised by *in-situ* intercalative polymerisation showed a higher thermal stability which was most likely due to a decrease in the relative amount of PMMA end-capped by carbon-carbon double bonds and as a result of reduced coupling /disproportionation reactions. Extracted PMMA chains were less stable than when intercalated, Blumstein proposed that this enhanced thermal stability was not only due to difference in chemical structure, but also to the macromolecules in the silicate galleries having restricted thermal motion.

Polymer-clay nanocomposites have their origin in the pioneering research conducted at Toyota Central Research Laboratories (TCRL) where nylon and MMT were successfully integrated. In the late 1980's, TCRL developed a completely new concept for the

improvement of plastic parts for the automotive industry by incorporating nanocomposite fillers. This research incorporated a bentonite clay which had been used in industry for more than 100 years.

Fukushima & Inagaki [1-112], showed that the replacement of the inorganic cations in the clay galleries with alkylammonium cations could be used to compatibilise the surface chemistry of the clay with a hydrophobic polymer matrix. ε-caprolactam was polymerised in the gallery region of the organoclay to form a nylon(6)–clay nanocomposite [1-113]. At a clay loading of only 4.2 wt%, the hybrid exhibited a doubling of modulus, a 50 % increase in strength, and the heat distortion temperature (HDT) increased by 85 °C compared to the pristine polymer (table 1.8).

Sample	Clay (Wt%)	Tensile Strength (MPa)	Tensile Modulus (GPa)	Impact (KJ/m^3)	HDT (°C @ 18.5 Kg/cm^2)
Nylon-6-MMT Nanocomposite	4.2	107	2.1	2.8	152
Nylon-6-MMT composite	5.0	61	1.0	2.2	89
Nylon-6	0	69	1.1	2.3	65

Table 1.8   Comparative physical data for Nylon-6, Nylon-6-MMT composite and Nylon-6-MMT nanocomposite [1-113 & 1-114].

It was also demonstrated that organoclays exfoliated in a nylon-6 matrix greatly improved the dimensional stability, the barrier properties and even the flame retardant properties [1-115 - 1-117]. The breakthrough of the nylon-6-MMT nanocomposite led to the first practical application as the material used for the timing belt covers on Toyota Camry vehicles [1-118]. Other recent applications of nanocomposite materials are:

(a) Wilson's Double-Core tennis balls developed at Cornell University. This material is composed of vermiculite exfoliated in butyl-rubber which reduces the materials permeability to gases.

(b) GM introduced an exterior step component on their midi-vans in the USA. This material has been described as a thermoplastic olefin (TPO) with a 2.5 wt% organoclay content. The resulting material is reported as being as stiff as and much lighter than parts with 10 times the amount of talc filler.

Supplier & Tradename	Matrix Resin	Nano-Filler	Target Market
Bayer AG (Durethan LPDU)	Nylon 6	Organo-clay	Barrier films
Clariant	PP	Organo-clay	Packaging
Creanova (Vestamid)	Nylon 12	Nano-tubes	Electrically conductive
GE Plastics (Noryl GTX)	PPO/Nylon	Nano-tube	Automotive painted parts
Honeywell (Aegis)	Nylon 6 Barrier Nylon	Organo-clay Organo-clay	Multi-purpose Bottles and film
Hyperion	PETG, PBT PPS, PC, PP	Nano-tube	Electrically conductive
Kabelwerk Eupen of Belgium	EVA	Organo-clay	Wire & cable
Nanocor (Imperm)	Nylon 6 PP Nylon MDX6	Organo-clay Organo-clay Organo-clay	Multi-purpose Molding PET beer bottles
Polymeric Supply	Unsaturated polyester	Organo-clay	Marine, transportation
RTP	Nylon 6, PP	Organo-clay	Multi-purpose, electrically conductive
Showa Denko (Systemer)	Nylon 6 Acetal	Clay, mica Clay, mica	Flame retardance Multi-purpose
Ube (Ecobesta)	Nylon 6, 12 Nylon 6, 66	Organo-clay Organo-clay	Multi-purpose Auto fuel systems
Unitika	Nylon 6	Organo-clay	Multi-purpose
Yantai Haili Ind. & Commerce of China	UHMWPE	Organo-clay	Earthquake-resistant pipe

Table 1.9   Nanocomposite suppliers, components and applications.

Table 1.9 shows a partial listing of companies marketing nanocomposite materials for different applications.

Polymers filled with nanometre-size materials have different properties than polymers filled with conventional materials. Some properties attributed to nanocomposites, like increased thermal stability and tensile strength can be achieved by using a higher conventional filler loading, but this would be at the expense of increased weight of the material. Also, properties like material clarity or improved barrier properties cannot be duplicated by filled resins at any loading. The best nanocomposite properties are believed to be obtained if the clay is fully exfoliated into single clay layers with a thickness of about 1 nm and a diameter of 20-500 nm. During delamination of the clay agglomerates, the clay structure reduces from cuboid agglomerates to flat platelets. The shape of clay platelets is usually expressed in terms of its aspect ratio, i.e. the ratio between the diameter and the thickness of a platelet.

As a result of their small dimensions, the clay platelets have a large specific surface area of about 700 m²/g. Their small size also results in small inter platelet distances in a polymer-clay nanocomposite. At a loading of 1 wt% of clay these distances are about 250 nm while they are merely 10 nm at a loading of 20 wt%.

The additive benefits of nanocomposites have been identified to include [1-119 - 1-121]:

- increased thermal stability and fire resistance
- increased reinforcement and impact strength
- improved gas/liquid barrier properties
- improved abrasion resistance
- reduced shrinkage and residual stress
- altered electronic and optical properties

1.6.4   Fire Resistance

Nanocomposites offer a new flame-retardant approach, these benefits have been identified and NIST has formed a consortium to study the flammability of polymer-clay nanocomposites.

1.6.4.1   Thermal Stability
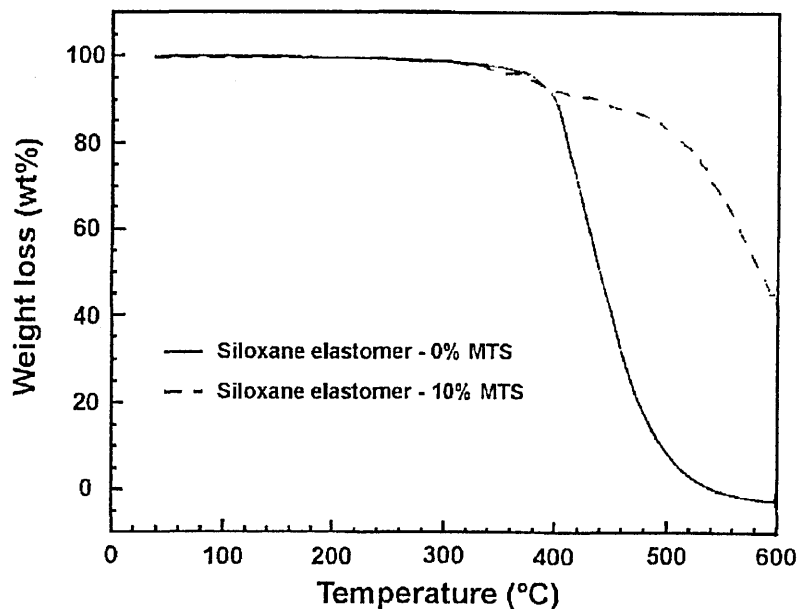
Figure 1.13   TGA traces for PDMS (solid line) and PDMS nanocomposite (dashed line) containing 10 wt% organo-modified MMT.

The thermal stability of materials has been traditionally assessed by thermogravimetric analysis (TGA), where the sample mass loss by volatilisation of degraded by-products is monitored as a function of temperature. Since Blumstein's early work, several authors have drawn attention to the thermal stabilisation brought by polymer-clay nanocomposite.

Burnside & Giannelis [1-122] used TGA (under N_2) to measure the thermal stability of cross-linked poly(dimethylsiloxane) (PDMS) in which 10 wt% of org-MMT was exfoliated. When compared to unfilled cross-linked PDMS (fig. 1.13), the TGA showed a large shift in weight loss towards higher temperature, with a stabilisation as high as 140 °C at 50 % weight loss. This was attributed to hindered out-diffusion of the volatile decomposition products (i.e.

mainly cyclic silicates), which may have been a direct result of the decrease in permeability which has been theorised for exfoliated nanocomposites.

Wang *et al.* [1-123] also studied nanocomposites based on cross-linked PDMS using slightly different operating conditions in order to produce mainly intercalated structures. These materials showed increased thermal stability for nanocomposites intercalated with 8.1 vol% of org-MMT but it was limited to about 60 °C at 50 % of weight loss. The increased thermal stability (also reported for silica-based nanocomposites in the same study) was attributed to the inactivation of the active centres in the main silicone chain, decomposition by interaction with the filler or by prevention of the unzipping degradation occurring through physical and chemical cross-linking points built up between polymer chains and filler particles.

A shift to a higher decomposition onset temperature was reported for intercalated nanocomposites of PMMA [1-124], PS [1-125] and Epoxy [1-126] when prepared by emulsion polymerisation in the presence of water swollen Na-MMT. Doh & Cho [1-108] measured the onset of thermal decomposition by TGA (N_2) for intercalated PS-based nanocomposites produced by *in-situ* polymerisation of styrene using various org-MMTs. They collected the decomposition onset temperatures of PS-based nanocomposites with increasing filler content together with a Na-MMT microcomposite for comparison. It was shown that a large increase in the onset of decomposition occurred for nanocomposites at very low filler content and quickly levelled off. The threshold was reached for filler content as low as 0.3 wt% when intercalating an organoclay modified with a dimethylbenzyloctadecylammonium cation, which was considered to be compatible with PS. In contrast, Na-MMT did not modify the decomposition onset of the PS matrix. Another useful feature of nanocomposites in which the thermal properties improvement occurs at very low filler content, is that it often makes the obtained material cheaper, lighter and easier to process than more conventional microcomposites.

The extent of the thermal stabilisation in nanocomposites may also arise from the nature of the thermal degradation mechanism, which is often different from one polymer to another. When polyimide-clay nanocomposites [1-127] were thermally degraded under N_2, their thermal stability was only enhanced by approximately 25°C (at 50% of weight loss) which was much less than the 140°C shift observed in exfoliated PDMS nanocomposites.

The thermal stability of EVA intercalated-exfoliated nanocomposites were investigated with TGA under helium (thermo-degradation) and under air (thermo-oxidative degradation) [1-128]. EVA is known to degrade in two consecutive steps, the first one, identical for both oxidative and non-oxidative degradations, results from the loss of acetic acid and occurs between 350 and 400°C. The second step involves the thermal degradation of the unsaturated backbone either by radical scission (non-oxidative route) or by thermal combustion (oxidative route). The samples studied were an unfilled EVA matrix with a vinyl acetate content of 27 wt%, a 5 wt% Na-MMT/EVA microcomposite and a 5 wt% org-MMT/EVA nanocomposite. When the second degradation step was compared under the different atmospheres, the Na-MMT was shown to have no influence on the thermal degradation of EVA under helium, however, a positive shift of 40 °C was observed in the DTG T_{max} when measured under air.

An explanation for this behaviour is the generation of char that clearly appears under oxidative degradation. Char formation acts as a physical barrier between the polymer medium and the zone where flame combustion occurs.

Also within this study, the effects on DTG T_{max} under oxidative degradation conditions at different Na-MMT loadings in the EVA-based nanocomposites were studied. No additive thermal stability was observed until a 2.0 wt% loading was reached, the optimal thermal stability was shown to be between 3.0 – 5.0 wt%, and above this loading the thermal stability was shown to decrease. This behaviour may account for a change in the ratio of

exfoliated to intercalated species with increased clay loading. At lower clay loadings, an exfoliated phase may have been dominant, but the loading of exfoliated platelets may not have been sufficient to promote the thermal stability of the polymer matrix through char formation. The increase in clay loading between 2.0-5.0 wt%, would have increased the concentration of exfoliated platelets dispersed throughout the EVA matrix. This could have led to the creation of an optimal platelet dispersion, from which, a char layer would have formed more completely, and by doing so, increased the thermal stability of the PCN. At higher clay loadings, the agglomeration of these clay platelets may have increased, char formation would have been discrete and increasingly reduced. This change to the physical arrangement of components in the PCN would not create a physical barrier to decomposition and would not maintain good thermal stability.

1.6.4.2   Flame Retardancy

The flame retardant properties of nanocomposites have been reviewed by Gilman [1-129]. The pilot-scale method used to measure the flame retardant behaviour of a material was cone calorimetry which produced data relating to the heat release rate (HRR), peak heat release rate (pHRR), mass loss rate (MLR), heat of combustion and smoke emission. Samples were exposed to a given heat flux (often taken as 35 kW/m^2) and the results were recorded as a function of time. The reduction of a pHRR has previously been used as the evidence for the efficiency of a flame retardant (fig. 1.14 and 1.15).

Experiments which were conducted in a radiative gasification apparatus [1-130] showed that the flame retardant effect of nanocomposites mainly arises from the formation of char layers obtained through the collapse of the exfoliated and/or intercalated structures. This multi-layered silicate structure may act as an excellent insulator and mass transport barrier, slowing down the escape of the volatile decomposition products as observed in nylon-6 but also in thermoset nanocomposites [1-131].
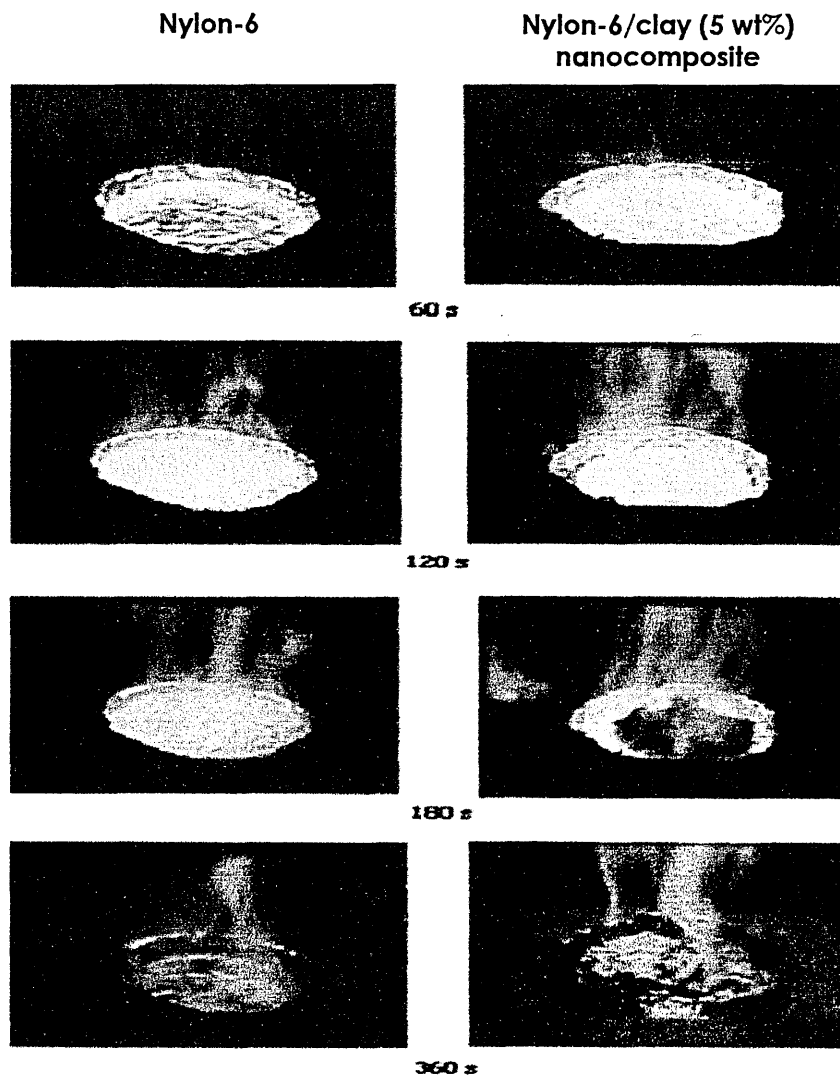
Figure 1.14 Formation of char layer in Nylon-6 / 5wt% org-MMT. This char formation impedes the movement of volatilised polymer from the interior of a plastic, denying fuel at the air/surface interface. Char formation delays fire propagation and prevents the formation of burning droplets of polymer material, e.g. Nylon-6/5wt% clay, pHRR ↓ 70%, HDT ↑ 130% [1-129].

Both thermoplastic and thermoset nanocomposites with exfoliated and intercalated structures have been reported, and the same interlayer spacing (~ 13 Å) has always been reported for the recovered chars as analysed by XRD. This implied the formation by combustion of a residue of the same nature. A Nylon-6 nanocomposite, filled with 2 wt% org-MMT has also been used as an additive to replace pentaerythritol (in order to avoid exudation and water solubility) in an intumescent flame retardant formulation using ammonium polyphosphate (APP) [1-130]. This formulation showed very good fire retardant

properties, increasing the low oxygen index (LOI) values by 5% for the best APP/nylon-6 nanocomposite composition and highly decreasing the HRR values.
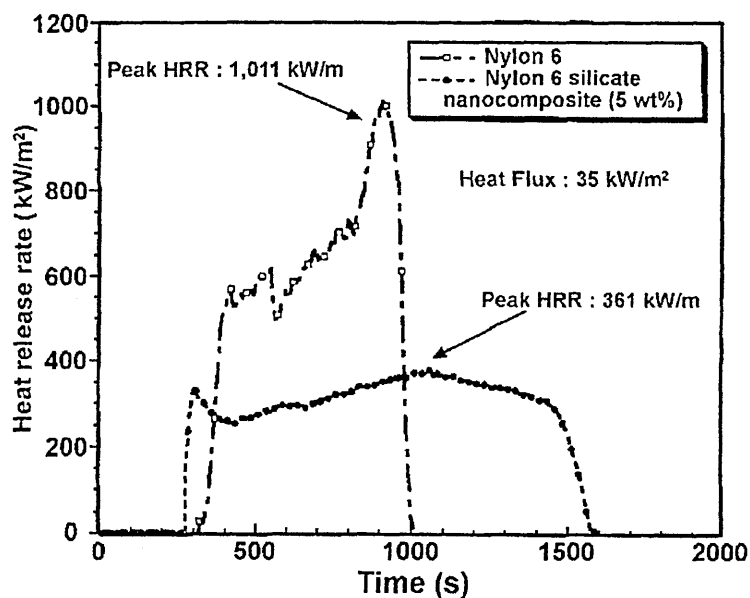
Figure 1.15 **Comparison of the HRR plots for nylon-6 and nylon-6-MMT nanocomposite (5 wt%) at 35 kW/m2 heat flux - showed a 63 wt% reduction in HRR for the nanocomposite [1-129].**

1.6.5 Mechanical Properties

An unexpected large increase in the moduli (tensile or Young's modulus and flexural modulus) of PCNs with organoclay loadings as low as 1 wt% has previously been shown. PCN material stiffness was shown to be substantially enhanced whatever the method of preparation, examples of this have been shown through PCN polymerisation within org-MMT (NCH) [1-115], polymerisation within protonated ε-caprolactam swollen MMT (L-NCH) [1-133], and polymerisation of ε-caprolactam, an acid catalyst and natural MMT (one-pot-NCH) [1-134].

1.6.5.1 Tensile Modulus (Young's Modulus)

The tensile or Young's modulus of a material is a measurement of its stiffness. This property has been shown to be strongly improved when PCNs are formed. Nylon-6 PCNs obtained through the intercalative ring opening polymerisation of ε-caprolactam, leading to the

formation of exfoliated nanocomposites, which showed a dramatic increase in tensile modulus at low organoclay loadings.

Nylon-6-ADA-MMT (wt%)	Flexural Modulus (MPa)	Tensile Modulus (MPa)	HDT(°C)
0%	2836	2961	56
2%	4326 (53%)	4403 (49%)	125 (123%)
4%	4578 (61%)	4897 (65%)	131 (134%)
6%	5388 (90%)	5875 (98%)	136 (143%)
8%	6127 (116%)	6370 (115%)	154 (175%)

Table 1.10   The property effects on Nylon-6-ADA-MMT with increased organoclay loadings [1-115].

The tensile modulus and other properties of exfoliated nylon-6 PCNs with various clay loadings were measured at 120 °C [1-115] (table 1.10). The samples were produced by the *in-situ* polymerisation of ε-caprolactam in the presence of protonated aminododecanoic acid (ADA)-modified MMT (average length: 1000) and saponite (500). The tensile modulus showed greater increase with the MMT, which showed that the average length of the layers, and in turn to the aspect ratio of the dispersed platelets. Also, the nylon-6-MMT PCNs were believed to show greater levels of exfoliation [1-134].

In contrast to the above results, intercalated structures (i.e. no exfoliation) such as for PMMA [1-124] and PS [1-125] based PCNs, obtained by emulsion polymerisation in presence of water-swollen Na-MMT were considered. The increase in tensile modulus was shown to be relatively weak, for example an increase of only 0.09 GPa was shown, from 1.21 GPa for PMMA to 1.30 GPa for PMMA containing 11.3 wt.% intercalated MMT. These results attested to the inefficiency of intercalated structures to improve the stiffness of these PCNs.

1.6.5.2   Stress at Break

In intercalated and exfoliated PCNs, the stress at break (which expresses the ultimate strength that the material can bear before break) has been reported to vary greatly, depending upon the nature of the interactions between the matrix and the filler. In PS intercalated nanocomposites [1-125], the ultimate tensile stress was reported to be lower than an exfoliated PS nanocomposite and reduced further as the clay loadings were increased. This reduction in properties was attributed by the authors to the fact that only weak interactions existed at the PS-MMT interfaces in the intercalated hybrids, whilst the exfoliated hybrids had stronger, polar interactions which strengthened the clay-polymer interface.

1.6.5.3   Impact Properties

The impact properties have been measured for nylon-6-based nanocomposites prepared either by *in-situ* polymerisation of ε-caprolactam using protonated aminododecanoic acid-exchanged MMT [1-115] or by melt intercalation of nylon-6 in octadecylammonium exchanged MMT [1-135]. Both methods lead to exfoliated nanocomposites especially when the filler content does not exceed 10 wt% (at higher loadings, melt-intercalation provides partially exfoliated/partially-intercalated materials). The impact properties have not been shown to be significantly reduced by the formation of nylon-6-MMT PCNs, whichever preparation process was used. In the case of *in-situ* polymerisation, the Izod impact strength is reduced from 20.6 to 18.1 J/m when 4.7 wt% of organoclay was incorporated. Charpy impact testing showed a similar reduction in the impact strength with a drop from 6.21 kJ/m² for the filler-free matrix down to 6.06 kJ/m² for the 4.7 wt% nanocomposite. This relatively good resistance to impact, together with a high tensile modulus, good flexural modulus (i.e. measure of resistance to bending under load) and enhancement of the increase in the HDT going from 65 °C for pure nylon-6 to more than 150 °C for the nanocomposites, have allowed this material to replace glass fibre reinforced nylon or PP in the production of timing belt covers of automotive engines [1-118]. The

timing belt cover, produced by injection-molding, showed good rigidity, excellent thermal stability and no warp. Another additional benefit was a 25 % reduction in the weight of the material, this was due to the very small content of inorganic material in the final composition.

1.6.6 Gas/Liquid Barrier Properties

The high aspect ratio characteristic of clay platelets in exfoliated nanocomposites has been found to impart a tortuous path (fig. 1.16) to the diffusion of gas and liquid molecules, highly reducing the permeability in films prepared from such materials [1-136].
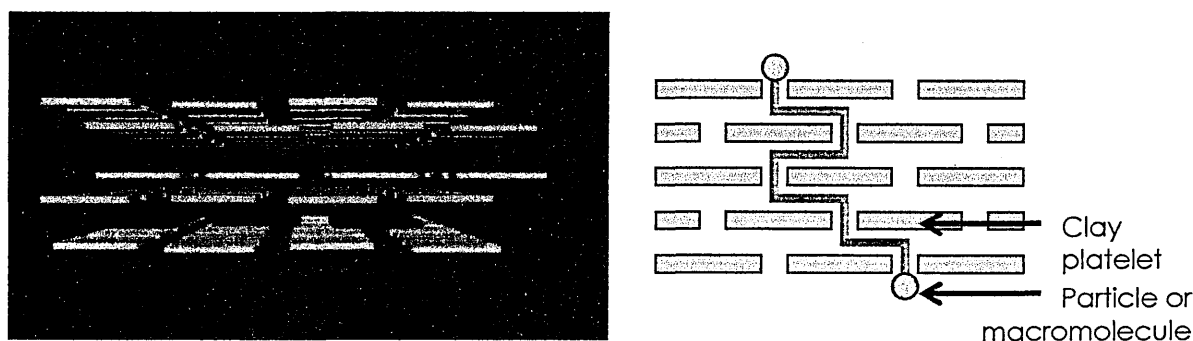
Figure 1.16   Schematic diagrams representing the barrier to diffusion expressed in the Tortuous Path Theory [1-136].

The effect on water permeability of both partially and totally exfoliated poly(imide)-based nanocomposites has been reported by Yano *et al.* [1-137], using organoclay with different layer lengths. Fig. 1.17 presents the clay length dependence of the relative permeability coefficient for poly(imide) filled with 2 wt% of organoclay, either exfoliated MMT and synthetic mica, or intercalated clay tactoids (hectorite and saponite). A relatively good agreement between the experimental values and the corresponding theoretical curve was achieved, as the length of the clay increases, the relative permeability decreases drastically. These results indicated that the best gas barrier properties would be obtained in exfoliated PCNs with a high aspect ratio.
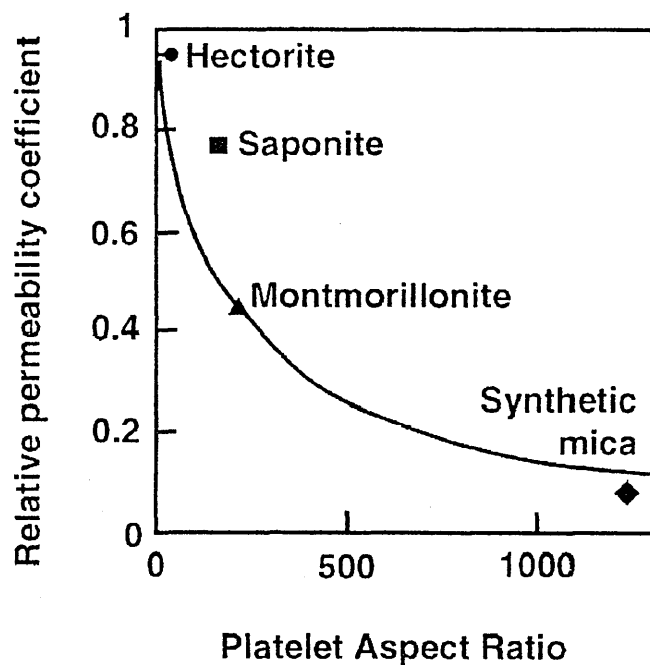
Figure 1.17   **Clay length dependence on the relative permeability coefficient for poly(imide)/clay nanocomposites [1-138].**

The permeability to carbon dioxide has been measured for a partially-exfoliated poly(imide)-PCN by Lan *et al*. [1-138]. The relative permeability values, i.e. Pc/Pp where Pc and Pp are the composite and the unfilled polymer permeability, respectively, were plotted as a function of the filler volume fraction (fig. 1.18). These plots show the dramatic effect that increased aspect ratio has on the relative permeability.

Permeability to water vapour has also been investigated for exfoliated nanocomposite based on poly(ε-caprolactone) (PCL), synthesised by *in-situ* polymerisation of the lactone monomer inside an org-MMT [1-139]. In order to produce nanocomposite films with different filler contents, PCL nanocomposite containing 15 wt% (6 vol%) of exfoliated MMT was separately prepared and mixed in variable composition with a commercial preformed PCL by co-dissolution in toluene followed by solvent casting.

49
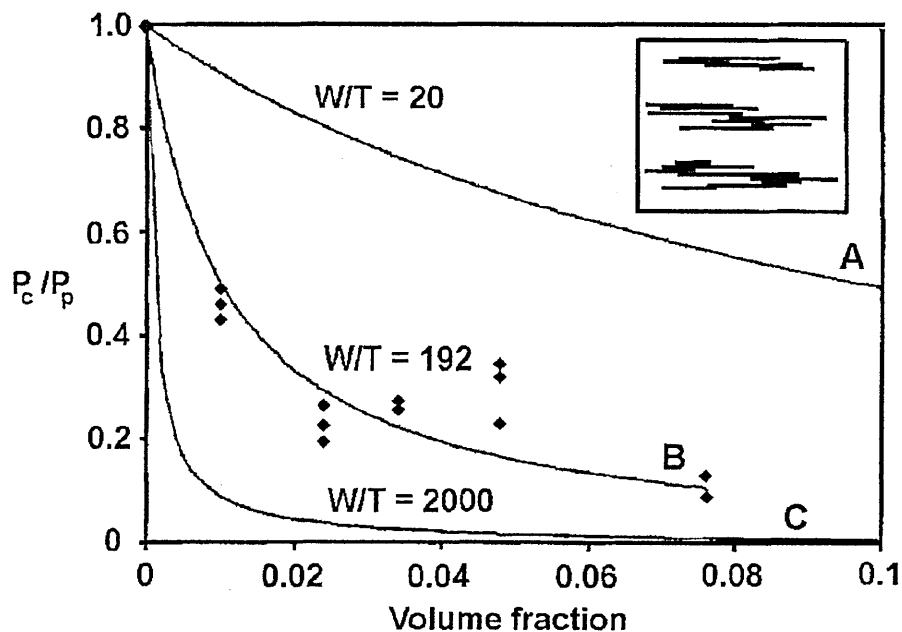
Figure 1.18 CO₂ permeability of polyimide clay composites prepared by curing CH₃(CH₂)₁₇NH₃ MMT-poly(amic acid) films at 300°C. Curves A and C were calculated for filler with an aspect ratio of 20 and 2000, respectively, Curve B was generated by least squares fitting of the permeability equation to the experimental data [1-138].

Again, a dramatic drop in the relative permeability of the polymer coefficient is triggered by dispersing increasing amounts of layered nanofiller. A relative permeability of 0.2 (unfilled PCL permeability) was measured for a filler loading of 4.8 vol%. Curve fitting for the relative permeability against organoclay loading led the authors to conclude to an aspect ratio of 70, which was well below the value expected for exfoliated MMT would offer the greatest barrier to permeability. The authors explained this apparent discrepancy by the fact that the fitting model was originally developed for particles totally oriented parallel to the film plane. However, under the experimental conditions used for the film formation, the clay platelets may not have been so well aligned within the host polymer and may have even formed aggregates. Bayer has recently commercially produced a new grade of plastic film for food packaging, this material is known as Durethan1 LPDU 601. This film is based on a exfoliated nylon-6-PCN. Studies on the films have shown this material to offer improved gas barrier properties (i.e. the oxygen transmission rate was halved compared with the pure nylon-6), improved transparency, gloss and increased tensile modulus [1-140].

1.7 Polystyrene Clay Nanocomposites (PSCN)

Several attempts to produce polystyrene-clay nanocomposites (PSCN) have been reported in the literature. Early attempts by Friedlander & Grink [1-141] and Blumstein [1-111] to impregnate clay with styrene monomer followed by polymerisation, showed little or no expansion of the d-spacing of the clay layers, which lead to confusion over the state of the polystyrene within the clay galleries. Kato *et al.* [1-142] were the first to report the intercalation of styrene into a stearyltrimethyl-ammonium (C_{18}) cation exchanged MMT.

1.7.1 *in-situ* Polymerisation

Alternative methods for the inclusion of polymer into the gallery spaces have been reported. Akelah & Moet [1-143] prepared PSCN from acetonitrile using Na-MMT which was cation exchanged with vinyl-benzyltrimethylammonium chloride. The products were reported to be intercalated PSCN with a maximum d-spacing of 24.5 Å. Similarly, Fu & Qutubuddin [1-144] developed the process of *in-situ* polymerisation further by using vinylbenzyldimethyldodecylammonium chloride (VDAC) surfactant, which again this included a vinyl bond. The vinyl bond of the VDAC surfactant was soluble in the styrene monomer and was thought to enter into the polymerisation reaction, which lead to the production of an exfoliated PSCN. This PSCN was prepared by the direct dispersion of organoclay within styrene monomer which was followed by initiating with AIBN, before curing at 60 °C/48 hrs.

Another process for fabricating polystyrene-clay nanocomposites was developed and reported by Giannelis *et al.* [1-145] via polymer melt intercalation. Problems associated with this are similar to those mentioned earlier, i.e. those of organophilic-organophobic interactions, and as such, the diffusion of molten polymer into the galleries is very slow, dependant on factors such as temperature, molecular weight of polymer and organocation chain length [1-146 & 1-147]. Doh & Cho [1-108], prepared PS-MMT intercalated nanocomposites by polymerisation in the presence of organophilic clay. This

intercalated PSCN showed greater thermal stability than pure PS. In PSCNs with an organoclay containing benzyl-units similar to styrene, the thermal stability was shown to be higher than for other PSCNs with organoclays containing quaternary alkylammonium cations. This study concluded that the structure and properties of surfactant used in production of an organoclay could play an important role in determining the properties of PCNs.

1.7.2 Melt Intercalation

Melt intercalation of PS and its derivatives has been widely studied. Vaia & Giannelis [1-147] studied PS as the matrix for dispersing different clay species. Li-fluorohectorite (CEC = 150 mEq/100 g), saponite (100 mEq/100 g), and Na-MMT (80 mEq/100 g) were modified using various ammonium cations: dioctadecyldimethylammonium, octadecyltrimethyl-ammonium and a series of primary alkylammonium cations with C_n = 6, 9, 16 & 18. PSCNs were synthesised by statically annealing (i.e. without mixing) an intimate pelletised mixture of organoclay in PS (Mw = 30,000, Mw/Mn = 1.06) under vacuum at 170 °C, a temperature well above the PS glass transition [1-148].

The results of this study indicated that for a given alkyl surfactant, increasing the CEC from 80 to 120 mEq/100 g allowed for PS intercalation to occur. At lower CECs and when the organic content of the gallery was lowest, no intercalation was observed. Under these conditions, the aliphatic alkyl chains of the organocations adopted a monolayer arrangement characterised by low gallery height. Interestingly enough, intercalation took place at lower CECs at the condition to modify the clay surface with ammonium cation bearing two long alkyl chains. However, excessive packing of the chains all along the layer surface (high CEC and two long alkyl chains per cationic head) lead to the formation of a non-intercalated structure as predicted by the theory introduced by Vaia & Giannelis [1-147]. The authors also found that polymer intercalation depended on the length of the exchange ammonium cation as well as on the annealing temperature. At annealing

temperatures ≤ 160 °C and for C_n < 12, no intercalation was detected, while for higher chain length organocations PS was readily intercalated. At 180 °C, intercalation occurred at whatever the ammonium chain length. Also reported within this study were the effects of PS molecular weight (MW). Contrary to the prediction that high MW PS would be excluded on the basis of size, intercalation was shown to occur at all different PS MWs. The only difference between the preparation processes for these samples was the period of time needed for the intercalation to proceed; this period increased from 6 h for a MW = 30,000 to 24 h for MW = 90,000 and up to 48 h for MW = 400,000 at 160°C. The high MW PS chains were believed to have decreased the kinetic rate of intercalation by decreasing the diffusion of the PS chains into the galleries.

Vaia et al. [1-149] studied the kinetics of melt intercalation by following the time evolution of XRD diffraction patterns for statically annealed PS/octadecylammonium exchanged fluorohectorite. The change in intensity of the pristine and intercalated diffraction peaks with time was reported as a reflection of the kinetic rate of the PS intercalation process (fig. 1.19). By integrating the intensity of both the non-intercalated and intercalated peaks, the fraction of intercalated fluorohectorite was estimated as a function of the annealing time.
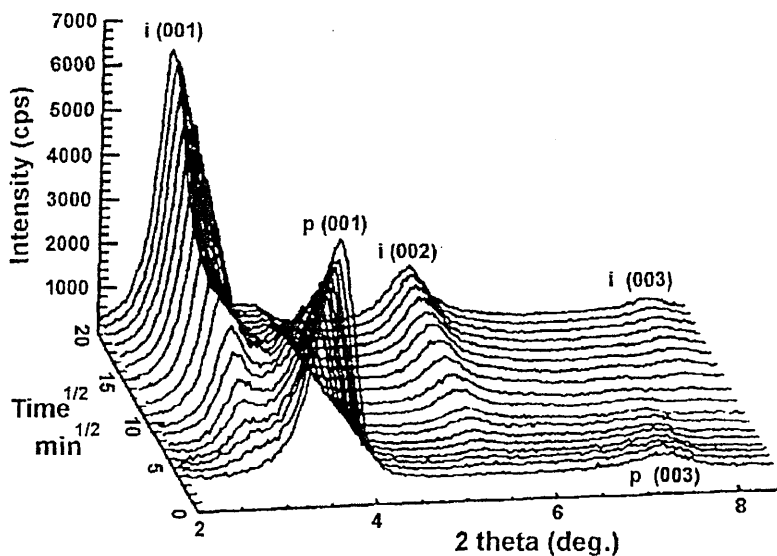
Figure 1.19   XRD patterns for a organo-fluorohectorite/PS pellet annealed in situ at 160°C in vacuum. $p_{(001)}$ and $p_{(002)}$ locate the basal reflections for the unintercalated fluorohectorite while $i_{(001)}$, $i_{(002)}$ and $i_{(003)}$ correspond to the basal reflections for the intercalated nanocomposite that is forming with time [1-149].

The influence of both the annealing temperature and PS MW were then determined. Higher annealing temperatures and lower MW were reported to increase the rate of PS intercalation.

To give a more concrete interpretation of the kinetic data, the morphology of the modified MMT was examined by TEM. The authors found that the average silicate agglomerate (approx. diameter ~175 mm) consisted of many smaller cubic platelets, and were termed primary particles. Based on this morphology and TEM observations of partially intercalated composites, it was reported that the accessibility of the interlayer to the polymer chains depended on the location and orientation of the primary particles within the agglomerates and on the location and orientation of the crystallites within the primary particles. This meant that the crystallites near the edge would be more accessible to polymer chains than those closer to the centre. Since the clay layers are impenetrable, the polymer must have entered the gallery from the edges of the crystallites. The authors observed that, under their experimental conditions, the polymer penetrated the agglomerate and surrounded the primary particles before the occurrence of substantial intercalation, therefore, they assumed that the polymer penetration within the agglomerate was not a limiting step for intercalation. Furthermore, they demonstrated that the rate of PS intercalation was dependent upon the size of the primary particles, bigger primary particles being less intercalated than smaller ones, for a given annealing time.

This size dependence was explained by the lack of a significant difference in the mass transport between and through the crystallites within a given primary particle, and so, PS intercalation was described as a Fickian process with a single diffusivity. The PS diffusion into the primary particles was sketched as a mass flow through the curved lateral surface of a cylinder bearing impermeable flat circular faces of area equal to the mean primary particle size. The activation energy of the melt intercalation was calculated based on the experimental values of the effective diffusional rate obtained at different temperature.

Assuming an Arrhenius temperature dependence, the activation energy for the PS (Mw = 30,000 and Mw/Mn = 1.06)/ modified fluorohectorite composite was 166 kJ/mol, comparable to the activation energy measured for self-diffusion of PS (167 kJ/mol) [1-149]. This indicated that the largest energy barrier to PS intercalation is comparable to that of PS chain motion within the polymer melt. Since mass transport into the primary particle had been observed to be the limiting step to complete intercalation, any dynamic mixing should decrease the intercalation time by breaking down the primary particles and increasing the sample uniformity, this opened the way to the preparation of intercalated PS mixture within a few minutes.

Vaia et al. [1-146] have synthesised both ordered and disordered intercalated nanocomposites by mixing PS with MW = 30,000 or MW = 400,000, respectively, with octadecylammonium-exchanged fluorohectorite; and, PS with a MW = 30,000 or MW = 55,000 with poly(3-bromostyrene) with dodecylammonium-exchanged fluorohectorite on the other side. TEM characterisation showed that the ordered intercalated materials exhibited regular microstructures which were similar to the non-intercalated organo-fluorohectorite. In this case, the polymer intercalation occurred as a front which penetrated the primary particles from the external edges while for disordered intercalated systems, a heterogeneous microstructure is observed, with pronounced interlayer disorder with greater spacing towards the polymer-primary particle boundary. In the latter PSCNs, individual silicate layers were observed near the edges, whereas small coherent layer packets separated by polymer-filled gaps were prevalent inside the primary particle. This study also showed that intercalation was favoured by the presence of defects in the layer stacking that would allow the polymer to penetrate more easily into the gallery spaces.

PCNs can also be formed using emulsion polymerisation, i.e. the clay is dispersed in an aqueous solution containing a surfactant. In an aqueous environment the interlayer expands and the presence of surfactant is thought to stabilise the monomer by reducing its

hydrophobicity, allowing it to enter the clay galleries more readily. Polymerisation is achieved by using a free-radical initiator and the resulting PCN would then be precipitated by using a metal salt of high ionic strength, e.g. Al(III) salts. The resulting latex then requires extraction with organic solvents to remove the included water. Examples of this have been reported using PS and PMMA [1-124 & 1-125].

PSCNs have been prepared by both the *in-situ* polymerisation and melt intercalation methods. Zhu *et al.* [1-150] prepared both intercalated and exfoliated structure PSCNs using a bulk polymerisation technique; and reported that the intercalated or exfoliated structure of the nanocomposite depended upon the nature of the organocation.

Tseng *et al.* [1-151] reported the preparation of syndiotactic PS/modified-clay nanocomposites by solution blending a mixture of pure s-PS and an organophilic clay in dichlorobenzene. PSCNs have also been prepared from PS and Na-MMT using an emulsion polymerisation technique [1-125]. A comparison of the solution, emulsion, suspension and bulk polymerisation techniques along with melt blending has also been performed [1-152].

Zeng *et al.* [1-153, 1-154] prepared PSCNs via *in-situ* bulk polymerisation and studied the effects of initiators and clay surface chemical modification. A shear-induced ordered structure in an exfoliated PSCN was reported by Chen *et al.* [1-155]. The self-assembly behaviour was measured by XRD patterns, TEM, and FTIR dichroism technique. Compared with the broad amorphous peaks of the PS, a series of sharp XRD peaks were observed for the extruded PS/clay nanocomposite pellet sample, showing that an ordered structure occurred under shear flow.

1.8 Unsaturated Polyester-Clay Nanocomposites (UPCNs)

Conventional composites are based on microscale reinforcement. Unsaturated polyesters are widely used as a matrix for composites because of their low cost and excellent

chemical resistance. Research in the area of unsaturated polyester-clay nanocomposites (UPCNs) has to date been limited. As a result what follows are the results of an almost exhaustive list.

Lee & Giannelis [1-156] were the first to report partially-exfoliated MMT in UPCNs. Kornmann *et al.* [1-157] later synthesised UPCNs by modifying MMT with silanes and dispersing it in unsaturated polyester resin (UPR) prior to curing. The clay was reported to be partially delaminated and substantial improvements of in its mechanical properties were observed over UPR. They also found that the fracture toughness doubled by dispersing merely 1.5 vol% of MMT with concomitant increases in other mechanical properties.

Suh *et al.* [1-158] reported that the properties seen with UPCN were greatly dependent on the preparation procedure, with respect to the order of mixing of the clay, polyester resin and promoter (styrene monomer), as well as, the cure conditions. The structures of UPCN with Na-MMT were investigated by XRD (fig. 1.20) and TEM and the formation mechanism was studied using DMTA, solution and melt rheometry.
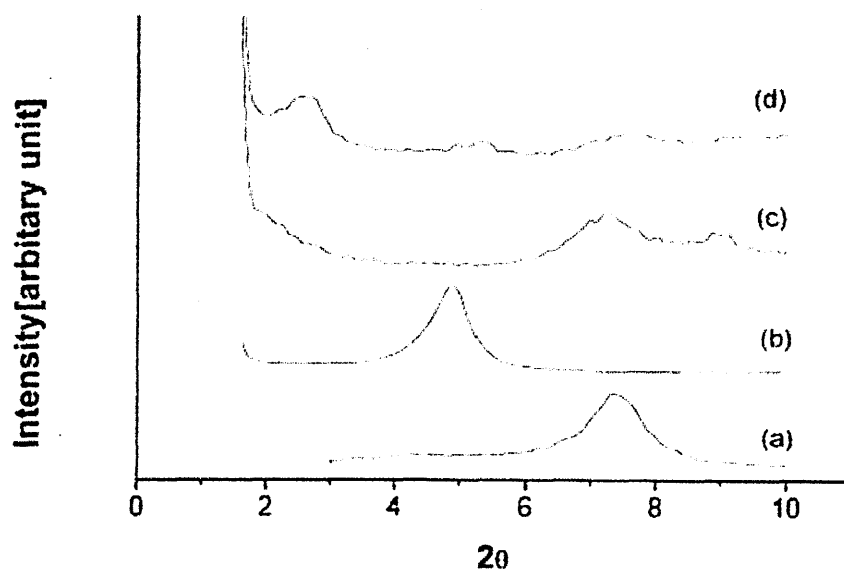
Figure 1.20   XRD data for UP with dodecyl ammonium-treated silicate nanocomposite system (C20A): (a) virgin MMT; (b) dodecyl ammonium-treated MMT; (c) virgin MMT and UP nanocomposite; and (d) dodecylammonium-treated MMT and UP nanocomposite [1-158].

57

These techniques enabled the authors to elucidate that the styrene monomer moved more easily than uncured UP chains, which may generate higher styrene monomer concentrations in the MMT gallery than in any other part in a simultaneous mixing system. When polymerisation occurred in these conditions, the total cross-linking density of the sample decreased, due to the low concentration of styrene in the uncured UPR.

This UPCN formation mechanism, became clearer when a sequential mixing method was used. The styrene monomer was thought to diffuse to the gallery of the MMT already pre-swollen with UPR to an extent. It was thought that the cross-linking density and T_g of UPCNs increased to some extent. As mixing time increased, the styrene monomers and curing agents would be more dispersed inside and outside of the silicate layers. Therefore, the cross-linking reaction would take place homogeneously inside and outside of the silicate layers, and cross-linking density would reach the degree of cross-linking density of the cured UPR. This work highlighted that nanocomposite formation mechanisms and manufacturing processes need to be carefully considered when UPCNs are manufactured using several kinds of polymers or monomer–polymer pairs which have large MW differences. The experimental considerations should be based around multi-intercalating nanocomposite systems, nanocomposite systems using compatibilisers and multi-component polymer nanocomposite systems.

Bharadwaj et al. [1-159] produced UPCNs by dispersing methyltallow bis-2-hydroxyethyl quaternary ammonium chloride modified MMT in pre-promoted polyester resin and subsequently cross-linked at room temperature. The formation of a nanocomposite was confirmed by XRD and TEM. The structural morphology was studied at different length scales and was reported as being a dispersion of intercalated/exfoliated aggregates of clay sheets in the matrix. The resulting UPCNs were characterised for thermal, rheological, mechanical, gas transport and optical transmission properties.

Although there was morphological evidence which showed the formation of a UPCN structure, the tensile modulus and loss of storage modulus were progressively decreased with increased clay loadings. The rate of thermal degradation was also hastened upon the formation of a nanocomposite (fig. 1.21).
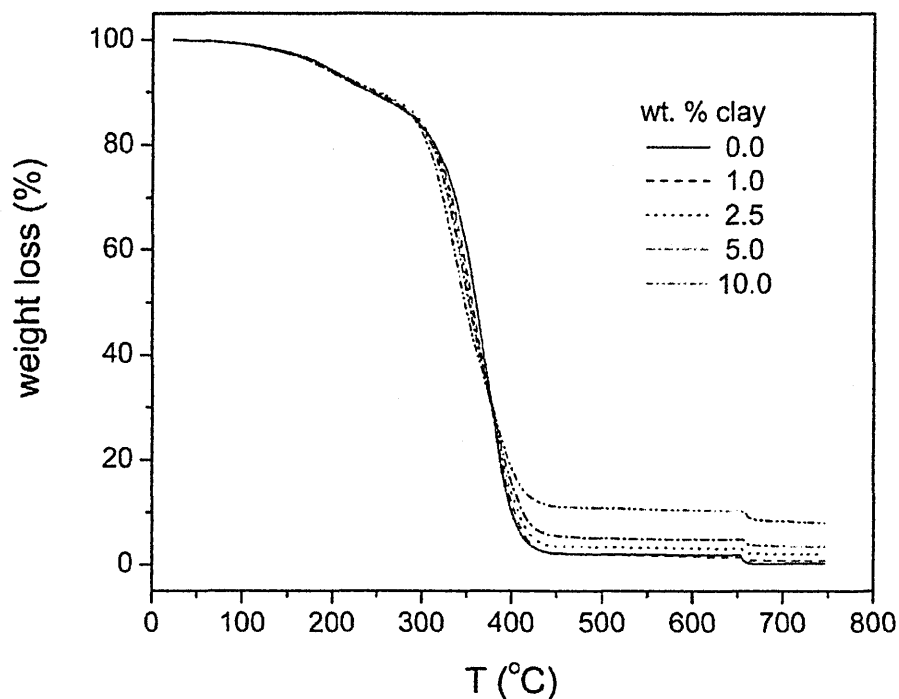
Figure 1.21   TGA thermal degradation profiles for the cross-linked UPCN at different concentrations of clay [1-159].

These trends were hypothesised as being due to a progressive reduction in the degree of cross-linking with increasing clay concentration. While this explanation was reasonable, the authors noted that a lack of detailed knowledge of the structure of the polyester resin prevented then from making a detailed explanation.

Oxygen permeability was found to be reduced with increasing clay concentrations. The barrier properties were found to correlate well with the observed morphology, this result was in keeping with the increasingly tortuous path for the diffusing penetrant (fig. 1.22).

An observed reduction in the loss and storage modulus, tensile modulus and oxygen permeability values at the 2.5 wt% clay concentration was found to be greater when compared to that seen at higher concentrations. This behaviour was traced to the exfoliation occurring on a more global scale in the 2.5 wt% case presumably leading to a greater drop in the degree of cross-linking. However, the authors also recognised that this property reduction may in part be due to the clay-compatibiliser-polymer interface and the effects of the organic compatibiliser on the matrix resin.
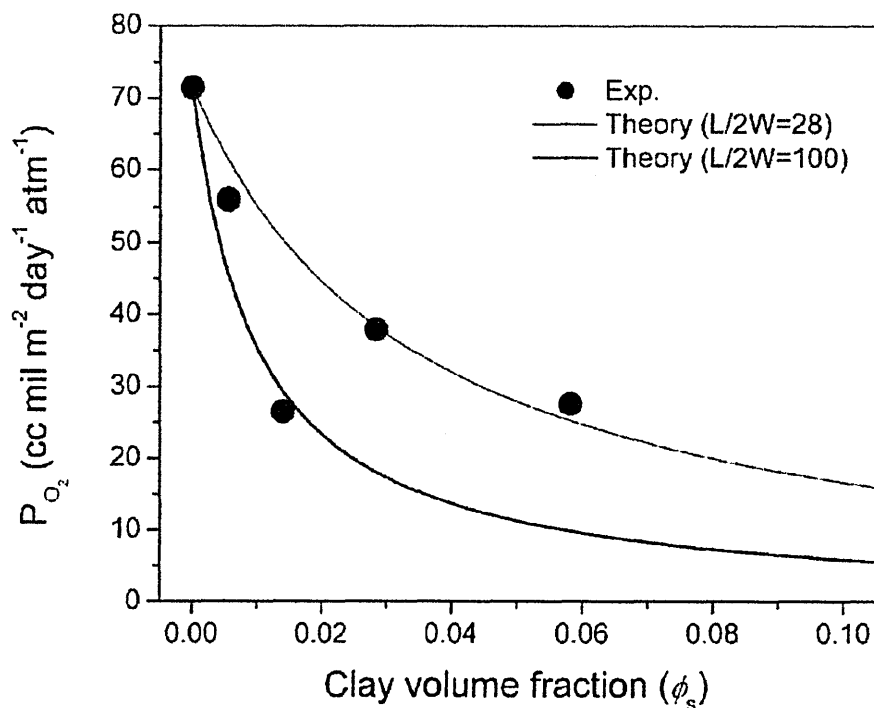
Figure 1.22   Oxygen permeability of the cross-linked polyester-clay nanocomposites as a function of clay volume fraction at 40°C and 90% relative humidity. Experimental data and theoretical fits are displayed [1-159].

UPR nanocomposites have recently been produced by incorporating nanoparticles of TiO_2 (titania) [1-160] and Al_2O_3 (alumina) [1-161], which produced mixed results. The dispersal of TiO_2 in a commercially available, highly cross-linked polyester resin, had a significant effect on fracture toughness. Even at volume fractions as low as 1, 2, and 3 vol.%, increases in toughness of 57, 42, and 41%, with respect to the neat polyester. The slight decrease in toughness beyond 1 vol.% is attributed to a slight increase in agglomerations beyond this

point. Also, the inclusion of the nanoparticles was reported to contribute to a moderate stiffening behaviour of the material.

Alternatively, when Al_2O_3 particles were incorporated at various volume fractions, any enhancement of fracture toughness was strongly influenced by the particle-matrix adhesion [1-158]. Untreated particles exhibited very poor bonding with the unsaturated polyester matrix, which resulted in a lack of crack trapping, and so, no enhancement of fracture toughness. Similar results were obtained independent of particle size. However, the use of an organofunctional silane to enhance particle-matrix bonding alleviated this issue and resulted in significantly higher fracture toughness values [1-161].

Chapter 1 - References

[1-1]   Gilman J.W., Jackson C. L., Morgan A. B., Harris R. H., Manias E., Giannelis, E. P., Wuthenow M., Hilton D., Phillips S.H., *Chem. Mater.*, **12**, 2000, 1866.

[1-2]   Bertalan G., Marosi G., Anna P., Ravadits I., Csontos I. & Toth A., *Solid State Ionics*, **141**, 2001, 211.

[1-3]   Murphy J., *Flame retardants: trends and new developments*, Plastic Additives and Compounding, 16-20, April, 2001.

[1-4]   *Flame retardant additives*, Plastic Additives and Compounding, 20-23, May, 2000.

[1-5]   Burnside S. & Giannelis E., *Chem. Mater.*, **7**, 1995, 1597.

[1-6]   Lee J., Yakekoshi T. & Giannelis E., Mater. Res. Soc. Symp. Proc., **457**, 1997, 513.

[1-7]   Telford, C., Market Perspectives of Nanocomposites, Consultant: SRI Consulting Business Intelligence.

[1-8]   Grimshaw R. W., *Chemistry and Physics of Clays and Allied Ceramic Materials*, 4th Ed., 1971.

[1-9]   Berry L.G. and Mason B., *Mineralogy-concepts, descriptions, determinations*, W. H. Freeman & Company (London), 1959.

[1-10] Cox K.G., Price N. B. and Harte D., *Introduction to the Practical Study of Crystals, Minerals and Rocks*, rev. 1st Ed., Mc-Graw-Hill (London), 1974, 127.

[1-11] Newman A.C.D. & Brown G., *The Chemical Constitution of Clays*, Chap. 1 in Newman A.C.D. (Ed.) *Chemistry of clay and clay minerals*, Mineralogical Society, Monograph No. 6. Wiley-Interscience, New York, 1987.

[1-12] Stackhouse S., Coveney P. V., Sandre E., *J. Am. Chem. Soc.*, **123**, 2001, 11764.

[1-13] Hofmann U., Endell K. & Wilm D., *Z. Kristallogr.*, **86**, 1933, 340.

[1-14] Maegdefrau E. & Hofmann U., *Z. Kristallogr.*, **98**, 1937, 299.

[1-15] Hendricks S. B., *J. Geol.*, **50**, 1942, 276.

[1-16] Edelman C. H. & Favejee J. C. L., *Z. Kristallogr.*, **A102**, 1940, 417.

[1-17] Montmorillonite B&S Model, Website: Building the phyllosilicates, last accessed: 15.8.2003, URL: http://pubpages.unh.edu/~harter/crystal.htm

[1-18] Kaolinite B&S Model, Website: Building the phyllosilicates, last accessed: 15.8.2003, URL: http://pubpages.unh.edu/~harter/crystal.htm

[1-19] MacEwan D.M.C., Trans. Faraday Soc, **44**, 1947, 349.

[1-20] Hedges, J. I. and Oades, J. M., Materials Today, **6**, 2003, 20.

[1-21] Chilingarian G.V. and Vorabutr P., *Drilling and Drilling Fluids*, Elsevier (Amsterdam), 1981.

[1-22] Rodriguez C. and Bugay D.E., *J. Pharm. Sci.*, **86**, 1997, 263.

[1-23] Essington M.E., *Soil Sci.*, **158**, 1994, 181.

[1-24] Sastry N.V., Sequaris J. M. & Schwuger M. J., *J. Colloid Interface Sci.*, **171**, 1995, 224.

[1-25] Gonzalez-Pradas E., Villafranca-Sanchez M. & Perez M., Agrochimica, **37**, 1993, 104.

[1-26] Luptakova V., Horvath I., Perjessy A. & Pukyera K., Chem. Pap., **46**, 1992, 157.

[1-27] Greenland D.J., *Soils Fert.*, **28**, 1965, 415.

[1-28] Carrizosa M. J., Koskinen W. C., Hermosin M. C. & Cornejo J., *App. Clay Sci.*, **18**, 2001, 223.

[1-29] Jaynes W.F. & Boyd S.B., *Soil Sci. Am. J.*, **55**, 1991, 43.

[1-30] Adam J. M., *Appl. Clay Sci.*, **2**, 1987, 309.

[1-31] Balantine J.A., *Chemical Reactions in Organic and Inorganic Constrained Systems*, Reidel (Dordrecht), 1986, 197.

[1-32] Haderlein S.B. & Schwarzenbach R.P., Transport and Reactive Processes in Aquifers, Balkema (Rotterdam), 1994, 67.

[1-33] Haderlein S.B. & Schwarzenbach R.P., *Environ. Sci. Technol.*, **27**, 1993, 316.

[1-34] Haderlein S.B., Weissmahr K. & Schwarzenbach R.P., *Environ. Sci. Technol.*, 1994

[1-35]   Yariv S., *Int. J. Trop. Agri.*, **6**, 1988, 1.

[1-36]   Peker S., Yapar S. & Besun N., *Colloids Surf.*, **104**, 1995, 249.

[1-37]   Lacher M., Lahav N. & Yariv S., *J. Thermal Anal.*, **40**, 1993, 41.

[1-38]   Lahav N., Lacher M. & Yariv S., *J. Thermal Anal.*, **39**, 1993, 1233.

[1-39]   Yariv S., Lahav N. & Lacher M., *J. Thermal Anal.*, **42** (1994), 13.

[1-40]   Lorprayoon V. & Condrate R.A., *Clays Clay Miner.*, **29**, 1981, 71.

[1-41]   Bosetto M., Arfaioli P. & Fusi P., *Soil Sci.*, **155**, 1993, 105.

[1-42]   Laird D.A., Barriuso E., Dowdy R.H. & Koskinen W.C., *Soil Sci. Soc. Am. J.*, 158, 1994, 181.

[1-43]   Theng B.K.G., The chemistry of clay-organic reactions, Adam Helgier Ltd., 1974, 211-238.

[1-44]   Harper M. & Purnell C.J., *Environ. Sci. Technol.*, **24**, 1990, 55.

[1-45]   Barrer R.M., *Clays Clay Miner.*, **37**, 1989, 385.

[1-46]   Ruiz-Conde A., Ruiz-Amil A., Perez-Rodriguez J. L., Sanchez-Soto P.J. & de la Cruz F.A., *Clays Clay Miner.*, **45**, 1997, 311.

[1-47]   Dashman T. & Stotzky G., *Soil Biol. Biochem.*, **14**, 1982, 447.

[1-48]   Mizutani T., Takano T. & Ogoshi H., *Langmuir*, **11**, 1995, 880.

[1-49]   El-Batouti M., Zaghloul A., Hanna M.T., *J. Colloid Interface. Sci.*, **180**, 1996, 106.

[1-50]   McBride M., *Surface chemistry of soil minerals: in Minerals in the Soil Environment*, 2nd Ed., Soil Science Society of America, Madison, Wisconsin, 1989, 35.

[1-51]   Lagaly G., *Introduction: From clay mineral-polymer interactions to clay mineral-polymer nanocomposites*, App. Clay Sci., **15**, 1999, 1.

[1-52]   Lee J., Mortland M., Boyd S. & Chiou C., *J. Chem. Soc. Faraday Trans.*, **85**, 1989a., 2953.

[1-53]   Jaynes W. & Boyd S., *Journal of the Air & Waste Management Association*, **40**, 1990, 1649.

[1-54]   Wada K., *Amer. Miner.*, **46**, 1961, 78.

[1-55]   Sidheswaran P., Mohan S.V.R., Ganguli P. & Bhat A. N., *Indian J. Chem.*, **26A**, 1987, 994.

[1-56]   Sidheswaran P., Bhat A.N. & Ganguli P., *Clays Clay Miner.*, **38**, 1990, 29.

[1-57]   Olejnik S., Aylmore L.A.G., Posner A.M. & Quirk J., *J. Phys. Chem.*, **72**, 1969, 241.

[1-58]   Talbert R.E. & Fletchal O. H., *Weeds*, **13**, 1968, 46.

[1-59]   Lagaly G, Clay organic interactions, *Phil.Trans.R.Soc.Lond*, **3**, 1984, 315.

[1-60]   Olejnik S, Posner A.M and Quirk J.P, *Clay Minerals*, **8**, 1970, 421.

[1-61]   Pinck L.A. & Holton W.H., Allison F.E., *Soil Sci.*, **91**, 1961, 22.

[1-62]   Frissel M.J. & Bolt G. H., *Soil Sci.*, **94**, 1962, 284.

[1-63]   Grim R.E., Allaway W.H. & Cuthbert F.L., *J. Am. Ceram. Soc.*, **30**, 1947, 137.

[1-64]   Okada A., Kawasumi M., Usuki A., Kojima Y. & Kamigaito O., *Mat. Res. Soc. Proc.*, **171**, 1990, 45.

[1-65]   Weiss A., Organic derivatives of mica-type layer silicates, *Angew. Chem Int. Et.*, **2**, 1963, 134.

[1-66]   Jordan J.W., Organophilic bentonites, *J. Phys. Colloid Chem.*, **53**, 1949, 294.

[1-67]   Ogawa M. & Kuroda K., *Bull. Chem. Soc. Jpn.*, **70**, 1997, 2593.

[1-68]   Laus M., Camerani M., Lelli M., Sparnacci K., Sandrolini F. & Francescange O., *J. Mater. Sci.*, **33**, 1998, 2883

[1-69]   Weimer M.W. & Chen H., Giannelis E.P. & Sogah D.T., *J. Am. Chem. Soc.*, **121**, 1999, 1615.

[1-70]   Lan T., Kaviratna P.D. & Pinnavaia T. J., *Mechanism of clay tactoid exfoliation in epoxy-clay nanocomposites*, Chem. Mater., **7**, 1995, 2144.

[1-71]   Lan T. & Pinnavaia T.J., Clay-reinforced epoxy nanocomposites, *Chem. Mater.*, **6**, 1994, 2216.

[1-72]   Wang Z. & Pinnavaia T.J., *Hybrid organic-inorganic nanocomposites: exfoliation of magadiite nanolayers in an elastomeric epoxy polymer*, Chem. Mater., **10**, 1998, 1820.

[1-73]   Messersmith P.B. & Giannelis E.P., *Synthesis and Characterization of Layered Silicate-Epoxy Nanocomposites*, Chemistry of Materials, **6**, 1994, 1719

[1-74]   Grim R.E., *Clay Mineralogy*, McGraw-Hill, New York, 1968

[1-75]   Theng B.K.G., *The Chemistry of Clay Organic Reactions*, Adam Hilger, London, 1974

[1-76]   Lagaly G., Characterisation of clays by organic compounds, *Clay Miner.*, **16**, 1981, 1

[1-77]   Jones T.R., The properties and uses of clays which swell in organic solvents, *Clay Miner.*, **18**, 1983, 399

[1-78]   Newman A.C.D. (Ed.), *Chemistry of Clays and Clay Minerals*, Longman, London, 1987

[1-79]   Favre H. & Lagaly G., Organo-bentonites with quaternary alkylammonium ions. *Clay Miner.*, **26**, 1991, 19

[1-80]   Hackett E., Manias E. & Giannelis E.P., Molecular dynamics simulations of organically modified layered silicates. *J. Chem. Phys.* **108**, 1998, 7410

[1-81]   Tanabe, K., *Solid Acids and Bases*, Academic Press, New York, 1970.

[1-82]   Germain, J.E., *Catalytic Conversions of Hydrocarbons*, Academic Press, London, 1969.

[1-83]   Rudham, R. & Stockwell, A., *Specialist Periodical Reports: Catalysis*, **2**, 1, 1978.

[1-84]   McMurry J., Organic Chemistry, 4th Ed., Ch. 24 - Aliphatic Amines, Brooks/Cole Pub. Co.

[1-85]   Xie W., Gao Z., Liu K., Pan W-P, Vaia R., Hunter D. & Singh A., Thermal Characterization of Organically Modified Montmorillonite, *Thermochimica Acta*, **368**, 2001, 339.

[1-86]   Xie W., Gao Z., Pan W-P, Hunter D., Singh A. & Vaia R., Thermal Degradation Chemistry of Alkyl Quaternary Ammonium Montmorillonite, *Chem. Mater.*, **13**, 2001, 2979.

[1-87]   Xie W., Xie R., Pan W-P, Hunter D., Koene B., Tan L. & Vaia R., Thermal Stability of Quaternary Phosphonium Modified Montmorillonites, *Chem. Mater.*, **14**, 2002, 4837.

[1-88]   Bond, G.C., *Heterogeneous Catalysis: Principles and Applications*, 2nd Ed., Oxford Science Publications, 1987.

[1-89]   Lunt, J., Large-scale production, properties and commercial applications of polylactic acid   polymers, *Polymer Degradation and Stability*, **59**, 1998, 145.

[1-90]   Vink E.T.H., Rábago K.R., Glassner D.A. and Gruber P.R., Applications of life cycle assessment to NatureWorks polylactide (PLA) production, *Polymer Degradation and Stability*, **80**, 2003, 403

[1-91]   Mark H. and Whitby G.S. (Ed), Collected Papers of Wallace H. Carothers on High Polymeric Substances, High Polymers, Vol. I, Interscience Publishers, New York, 1940

[1-92]   British Plastics Federation, BPF History, Last accessed: 12.8.2003, URL: http://www.bpf.co.uk/bpf/profile/history_of_bpf/

[1-93]   Brydson, J., Plastics Materials, 7th Ed., Oxford: Butterworth-Heinemann, 2000

[1-94]   Pritchard, G., Plastic Additives: an A-Z Reference, Chapman and Hall, 1997

[1-95]   Engelhardt, T., *Industrial Applications of Nanocomposite Fillers based on organic intercalated bentonites*, IMA 2002 Conference Proceedings, Brussels 6th June, 2002

[1-96]   DuBois, J.H., Plastics, 6th Ed., Van Nostrand Reinhold, 1981

[1-97]   Gerspacher M., O'Farrell C.P., Yang H.H., *Elastomerics*, **122**, 1990, 23

[1-98]   Schroder A., Kluppel M., Schuster R.H., Heidberg J., *Carbon*, **40**, 2002, 207.

[1-99]   Mark J.E., *Ceramic reinforced polymers/polymer-modified ceramics*, *Polym. Eng. Sci.*, **36**, 1996, 2905.

[1-100]   Reynaud E., Gauthier C., Perez J., Nanophases in polymers, Rev. Metall./Cah. Inf. Tech., **96**, 1999, 169.

[1-101]   von Werne T. & Patten T.E., Preparation of structurally well defined polymer-nanoparticle hybrids with controlled/living radical polymerization, *J. Am. Chem. Soc.*, **121**, 1999, 7409

[1-102]   Herron N. & Thorn D.L., Nanoparticles: Uses and relationships to molecular clusters, *Adv. Mater.*, **10**, 1998, 1173.

[1-103]   Calvert P., Potential applications of nanotubes, *Carbon Nanotubes*, CRC Press, Boca Raton, FL, 1997, 277.

[1-104]   Theng B.K.G., *The Chemistry of Clay-Organic Reactions*, Wiley, New York, 1974.

[1-105]   Ogawa M. & Kuroda K., Preparation of inorganic-organic nanocomposites through intercalation of organo-ammonium ions into layered silicates, *Bull. Chem. Soc.*, **70**, 1997, 2593.

[1-106] Kojima Y., Usuki A., Kawasumi M., Okada A., Fukushima Y., Karauchi T., Kamigaito O., Mechanical properties of nylon-6-clay hybrid, J. Mater. Res., 6, 1993, 1185.

[1-107] Giannelis E.P., Krishnamoorti R., Manias E., Polymer-silica nanocomposites: model systems for confined polymers and polymer brushes, Adv. Polym. Sci., 118, 1999, 108.

[1-108] Doh J.G. & Cho I., Synthesis and properties of polystyrene-org-MMT hybrid, Polym. Bull., 41, 1998, 511

[1-109] Weimer M.W., Chen H., Giannelis E.P., Sogah D.Y., Direct synthesis of nanocomposites by in-situ living free radical polymerisation using a silicate-anchored initiator, J. Am. Chem. Soc., 121, 1999, 1615.

[1-110] Oriakhi C., Nano sandwiches, Chem. Br., 34, 1998, 59.

[1-111] Blumstein, A., J.Polym. Sci., A3, 1965, 2665.

[1-112] Fukushima, Y. & Inagaki, S., J. Inclusion Phenom., 5, 1987, 473.

[1-113] Usuki A., Kawasumi M., Kojima Y., Okada A., J. Mater. Res., 8, 1993a, 1174.

[1-114] Usuki A., Kojima Y., Kawasumi M., Okada A., Fukushima Y., Kurauchi T., Kamigaito O., J. Mater. Res., 8, 1993b, 1179.

[1-115] Kojima Y., Usuki A., Kawasumi M., Okada A., Fukushima Y., Kurauchi T., Kamigaito O., J. Mater. Res., 8, , 1993a, 1185.

[1-116] Kojima Y., Usuki A., Kawasumi M., Okada A., Kurauchi T., Kamigaito O., J. Appl. Polym. Sci., 49, 1993b, 1259.

[1-117] Gilman J.W., Kashiwagi T., Lichtenhan J.D., Nanocomposites: a revolutionary new flame retardant approach. SAMPE J., 33, 1997, 40.

[1-118] Okada A. & Usuki A., Mater. Sci. Eng., C3, 1995, 109.

[1-119] Dubois P. & Alexandre M., Mater. Sci. Eng., 28, 2000, 1.

[1-120] Gilman J., App. Clay Sci., 15, 1999, 31.

[1-121] NIST: Building and Fire Research Laboratory, last accessed 2.28.2001, URL: http://www.bfrl.nist.gov/objectives/fsm/FSM_od2000.htm

[1-122] Burnside S.D. & Giannelis E.P., Chem. Mater., 7, 1995, 1597.

[1-123] Wang S.J., Long C.F., Wang X.Y., Li Q., Qi Z.N., J. Appl. Polym. Sci,. 69, 1998, 1557.

[1-124] Lee D.C., Jang L.W., J. Appl. Polym. Sci., 61, 1996, 1117

[1-125] Noh M.W., Lee D.C., Polym. Bull., 42, 1999, 619

[1-126] Lee D.C., Jang L.W., J. Appl. Polym. Sci., 68, 1998, 1997

[1-127] Tyan H.L., Liu Y.C., Wei K.H., Enhancement of imidization of poly(amic acid) through forming poly(amic acid)/organoclay nanocomposites, Polymer, 40, 1999, 4877

[1-128] Beyer, G., Polymer News, November 2001.

[1-129] Gilman J.W., Flammability and thermal stability studies of polymer layered-silicate (clay) nanocomposites, Appl. Clay Sci. 15, 1999, 31

[1-130] Gilman J.W., Kashiwagi T., Lomakin S., Giannelis E.P., Manias E., Lichtenhan J.D., Jones P., Nanocomposites: radiative gasification and vinyl polymer flammability, in: Proceedings of the 6th European Meeting on Fire Retardancy of Polymeric Materials (FRPM'97), University of Lille, France, 24-26, 1997, 203.

[1-131] Gilman J.W., Kashiwagi T., Brown J.E.T., Lomakin S., Flammability studies of polymer layered silicate nanocomposites, SAMPE J. 43, 1998, 1053

[1-132] Dabrowski F., Le Bras M., Bourbigot S., Gilman J., Kashiwagi T., PA-6 MMT nanocomposite in intumescent fire retarded EVA, in: Proceedings of the Eurofillers '99, Lyon-Villeurbanne, France, 6-9, Sept 1999.

[1-133] Kojima Y., Usuki A., Kawasumi M., Okada A., Kurauchi T., Kamigaito O., Synthesis of nylon-6-clay hybrid by MMT intercalated with e-caprolactam, J. Polym. Sci., 31, 1993, 983.

[1-134] Kojima Y., Usuki A., Kawasumi M., Okada A., Kurauchi T., Kamigaito O, One-pot synthesis of nylon-6-clay hybrid, J. Polym. Sci Part A: Polym. Chem. 31 (1993) 1755±1758.

[1-135]   Liu L.M., Qi Z.N., Zhu X.G., Studies on nylon-6 clay nanocomposites by melt-intercalation process, *J. Appl. Polym. Sci.* **71**, 1999, 1133.

[1-136]   Nielsen L. E., *J. macromol. Sci.* **A1**, 1967, 929.

[1-137]   Lan T., Kaviratna P.D., Pinnavaia T.J., On the nature of polyimide±clay hybrid composites, *Chem. Mater.* **6**, 1994, 573.

[1-138]   Yano K., Usuki A., Okada A., Synthesis and properties of polyimide±clay hybrid films, *J. Polym. Sci. A: Polym.Chem.* **35**, 1997, 2289.

[1-139]   Messersmith P.B., Giannelis E.P., Synthesis and barrier properties of poly(e-caprolactone)-layered silicate nanocomposites, *J. Polym. Sci.: Part A Polym. Chem.* **33**, 1995, 1047

[1-140]   Scherer C., PA Film grade with improved barrier properties for flexible food packaging applications, Proceedings: New plastics'99, London, 2-4 Feb 1999.

[1-141]   Friedlander H.Z. & Grink C.R., *J. Poly. Sci.- Poly. Lett.*, **2**, 1964, 475.

[1-142]   Kato C., Kuroda K. & Takahara H., *Clay and Clay Minerals*, **29**, 1981, 294.

[1-143]   Akelah A. & Moet A., *J. Mater. Sci.*, **31**, 1996, 3189.

[1-144]   Fu X. & Qutubuddin S., *Mater. Lett.*, **42**, 2000, 12.

[1-145]   Giannelis E.P., Vaia R. & Ishii H., *Chem. Mater.*, 5, 1993, 1694.

[1-146]   Vaia R.A., Jandt K.D., Kramer E.J. & Giannelis E.P., *Chem. Mater.*, 8, 1996, 2628.

[1-147]   Vaia R.A. & Giannelis E.P., *Macromolecules*, **30**, 1997, 8000.

[1-148]   Vaia R.A., Ishii H. & Giannelis E.P., *Chem. Mater.*, **5**, 1993, 1694.

[1-149]   Vaia R.A., Jandt K.D., Kramer E.J., Giannelis E.P., *Macromolecules*, 28, 1995, 8080.

[1-150]   Zhu J., Morgan A.B., Lamelas F.J., Wilkie C.A., *Chem Mater.*, **13**, 2001, 3774.

[1-151]   Tseng C.R., Wu J.Y., Lee H.Y., Chang F.C., *Polymer*, **42**, 2001, 10063.

[1-152]   Wang D., Zhu J., Yao Q., Wilkie C.A., *Chem Mater.*, 14, 2002, 3837.

[1-153]   Zeng C., Lee L.J., *Ann Tech Conf Soc Plast Eng.*, 2, 2001, 2213.

[1-154]   Zeng C., Lee L.J., *Macromolecules*, 34, 2001, 4098.

[1-155]   Chen G.M., Ma Y.M., Qi Z.N., *Journal of Chinese University Chemistry*, **22**, 2001, 872

[1-156]   Lee, JD, and Giannelis, E.P., Polymer Preprints, **38**, 1997, 688.

[1-157]   Kornmann, X., Berglund, L.A., Sterte, J. & Gianellis, E.P., *Polym. Eng. &Sci.*, **38**, 1998, 1351

[1-158]   Suh, D.J., Lim, Y.T., Park, O.O., *Polymer*, 41, 2000, 8557.

[1-159]   Bharadwaj, R.K., Mehrabi, A.R., Hamilton, C., Trujillo, C., Murga, M., Fan, R., Chavira, A. & Thompson, A.K., *Polymer*, **43**, 2002, 3699.

[1-160]   Evora, V.M.F. & Shukla, A., *Mater. Sci. Engng.*, 2003, Article in press/Uncorrected proof.

[1-161]   Zhang, M. & Singh, R.P., *Mater. Lett.*, 4671, 2003, Article in press/Uncorrected proof.

2

Materials and Experimental Methods

In this section the materials, procedures and experimental techniques used in this thesis will be described.

2.1 Clay Preparation and Exchange Procedures

2.1.1 Sodium Ion Exchanged Clays

2.1.1.1 Mineral Colloid British Pharmacopoeia (MCBP)

Bentonite is a soft clay substance essentially composed of the montmorillonite group. The impurities in bentonites can include quartz, calcite, dolomite, feldspar, gypsum and iron oxide, depending upon the nature of the weathering, environment and the original composition of the volcanic material.

The first series of experiments used Mineral Colloid British Pharmacopoeia (MCBP), a bentonite clay supplied by ECC International Ltd. The raw material was dispersed in 1 kg batches in an excess of deionised water within two 45 litre polypropylene containers. The clay/water mixture was then stirred at regular intervals until a clay suspension was formed. The containers acted as sedimentation tanks, the impurities within the processed clay settling to the bottom and the largely purified montmorillonite composition remaining in suspension. The clay that was suspended within the top 10 cm of the mixture was collected, centrifuged (17,000 rpm / 1 hr) and air-dried. When dry, the clays were ground and sieved to pass through a 105 μm mesh, to ensure particle scale. This procedure provided purified montmorillonite clay which could be further utilised for exchange procedures.

The aim of this approach was to produce a sodium exchanged form of the montmorillonite clay, into which it would be easier to exchange quaternary ammonium cations and make the gallery surfaces organophilic. To make this possible, it was necessary to convert the purified MCBP (with its various hydrated gallery cations (E.g. majority Na^+, K^+, Ca^{2+}, Mg^{2+})) into sodium clay by exchange with NaCl.

MCBP was mixed in an excess Na$^+$ solution, 6 g in 120 ml (1M NaCl) at 200 rpm/24 hr, after which the clay-slurry was centrifuged at 17,000 rpm/1 hr. The supernatant of each sample was then extracted to measure its conductivity; the product was then homogeneously re-suspended in deionised water and spun down. This process was repeated 8-10 times until the supernatant conductivity was measured to be below 50 μS, a measurement below which there was designated to be no ionic product remaining in the solution. The samples were then air-dried for 48 hr.

2.1.1.2   Sodium Ion Exchanged Cloisite

Na-MMT (Cloisite) is a natural Na$^+$ montmorillonite supplied by Southern Clay Products. This high purity montmorillonite was subjected to the same Na$^+$ exchange procedure as MCBP.

2.1.2   Organoclay Exchange

The cationic exchange capacity (CEC) is reported in terms of milliequivalents (mEq) of the molecular weight of surfactant per 100 g of the dry solid. The amount used was varied for the different clay minerals. The CEC of a clay species is a measure of the number of cations adsorbed on its surface once it has been washed free of excess salt solution. CEC is stated in milliequivalents per 100 g of dried material (mEq/100 g).

The measured amount of fixed cation varies with the charge of the exchange cation. The charge on the external surface of clays is usually of the order of 5-10 mEq/100 g, whereas the charge present on sites between the layers of a clay can vary between 40-150 mEq/100g. This phenomenon makes it possible to distinguish two kinds of clay, those with low exchange capacities (~10 mEq/100 g, E.g. Kaolinite) and those with high exchange capacities (40-150 mEq/100 g, E.g. MMT) [2-1].

The soluble gallery cations may affect the adsorbed water arrangement in several ways. Principally, by providing a bond of varying strength, which holds the layers together and

controls the concentration of adsorbed water. The effectiveness of the soluble cations (in this regard) depends on their size and charge, i.e. Na^+, K^+ would develop a weak clay structure; clay slurry containing these ions would be capable of adsorbing large concentrations of water. Ca^{2+}, Mg^{2+} would develop stronger links and clay slurry containing them would adsorb lower water concentrations. The replacing power of exchangeable cations increases with increasing valence and decreasing radius. A frequently quoted order of replacing power is sodium < potassium < calcium < magnesium < ammonia < hydrogen < iron < aluminium.

2.1.2.1 Quaternary Ammonium Exchanged Na-MMT (MCBP)

The exchange of cationic species was performed by immersing quantities of Na^+ clay in aqueous solutions containing various quaternary ammonium salts, (i.e. bromide). Na-MCBP samples were exchanged with alkyltrimethylammonium cations of varying alkyl chain length: octyltrimethylammonium, OTAB ($C_n = 8$)

dodecyltrimethylammonium, DTAB ($C_n = 12$)

tetradecyltrimethylammonium, TTAB ($C_n = 14$)

cetyl(hexadecyl)trimethylammonium, CTAB ($C_n = 16$)

The cation loading of the surfactants on the clay was related to the CEC of MCBP (80 mEq/100 g). This was calculated from:

$$\text{Mass of Organocation} = \frac{\text{Mass of Clay/g} \times \text{CEC of Clay/mEq/g} \times \text{Multiple of CEC} \times (M_w \text{ Organocation (amu)} / \text{Cation Charge})}{1000} \text{ /g}$$

Mass of Clay	CEC of Clay	Multiples of CEC	Molecular Weight	Cationic charge		Mass Required
1	0.8	0.5	364.46	1		0.145784
1	0.8	1	364.46	1		0.291568
1	0.8	2	364.46	1		0.583136

Table 2.1   CEC Exchange Mass, Example: Organocation = CTAB ($C_n = 16$).

For the purposes of initial experiments Na-MCBP was loaded at different multiples of the CEC to study what effect organocation deficiencies and excesses would have on the thermal decomposition of the products (table 2.1).

The mass of Na-MCBP to be exchanged, usually between 5-10 g (due to the need for a well dispersed mixture), was suspended in 100 ml deionised water within a 250 ml conical flask. This clay slurry was sonicated for 10 minutes to swell the clay galleries with water. The calculated mass of alkyltrimethylammonium salt was then added to the conical flask, stoppered and placed on a NBS Gyrotory Shaker G76D at 200 rpm/24 hr.

These samples were repeatedly washed with deionised water and then centrifuged at 17,000 rpm/1 hr and then air-dried for 48 hr to produce the exchanged samples for analysis. This method of preparation was also used to prepare the samples which were used as the organoclay species in subsequent polymer-clay nanocomposite preparations. To alleviate any anomalies that may have occurred in sample preparation all samples were prepared in triplicate.

2.1.2.2 Industrially Produced Organoclays: Ta15-MMT, Ta20-MMT and Bz-MMT

Industrially produced organoclays were supplied by Southern Clay Products. These organoclays were prepared by cation exchanging Na-MMT with dialkyldimethylammonium cations and a benzyl variation of this surfactant. The alkyl chains were derived from hydrogenated tallow which is composed predominantly of octadecyl chains ($C_n = 18$) with small amounts of lower homologues, specifically 65 % - $C_n = 18$; 30 % - $C_n = 16$; 5 % - $C_n = 14$).

These samples were used for further studies on the effect of incorporating greater concentrations of alkyl groups than were used in the previous Na-MCBP samples and

possibly the effect of the concentration of quaternary ammonium cations within the galleries of MMT (fig. 2.1 & 2.2):

$$CH_3 — N^+ — HT$$
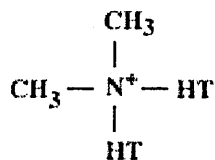
Figure 2.1   **Ta15-MMT (C15A), modifier concentration = 125 mEq / 100 g clay**
dimethyl dihydrogenated tallowalkyl ammonium MMT

$$CH_3 — N^+ — HT$$
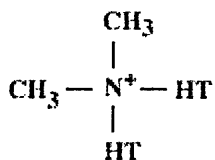
Figure 2.2   **Ta20-MMT (C20A), modifier concentration = 95 mEq / 100 g clay**
dimethyl dihydrogenated tallowalkyl ammonium MMT

and also, to study the compatibility of organoclays with benzyl functionality (Bz-MMT) (fig. 2.3) with PS:

$$CH_3 — N^+ — CH_2 — \bigcirc$$
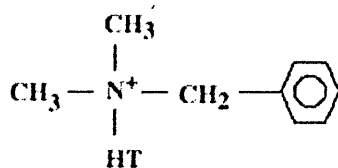
Figure 2.3   **Bz-MMT (C10A), modifier concentration = 125 mEq / 100 g clay**
dimethyl hydrogenated tallowalkyl benzyl ammonium MMT

2.1.2.3   Silane Modified MMT (Prepared by Scott-Bader)

Silanes were used as coupling agents to surface-modify Na-MMT for a further reaction with unsaturated polyester resin. The silanes that were used were alkylammonium silanes. Hydrolysed silane compounds were condensed to form highly reactive silanols, these were expected to hydrogen bond to hydroxyl groups on the clay surface. By drying these exchanged materials, a condensation reaction occurred between neighbouring silanols and the surface hydroxyls would have led to the formation of multiple covalent bonds between the coupling agent and the clay surface (fig. 2.4).

These coupling (cross-linking) agents are believed to act as molecular bridges between the polymer and the clay surface and have the potential to substantially improve the bond strength between organic polymers and clay particles. This organic surface modification provides a route for the introduction of polymer molecules into the MMT gallery spaces. Another possible advantage of silane modification was the satiating of Al and Si atoms exposed at the clay edges which are only partially hydrolysed to silanol (SiOH) and aluminol (AlOH) groups. Any unsaturated edge sites are much more reactive than the saturated basal sites, and so, any unfavorable interactions between these edge sites on the clay and the intercalating polymer matrix may be overcome by the use of silane coupling agents to modify the edges [2-2, 2-3].
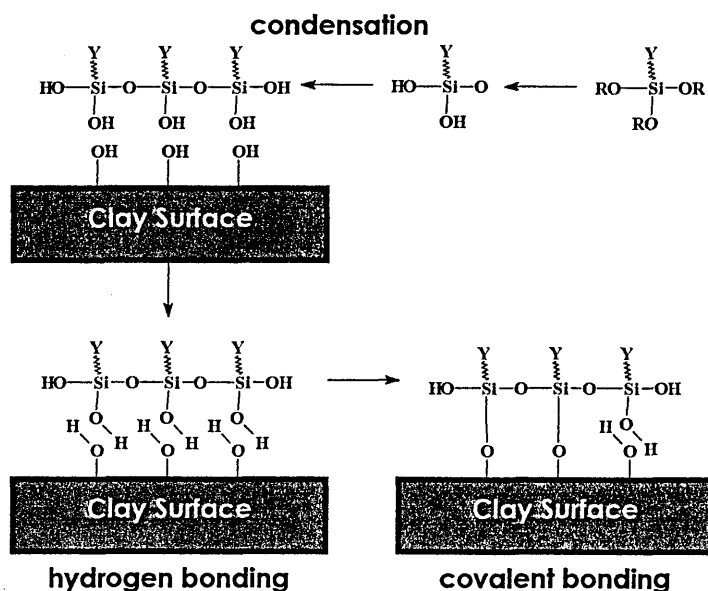
Figure 2-4   **Schematic diagram of the silane modification of a generic clay surface (Y = alkyl modification).**

2.1.2.4   Phenylphosphonic Acid (PPA) Modification of Kaolin

Phenylphosphonic acid (PPA) undergoes a topotactic reaction with the available hydroxyls of the gibbsite sheet of kaolin during reflux in a water-acetone mixture at 70 °C. This reaction should result in significant structural modifications to the kaolin host, resulting in the formation of covalent bonds.

73

1.5 g of a kaolin sample was dispersed in 300 cm³ of a 1:1 (v/v) distilled water:acetone mixture to which was added 2.75 g of PPA. The reaction was carried out at 68 °C in a 500 cm³ round-bottomed flask fitted with a reflux condenser. The kaolin-PPA sample (KPPA) was treated for periods of 3, 9, 15, 21 and 28 days. At the end of the reaction time the samples were subjected to five consecutive processes of centrifugation (i.e. 4000 rpm/30 min) and washings with acetone. The solid white residue was then allowed to dry in air at room temperature for 24 h, before characterisation tests were conducted.

2.2   Polystyrene-Clay Preparation and Formulation

2.2.1   Styrene Distillation

Styrene (99 %) was supplied by Aldrich Chemicals. The standard product was supplied containing an inhibitor (4-tert-butylcatechol, 10-15 ppm) to hinder self-polymerisation whilst in storage, to remove this, and improve the quality of the styrene, batches were washed and distilled when required.

Distillation Procedure: Styrene was washed with weak (10-20 %) aqueous NaOH (caustic soda) in a separating funnel to remove the inhibitor. After separating and washing with deionised water followed by a salt water wash (to aid layer separation), the styrene was then 'dried' by adding anhydrous $MgSO_4$ and leaving for 1 hr. The styrene was then distilled under vacuum/N_2 to give the final fractions and the major yield. Note: Styrene could have been distilled under atmospheric pressure (i.e. reduced pressure/greater separation of boiling points) to get purer fractions, but yield would have been reduced.

2.2.2   Polystyrene-Clay Nanocomposites (PSCN)

In experiments, similar to those conducted by Doh and Cho [2-4] and LeBaron *et al.* [2-5], polystyrene-clay nanocomposites (PSCN) were prepared with variations in the procedure, temperature, composition and reaction vessel. These nanocomposites were produced based on the basic nanocomposite theory that if the polarity of the monomer was

sufficiently matched by the organoclay, it would be intercalated into the galleries of MMT, which following polymerisation would lead to an exfoliated PS-clay structure. During this research the majority of nanocomposite materials that have been produced used styrene to produce a polymer matrix, with different organoclays incorporated as additives to confer thermal and physical enhancements.

2.2.3 PSCN - Procedure

2.2.3.1 PSCN - Sample Mass and Mixing Speed

Organoclay, initiator and 50 ml/45 g of styrene (N.b. relative density (water = 1) : 0.9, $0.9g/cm^3$ [2-6]) were added to a 150 ml round bottomed flask. A variety of organoclays and initiators were added at a range of concentrations as wt% equivalents to the volume of styrene. The organoclays were added in the range 0.09 g/0.2 wt% to 2.25 g/5.0 wt% and the initiators were added at 0.23 g/~0.5 wt%, 0.45 g/1.0 wt% and 0.90 g/2.0 wt%. The styrene was stirred (15 mins/200 rpm/N_2). The organoclay was added gradually (over 1-5 mins) whilst the styrene was being mixed, then the initiator was added and the mixture stirred for a further 30 mins/200 rpm. The mixing and pre-polymerisation stages were conducted under a nitrogen atmosphere to reduce oxidation of the final product.

2.2.3.2 PSCN - 1st Cure Profile

Samples produced early in this study, to investigate the effect of varying initiator type, were transferred after mixing to stoppered glass tubes (50 x 25 mm) and polymerised at 50 °C/72 hr to obtain the PS-clay hybrids. The polymerised PS-clay samples were then removed from the tubes, and post-cured at 80 °C/12 hr, before being cooled to RT and removed from the mold. The glass stoppered tubes were chosen as casting molds to produce samples with a regular size and shape that could be easily sectioned for analytical samples.

2.2.3.3   PSCN - 2nd Cure Profile

Samples produced later (and for the majority of the remainder of the study) were cured by heating the PSCN mixtures to ~110 °C/5 mins to induce polymerisation, then cooling at RT/15 min/N_2, before then heating the samples at 80 °C/30 min/N_2 to propagate the polymerisation. The viscous mixtures were then transferred to circular aluminium moulds (10 x 550 mm) and cured at 80 °C/24 hr followed by a post-cure period at 50 °C/24 hr.

The aluminium molds with polished inner surfaces were chosen as an alternative to glass stoppered tubes to resist temperature and to give an end-product with as smooth a surface as possible. As well as speeding up production of PSCN, the final disc-shaped samples produced from the 2nd cure profile also reduced post-production sample preparation for XRD analysis.

2.3   Unsaturated Polyester-Clay Nanocomposite (UPCN),

Preparation and Formulation

The unsaturated polyester-clay nanocomposites (UPCN) were synthesised by silane-treating the clay (as described in section 2.1.2.3) and mixing it with the resin prior to curing.

2.3.1   Resin Reactor

A two litre resin reactor was used to contain the unsaturated polyester resin (UPR) mixture, a temperature controlled heating mantle, mechanical overhead stirrer, steam heated reflux condenser were added and nitrogen was bubbled through the mixture.

2.3.2   Reaction Mixture/Procedure

The polyester resins were produced by the polymerisation reaction between glycols with unsaturated and saturated anhydrides. The UPCNs were synthesised by reacting the clay with a silane compatibiliser and then mixing it with the resin (i.e. 4 wt%) prior to curing. The procedure used to produce the UPCN materials was as follows:

76

i)   590 g (4 moles) of phthalic anhydride, 196 g (2 moles) of maleic anhydride and 180 g (2.5 moles) of propylene glycol were added to the resin reactor.

ii)   The reaction mixture was then heated at 190-200 °C for 10 hours (until an equivalent amount of water had been collected).

iii)   Then 150 mg of hydroquinone (inhibitor) was added.

iv)   The mixture was then cooled to 140 °C.

v)   The resin was then discharged and blended with 600 g of cold styrene, 3.0 g Benzoyl Peroxide (BPO) initiator and 60 g silane-modified MMT.

vi)   The mixture was then poured into moulds, which consisted of waxed glass sheets spaced 5 mm apart by dividers, sealed with silicon grease and clamped together.

vii)   The mixture cured at RT for 24 hrs, before the different post-cure treatments were applied.

The materials were subjected to two different post-curing processes:

- The lower temperature - Lloyds post-cure (LDS): 50 °C for 16 hours
- The higher temperature - Scott-Bader post-cure (SB): 70 °C for 16 hours

2.4　　　　Analytical and Characterisation Techniques

The following techniques were used within this thesis to analyse and characterise clays, organoclays and nanocomposite materials.

2.4.1　　　　X-Ray Diffraction (XRD)

2.4.1.1　　　　XRD Theory

X-Rays were discovered by Wilhelm Röntgen in 1895, for which he was awarded the first Nobel Prize in Physics in 1901. He discovered that in an experiment with high-energy electrons, another type of radiation was being produced which had the following unique properties:

   a. it travelled in straight lines

   b. it was exponentially absorbed in matter with the exponent proportional to the mass of the absorbing material

   c. it darkened photographic plates

   d. it made shadows of absorbing material on photosensitive paper (this led directly to the use of X-rays in medicine.)

Max von Laue (1912) theorised that x-rays could also be diffracted if the slits were small enough. Since it was understood that molecular spacing in crystalline materials were in the order of 10^{-10} m, he devised an experiment in which x-rays were allowed into a lead box containing a crystal, with sensitive film behind the crystal. When the films were developed there was a large central point from the incident x-rays, but also many smaller points in a regular pattern. These could only be due to the diffraction of the incident beam and the interference of many beams. By using a crystal as a diffraction grating, von Laue had proved the x-rays were not particles, but waves of light with very small wavelengths.

Lawrence Bragg and his father W.H. Bragg used von Laue's discovery and, for monochromatic radiation, were able to show that diffraction could be treated geometrically like reflection, and derived Bragg's law, which allows diffraction to be treated in simple mathematical terms. The Bragg equation provides a simplified framework for diffraction that works for basic calculations:

$$\text{Eq}^n\ 2\text{-}1 \qquad n\lambda = 2d \sin \theta$$

where:

n = integer, λ = wavelength of x-rays, d = basal spacing of crystal, θ = diffraction angle

In the early 1930's XRD was applied by soil scientists to elucidate the crystalline structure of clay minerals. Hendricks & Fry (1930) [2.7] and Kelley *et al.* (1931) [2.8] provided evidence for these postulations. Subsequently, Hendricks & Teller [2.9] introduced the theoretical basis for XRD from a stack of clay mineral layers. XRD is a powerful technique that can be used to identify the crystalline phases in materials [2.10-2.12].

In the context of this thesis, XRD was used to:

a. evaluate the d_{001} spacing of swelling minerals to determine if potential probe molecules have successfully intercalated into the interlayer space.

b. determine the molecular orientation of surfactant molecules in the interlayer space of swelling minerals.

c. identify the level of dispersion within polymer matrices indirectly via the presence of crystalline mineral phases.

In terms of reproducibility, XRD is dependent on many factors including sample length, thickness, position, alignment, sample homogeneity and the quality of the standards used. Also, quantitative XRD does not have the ability to determine the differences between surface and bulk mineralogy. Instead, it provides information about the bulk properties of

whole molecular populations, information averaging as many as perhaps 10^{11}-10^{12} unit cells of billions of crystals [2.13].

2.4.1.2 XRD Analysis
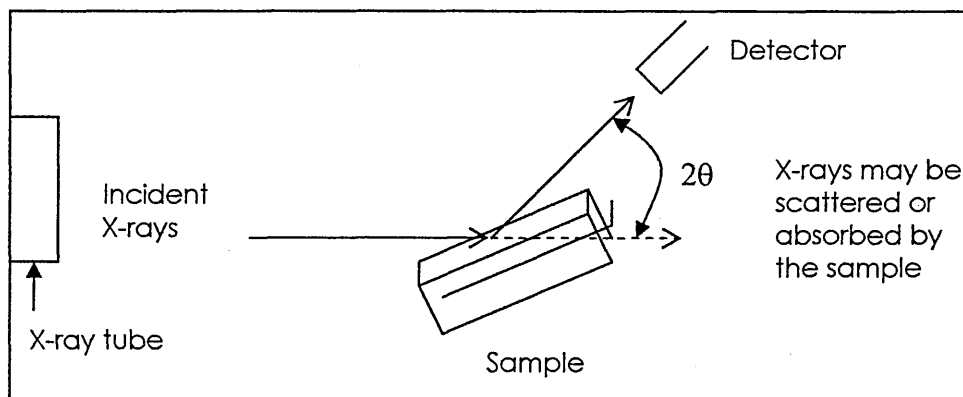
Figure 2.5 **Schematic diagram of the XRD analytical process.**

X-rays are produced when high speed electrons strike the atoms of another substance. Within the X-ray diffractometer, the tube where the X-rays are produced is under vacuum, inside this tube the electrons are generated by a glowing tungsten filament (the cathode). The electrons are then accelerated by voltages (15-60 kV) in order to strike a Cu or Cr target (the anode). The accelerated electrons strike the inner more tightly bound electrons of the target and knock them out of their orbital positions, away from the influence of their respective nuclei. This produces electron vacancies, which are filled by higher orbit electrons dropping inwards to fill the vacancy. The subsequent drop involves the production of an X-ray photon, the energy of which is proportional to the difference between the energy levels of the orbitals. This energy difference is dependent on the number of protons in the nucleus attracting the electrons. The wavelength of Cu K α radiation is about 1.5418 Å while the wavelength of Cr K α radiation is about 2.928 Å, in the resultant XRD spectra Cu radiation does not spread the peaks out as much as Cr radiation.

When X-rays pass through sample matter, the radiation interacts with the electrons in the atoms, which results in scattering of the radiation. If the atoms are organised in planes (i.e.

the matter is crystalline) and the distances between the atoms are of the same magnitude as the wavelength of the X-rays, constructive and destructive interference will occur [2.14]. In a typical experiment the diffracted intensity (of the scattered x-rays that obey Braggs Law) is measured as a function of the diffraction angle (2θ) and the orientation of the sample, which yields the diffraction pattern.

Diffraction will occur if a beam of x-rays falls on a series of atom-bearing planes, each a distance d apart, at an angle θ, if the Bragg Law:

$$\text{Eq}^n \text{ 2-2} \qquad n\lambda = 2d \sin \theta$$

By rearranging this equation the d spacing may be calculated, i.e.

$$\text{Eq}^n \text{ 2-3} \qquad d = n\lambda / \sin \theta$$

The terminology used for the spacing, i.e. d_{001}, derives from the particular plane of the crystals in the unit cell that is being measured [2.15]. As the sample is rotated through the incident beam different planes of regular crystalline form are encountered and it is these that are given the indices according to their position in the unit cell.

2.4.1.3 XRD Experimental Parameters

All clay and organoclay samples were prepared by grinding them for 30 seconds and then adding distilled water to form a dilute suspension, followed by application of the suspension to a glass slide with a pipette. The sample was then allowed to air-dry under a protective cover. Samples were offered to a detector as either:

a. a deposited film, obtained by smearing a clay solution on a glass slide and allowing the film to dry as described above,

b. a powder, by compacting a finely ground sample into an aluminium sample holder, or,

c. a solid sample (polymer-clay nanocomposites)

Studies were conducted on either a Philips PW3710 (Cu) or PW1710 (Cr) X-ray Diffractometer, operating at 40 kV and 40 mA. During experiments, it was possible to rotate the detector by using a goniometer in order to reach the required angle (possible range 1.8-75°). For preliminary identification of clay minerals, scanning from 1.8-40° 2θ is usually considered adequate [2.16]. The diffraction patterns were recorded with an angle range of 1.8-40° 2θ at a scan rate of 2° 2θ per minute unless otherwise stated.

2.4.2 Thermo-Gravimetric Analysis (TGA)

2.4.2.1 Thermal Analysis Techniques

The thermal stability of mineral complexes may be investigated using a variety of thermal techniques; these include thermo-gravimetric analysis (TGA), differential thermal analysis (DTA), differential scanning calorimetry (DSC) and thermo-mechanical analysis (TMA). In this research, TGA was the main thermal analysis technique (also coupled with mass spectrometry (TG-MS)), TGA was used to measure the shifts in mass desorption as a function of the type or amount of additive in a clays and polymer materials.

2.4.2.2 TGA Analytical Process
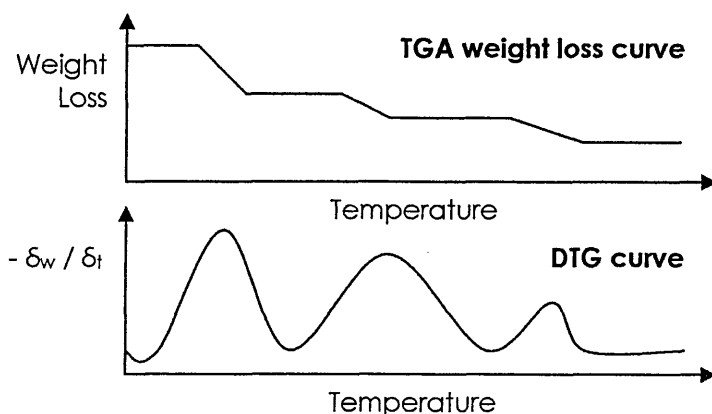
Figure 2.6   Diagrammatic representation of TGA / DTG data output curves.

82

TGA is the process of continually recording a sample's weight when subjected to a precise temperature program [2.17]. Samples may be heated from room temperature to 1200°C. The TG weight loss curve plots weight loss on the y axis and temperature increasing to the right on the x axis (fig. 2.6).

However, in this format, subtle weight changes may be difficult to determine. As an alternative representation, the negative derivative curve of the TG weight loss (i.e. $-dw/dt$: DTG) may be derived from the software, which is the rate of change in mass, with respect to the rate of change in temperature. These changes are shown as maxima, which can be related to changes observed in complementary thermal techniques, i.e. TG-MS.

TG analyses were able to resolve decomposition weight changes, however, TGA/DTG was not able to assign specific compounds to individual weight losses. TG-MS provided these results for organoclay decomposition. Previous examples of complimentary thermal analysis were shown by Paama et al. [2.18], who used TGA/DTG-FTIR analysis to determine the characteristic reactions occurring as archaeological samples were heated. Similarly, Thornley & Primmer [2.19] utilised TGA-evolved water analysis (EWA) to quantify clay minerals in whole rocks.

Several factors may influence the shape of a TG curve [2.20]:

A.   Sample size: Large samples may produce poorly resolved events. This may be due to: (i) a significant temperature gradient within the sample, and/or (ii) the difficult evolution of volatile products escaping from the sample. It was necessary to use a sample mass consistent with the capabilities of the thermo-balance. The samples which were analysed in this thesis were in the mass range 9.5-10.5 mg.

B.   Particle size distribution and packing density: These should vary as little as possible in order to optimise reproducibility.

C.   **The use of an inert atmospheres/gas flow:**   Nitrogen was used to suppress the oxidation of the organic material in the clays and composites analysed in this thesis. The effect of interaction of the sample and the gas involved with it is crucial. An atmosphere rich in decomposition products would have delayed the corresponding decomposition of the heated material until a higher temperature was reached. This principal is known as the Le Chatelier principal. Thus for the equilibrium:

$$X_{(solid)} \leftrightarrow Y_{(solid)} + Z_{(gas)}$$
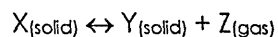
where when Z was produced by the system it would make it more difficult for X to decompose. Therefore a nitrogen flow rate of 20 cm^3 min^{-1} was used to remove Z.

D.   **The sample holder:** The sample container must not react with the sample as silica containers do with certain carbonates. Refractory crucibles were used in these studies (4 mm x 4 mm). The depth of the sample holder was also an important issue, as a shallow container would allow better exchange between the sample and its gaseous environment.

E.   **Heating rate:** Slow heating rates are used as standard for a variety of reasons. Often with increased heating rates the resolution of the TG curve will decrease as the difference between the actual temperature of the sample and the recorded temperature increases. Secondly maxima temperatures also increase with heating rate.   Therefore, heating rates of 10°C min^{-1} have been used throughout.

2.4.2.3   TGA Experimental Parameters

For samples where no evolved gas analysis was required, TGA was performed on a Mettler-Telodo TA8000 thermo-gravimetric analyser where a nitrogen gas flow was maintained at a rate of 20 cm^3 min^{-1}. The heating profile ensured that samples were first conditioned at 35 °C for 15 minutes in order to remove low temperature physisorbed components and obtain a stable weight reading. The temperature was then ramped at a rate of 10 °C min^{-1} up to 800 °C.

2.4.3 Evolved Gas Analysis (EGA) by Thermogravimetric-Mass Spectrometry (TG-MS)

A Unicam-Synergic Chemical Analysis System ('Synergy' system) was used to perform evolved gas analysis (EGA). The Synergy system consists of a thermobalance which recorded the weight loss of a sample, and the evolved gases were then detected by Mass Spectrometry (MS), where the output corresponded to different weight losses in real-time. This was referred to as real-time analysis because time/temperature related weight losses recorded using TGA could be related to spectrometric features shown by MS. For the purpose of this thesis, EGA by real-time MS will be known as TG-MS. MS produces a pattern consisting of a diagnostic pattern of charged particles and molecular fragments based on the ratio of mass:charge (m/z). Component analysis equipment of the TG-MS is linked via a series of temperature controlled transfer lines. Further parallel EGA by gas-phase FTIR and post-run analysis by OTM-GC-MS have so far been unavailable due to component failures.

2.4.3.1 EGA by TG-MS
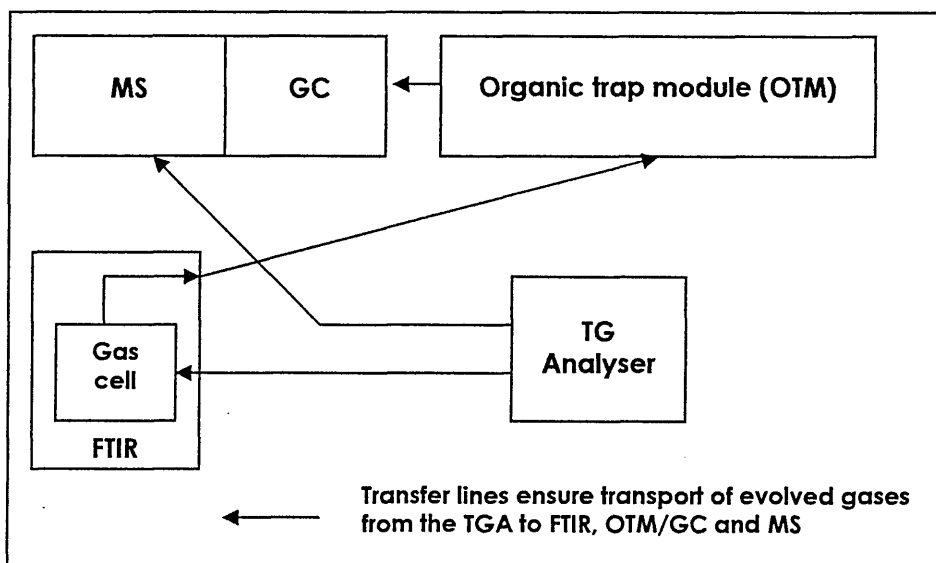
Figure 2.7 Diagrammatic representation of the SYNERGY EGA system.

2.4.3.2   Mass Spectrometer

An ATI Unicam Automass System 2 quadrupole mass spectrometer was used. In the course of this work, the MS was operated in the electron impact (EI), positive ionisation mode.

The MS consists of three main units: (i) Ion source, (ii) Ion analyser (quadrupole ion filter) and (iii) Mass detector.

2.4.3.2.1   Ion Source

The ion source was where the sample was introduced into the MS. In RT-MS, the TG-MS transfer line was directly interfaced with the ion source. The charged particles/ions used for mass analysis were formed by electron impact ionisation. The sample was passed through an electron beam (70 eV) and ionisation occurred when electrons struck sample molecules and imparted enough energy to remove other electrons from the sample molecules. For example, Methanol would undergo the following reaction in the ion source:

$$CH_3OH + 1 \text{ electron} \rightarrow CH_3OH^{+\bullet} \text{ (radical cation)} + 2 \text{ electrons}$$
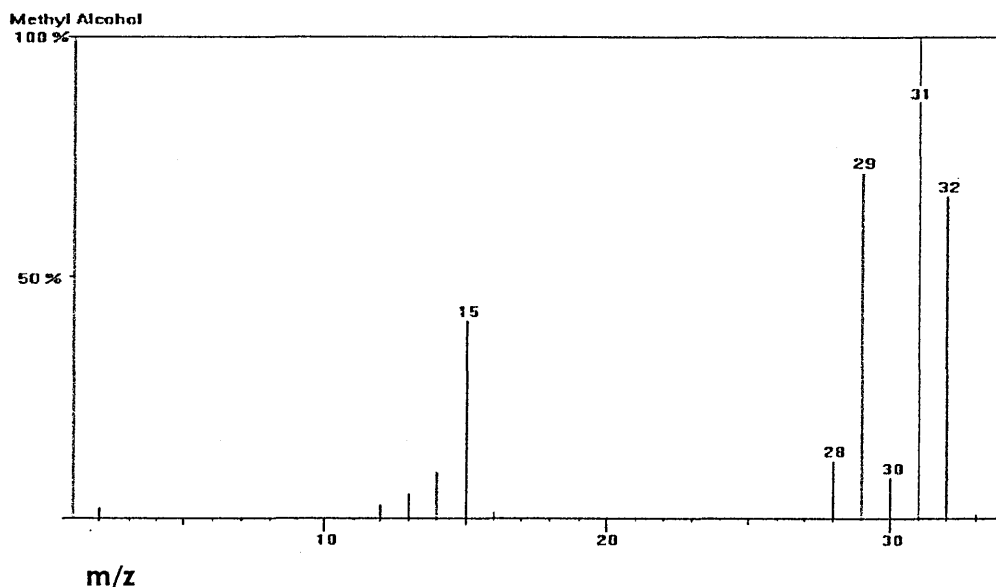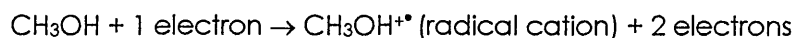
Figure 2.8   EI fragmentation pattern of methanol.

Electron impact ionisation usually produces singly charged ions containing one unpaired electron. The charged ion, which remains intact, is referred to as the molecular ion. Energy imparted by EI is more than that required to produce the molecular ion, this excess energy causes instability in the molecular ion, causing it to break into smaller fragments to give a characteristic mass spectrum. The methanol ion may be fragmented in various ways, with one fragment carrying the charge and one fragment remaining uncharged. For example:

$$CH_3OH^{+\bullet} \text{ (molecular ion)} \rightarrow CH_2OH^+ \text{ (fragment ion)} + H^{\bullet}$$

$$\text{or, } CH_3OH^{+\bullet} \text{ (molecular ion)} \rightarrow CH_3^+ \text{ (fragment ion)} + {}^{\bullet}OH$$
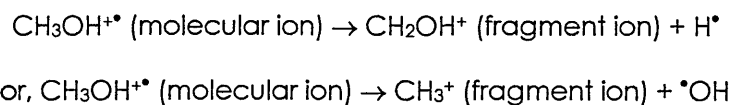
A typical EI fragmentation pattern of methanol is shown in fig. 2.8.

A schematic of the EI ion source is shown in fig. 2.9.
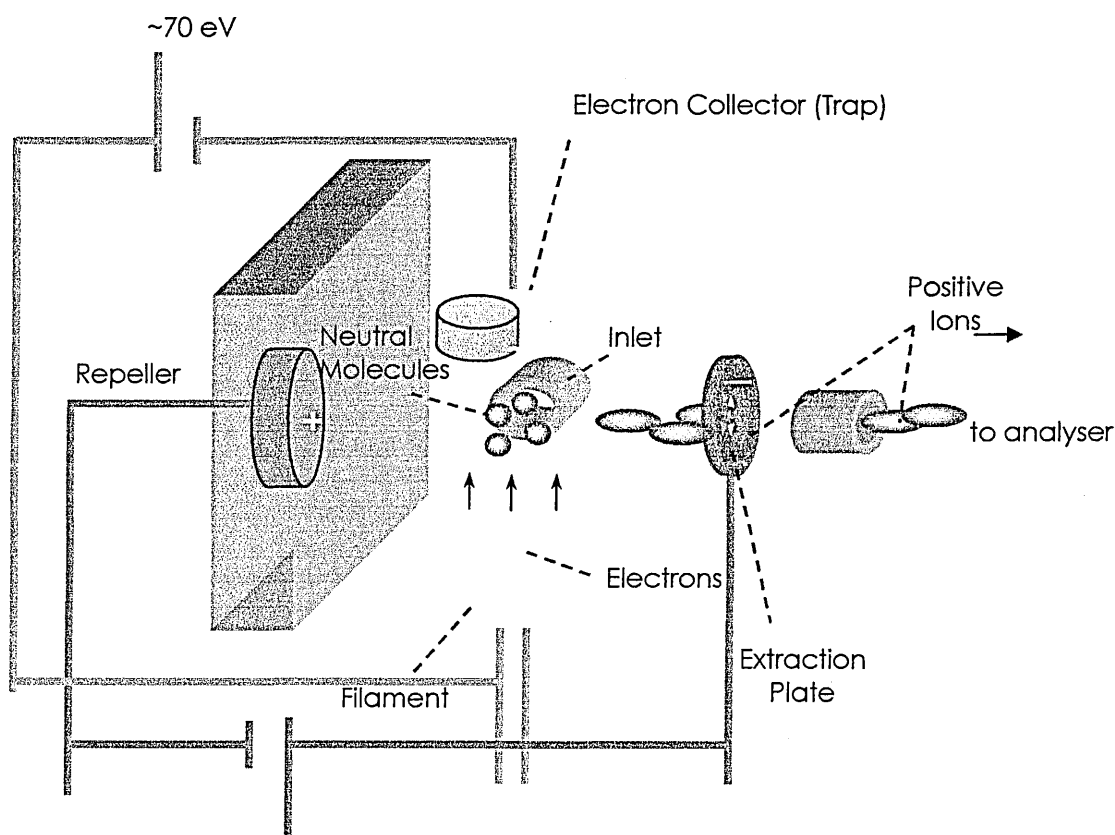
Figure 2.9   EI Ion Source.

From a qualitative viewpoint, the important features of this type of spectrum are:

i.   The ions produced are largely singly charged and the m/z ratio corresponds to the 'weight' of the elements involved. Not only is the elemental composition of each fragment ion accessible, but so are the molecular weight and molecular formula. These are probably the most important and discriminating pieces of information available to the analyst.

ii.   The ions produced may be related in most cases to the structure of the intact molecule using well-understood principles, which have a basis in theory.

iii. The mass spectra are reproducible. This is of crucial importance when libraries of reference spectra are used to aid structural determination.

However, there are two main disadvantages of EI, namely limitations in the range of compounds that may be successfully ionised and the utility of the resulting spectra. Samples must be volatile and thermally stable to yield an EI spectrum and this precludes the study of many unstable and thermally involatile analytes.

Fragmentation reactions may reduce the utility of EI spectrum by reducing the intensity of the molecular ion to a level that is not detectable. In these cases the molecular weight may not be determined and one of the single most valuable pieces of analytical information is lost. Therefore, the optimisation of the transfer line temperature and the introduction of the sample into the MS source were very important.

2.4.3.2.2   Ion Analyser (Quadrupole)

The molecular and fragment ions produced during ionisation of the sample were accelerated by manipulation of the charged particles through the mass spectrometer. Uncharged particles and fragments were pumped away. The quadrupole ion filter used positive and negative voltages to control the path of the ions. These ions travelled down a

path based on their m/z and were made to oscillate in the x and y directions by an electric field. El ionisation produces singly charged particles, so the charge (z) is one; therefore, an ion's path through the quadrupole would depend on its mass. A voltage consisting of a DC component and a radio frequency component was applied to adjacent rods with a 180° phase difference between the voltages applied to the two pairs. Therefore, if the $+(U+V \cos\varpi t)$ and $-(U+V \cos\varpi t)$ rods were fixed at a particular rf/dc voltage ratio, then one particular m/z would travel the successful path to the detector. However, voltages were not fixed, but were scanned across a range of rf/dc voltages whilst maintaining a constant U/V ratio, so that ever increasing masses could find a successful path through the rods to the detector.

2.4.3.2.3 Mass Detector

The MS detector works by producing an electronic signal when struck by an ion. A series of timing mechanisms integrated the signal abundance and associated it with a particular rf/dc voltage ratio (m/z). By doing this, the associated mass and signal abundance were correlated.

2.4.3.3 TG-MS Interface

The Synergy system uses a sniffer interface, to allow continuous operation of all acquisition techniques without any compromise in the quality of acquired data. This sniffer interface ensured that the evolved gases were sampled before they were allowed to diffuse throughout the entire volume of the TGA reaction cell [2.21].

The sniffer interface employed separate tubes for MS and FTIR sampling. They were constructed of a high temperature alloy and extend to a position just above the sampling cup where they were positioned so as not to interfere with the TGA hang-down wire. In the

case of the MS unit, the vacuum of operation served to draw the evolved gas. A schematic of the sniffer interface showing one transfer line is shown in fig. 2.10.
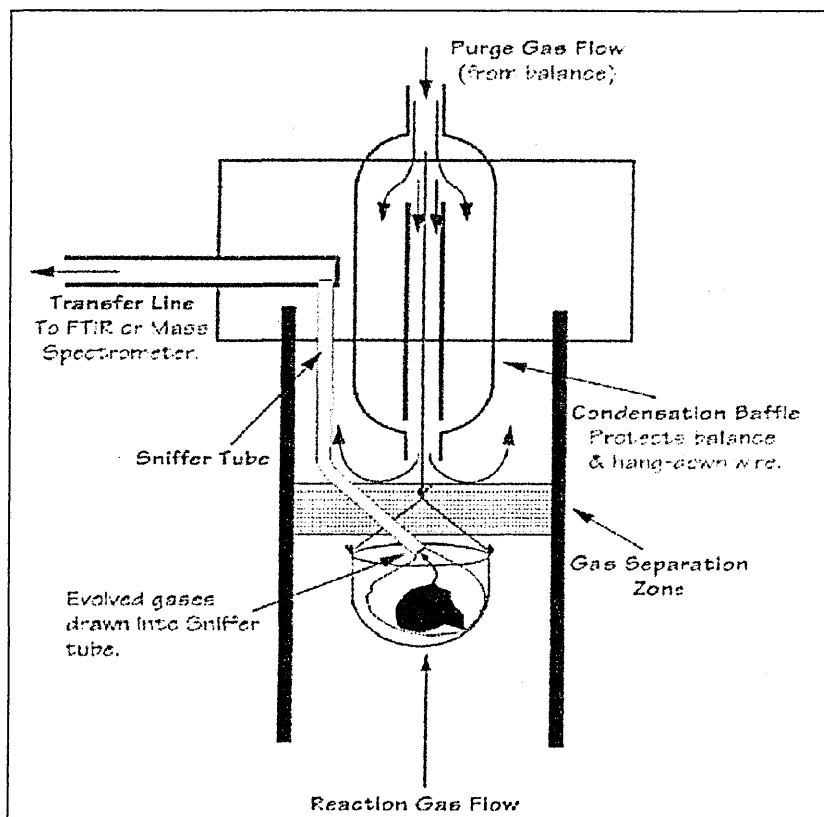
Figure 2.1   **Sniffer interface [2.22].**

2.4.4   Fourier Transform Infrared Spectroscopy (FT-IR)
2.4.4.1   General Theory of FT-IR
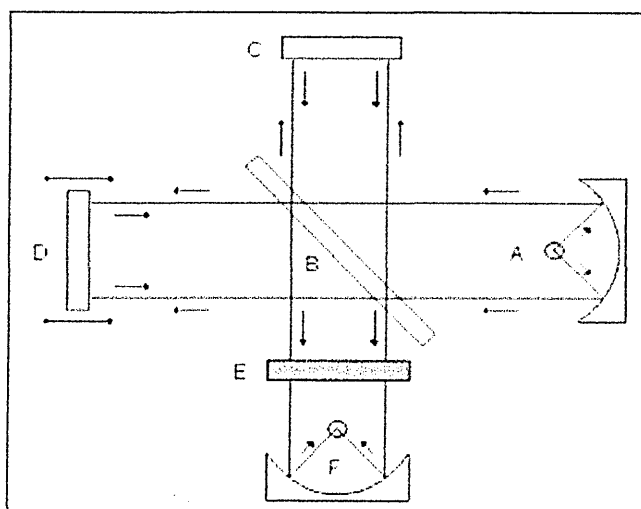
Figure 2.11   Schematic of a Michelson Interferometer.

The FT-IR instrument is based on a Michelson Interferometer (fig.2.11). The interferogram (in time domain) obtained from this set-up is converted to a spectrum (frequency domain) through mathematical procedures developed by Fourier [2.23-2.25].

In an interferometer the radiation from the source (A) is sent to a beam splitter (B) made from infrared transparent material, e.g. KBr. The beam is split into two beams, one of which passes through the beam splitter onto a moving mirror (D). The second beam is reflected from the beam splitter onto a stationary mirror (C). Both beams are reflected off the mirrors and recombined at the beam splitter. The recombined radiation is then passed through the sample (E) onto the detector (F).

FTIR has three major advantages over dispersive types of IR:

1. **Throughput (Jacquinot) advantage:** The Jacquinot advantage is due to the fact that no slits are needed in this set-up. Therefore the amount of radiation that reaches the detector is higher and an increased signal to noise ratio can be observed.

2. **Multiplex (Fellgett) advantage:** The Fellgett advantage is achieved because all frequency elements reach the detector simultaneously. Because of this the spectrum can be obtained in a very short time.

3. **Laser reference (Connes) advantage:** The Connes advantage is derived from the sampling method. The time interval at which information is sampled is determined by utilising a laser with a fixed wavelength (usually 632.8 nm). As the time interval can be measured very accurately the frequency domain spectrum obtained from the Fourier transformation is also very accurate. This allows the averaging of scans to reduce the signal to noise ratio of the final spectrum.

The spectral range in FT-IR spectrometers is determined by the type of beam splitter and detector used. In ATR (Attenuated Total Reflectance) experiments the type of ATR crystal will also influence the spectral range. The parameters that control the quality of an FT-IR spectrum therefore are:

- the velocity of the moving mirror

- the resolution

- the number of scans taken per spectrum

- mathematical calculations taken during the Fourier Transformation, e.g. Apodisation function.

2.4.4.2 Transmission Fourier Transform Infrared Spectroscopy

Transmission FT-IR is the most basic infrared sampling technique. The radiation is passed through the sample onto a detector.
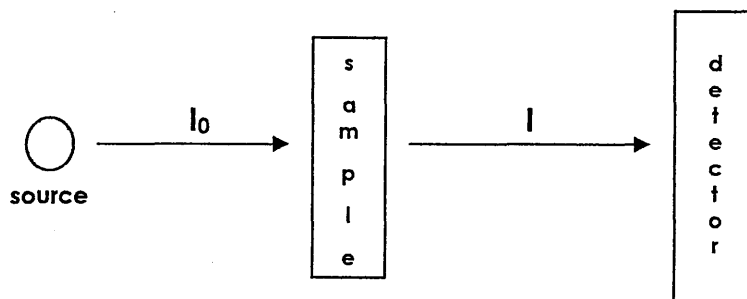
Figure 2.12   Schematic of the beam path in transmission measurements.

Transmission in these experiments is defined as:

$$\text{Eq}^n \text{ 2-4} \qquad T = \frac{I}{I_0} = \exp(-\alpha l)$$

where:

I: transmitted intensity, I_0: incident intensity, α: absorption coefficient, l: sample thickness

With this technique, information on the bulk of the sample can be obtained. The thickness of the samples that can be analysed by this method depends on the absorption properties of these samples. For strongly absorbing samples only thin films can be analysed. Samples

can also be presented pressed into KBr discs. This sample preparation can be time-consuming and difficult to reproduce.

2.4.4.3   Attenuated total reflectance Fourier Transform Infrared Spectroscopy (ATR-FTIR)

Attenuated total reflectance (ATR) spectroscopy, also known as Internal reflection spectroscopy (IRS), is especially suitable for the analysis of physically thick, strongly absorbing samples. The sample is placed in contact with an ATR crystal. The IR radiation sent through this crystal undergoes total reflection at the sample/crystal interface.
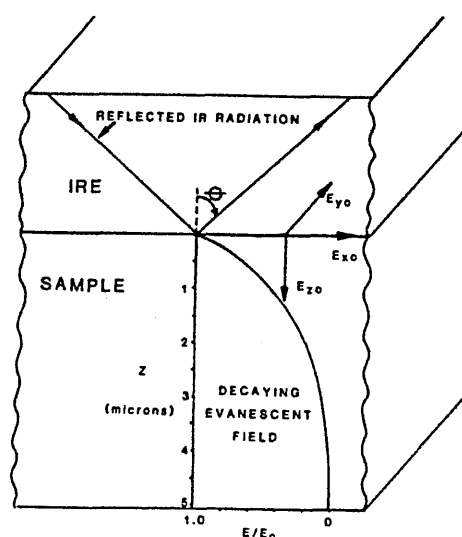
Figure 2.13   Evanescent field penetrating the sample [2.26].

The number of total reflections occurring is dependent on the size and geometry of the crystal as well as the angle of incidence of the incoming light [2.26].

Light travelling through a medium with a high refractive index (e.g. Diamond - refractive index = 2.42) (the IRE) to an interface with a material of lower refractive index creates an evanescent field that penetrates the sample at each point of total reflection. The evanescent field decays exponentially with increasing depth. The depth at which the field has dropped to 1/e (≈36.8 %) of its original value has been defined as the depth of

penetration. As this parameter has been arbitrarily defined by Harrick the naming has caused some confusion. The depth of penetration can be calculated using the following equation [2.26, 2.27].

$$\text{Eq}^\text{n}\ 2\text{-}5 \qquad d_p = \frac{\lambda_1}{2\pi(\sin^2\theta - n_{21}{}^2)^{0.5}}$$

where:

θ: Angle of incidence, $n_{21} = n_2/n_1$, n_1: refractive index of the IRE, n_2: refractive index of the sample, $\lambda_1 = \lambda/n_1$

Experiments with polypropylene and polystyrene on a KRS-5 crystal have shown that the actual depth sampled is greater than the depth of penetration as given by the equation above. The actual depth sampled is ~3d_p [2.26, 2.27].

Spectra for transmission and ATR experiments are similar if the assumption that the specimen thickness is >> d_p is valid with the exception that the coupling of the field to the dipoles in the specimen depends on the wavelength. The effective thickness (d_e) which is the equivalent thickness of a transmission sample which would produce the same energy absorption as a single internal reflection can therefore be calculated to enable comparisons between the spectra [2.23, 2.26, 2.27]. For these calculations the two possible polarisations of the incident light need to be taken into account. The transverse electric wave (TE) which is perpendicular to the plane of incidence and the transverse magnetic wave (TM) which is parallel to the plane of incidence.

$$\text{Eq}^\text{n}\ 2\text{-}6 \qquad d_e(TE) = \frac{n_{21}\cos\theta\,\lambda_1}{\pi\left(1 + n_{21}{}^2\right)\left(\sin^2\theta - n_{21}{}^2\right)^{0.5}}$$

$$\text{Eqn}\ 2\text{-}7 \qquad d_e(TM) = \frac{n_{21}\cos\theta\,\lambda_1\left(2\sin^2 - n_{21}{}^2\right)}{\pi\left(1 + n_{21}{}^2\right)\left(\sin^2\theta - n_{21}{}^2\right)^{0.5}\left[\left(1 + n_{21}{}^2\right)\sin^2\theta - n_{21}{}^2\right]^{0.5}}$$

where:

θ: Angle of incidence, $n_{21} = n_2/n_1$, n_1: refractive index of the IRE, n_2: refractive index of the sample, $\lambda_1 = \lambda/n_1$

From these equations it may be seen that the effective thickness sampled during the experiment can be varied by choosing suitable values for θ and n_{21}. High θ make the method more surface selective but at the same time decrease the number of reflections and therefore the sensitivity. High refractive indices for the IRE also increase the surface selectivity at the expense of spectral intensity. The choice of IRE is also influenced by other considerations such as durability, frequency range, cost and solvent resistance.

A major problem with ATR is the good sample contact required to obtain quantitative spectra. In order to get good contact the sample surface needs to be as flat as possible. This requirement has often cast doubt on the reproducibility of ATR measurements [2.26].

The detection range is dependent on the type of detector, the material of the beam splitter and the IRE. For ATR measurements a more sensitive detector needs to be used than for transmission as the energy reaching the detector is much lower because of absorption during the multiple reflections and losses in the optical system.

2.4.4.4 Diffuse Reflectance Infrared Fourier Transform Spectroscopy (DRIFTS)

Diffuse Reflectance Infrared Fourier Transform Spectroscopy (DRIFTS), is especially suitable for the analysis of powder samples.
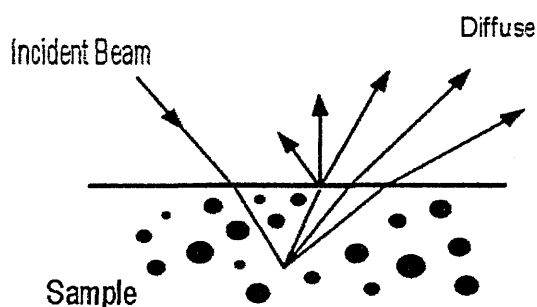
Figure 2.14   Schematic of diffuse reflectance studied in DRIFTS.

Diffuse Reflectance Infrared Fourier Transform Spectroscopy (DRIFTS) is a useful technique for measuring the amount of ionic compounds present in ceramic powders.

TWO ELIPTICAL MIRRORS

SAMPLE CUP

Incident
Radiation

To
Detector

FLAT MIRROR
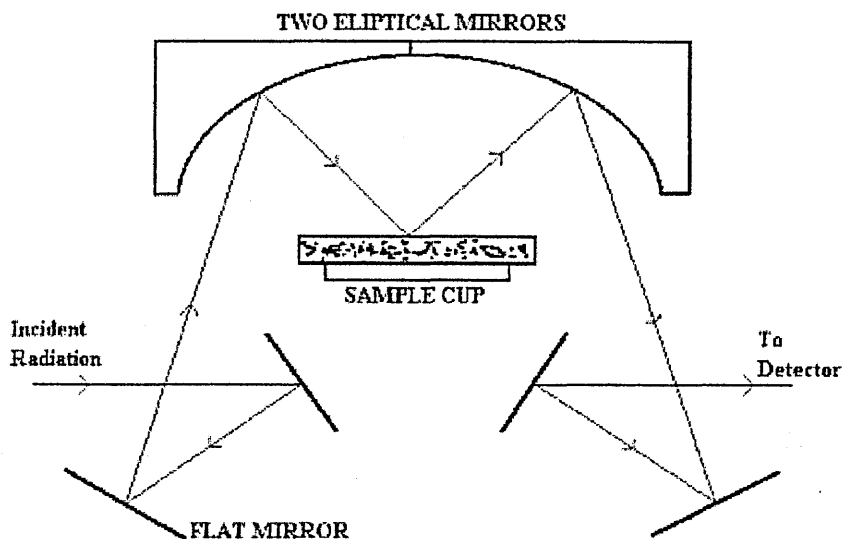
Figure 2.15   Schematic of DRIFTS attachment for FT-IR.

The advantages of using DRIFTS are [2.28]:

- It is a sufficiently sensitive technique in the Mid-IR spectral region, where compounds such as: sulfates, nitrates, phosphates and carbonates absorbs strongly. Detection of compounds in low concentrations is therefore possible.

- It is a very fast and specific method for analysing the clay powders for ionic compounds. Preparation of samples, recording of FTIR-spectra and data analysis can be carried out in a short duration.

DRIFTS has been applied to the analysis of a variety of powdered materials:

- Inorganic materials: cement [2.29], coals [2.30], kaolinite [2.31], silicon nitride [2.32] and calcium carbonate [2.33].

- Organic materials: carbohydrates [2.34] and caffeine [2.35].

Quantifying the concentrations of the chemical compounds by infrared spectrometry in powders is, however, a much more difficult task than in gas and liquid analysis. It has been recognised that parameters such as: particle sizes, sample packing density [2.35, 2.36], optical properties of the powder [2.37] all influence the measurements.

2.4.5   Environmental Scanning Electron Microscope (ESEM)

ESEM studies were conducted using a Philips XL30 ESEM-FEG coupled with an Oxford Instruments LINK-ISIS Energy Dispersive X-ray Analyser (EDX).   ESEM microscopes are specifically designed to study samples such as polymers without prior specimen preparation, because the ESEM is not reliant on a conducting surface as in SEM. Samples that conduct electricity are easier to study because the unimpeded flow of electrons to ground minimises problems associated with the build-up of charge. Because the sample chamber is not at a very high vacuum this alleviates the need for a conductive coating as gas ionisation neutralises the charge build-up. Therefore samples that are wet or non-conductive may be examined in water vapour or other gases such as CO_2 or N_2 at near atmospheric pressures, due to the ESEM's unique vacuum system.   Under such environmental conditions magnifications of up to x 50,000 (with resolutions guaranteed to 100 Å) are possible.

A differential pumping system allows the entire ESEM specimen chamber to be maintained at a controlled gas pressure separately from the field emission gun (FEG). An automatic servo system gives an operating chamber pressure that can be held constant between 1–20 torr.

Specimen temperature can range from -200°C to 1000°C, moisture content and gas environment can also be manipulated precisely and at will, while continuously observing the sample. Real-time processes such as wetting, drying, absorption, melting, corrosion and crystallisation can be recorded. The ESEM's computer driven 5-axis stage is useful for making accurate long-distance measurements and for automatically returning to the exact spatial co-ordinates on the sample after removal for experimental treatments [2-38].

2.4.6   Atomic Force Microscopy (AFM)

Atomic force microscopy (AFM) operates by measuring attractive or repulsive forces between an atomically sharp tip and sample surface [2-39]. The force between the tip and the sample surface is very small, usually less than 10^{-9} N.
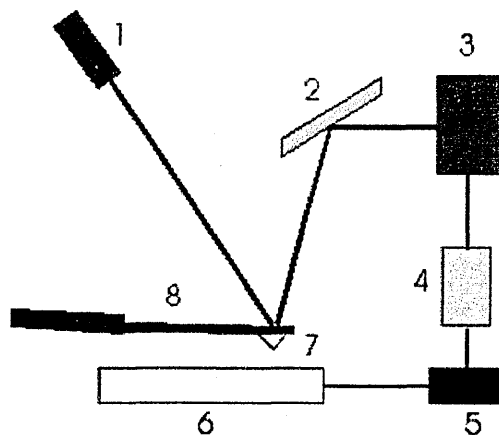
Figure 2.16   Schematic of AFM components: 1-Laser, 2-Mirror, 3-Photodetector, 4-Amplifier, 5-Register, 6-Sample, 7-Probe, 8-Cantilever.

When an AFM tip is scanned over a sample surface, feedback mechanisms enable the piezo-electric scanners to maintain the tip at a constant force (to obtain height information), or height (to obtain force information) above the sample surface. Tips are typically made from Si_3N_4 or Si, and extended down from the end of a cantilever.
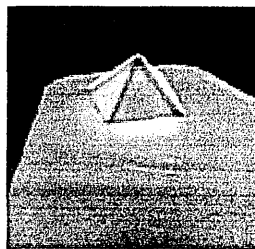
Figure 2.17   Image of an AFM tip [2-40].

The AFM head has an optical detection system in which the tip is attached to the underside of a reflective cantilever. A diode laser is focused onto the back of a reflective cantilever. As the tip scans the surface of the sample, moving up and down with the contour of the surface, the laser beam is deflected off the attached cantilever into a dual

element photodiode. The photodetector measures the difference in light intensities between the upper and lower photodetectors, and then converts to voltage. Feedback from the photodiode difference signal, through software control from a computer, enables the tip to maintain either a constant force or constant height above the sample. In the constant force mode the piezo-electric transducer monitors real time height deviation. In the constant height mode the deflection force on the sample is recorded. To obtain useful AFM results, the AFM head needs to be vibrationally isolated from its surroundings. This isolation unit consists of a concrete base attached to bungee cords firmly anchored to a stable freestanding tripod.

2.4.6.1 AFM Tip-Sample Interaction

The way in which image contrast is obtained can be achieved in many ways. The three main classes of interaction are contact mode, tapping mode and the phase-imaging option, and non-contact mode.

2.4.6.2 Tapping Mode

When operated in air or other gases, the cantilever is oscillated at its resonant frequency (often hundreds of kilohertz) and positioned above the surface so that it only taps the surface for a very small fraction of its oscillation period. This is still contact with the sample in the sense defined earlier, but the very short time over which this contact occurs means that lateral forces are dramatically reduced as the tip scans over the surface. When imaging poorly immobilised or soft samples, tapping mode may be a far better choice than contact mode for imaging [2-41].

Phase Imaging is an extension of the tapping mode and was the most commonly used technique in this thesis. By mapping the phase of the cantilever oscillation during the tapping mode scan, phase imaging may detect variations in composition, adhesion, friction, viscoelasticity, and perhaps other properties. The applications include mapping of

different components in composite materials, identification of contaminants and differentiating regions of high and low surface adhesion or hardness. In many cases, often providing additional information more rapidly and with higher resolution.

2.4.6.3 Advantages of AFM

As a method for imaging a sample surface, compared with a scanning electron microscope (SEM), AFM provides good topographical contrast, direct height measurements and unobscured views of surface features without the need for prior coating. Compared with transmission electron microscopes (TEM), 3-D AFM images are obtained without expensive sample preparation and yield far more complete information than the 2-D profiles available from cross-sectioned samples used in TEM.

2.4.7 Gel Permeation Chromatography (GPC)

Gel permeation chromatography (GPC), also referred to as size exclusion chromatography (SEC) is a liquid column chromatographic technique that separates molecules on the basis of their sizes or hydrodynamic volumes with respect to the average pore size of the packing.
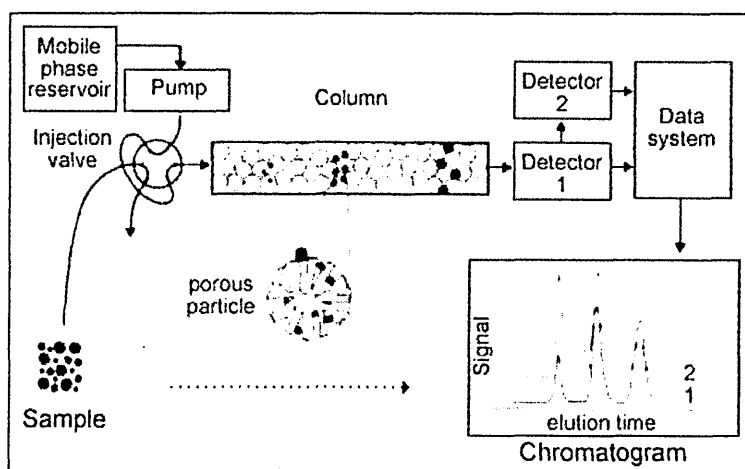
Figure 2.18   Schematic of GPC system [2-42].

Analysis of selected samples by GPC was conducted at Scott-Bader to measure differences in the molecular weight and polydispersity of selected polystyrene nanocomposite materials.

The GPC approach uses columns containing finely divided, porous particles [2-43, 2-44]. The sample molecules are introduced into a stream of solvent (mobile phase) and are then pumped to flow through a bed of a porous polymer or silica-based particles (stationary phase). The sample molecules that are smaller than the pore size enter the stationary-phase particles, and so, have a longer path/retention time than larger molecules that cannot enter the pore structure. Small molecules can enter virtually every pore, and so, are eluted last. The sizes of the mid-size molecules regulates the extent to which they can enter the pores of the stationary phase. Larger molecules are excluded and, therefore, are rapidly carried through the system. Therefore, the larger molecules elute earlier in the chromatogram, while the smaller molecules elute later. This system is largely an entropically governed phenomenon, with motion in and out of the pores being statistically governed by Brownian motion and flow rate.

2.4.7.1   GPC Experimental Parameters

All selected samples were analysed on an Agilent 1100 Series GPC Analysis system using Polymer Laboratories GPC software. Selected samples were introduced into a stream of THF eluent (*1wt% in 10ml*) that was pumped at 0.5 ml/min through a bed of a porous silica-based particles (i.e. 2x Shodex GPC KF-604) with a polystyrene size exclusion limit relative to a MW of 400,000, at 45°C. A variable wavelength detector was used to detect changes in the absorption of UV light (100-400 nm) by the eluted mobile phase.

2.4.8   X-ray Fluorescence (XRF) Spectrometry

An XRF spectrometer was used for quality assurance by determining the quantity of elemental oxides present in all Na^+ exchanged clay samples.

2.4.9 ^{31}P NMR

Kaolin samples exchanged with phenylphosphonic acid (KPPA) were submitted to the EPSRC NMR facility at Durham University for ^{31}P NMR. ^{31}P NMR was used as a characterisation technique to analyse any phosphorous shifts in the different KPPA systems.

Chapter 2 - References

[2-1]   Grim, R.E., Clay Mineralogy: McGraw-Hill, New York, 1968, 596.
[2-2]   Sposito, G., *Surface Chemistry of Soils*. Oxford Univ. Press, Oxford, 1984.
[2-3]   White, G. N., Zelazny, L. W., *Clays Clay Minerals*, 1988, **36**, 141.
[2-4]   Doh, J.G. and Cho, I., *Polymer Bulletin*, 1998, **18**, 97.
[2-5]   LeBaron, P.C, Wang, Z. and Pinnavaia, T.J., *App. Clay Sci.*, 1999, **15**, 11.
[2-6]   ICSC:0073, Styrene, Last accessed: 12.8.2003, URL: http://www.cdc.gov/niosh/ipcs/ipcs0073.html
[2-7]   Hendricks S.B, Fry W.H. Soil Science, 1930, 29, 457.
[2-8]   Kelley W.P, Dore W.H and Brown S.M. *Soil Science*, 1931, **31**, 25.
[2-9]   Hendricks S.B, Tellet E., *J. Phys. Chem.*, 1942, **10**, 147.
[2-10]   Berry L.G, Mason B, 'Mineralogy-concepts, descriptions, determinations', W.H Freeman & Company, London, 1959.
[2-11]   Brindley G.W, Brown G, 'Crystal Structures of Clay Minerals and their X-ray identification', Mineralogical Society, Monograph No: 5, Spottiswoode Ballantyne Ltd, London, 1980.
[2-12]   Cullity B.D, 'Elements of X-ray Diffraction' Addison Wesley, Reading, 1978.
[2-13]   Moore D.M, Reynolds C (JR), 'X-ray Diffraction and the Identification and Analysis of Clay Minerals', 2nd ed., Oxford University Press, 1997.
[2-14]   As ref. [2-13], Ch. 2, p 58.
[2-15]   Guy A., *Essentials of materials science*, McGraw-Hill Kogakusha Ltd 1976.
[2-16]   Skoog P., Holler F. & Nieman T., *Principles of Instrumental Analysis*, 5th Ed., Saunders College Publishing, 1998, 294.
[2-17]   Dodd J.W, Tonge K.H, Thermal methods (Currell, B.R, ed.) John Wiley & Sons, London, 44, 1987.
[2-18]   Paama L, Pitkanen and Peramaki P., *Talanta*, 2000, **51**, 349.
[2-19]   Thornley D.M, Primmer T.J., *Clay Minerals*, 1995, 30, 27.
[2-20]   Dodd J.W, Tonge K.H, Analytical Chemistry by Open Learning (ACOL): Thermal methods, Published on behalf of ACOL by John Wiley & Sons, London.
[2-21]   Green, Andrew. MWTF Minneapolis, Minnesota, 1994.
[2-22]   Czarnecki J, Thumin D, Gas Flow Separation: The Sniffer Interface, NATAS conference proceedings, Toronto, Canada (1995)
[2-23]   Griffiths, P. & de Haseth, J.A., Fourier Transform Infrared Spectrometry, Wiley&Sons, New York, 1986.
[2-24]   Materials Research Institute webpage, last accessed: 25.9.2003, URL: http://www.shu.ac.uk/schools/research/mri/pcas/
[2-25]   Maddams, B., *Int. J. Vibr. Spec.*, 2001, **5**, 3.
[2-26]   Mirabella, M., *Appl. Spec. Rev.*, 1985, **21**, 45.
[2-27]   Garton, A., Infrared Spectroscopy of Polymer Blends, Composites and Surfaces', Hanser Publishers, Munich, 1992.
[2-28]   Hamadeh, I.M., Yeboah, S.A., Trumbull, K.A., and Griffiths, P.R., Appl. Spec., 1984, **38**, 486.
[2-29]   Hughes, T.L., Methven, C.M., Jones, T.G.J., Pelham, S.E., Fletcher, P. and Hall, C., Advn. Cem. Bas. Mat., 1995, **2**, 91.
[2-30]   Porro, T.J. & Pattacini, S.C., *Appl. Spec.*, 1990, **44**, 1170.
[2-31]   Tsuge, A., Uwamino, Y., Ishizuka, T. & Suzuki, K., *Appl. Spec.*, 1991, **45**, 1377.
[2-32]   Hembree, D.M. & Smyrl, H.R., *Appl. Spec.*, 1989, **43**, 267.
[2-33]   Bak, J. & Kindl, B., *Appl. Spec.*, 1997, **51**, 1730.
[2-34]   Olinger, J.M. & Griffiths, P., *Appl. Spec.*, 1993, **47**, 687.
[2-35]   Agyare, S., Wang, S. & Griffiths, P.R., *Appl. Spec.*, 1984, **38**, 259.
[2-36]   Moradi, K., Depecker, C. & Corset, J., *Appl. Spec.*, 1994, **48**, 1491.
[2-37]   Krivacsy, Z. & Hlavay, J., *Spectrochimica Acta*, 1994, **50A**, 49.
[2-38]   Materials Research Institute webpage, last accessed: 25.9.2003, URL: http://www.shu.ac.uk/schools/research/mri/instr/esem.htm.
[2-39]   Binnig, G., Quate, C.F., and Gerber, C., Atomic force microscope. *Phys. Rev. Lett.*, 1986, **56**(9), 930.
[2-40]   Gallego-Juárez, J.A., Piezoelectric ceramics and ultrasonic transducers. *J. Phys. E: Sci. Instrum.*, 1989, **22**, 804.
[2-41]   Hoh, J.H. and Hansma, P.K. (1992) Atomic force microscopy for high-resolution imaging in cell biology. *Trends Cell Bio.*, 1992, **2**, 208.
[2-42]   Pasch, H. & Trathnigg, B., *HPLC of Polymers,* Springer-Verlag, Berlin, 1998.
[2-43]   Provder, T. (Ed.), *Chromatography of Polymers: Characterization by SEC and FFF*, American Chemical Society, Washington, DC, 1993.
[2-44]   Potschka, M. and Dublin, P.L. (Eds.), *Strategies in Size Exclusion Chromatography*, American Chemical Society, Washington, DC, 1996.

3

Thermal Stability of Organoclays

3.1   Introduction to Organoclay Studies

It has long been known that the exchangeable gallery cations of natural clays could be replaced by various organocations through a simple ion exchange process. These organocations may, for example, have an ammonium functional group, consisting of a nitrogen atom in an alkyl or quaternary ammonium complex, with a positive charge. This organocation would be exchanged onto the clay surface replacing Na^+, Ca^{2+},.... ions (i.e. preferentially absorbed to cation-exchange sites) and the free inorganic cations from the clays and halide ions from the amines would then be washed out (Lagaly, 1984) [3-1].

Cowan and White (1958) [3-2] studied the adsorption of straight-chain alkylammonium salts by Na-bentonites. A linear relationship was found between a change in the free energy of the alkylammonium surfactant and the number of carbon atoms in the aliphatic chain. The increment in the free energy was ascribed to Van der Waals interactions between the chains. Consequently, a mechanism for the exchange process was proposed in which the length of the hydrocarbon chain was considered to play the most important role. Similarly, Theng et al. (1967) [3-3] found that the affinity of a clay for the organic molecules was linearly correlated to the molecular weight of the alkylammonium ion, i.e. the greater the length of the alkyl chain, the greater the contribution to the physical forces of adsorption.

The stability of alkylammonium-MMT complexes has been partly attributed to the van der Waals attraction of hydrocarbon chains with their neighbouring chains and with the clay surface. Other contributions are believed to be due to the thermodynamic stabilisation of the alkylammonium ion at the clay surface when compared with the same ion hydrated in aqueous solution. As a result, organoclay complexes are generally thermally stable up to at least 175°C (Jones, 1983) [3-4].

The intercalation of alkylammonium ions with different chain lengths has been used to determine the layer charge distribution of clay minerals (Lagaly & Weiss, 1969 [3-5] and

Lagaly, 1994 [3-6]) and also to study the changes in the octahedral and tetrahedral charge of smectites after Li$^+$ fixation (Maes, 1979 [3-7], and Malla, 1987 [3-8]).

A variety of organocations have been used in industry for more than 60 years as thickeners and rheological agents for oil based drilling fluids, paints, greases, inks and as binders for oil based foundry sands (Jordan, 1949 [3-9]). Organoclays are also effective absorbents for removing organic contaminants from water. When non-polar molecules and dissolved organic compounds encounter organoclay particles with their alkyl chains protruding into a polar solvent (e.g. H_2O), these species would be attracted by the alkyl chains (i.e. because they are chemically similar). Since this partitioning activity takes place in the galleries of the clay particles, no stable binding to the surface of the clay occurs. Their use as adsorbents for organic compounds in water was mentioned as early as the 1960's (Street, 1963 [3-10] & Slabaugh, 1969 [3-11]), but most work has been conducted since the 1980's. The hydrophobic interactions that occur between non-polar organic pollutants and the alkyl chains of organoclays reduces the mobility of organic pollutants (i.e. in soil and waterways), like benzene derivatives (BTX) and phenols (i.e. non-ionic chemicals with low water solubility). This extends to the use of organoclays to remediate groundwater and industrial wastewater at underground storage tank sites, oil storage terminals, oil drilling sites and refineries, where the groundwater may be contaminated with oil, grease, phenolic compounds, aromatic and halogenated hydrocarbons (Boyd, 1991 [3-12] and Brixie & Boyd, 1994 [3-13]).

Depending on the size of the organic cations and the layer charge of the mineral, the alkyl chains of the organocations may be arranged in different configurations within the gallery space, and so, may impart steric/size exclusion thresholds for the adsorption of organic molecules.

Cation exchange of a normally hydrophilic silicate surface renders it organophilic, this makes it possible to intercalate the clay's gallery space with many different engineering polymers. The role of alkylammonium cations in an organoclay for the production of nanocomposites is to lower the surface energy of the inorganic host, and so, improve its wetting characteristics with respect to the polymer. Also, the alkylammonium cations may have functional groups that could either react with the polymer [3-14] or initiate the polymerisation of monomers [3-15] to improve the strength of the interface between the inorganic host and the polymer.

In this chapter, the focus has been to exchange *N*-alkylammonium and quaternary alkylammonium cationic species with variable carbon chain lengths, into Na-form clays with different crystallinity and homogeneity of charge distribution. Special emphasis was placed on the determination of whether the different organocations and clay compositions that were produced lead to improved thermal stability of the organocation. The thermal decomposition of the organic species, resulting from a Hoffman degradation process (outlined in section 1.4.3.1, ch. 1), was followed using RT-TG-MS. The clays and organocations that were chosen also permitted an investigation of how the layer charge and elemental composition of the octahedral sheet influenced the decomposition of the alkylammonium ions. In particular, the use of SWa-1 provided the possibility of determining if structural iron exerted any influence on the alkylammonium ion decomposition.

3.2   Materials and Methods

3.2.1   Clays Used

The <2 μm fractions of four bentonite clays were utilised in this study the general descriptions of each are given in table 3.1 and the structural compositions are listed in table 3.2. SWa-1 and SAz-1 clays were prepared in Bratislava for a previous research project and had been stored securely since.

Clay Specimen	Mineralogy	Source
Cheto (SAz-1)	Ca rich-MMT	Arizona, USA
Nontronite (SWa-1)	Ferruginous smectite	Washington, USA
Mineral Colloid British Pharmocopea (MCBP)	Na-MMT	Various sources, ECC International, Cornwall, UK
Cloisite	Na-MMT	Various sources, Southern Clay Products, Texas, USA

Table 3.1   General description of clays utilised throughout this thesis.

Sample	Structural Composition
SAz-1	$Si_4Al_{1.34}Mg_{0.6}Fe_{0.07}O_{10}(OH)_2.(H_2O)_n$
SWa-1	$Si_{3.64}Al_{0.42}Mg_{0.14}Fe_{1.46}O_{10}(OH)_2.(H_2O)_n$
MCBP	$Si_{3.64}Al_{0.42}Mg_{0.14}Fe_{1.46}O_{10}(OH)_2.(H_2O)_n$
Cloisite	$Si_{3.64}Al_{0.42}Mg_{0.14}Fe_{1.46}O_{10}(OH)_2.(H_2O)_n$

Table 3.2   Mineral Formulae for smectite species used in this thesis [3-3 & 3-16].

3.2.2   Alkylammonium Exchange

SAz-1 and SWa-1 were first saturated with Na^+ using a 1M NaCl solution, then washed free of excess ions using de-ionised water and ethanol and air dried at 60 °C before being ground to pass through a 200 μm sieve. 100 mg of the Na-form clay was then exchanged with 2 ml of 0.1M aqueous solutions of primary alkylammonium salts of increasing chain length from C_6 to C_{16} [3-6].

MMT was saturated with Na^+ by dispersing 5 g clay in 150 ml 1M NaCl, washed free of excess ions by centrifuging the Na-form clay down from a slurry (clay and deionised water) and was repeated until the conductivity of the supernatant was below 50 μS, ensuring no ionic product remained in the solution [3-17]. The samples were then covered on the laboratory bench and air-dried for 48 hours. After drying, samples were ground to pass

through a 200 μm sieve. This clay was then exchanged with quaternary alkylammonium salts with chain lengths of C_8, C_{12}, C_{14} and C_{16}, to run as a comparative study with the Slovak clays. The organocation loading on the clay was linked to the cation exchange capacity (CEC) of MCBP (80 mEq / 100g). In the initial experiments the clay was loaded at different quantities with respect to the CEC (i.e. 1.0 x, 2.0 x, etc..) to study the effect this would have on the physical properties of the organoclay and its inclusion in subsequent polymer-clay nanocomposites. All samples were prepared in triplicate to alleviate any anomalies.

3.2.3 X-ray Diffraction Analysis (XRD)

XRD was utilised to determine the spacing between the expanded layers of the different organoclays, using a Philips PW3710 (Cu tube) and PW1710 (Cr tube) X-ray diffractometers. The same experimental procedure and operational conditions, as described in section 2.4.1.3, ch. 2, were used to obtain the diffraction traces.

3.2.4 Thermo-Gravimetric Analysis (TGA)

TGA was utilised to measure the thermal stability of the Na+ clays and the respective organoclay derivatives, using a Mettler TG50 Thermobalance. The same experimental procedures and operational conditions, as described in section 2.4.2.3, ch. 2, were used to obtain the thermograms.

3.2.5 Real-Time TG-MS Analysis

The mass spectra of the gases evolved during the heating process were recorded using the same thermobalance (Cahn TG131) - MS assembly and experimental conditions given in section 2.4.3, ch. 2.

3.2.6 Sample Identification

Throughout this and subsequent chapters, the different organoclay species will be referred to with respect to the clay type, organocation species and alkyl chain length (Table 3.3).

Mineral / Organic Components	Abbreviation
SAz-1 / Na$^+$ exchanged SAz-1 / octylammonium cation, with $C_n = 8$ $\downarrow$ SAz-1 / octylammonium cation, with $C_n = 16$	**Na-SAz-1** **SAz-1-C$_8$** $\downarrow$ **SAz-1-C$_{16}$**
SWa-1 / Na$^+$ exchanged SWa-1 / octylammonium cation, with $C_n = 8$ $\downarrow$ SWa-1 / hexadecylammonium cation, with $C_n = 16$	**Na-SWa-1** **SWa-1-C$_8$** $\downarrow$ **SWa-1-C$_{16}$**
MCBP / Na$^+$ exchanged MCBP / octyltrimethylammonium cation, with $C_n = 8$ $\downarrow$ MCBP / hexadecyltrimethylammonium cation, with $C_n = 8$	**Na-MMT (MCBP)** **MCBP-C$_8$** $\downarrow$ **MCBP-C$_{16}$**
Cloisite / Na$^+$ exchanged	**Na-MMT (Cloisite)**
Cloisite / dimethyl, dihydrogenated tallow, quaternary ammonium Modifier concentration = 125 mEq/100g clay	**C15A**
Cloisite / dimethyl, dihydrogenated tallow, quaternary ammonium Modifier concentration = 95 mEq/100g clay	**C20A**
Cloisite / dimethyl, benzyl, hydrogenated tallow, quaternary ammonium Modifier concentration = 125 mEq/100g clay	**C10A**

Table 3.3   Sample Identification for SAz-1, SWa-1, MCBP and Cloisite Organoclays.

3.3   Na-SAz-1 + Alkylammonium Cations ($C_nNH_3^+$)

3.3.1   Description/Reason for Use

Na-SAz-1 (Cheto) clay is a sodium-exchanged smectite with a high surface charge. The interlayer cations in this series of samples were exchanged with N-alkylammonium cations with chain lengths ranging from C_6 to C_{16}, at a concentration that was equivalent to 1 x CEC of SAz-1 (120 mEq/100g). In this section the XRD spectra, TGA/DTG traces and comparative TG-MS data for the desorption /decomposition of the alkylammonium cations have been described, the specific trends of which are discussed below.

3.3.2 X-ray Diffraction (XRD) of SAz-1-C_nNH$_3$

Due to the availability of only a small quantity of each sample it was not possible to record the basal spacings of these samples as well as conducting TGA and TG-MS analysis. However, the basal spacings of these samples were previously analysed by Komadel & Janek [3-17], and their XRD results are presented in fig. 3.1. The basal spacings showed a step-wise increase as the alkylammonium cation increased in chain length, increasing from 13.6 Å at C_8 to 17.8 Å at C_{12}. According to Jaynes & Boyd [1-29] this increase would signify a change in arrangement for the alkylammonium cations from a monolayer arrangement (13.6 Å) to a bilayer arrangement (17.7 Å), with characteristic intermediate regions due to the charge density heterogeneity of the smectite.
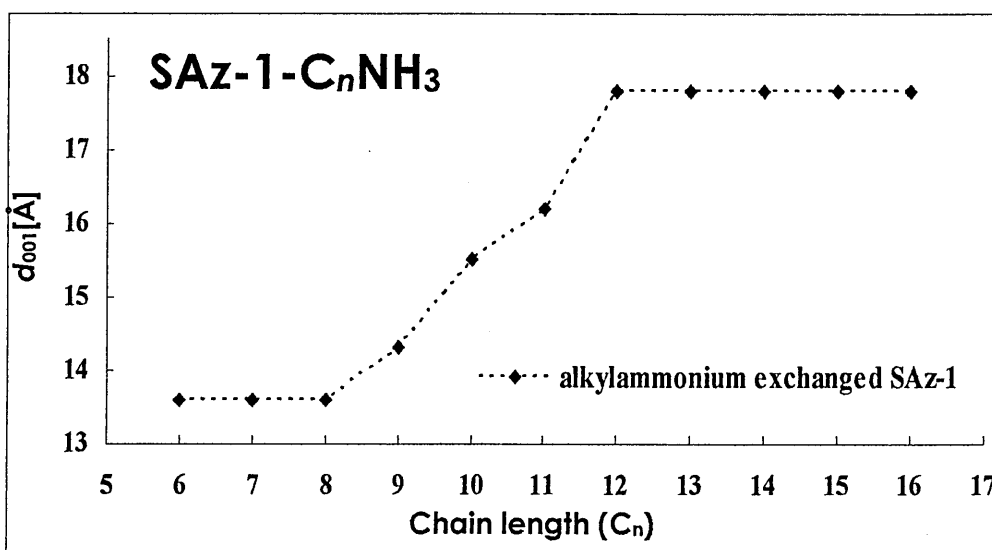
Figure 3.1   Alkylammonium exchanged SAz-1. Effect of chain length of alkylammonium ions on basal spacing [3-17].

These results were in agreement with the results of Lagaly & Weiss's extensive study of approximately 200 bentonite clays [3-5].

3.3.3 Thermo-Gravimetric Analysis (TGA) of SAz-1-C_nNH$_3$

The derivative thermograms of the SAz-1-C_nNH$_3$ samples (fig. 3.3) showed several thermal desorption events, these could be grouped to form temperature ranges within which the

thermal desorption maxima would vary 35-150 °C, 150-500 °C and small weight loss >500 °C. An assignment of the events occurring within these temperature ranges is displayed in table 3.4.

Desorption temperature	Assignment
35 - 150 °C	evolution of physisorbed water
150 - 500 °C	decomposition of organocations producing aliphatic species, ring compounds, ammonia, water and CO_2
> 500 °C	clay dehydroxylation and CO_2 evolution

Table 3.4   **Assignment for desorption maxima occurring within specific temperature ranges for SAz-1-C_nNH_3 TGA.**

Below 150 °C, the alkylammonium chains were thermally stable, and so, weight loss was attributed to physically trapped water being thermally desorbed. Weight loss between 35-150 °C could be seen to be relatively constant, across all alkyl chain lengths, at approximately 8 wt% (table 3.5).

The alkylammonium cations were primarily desorbed from the SAz-1 galleries between 150 °C and 500 °C. As the length of the alkyl chain increased, the profile of the thermal events changed, with the majority of the thermal desorption occurring around a maximum at 390 °C when C_n = 6, which shifted to slightly lower temperatures until the maximum for C_n = 16 was seen at 370 °C (fig. 3.3). Weight losses between 150-300 °C were relatively constant, but across the range 300-500 °C appeared to successively increase with increasing chain length. Weight losses from organocations with alkyl chains > C_n = 12 increased markedly below 380 °C (fig. 3.4, table 3.5). Weight losses above 500 °C decrease slightly from 4.7 wt% at C_n = 6 to 3.7 wt% at C_n = 8. Increases in alkyl chain length above C_n = 8 resulted in a constant weight loss at approximately 3.6 wt%.
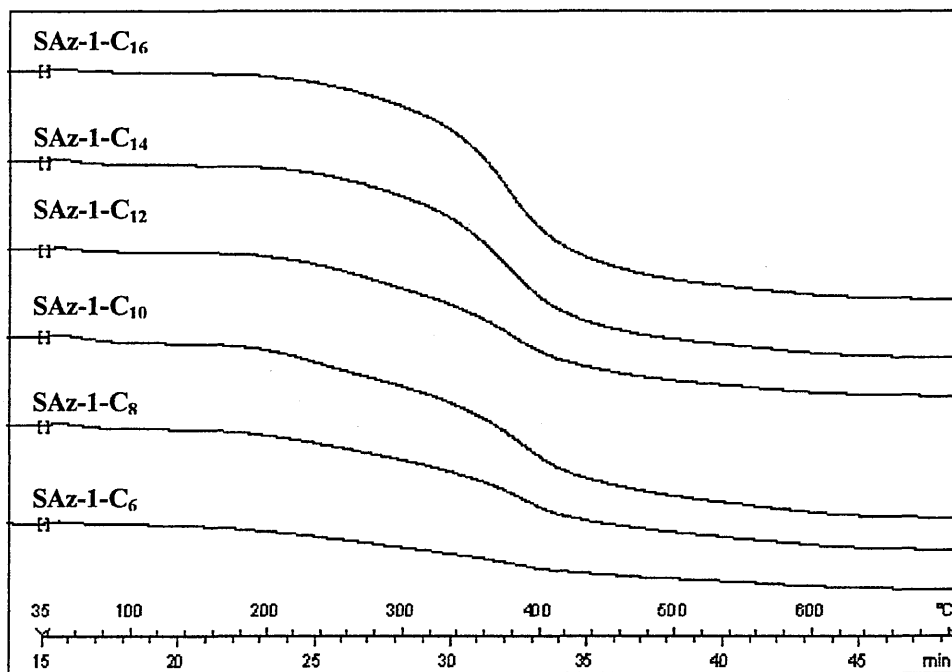
Figure 3.2   Comparison of TGA data for Na-SAz-1 exchanged with C_6NH_3 (Bottom) to $C_{16}NH_3$ (Top).

Lab: Andy Cunningham   METTLER TOLEDO STAR^e SW 7.01
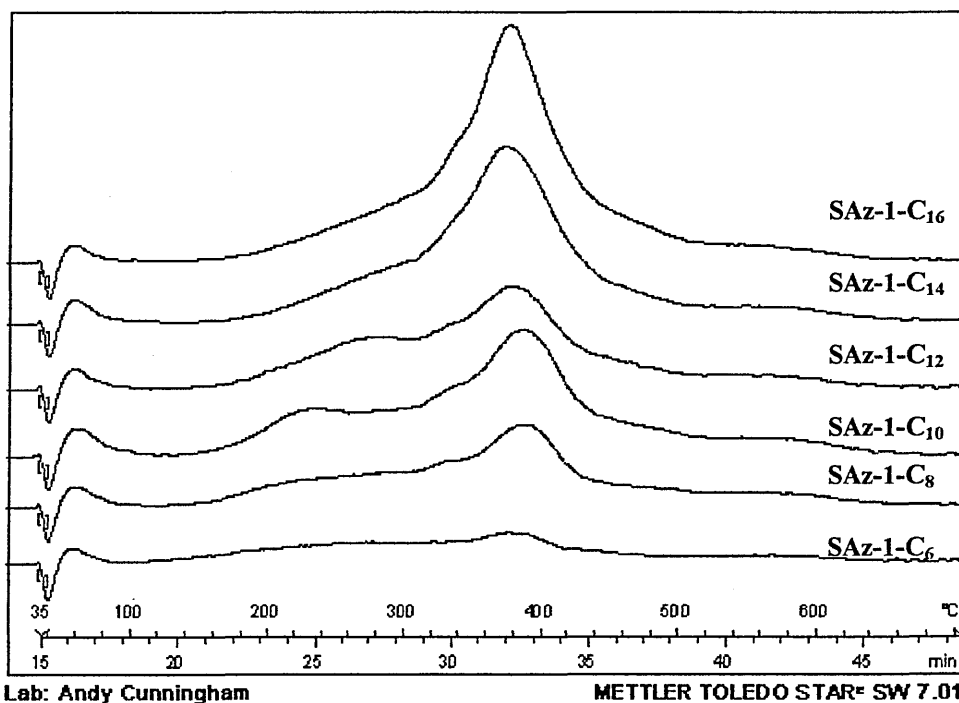
Figure 3.3   Comparison of DTG data for Na-SAz-1 exchanged with C_6NH_3 (Bottom) to $C_{16}NH_3$ (Top).

113

SAz-1	Desorption Temperature Ranges						Total %Wt loss
	35-150 °C	151-250 °C	251-310 °C	311-380 °C	381-500 °C	> 500 °C	
$C_6NH_3^+$	0.8	3.3	2.7	3.9	4.3	4.7	19.7
$C_7NH_3^+$	0.7	2.5	3.0	4.2	5.7	4.2	20.3
$C_8NH_3^+$	0.9	2.6	2.6	4.8	6.6	3.7	21.2
$C_9NH_3^+$	0.9	2.6	2.7	5.1	7.0	3.6	21.9
$C_{10}NH_3^+$	0.9	2.8	3.1	5.1	8.2	3.4	23.5
$C_{11}NH_3^+$	0.9	2.4	3.7	5.4	8.3	3.6	24.3
$C_{12}NH_3^+$	0.7	2.3	4.4	6.9	7.6	3.6	25.5
$C_{13}NH_3^+$	0.8	1.6	3.8	8.3	8.6	3.7	26.8
$C_{15}NH_3^+$	0.8	1.4	3.4	9.5	10.0	3.8	28.9
$C_{16}NH_3^+$	0.7	1.5	3.7	11.5	11.7	3.6	32.7

Table 3.5   Comparison of the weight losses for Na-SAz-1-C_nNH_3 at different temperature ranges between 35-800 °C with increasing chain length. *N.b Temperature ranges selected to compare with other samples later in this thesis and excenuate shifts in different desorption maxima.*
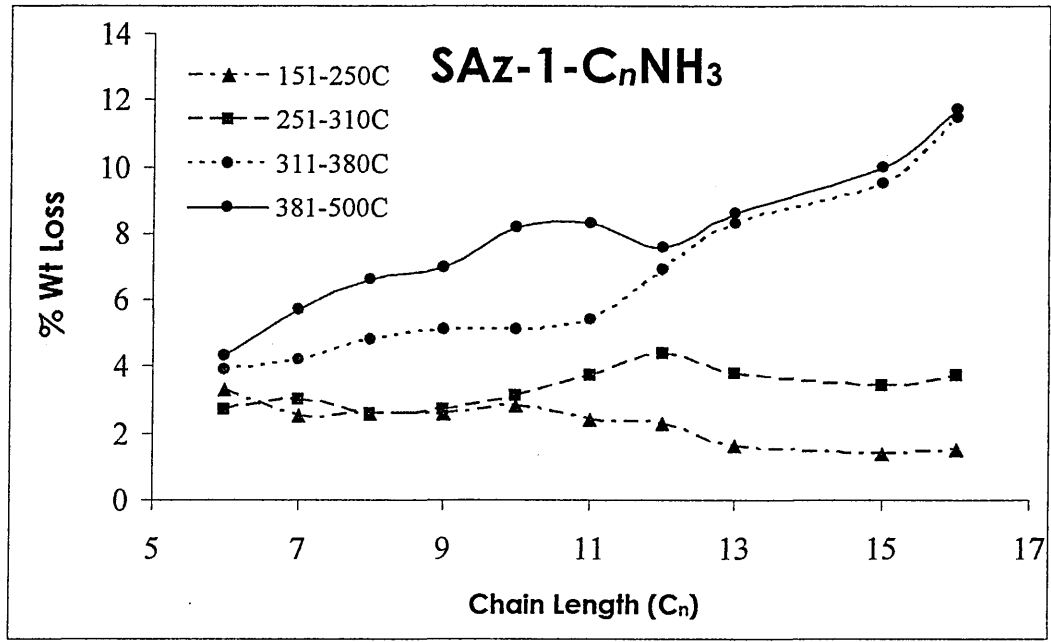
Figure 3.4   Comparison of the percentage weight loss occurring at different temperature ranges (151-250 °C, 251-310 °C, 311-380 °C and 381-500 °C) for alkylammonium exchanged SAz-1.

After an extensive survey of the possible species arising from the alkylammonium cations in contact with the clay surface, the decomposition products were identified and segregated into 3 categories (table 3.6).

Category	Assignment/Group
1	Water [m/z = 18], and CO_2 [m/z = 44]

2	Linear aliphatic species:
	    Alkyls [m/z = 43, 57, 71, 85]
	    Alkenyls [m/z = 41, 55, 69, 83]

3	Ring compounds: See table 3.7

Table 3.6   Specifications of the 3 categories for TG-MS Assignment.

3.3.4.1   Water [m/z = 18] and CO_2 [m/z = 44]

The intensity of the water [m/z = 18] signal from the C_n = 8 sample was high, as expected, due to the large amount of water located in the SAz-1 gallery around the shorter-chain alkylammonium cations. The signal was saturated at higher temperatures for the $SAz\text{-}1\text{-}C_{12}$ and $SAz\text{-}1\text{-}C_{16}$ samples, with only slight deviations from the saturated signal offering any indication that the amount of evolved water was decreasing (fig. 3.6). At temperatures > 500 °C the signal intensity steadily declined, indicating exhaustion of physisorbed water and the continued depletion of hydroxyl groups.

In contrast, increases in the formation of CO_2 [m/z = 44] were observed as the alkyl chain length increased. CO_2 was evolved throughout the range of 35-800 °C. In the C_n = 8 sample (fig.3.7), the majority of [m/z = 44] was evolved around three maxima (i.e. 310 °C,

380 °C and 547 °C). For $C_n = 12$, the maxima appeared to have shifted to higher temperatures (i.e. 371 °C, 437 °C and > 600 °C) and had greater intensities than in C_8.
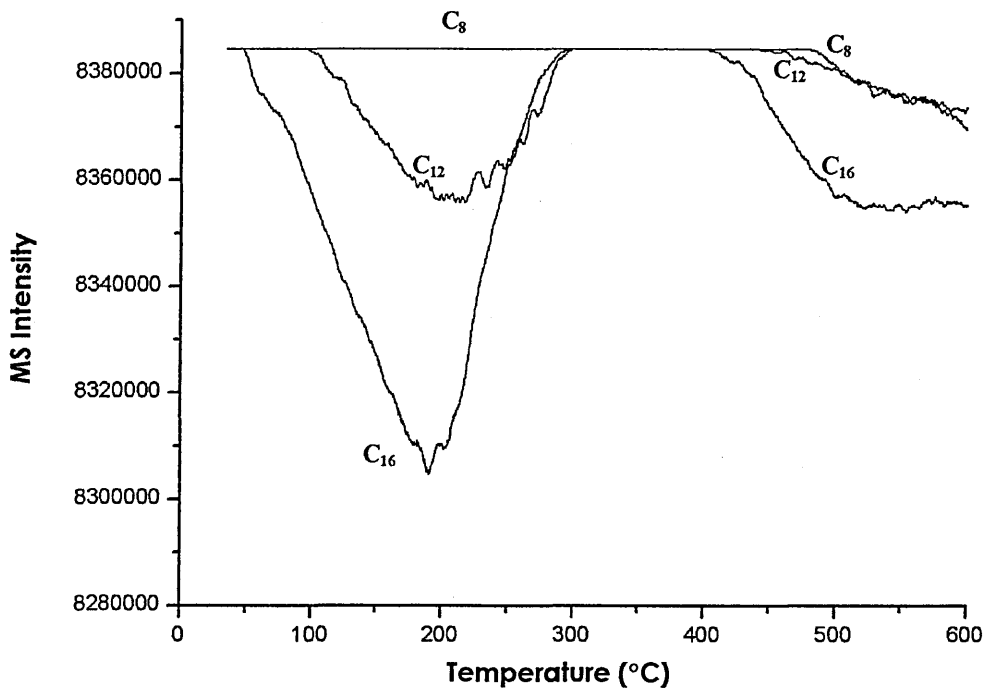
Figure 3.6   Shape of water [H_2O - m/z = 18] evolution with the increase in alkylammonium chain length from C_8 to C_{16} for SAz-1.
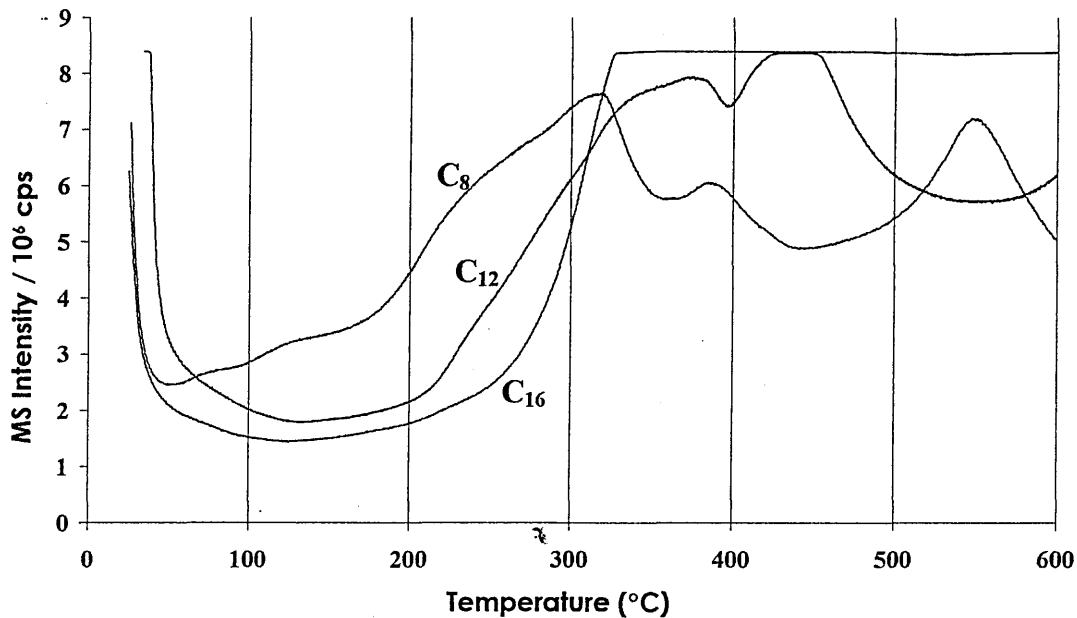
Figure 3.7   Shape of carbon dioxide [CO_2 - m/z = 44] evolution with the increase in alkylammonium chain length from C_8 to C_{16} for SAz-1.

At C_n = 16, the initial positive incline of the first maximum appeared at a higher temperature, however, after 320 °C the MS detector became saturated. When the C_n = 16 sample was heated at 120 °C/16 h before analysis, the resulting mass spectrum of CO_2 [m/z = 44] was greatly reduced in intensity, it showed [m/z = 44] being desorbed most intensely about a single maximum at approximately 450 °C.

3.3.4.2   Aliphatic Hydrocarbons,

Alkyls [m/z = 43, 57, 71, 85] and Alkenyls [m/z = 41, 55, 69, 83]

Analysis of the TG-MS data for the three different alkylammonium chain lengths shows that the alkyls were desorbed prior to the evolution of their unsaturated alkenyl analogues. The intensity of the individual fragment ions evolved was seen to decrease with increasing mass/charge ratio (m/z), (fig. 3.8).
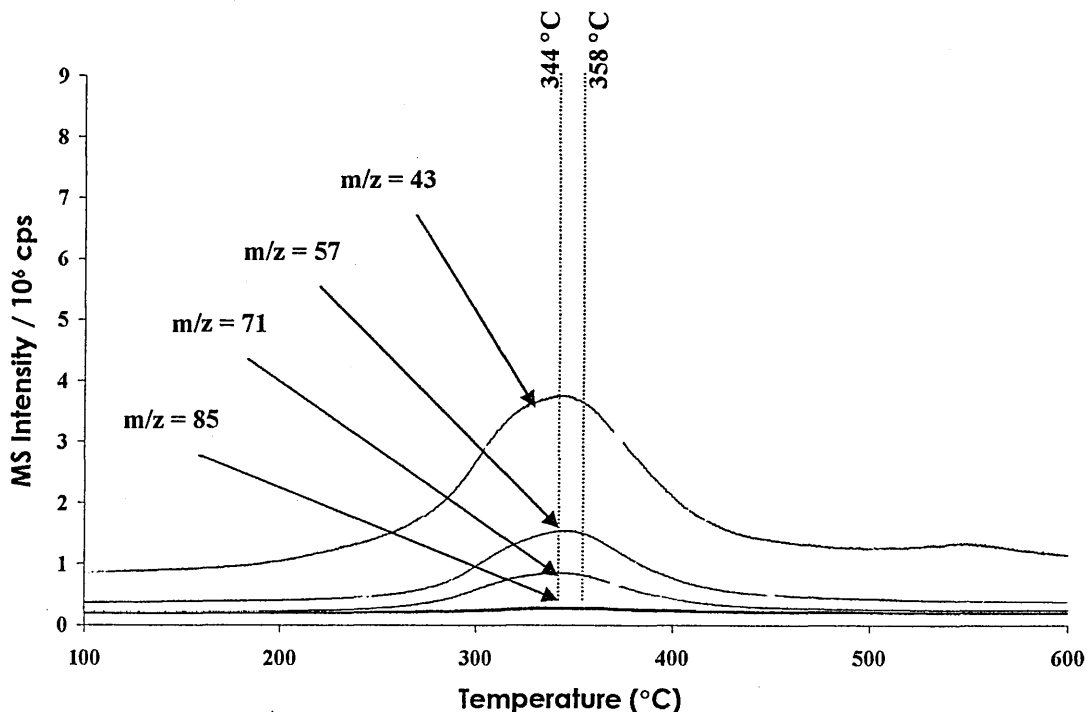
Figure 3.8   RT-TG-MS ion chromatograms for the desorption of linear alkyls (i.e. propyl (m/z = 43), butyl (m/z = 57), heptyl (m/z = 71) hexyl (m/z = 85)) and linear alkenyls (i.e. propenyl (m/z = 41), butenyl (m/z = 55), heptenyl (m/z = 69) hexenyl (m/z = 83)) from SAz-1-C$_8$.

When C_n = 8 (fig. 3.8), the alkyls and alkenyls were evolved between 200 and 450 °C, with alkyls most prominently desorbed at a maximum of 344 °C and alkenyls at a maximum of 358 °C. At C_n = 12, alkyls and alkenyls were thermally desorbed between 250 and 475 °C, alkyls at a maximum of 361 °C and alkenyls at a maxima of 369 °C. As the chain length increased again with the C_n = 16 sample, the temperature range over which the alkyls and alkenyls were desorbed narrowed to between 300 and 475 °C, with the onset of increased desorption shifting + 50 °C. As the temperature increased the intensity of the shorter chain alkenyls were seen to be greatly increased relative to their saturated analogues (as in fig. 3.8). As the chain length of the alkylammonium cations increased the linear alkyls and alkenyls were given off at successively higher temperatures. Increasing from approximately 344 °C and 358 °C at C_n = 8, to 361 °C and 369 °C at C_n = 12 and onto 374 °C and 377 °C at C_n = 16, respectively. As well as the desorption temperature of these species moving to increasingly higher temperatures the difference between the desorption maxima of the two types of species decreased with increasing chain length.

3.3.4.3 Ring Compounds

Even with short chain length (i.e. C_n = 8) cations, the majority of secondary species desorbed from SAz-1 were identified by MS as being ring compounds. These species were evolved as the result of (1) a Hoffman degradation of the organocation, followed by (2) an intramolecular reaction or "back-biting" mechanism occurring on the alkyl chain, all catalysed by acid-sites on the clay's gallery surfaces which results in the formation of new species. The secondary species which were evolved were identified from a comprehensive database search as those shown in table 3.7.

The C_n = 8 alkylammonium cations evolved these secondary species at or below the T_{max} in the total ion current (TIC) (i.e. approximately 350 °C). This created an asymmetric TIC trace due to the large quantity of species evolved between 275 and 350 °C. The ring

compounds were evolved as a series of closely spaced maxima at 290, 330, 340, 350 and 363 °C (fig. 3.3.4.3a/b).
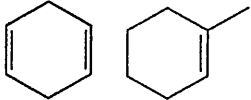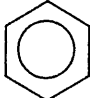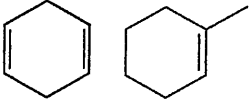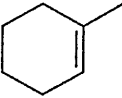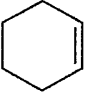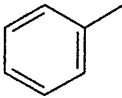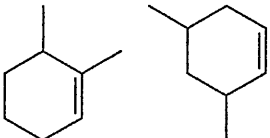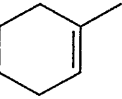
m/z ratio	Assignment	Structure
77	1,3-cyclohexadiene and 1-methylcyclohexene	
78	benzene	
79	1,3-cyclohexadiene and 1-methylcyclohexene	
81	1-methylcyclohexene	
82	1-cyclohexene	
91 + 92	toluene	
95	1,6 dimethylcyclohexene or 3,5 dimethylcyclohexene	
96	1-methylcyclohexene	

Table 3.7   **Assignment and structure of identified ring compounds in order of increasing mass/charge ratio.**

Benzene [m/z = 78] showed larger concentrations than other ring compounds across the temperature range 200-290 °C. Above this, the intensity/concentration of methylcyclohexene [m/z = 81], cyclohexadiene [m/z = 79] and cyclohexene [m/z = 82] dominated the evolved spectra. The plot for toluene [m/z = 91] / [m/z = 92] appeared to contain two events characterised by an lower temperature maximum at 330 °C and a higher temperature maximum at 363 °C. A maximum at 340 °C reflected the desorption of benzene [m/z = 78] and cyclohexene [m/z = 82] and this was followed by cyclohexadiene/methylcyclohexene [m/z = 77], cyclohexadiene/ methylcyclohexene [m/z

= 79], methylcyclohexene [m/z = 81], 1,6 dimethylcyclohexene/3,5 dimethylcyclohexene [m/z = 95] and methylcyclohexene [m/z = 96] being desorbed at a maximum at approximately 350 °C. The intensity of methylcyclohexene [m/z = 81] is shown to be at least double that of any other species evolved (MS Intensity = 2 x 10^6 cps). In contrast to the major evolution of the longer-chain linear alkyls/alkenyls (E.g. C_5 and C_6) the evolution of ring compounds occurred over a much narrower temperature interval, with the possible exception of benzene.

The C_n = 12 alkylammonium cations evolved these secondary species at or slightly above the maxima of the TIC which was approximately 25 °C higher than C_8, at 375 °C. Therefore, the TIC trace appeared relatively symmetrical. The ring compounds evolved were represented by three events / maxima. Benzene [m/z = 78] displayed a clear lower temperature maximum near 290 °C with a second maximum at 375 °C. This behaviour is not fully understood but could be due to competing decomposition mechanisms being employed. This second maximum was also the temperature at which cyclohexadiene/methylcyclohexene [m/z = 77], cyclohexadiene/ methylcyclohexene [m/z = 79], methylcyclohexene [m/z = 81], cyclohexene [m/z = 82], and 1,6 dimethylcyclohexene/3,5 dimethylcyclohexene [m/z = 95] and methylcyclohexene [m/z = 96] were desorbed. The third maxima (385 °C) in the desorption profile signified the evolution of toluene [m/z = 91] / [m/z = 92] which had not only shifted to a higher temperature but was also evolved as a single broad event. The relative intensities of the evolved species remained the same.

As with the RT-TG-MS results from the C_{12} samples, the C_{16} RT-TG-MS data showed a shift in the TIC to higher temperatures, due to decomposition above 375 °C increasing, which was again evident in the asymmetric shape of the TIC. The ring compounds evolved were represented by two maxima.
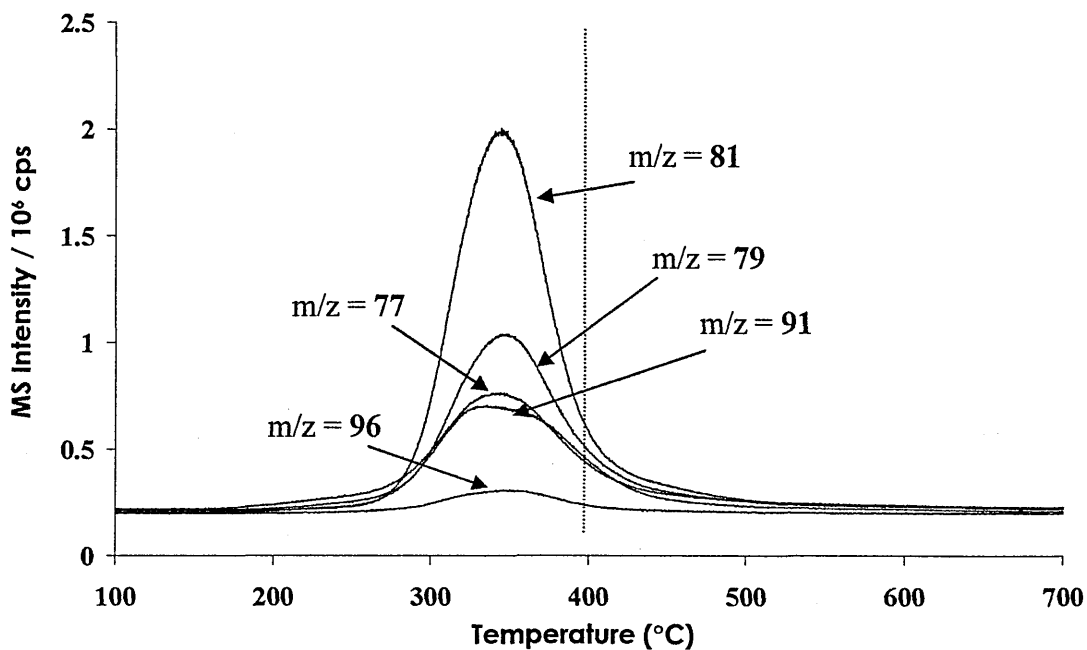
Figure 3.9   RT-TG-MS ion chromatograms for the desorption of the following ring
              compounds: cyclohexadienyl/methylcyclohexenyl (m/z = 77),
              cyclohexadienyl (m/z = 79), methylcyclohexenyl (m/z = 81), tolyl (m/z = 91)
              and methylcyclohexenyl (m/z = 96)) from SAz-1-C_8.

Figure 3.10   RT-TG-MS ion chromatograms for the desorption of the following ring
              compounds: benzyl (m/z = 78), cyclohexenyl (m/z = 82), tolyl (m/z = 91 &
              92) and 1,6 dimethylcyclohexenyl or 3,5 dimethylcyclohexenyl (m/z = 95)
              from SAz-1-C_8.

121
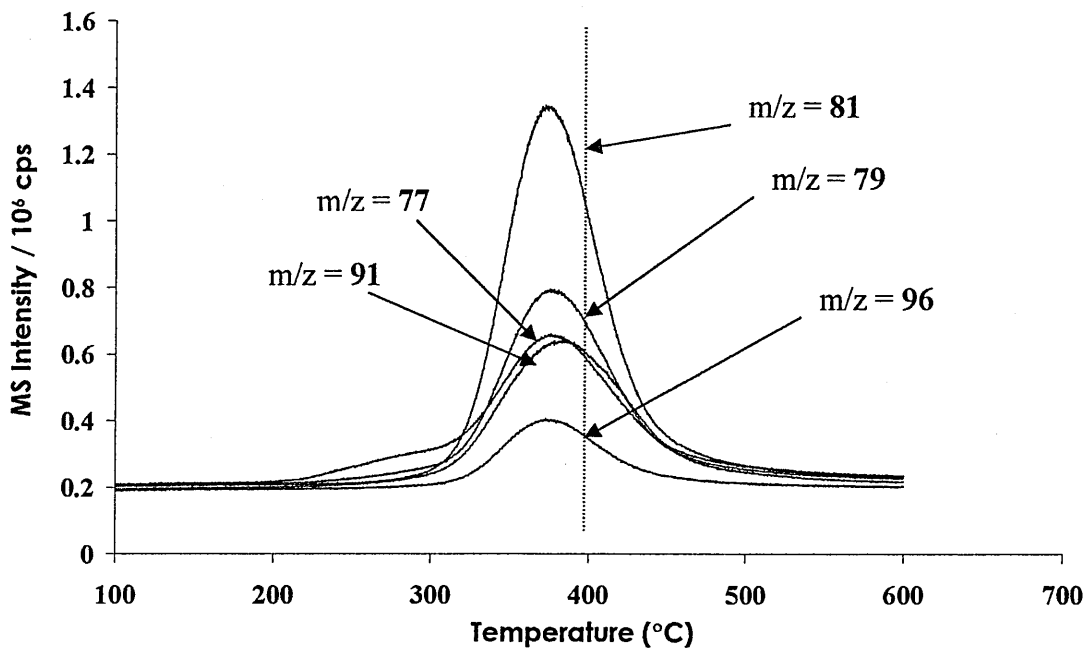
Figure 3.11   RT-TG-MS ion chromatograms for the desorption of the following ring compounds: cyclohexadienyl/methylcyclohexenyl (m/z = 77), cyclohexadienyl (m/z = 79), methylcyclohexenyl (m/z = 81), tolyl (m/z = 91) and methylcyclohexenyl (m/z = 96)) from SAz-1-C_{12}.
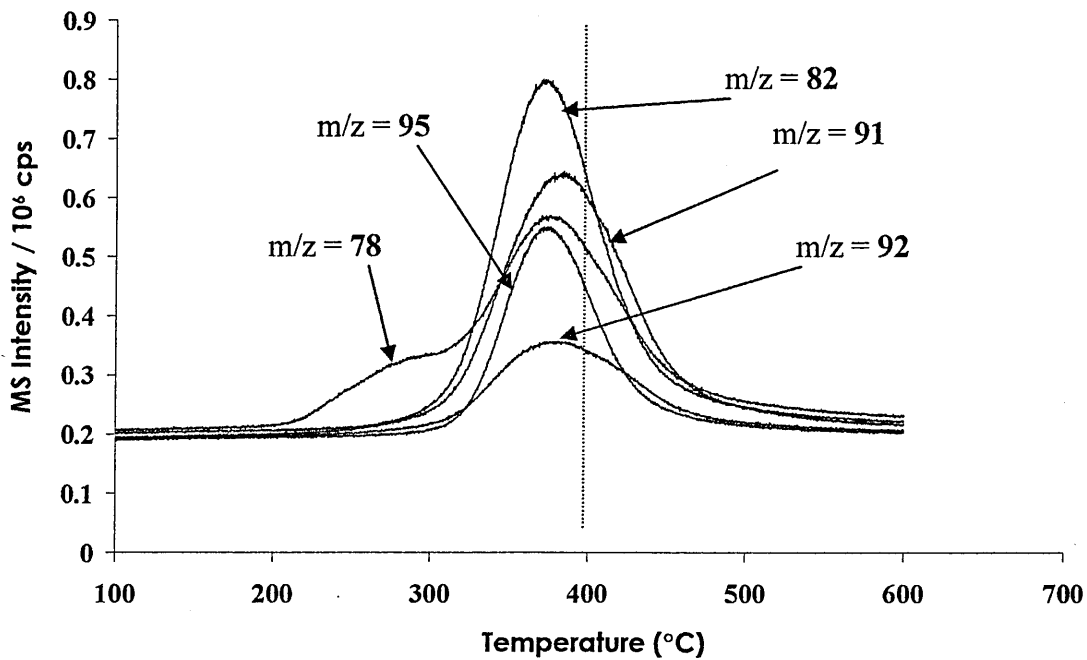
Figure 3.12   RT-TG-MS ion chromatograms for the desorption of the following ring compounds: benzyl (m/z = 78), cyclohexenyl (m/z = 82), tolyl (m/z = 91 & 92) and 1,6 dimethylcyclohexenyl or 3,5 dimethylcyclohexenyl (m/z = 95) from SAz-1-C_{12}.

122
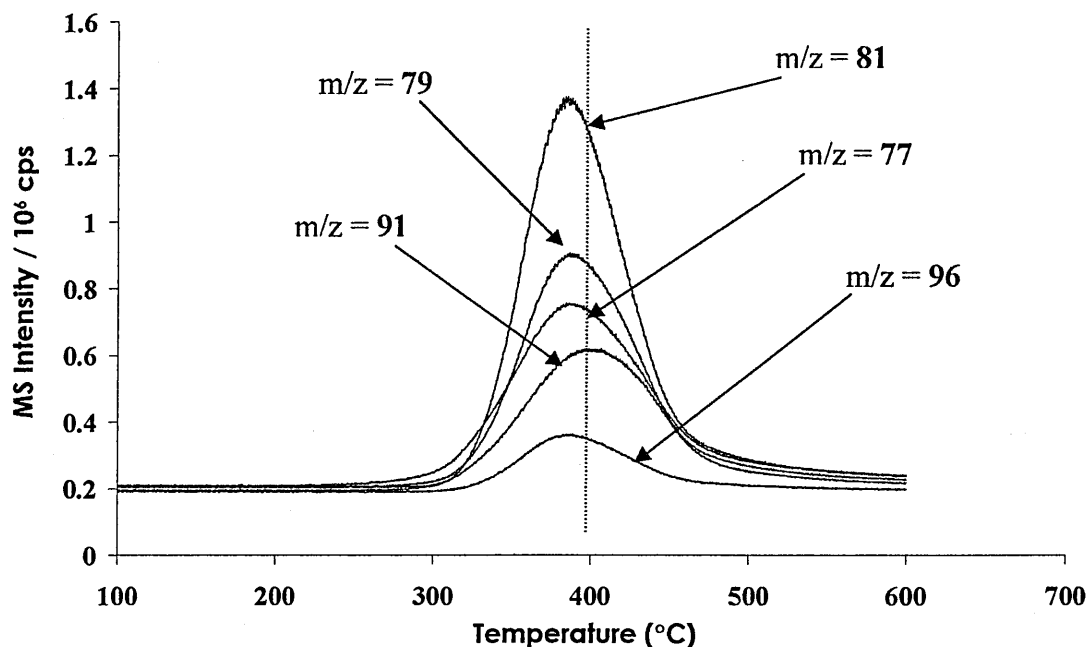
Figure 3.13   RT-TG-MS ion chromatograms for the desorption of the following ring
compounds: cyclohexadienyl/methylcyclohexenyl (m/z = 77),
cyclohexadienyl (m/z = 79), methylcyclohexenyl (m/z = 81), tolyl (m/z = 91)
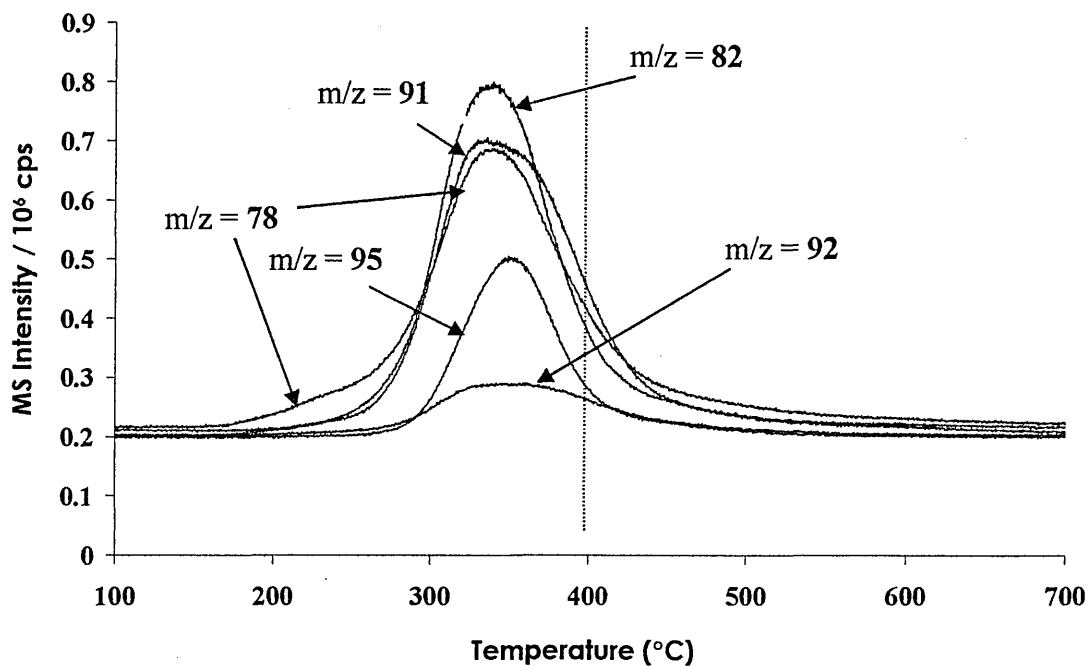and methylcyclohexenyl (m/z = 96)) from SAz-1-C_{16}.
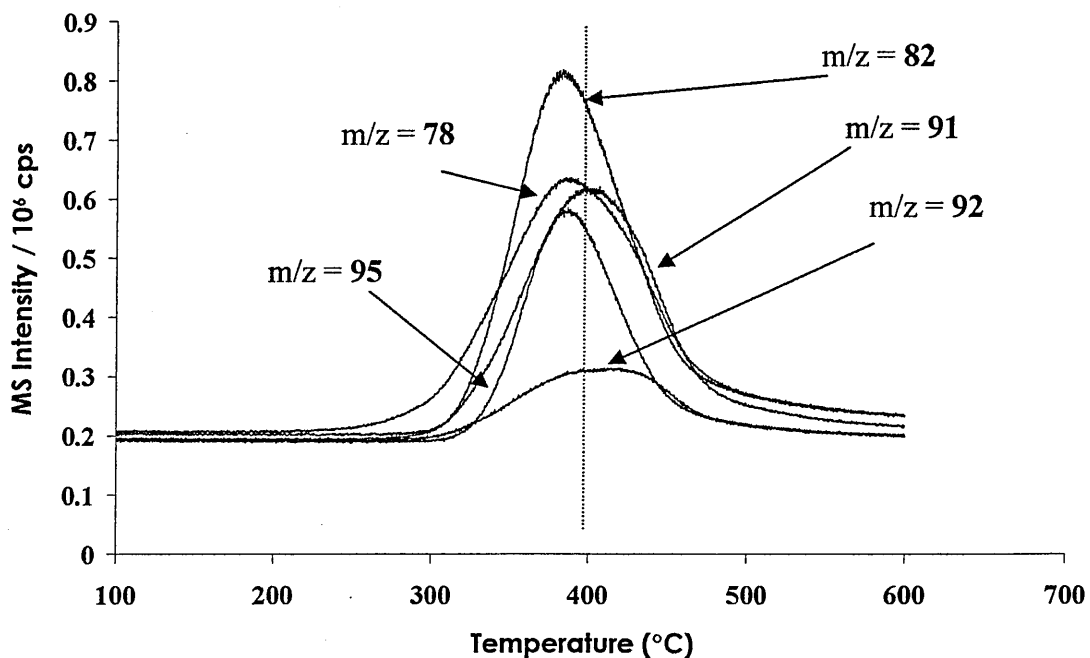
Figure 3.14   RT-TG-MS ion chromatograms for the desorption of the following ring
compounds: benzyl (m/z = 78), cyclohexenyl (m/z = 82), tolyl (m/z = 91 &
92) and 1,6 dimethylcyclohexenyl or 3,5 dimethylcyclohexenyl (m/z = 95)
from SAz-1-C_{16}.

123

Benzene [m/z = 78] was again evolved at lower temperatures than other species but the main maximum for this species coincided with that of cyclohexadiene/methylcyclohexene [m/z = 77], cyclohexadiene/ methylcyclohexene [m/z = 79], methylcyclohexene [m/z = 81], cyclohexene [m/z = 82], and 1,6 dimethylcyclohexene/3,5 dimethylcyclohexene [m/z = 95] and methylcyclohexene [m/z = 96] at 384 °C. This also occurred in the C_{12} sample. The second maximum (400 °C) signifying the evolution of toluene [m/z = 91] / [m/z = 92], which was again evolved at a higher temperature but with a bias towards desorption in the 400-450 °C temperature range.

The RT-TG-MS results for SAz-1-C_nNH$_3$ correlated well with the thermograms obtained from the same samples on a Mettler TG50 thermo-analyser. This indicated that the identification of the thermally desorbed species could be adequately transposed from one set of data to the other.

3.3.5 Summary of Analysis of SAz-1-C_nNH$_3$

i) XRD - SAz-1-C_nNH$_3$

The basal spacings for SAz-1-C_nNH$_3$, shown in table 3.8, indicated that expansion of the interlayer occurred when exchanged with alkylammonium cation with C_n = 8-12.

C_n	6	7	8	9	10	11	12	13	14	15	16
d_{001} (Å)	13.6	13.6	13.6	14.3	15.5	16.2	17.8	17.8	17.8	17.8	17.8

Table 3.8   **Comparison of d_{001} for different alkyl chain lengths (C_n) exchanged onto SAz-1.**

ii) TGA - SAz-1-C_nNH$_3$

The total weight loss from standard 10 mg samples increased as the length of the alkylammonium cation increased. Weight loss at < 150 °C, which was believed to be due to loss of water associated with the surfactants cationic head groups, remained relatively constant throughout the series of samples, at ~0.8 %. The alkylammonium cations were desorbed from the SAz-1 galleries between 150 °C and 500 °C. As the length of the alkyl

chain increased, the profile of the thermal events changed, the majority of the thermal desorption occurred at maxima of 390 °C at C_n = 6 and shifted to 370 °C when C_n = 16. Weight loss > 500 °C, believed to be due to dehydroxylation of the clay, CO_2 formation and the release of metal carbonates, also remained constant throughout the series of samples, at ~3.6 wt%.

C_n	6	7	8	9	10	11	12	13	14	15
Total % wt loss	19.7	20.3	21.2	21.9	23.5	24.3	25.5	26.8	28.9	32.7

Table 3.9 **Comparison of total weight loss for different alkyl chain lengths (C_n) exchanged onto SAz-1.**

iii)   **RT-TG-MS - SAz-1-C_nNH_3**

a.   **Water [m/z = 18] and CO_2 [m/z = 44]**

Water [m/z = 18] was shown to be released between 35-800 °C. As the alkyl chain length of the organocation increased, decrease in the loss of water from detector saturation below 200 °C and above 450 °C were shown. CO_2 [m/z = 44] was shown to initially be released at low intensities, with larger signal intensities at lower temperatures for shorter alkyl chain lengths. As the length of the alkyl chain was increased, the signal intensity increased and the signal maxima shifted to higher temperatures, until in the C_{16} samples when the detector became saturated at 330 °C.

b.   **Aliphatic Hydrocarbons**

TG-MS results showed that alkyl [m/z = 43, 57, 71, 85] and alkenyl [m/z = 41, 55, 69, 83] species were desorbed over different temperature ranges and showed successively higher thermal desorption maxima with increasing alkyl chain length (table 3.10).

C_n	Desorption Temp. Range (°C)	Alkane Maxima (°C)	Alkene Maxima (°C)
8	200-500	344	358
12	250-475	361	369
16	300-475	374	377

Table 3.10   Comparison of desorption characteristics with increasing alkyl chain length for SAz-1-C_n.

c.   **Ring Compounds**

A large number of ring compounds were thermally desorbed from the different SAz-1-C_nNH$_3$ samples. To summarise the pattern of ring compound desorption, the temperature ranges and maxima temperatures are shown in table 3.11 and the relative intensities of these maxima are shown in table 3.12.

m/z	Thermal Desorption Maxima (°C)		
	C_8	C_{12}	C_{16}
81	350	375	384
79	350	375	384
82	340	375	384
77	350	375	384
78	340	290 / 375	384
91	330 / 363	385	400
95	350	375	384

Table 3.11   Comparison of the thermal desorption maxima temperatures with increasing alkyl chain length for SAz-1-C_n. (results in order of decreasing relative MS intensity).

m/z	MS Intensity / 10^6 cps		
	C_8	C_{12}	C_{16}
81	2	1.4	1.4
79	1	0.8	0.9
82	0.8	0.8	0.8
77	0.7	0.7	0.7
78	0.7	0.6	0.6
91	0.7	0.6	0.6
95	0.5	0.4	0.3

Table 3.12   Comparison of the relative intensities of the major ring compound thermal desorption maxima with increasing alkyl chain length for SAz-1-C_n. (results in order of decreasing relative MS intensity).

126

3.4   Na-SWa-1 + alkylammonium cations (C_nNH_3)

3.4.1   Description/Reason for Use

Na-SWa-1 (Nontronite) clay is a ferruginous smectite sourced from Washington, USA. This series of samples was exchanged with a range of alkylammonium cations with chain lengths ranging from C_6 to C_{16} (i.e. as SAz-1), at a concentration that was equivalent to 1 x CEC of SWa-1 (102 mEq/100g). Again, due to the availability of only small quantities of each sample it was only possible to conduct TGA and TG-MS.

3.4.2   X-ray Diffraction (XRD) of SWa-1-C_nNH_3

The XRD analysis on these samples was also conducted by Komadel & Janek [3.17]. SWa-1 has a lower charge density and has greater charge heterogeneity than SAz-1. As with the SAz-1-C_nNH_3 samples, the arrangement of alkylammonium cations within the gallery spaces of the SWa-1 host altered from a monolayer configuration at 13.6 Å, to a bilayer configuration at 17.8 Å (fig. 3.15). The transition between the two configurations occurred between the additions of the C_8-C_{13} alkylammonium cations, and so, the transition between monolayer and bilayer required larger surfactant molecules than SAz-1 (i.e. C_{12} = 17.8 Å) to expand the layers of the clay.
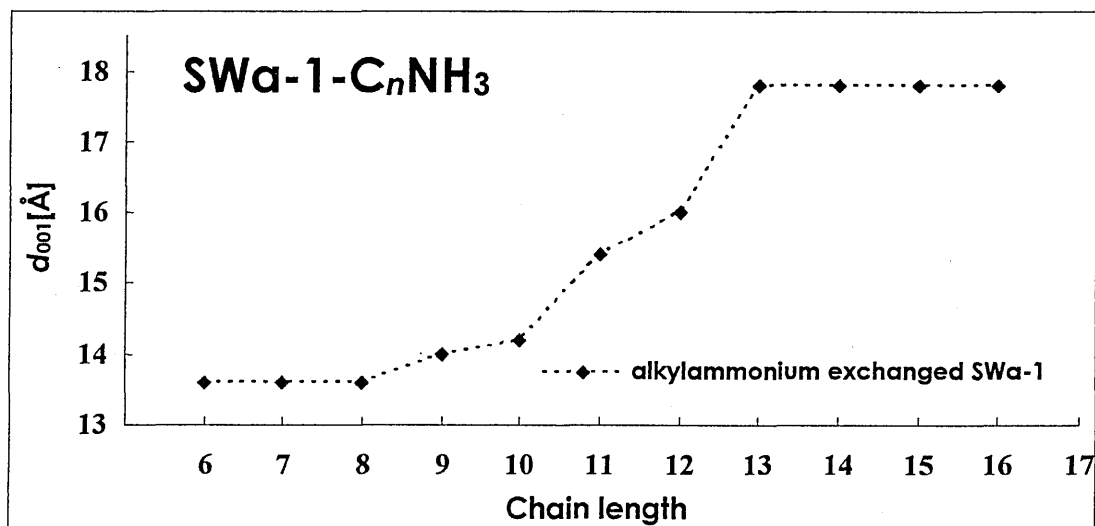
Figure 3.15   Alkylammonium exchanged SWa-1. Effect of chain length of alkylammonium ions on basal spacing [3-17].

3.4.3   Thermo-Gravimetric Analysis (TGA) of SWa-1-C_n

The derivative thermograms for the SWa-1 series exhibited seven defined thermal desorption maxima between 35 and 800°C. A summary of the assignment of these maxima is shown in table 3.13.

Desorption temperature	Assignment
35-150°C	evolution of physisorbed water
150-500°C	organocation decomposition events producing aliphatic, ring compounds, ammonia, water and CO_2
> 500°C	clay dehydroxylation and CO_2 evolution

Table 3.13   **Assignment for thermal desorption maxima occurring within specific temperature ranges for SWa-1-C_nNH$_3$ TGA.**

As the length of the alkyl chain was increased the weight loss between 35 and 150°C was shown to be reduced (fig. 3.17 and table 3.14). The desorption of physisorbed water may have been decreased because lower surface charge density of the SWa-1 host (relative to SAz-1) would have allowed the water molecules associated with the cationic head groups of the surfactants in the gallery spaces to be more easily desorbed because of the greater freedom for molecular movement at the gallery surface.

The majority of the weight loss again occurred in the temperature range of 150-500 °C. The C_n = 6 samples gave a thermal desorption maximum at 310 °C. This was accompanied by 'shoulders' at approximately 240 °C and 390 °C (fig. 3.17). As the alkyl chain length was increased the fragments and molecules being desorbed in the area underneath the 310 °C maximum became successively reduced, relative to an increase in the quantity of desorption products evolved under the maximum at 390 °C (table 3.14). This trend showed

a shift of majority weight loss to higher temperatures, but showed greater concentrations of lower temperature desorption products than SAz-1.
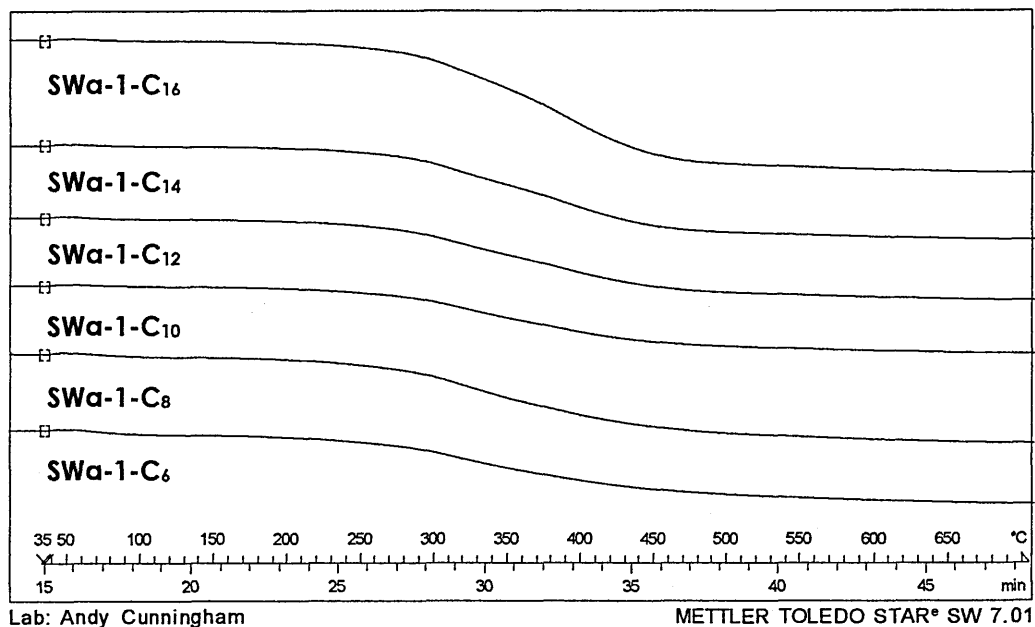
Figure 3.16   Comparison of TGA data for Na-SWa-1 exchanged from C_6NH_3 (Bottom) to $C_{16}NH_3$ (Top).
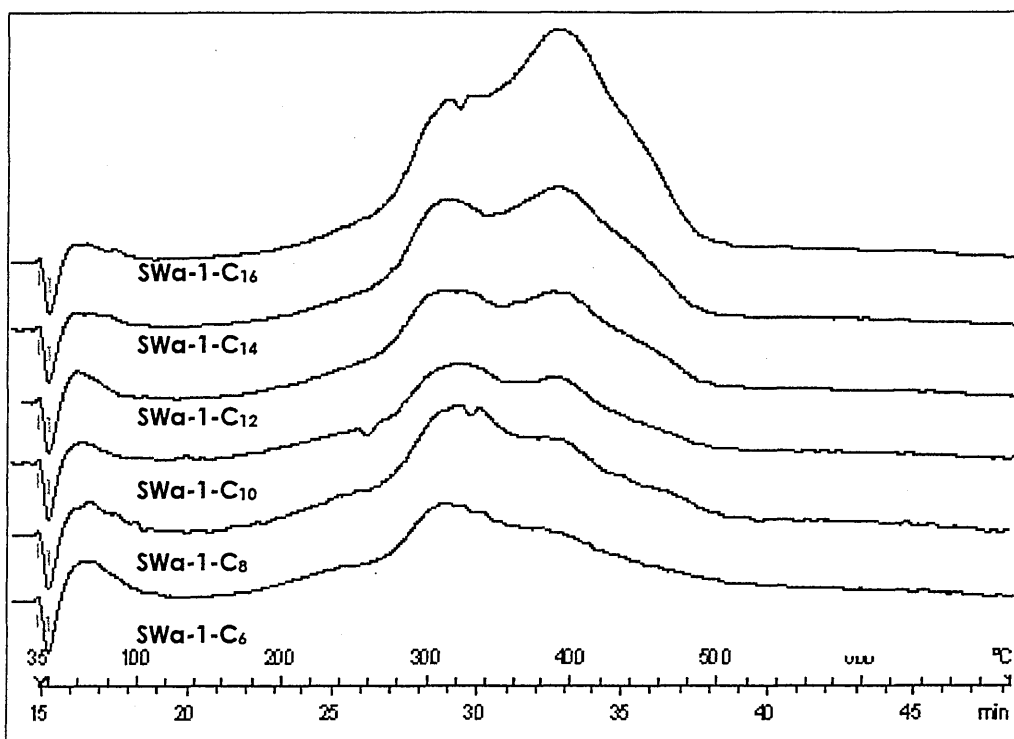
Figure 3.17   Comparison of DTG data for Na-SWa-1 exchanged with C_6NH_3 (Bottom) to $C_{16}NH_3$ (Top).

SWa-1	Desorption Temperature Ranges						Total %wt loss
	35-150 °C	151-250 °C	251-310 °C	311-380 °C	381-500 °C	> 500 °C	
$C_6NH_3^+$	1.0	1.7	3.0	4.8	4.3	2.7	17.5
$C_7NH_3^+$	0.8	1.3	3.0	5.3	4.8	2.6	17.8
$C_8NH_3^+$	1.0	1.8	2.7	5.7	5.1	2.7	19.0
$C_9NH_3^+$	0.8	1.6	3.0	6.0	5.3	2.6	19.3
$C_{10}NH_3^+$	0.5	1.7	3.3	6.4	5.5	3.1	20.5
$C_{11}NH_3^+$	0.6	2.0	3.7	6.4	6.3	2.4	21.4
$C_{12}NH_3^+$	0.5	1.8	3.4	6.8	7.5	3.1	23.1
$C_{13}NH_3^+$	0.4	1.9	3.1	7.8	8.0	2.6	23.7
$C_{14}NH_3^+$	0.3	1.4	3.9	6.9	8.8	2.6	23.9
$C_{15}NH_3^+$	0.4	1.3	3.0	8.0	9.0	2.5	24.2
$C_{16}NH_3^+$	0.4	1.2	3.8	8.0	11.4	1.8	26.6

Table 3.14   Comparison of the weight losses for SWa-1-C_nNH$_3$ at different temperature ranges between 35-800 °C with increasing chain length. N.b Temperature ranges selected to compare with other samples later in this thesis and excenuate shifts in different desorption maxima.
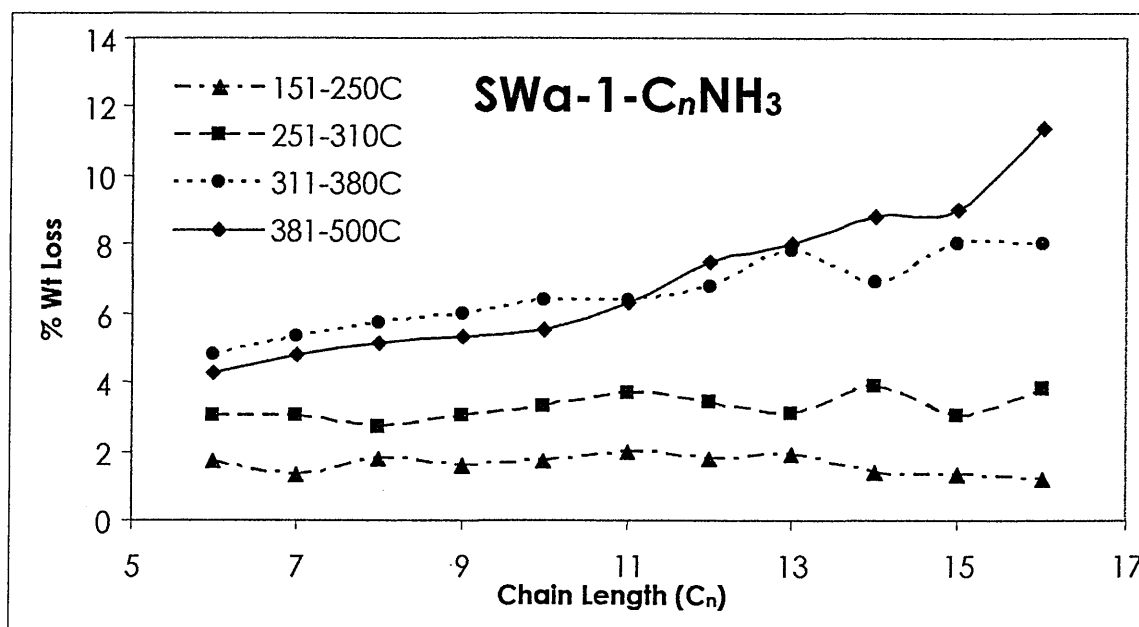
Figure 3.18   Comparison of the weight loss (%) occurring over different temperature ranges (151-250 °C, 251-310 °C, 311-380 °C and 381-500 °C) for alkylammonium exchanged SWa-1.

This shift was most evident in the C_{14}-C_{16} organoclay samples, where the lower temperature weight loss appeared as a shoulder to the maximum at 390 °C. Weight loss at temperatures > 500 °C was seen to fluctuate slightly, but remained relatively constant at an average 2.6 wt% loss, much less than was seen with SAz-1.

Overall, total percentage weight loss was reduced when compared with SAz-1, which again would have been due to SWa-1's lower surface charge density requiring lower quantities of alkylammonium cations at its more widely dispersed exchange sites.

These trends could relate to the more volatile products (e.g. short chain alkenyls) that would be released by shorter chain lengths (i.e. C_6-C_8) being desorbed under the lower temperature maximum (i.e. 310 °C). As the alkyl chain length was increased (i.e. C_9-C_{16}) this weight loss rapidly decreased and the bulk of the weight loss was gradually transferred to the higher temperature maximum (i.e. 390 °C) as the decomposition pathway of alkyl fragmentation was altered. This may be evidence of the easier fragmentation of longer chains into more stable fragments (e.g. C_6).

3.4.4 Thermogravimetry-Mass Spectrometry (TG-MS) of SWa-1 (C_8, C_{12}, C_{16})

The settings that were used for TG-MS were as previously stated. Also, the decomposition species were categorised as being the same as those evolved from SAz-1 samples (i.e. table 3.7).

3.4.4.1 Water [m/z = 18] and CO_2 [m/z = 44]

The water [m/z = 18] spectrum showed a signal intensity that was approximately four times more intense than that of the other species that were desorbed (fig. 3.19). Water [m/z = 18] was desorbed throughout the temperature profile of all the samples analysed. Loss of physisorbed water between 35 and 150 °C was seen in all samples. In SWa-1-C_8, significant
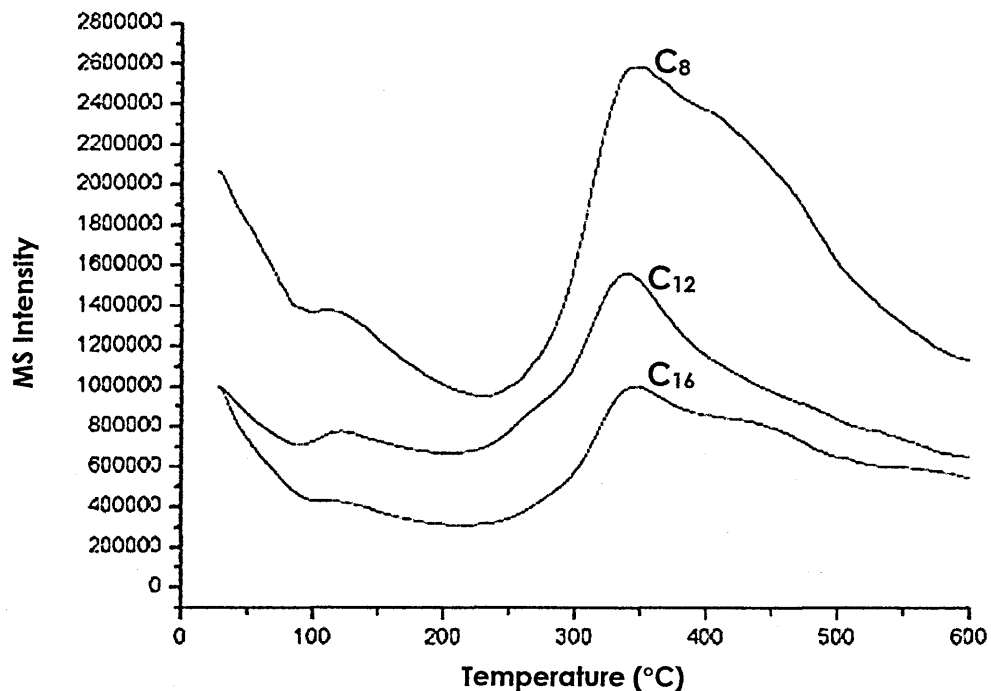
Figure 3.19   Shape of water [H_2O - m/z = 18] evolution with increased alkylammonium chain length from C_8 to C_{16} for SWa-1.
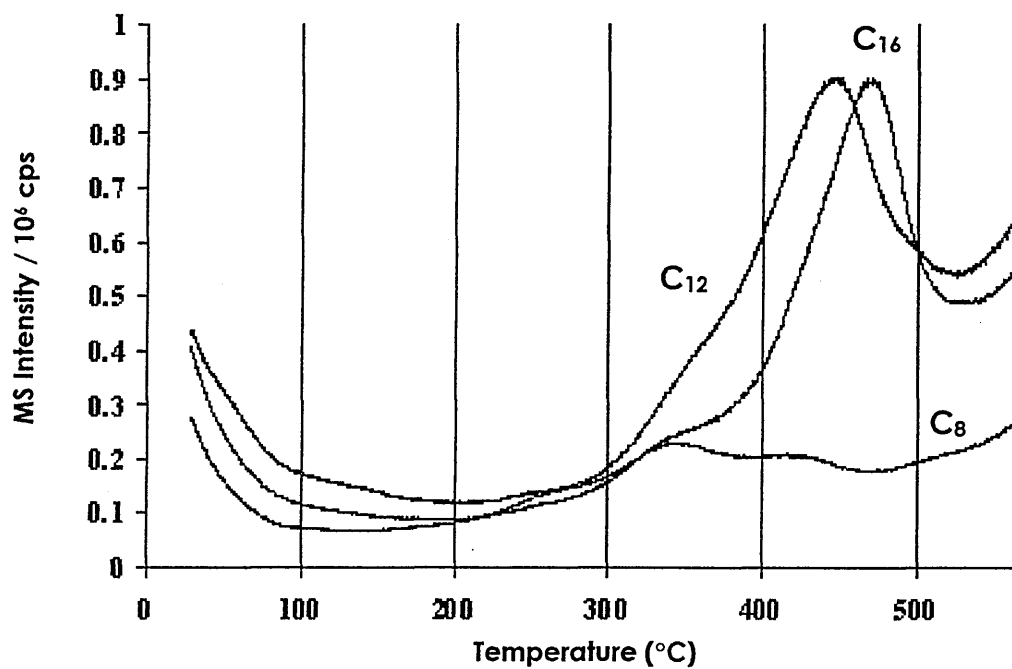
Figure 3.20   Evolution of CO_2 evolution with the increase in alkylammonium chain length (C_8-C_{16}) for SWa-1.

132

events/maxima could be seen at 120°C and 340°C, the latter event being bordered by other events which were disclosed at lower and higher temperatures, appearing as shoulders to the main peak. As the length of the alkyl chain was increased the signal intensity for water [m/z = 18] became reduced, as indicated by the TGA/DTG traces.

As the chain length was increased from C_8 to C_{12}, a large weight loss centred at approximately 400 °C was reduced with respect to the maximum at 340 °C. This change was reflected by a broadening of the TIC and its maximum increasing from approximately 350°C to 425°C. Further increase to C_{16}, led to a reduction of the 340 °C peak. As the signal decreased in intensity the thermal events unfolding from beneath the maxima at 340 °C became more widespread. A maxima at 425°C and centred around the clay's dehydroxylation at 550°C were shown to emerge. Again the shape of the TIC changed, showing two centres for desorption, decreasing around 340°C and becoming more increased around 425°C.

Shifts in the formation of CO_2 [m/z = 44] were observed between the SWa-1 samples, CO_2 being evolved throughout the whole temperature range 50-800 °C (fig. 3.20). SWa-1-C_8, showed CO_2 being thermally desorbed at five or more maxima. These losses were centred around 280, 350, 425, 570 and >600 °C, the latter temperature being the site of the most broad and intense loss observed. The SWa-1-C_{12} sample showed CO_2 [m/z = 44] losses at three events approximately 370 (shoulder), 445 and > 600 °C. The first two maxima became more defined in the SWa-1-C_{16} spectrum, the lower temperature peak being revealed at 340 °C as the higher temperature peak shifted from 440 to 470 °C.

3.4.4.2 Aliphatic Hydrocarbons,

Alkyls [m/z = 43, 57, 71, 85] and Alkenyls [m/z = 41, 55, 69, 83]

The C_n = 8 samples showed alkyls and alkenyls being evolved under two unresolved events, 358 °C and 400 °C (fig. 3.21). This contrasts with SAz-1-C_8 where maxima were at 344 and 358 °C (fig. 3.8). The mass spectra of desorbed linear alkyls showed lower intensities and a relatively even distribution between the two maxima (slightly more intense maximum at 400 °C), when compared with desorbed linear alkenyls. Although being desorbed over the same temperature range as their saturated alkane analogues, more of the linear alkenyls desorbed at the higher temperature, which led to the appearance of the lower temperature event appearing as a large shoulder to the main maximum. As with SAz-1, the intensity of the species evolved was seen to decrease with increasing mass/charge ratio.
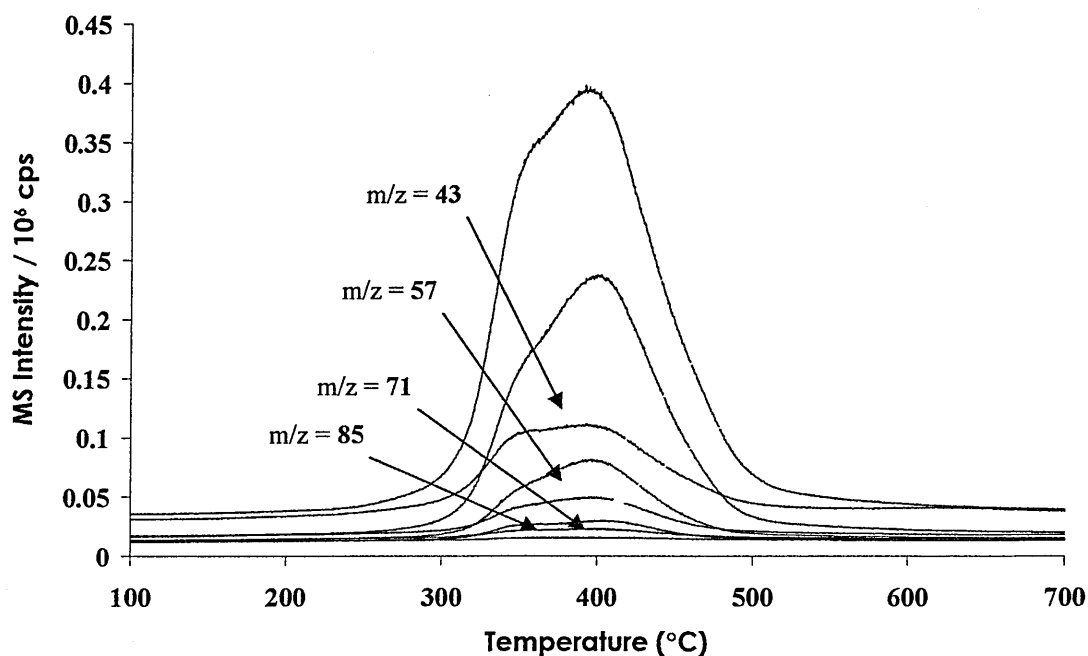
Figure 3.21   RT-TG-MS ion chromatograms for the desorption of linear alkyls (i.e. propane (m/z = 43), butane (m/z = 57), heptane (m/z = 71) hexane (m/z = 85)) and linear alkenyls (i.e. propenyl (m/z = 41), butenyl (m/z = 55), heptenyl (m/z = 69) hexenyl (m/z = 83)) from SWa-1-C_8.

C_n = 12 samples showed the alkyls and alkenyls being evolved under exactly the same maximum (400 °C) and over the same temperature range. The differences in the intensity between the alkyls and alkenyls remained the same as with C_n = 8.

At C_n = 16, both types of molecule were evolved at higher temperatures, with the alkyls being evolved at 425 °C and the alkenyls slightly higher at 435 °C. Also, the relative intensity of the shorter chain fragment ions for alkenyls was greatly increased compared to those for shorter chain linear alkane fragments.

As the length of the alkyl chain was increased the linear alkane and alkene species were desorbed at successively higher temperatures. Increasing from approximately 400 °C with a shoulder at 358 °C when C_n = 8 (more pronounced for the alkyls), to a maximum of 403 °C when C_n = 12 (symmetrical for alkenyls, asymmetric for alkyls with lower temperature shoulder) and onto 425 °C for alkyls and 435 °C for alkenyls at C_n = 16.

3.4.4.3　　Ring Compounds

The ring compounds that were desorbed from SAz-1 were the result of the Hoffman degradation process (i.e. as discussed in section 1.4.3.1, p. 24). Even with short chain length organocations (i.e. C_n = 8), the secondary species being desorbed from SAz-1 were aliphatic species, with ring compounds being derived as tertiary decomposition products (i.e. based on signal intensity). The ring compounds that were desorbed were identified as being the same as from the SAz-1 series (shown in table 3.7), however, the signal intensities were higher and the temperatures at which they were desorbed showed a significantly different profile.

The release of ring compounds from C_n = 8 occurred over the same temperature range as the release of alkyls/alkenyls (i.e. approx. 150-500 °C) (fig. 3.22 & 3.23). C_n = 8 desorbed its ring compounds at slightly varied temperatures around two maxima near 350 °C and 403

°C. The greatest concentration of each species was desorbed at approximately 350 °C, close to the main maximum in the TIC.

Benzene [m/z = 78] was shown to have greater intensity in the MS at temperatures up to 312 °C. From this temperature the intensity of cyclohexadiene [m/z = 79], methylcyclohexene [m/z = 81], cyclohexene [m/z = 82] and toluene [m/z = 91] dominated the evolved output. Toluene [m/z = 91] / [m/z = 92] was again evolved as a number of events characterised by maxima at 350 °C, 403 °C and 445 °C (decreasing in size with increasing temperature).

The maxima at approximately 350 °C reflected the desorption of benzene [m/z = 78] at 346 °C, followed by the desorption of toluene [m/z = 91] / [m/z = 92] and methylcyclohexene [m/z = 96] at 350 °C. The following species were evolved at slightly higher temperatures; cyclohexadiene/methylcyclohexene [m/z = 77] at 351 °C, cyclohexadiene [m/z = 79] and cyclohexene [m/z = 82] at 352 °C, methylcyclohexene [m/z = 81] at 355 °C and 1,6 dimethylcyclohexene/3,5 dimethylcyclohexene [m/z = 95] at 356 °C. All of these species had a less intense higher temperature maximum at approximately 400 °C, with the exception of toluene [m/z = 91]/[m/z = 92] which also had a third maximum at approximately 445 °C. The intensity of methylcyclohexene [m/z = 81] was shown to be much greater than the other evolved species.

The TIC for SWa-1-C$_{12}$ was relatively symmetric about a maximum at 400 °C, ring compounds were desorbed at, or slightly below the maximum of the TIC. Again, benzene [m/z = 78] had the highest intensity of any evolved ring compounds up to 336 °C (fig. 3.24 & 3.25). The asymmetric trace for benzene [m/z = 78] indicated that at least two significant events were occurring throughout it's desorption, the first around 340 °C and a second in line with the TIC maximum at 400 °C.

136

Figure 3.22   RT-TG-MS ion chromatograms for the desorption of the following ring compounds: cyclohexadienyl/methylcyclohexenyl (m/z = 77), cyclohexadienyl (m/z = 79), methylcyclohexenyl (m/z = 81), tolyl (m/z = 91) and methylcyclohexenyl (m/z = 96)) from SWa-1-C8.

Figure 3.23   RT-TG-MS ion chromatograms for the desorption of the following ring compounds: benzyl (m/z = 78), cyclohexenyl (m/z = 82), tolyl (m/z = 91 & 92) and 1,6 dimethylcyclohexenyl or 3,5 dimethylcyclohexenyl (m/z = 95) from SWa-1-C8.

137
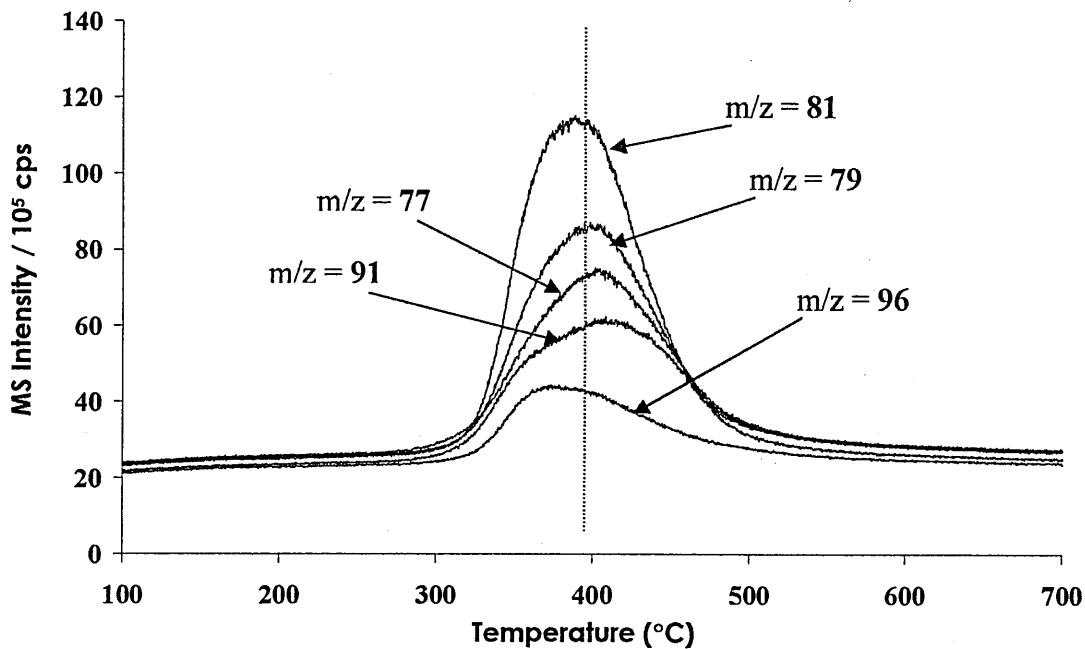
Figure 3.24   RT-TG-MS ion chromatograms for the desorption of the following ring compounds: cyclohexadienyl/methylcyclohexenyl (m/z = 77), cyclohexadienyl (m/z = 79), methylcyclohexenyl (m/z = 81), tolyl (m/z = 91) and methylcyclohexenyl (m/z = 96)) from SWa-1-C_{12}.
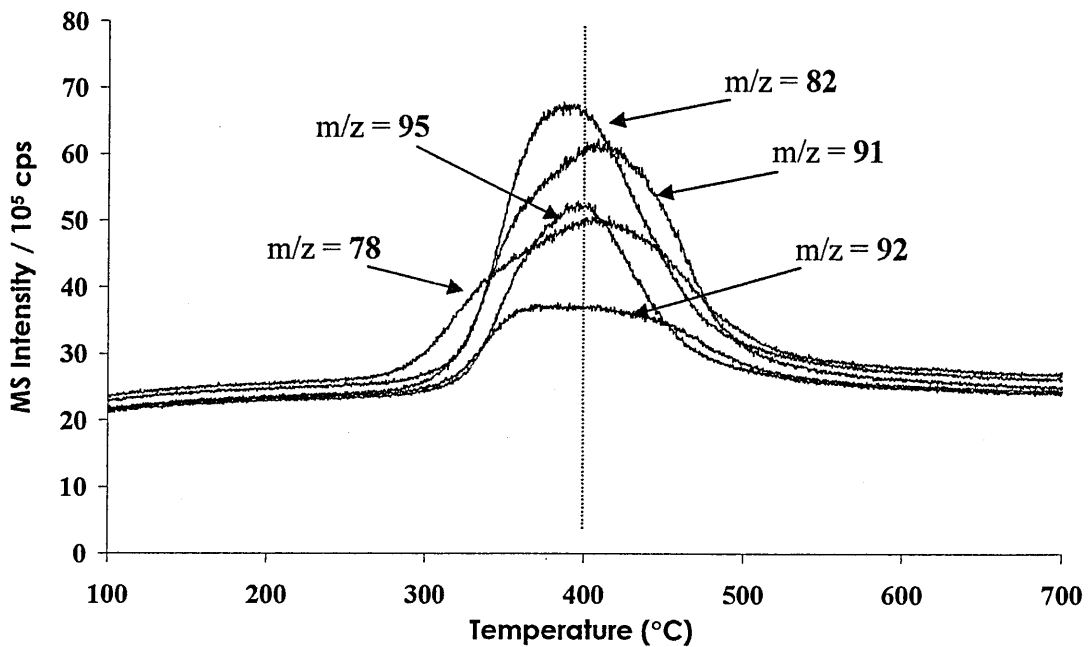
Figure 3.25   RT-TG-MS ion chromatograms for the desorption of the following ring compounds: benzyl (m/z = 78), cyclohexenyl (m/z = 82), tolyl (m/z = 91 & 92) and 1,6 dimethylcyclohexenyl or 3,5 dimethylcyclohexenyl (m/z = 95) from SWa-1-C_{12}.
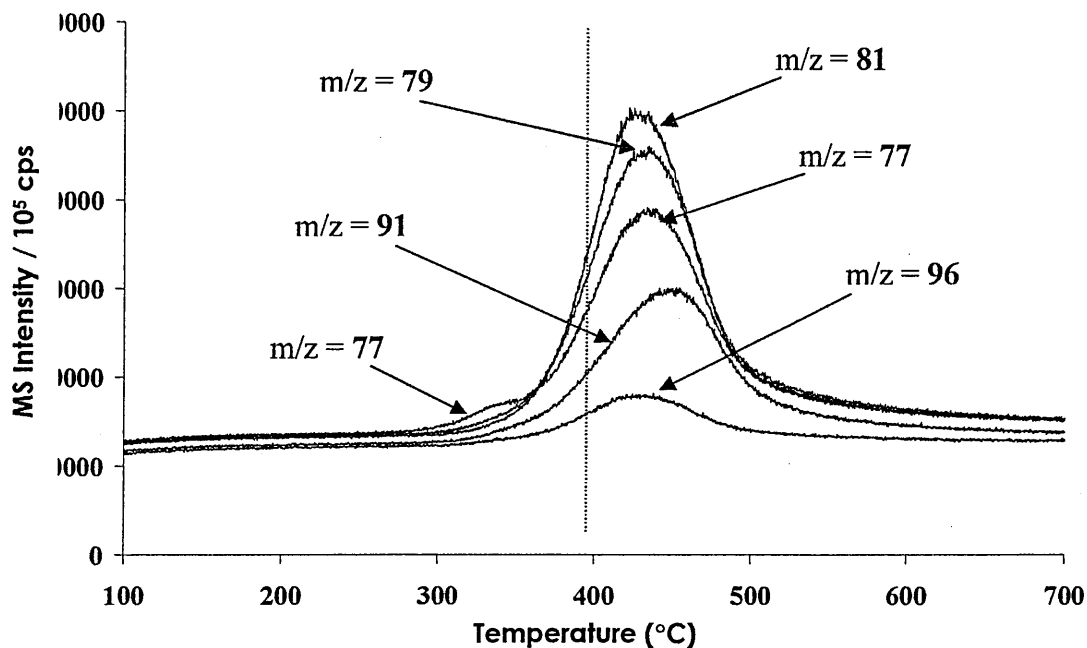
Figure 3.26   RT-TG-MS ion chromatograms for the desorption of the following ring
compounds: cyclohexadienyl/methylcyclohexenyl (m/z = 77),
cyclohexadienyl (m/z = 79), methylcyclohexenyl (m/z = 81), tolyl (m/z = 91)
and methylcyclohexenyl (m/z = 96)) from SWa-1-C_{16}.
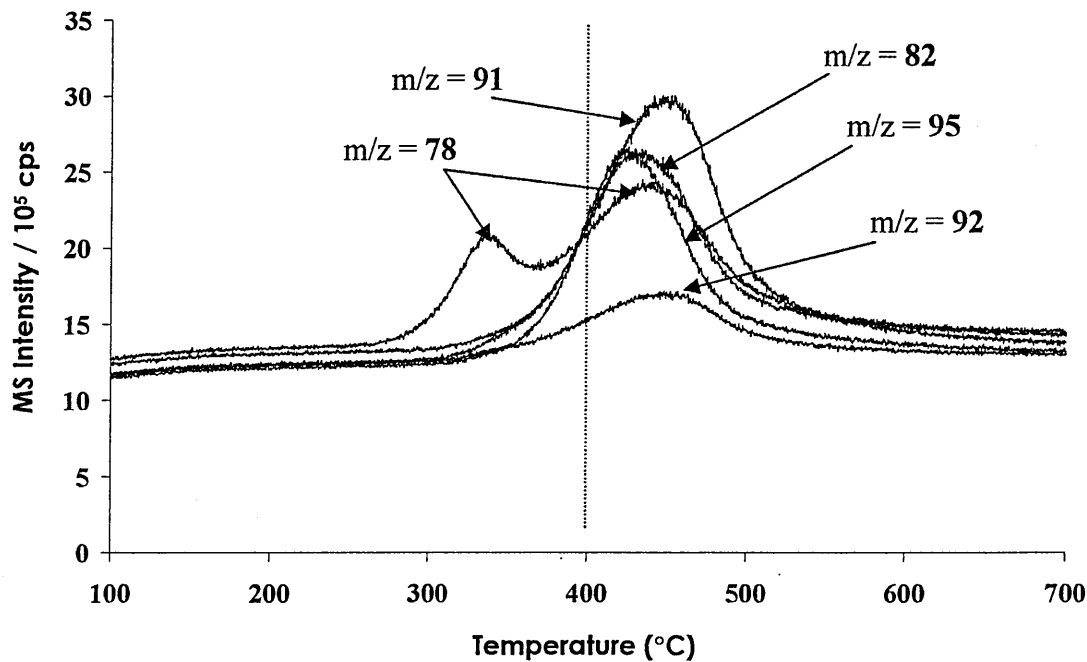
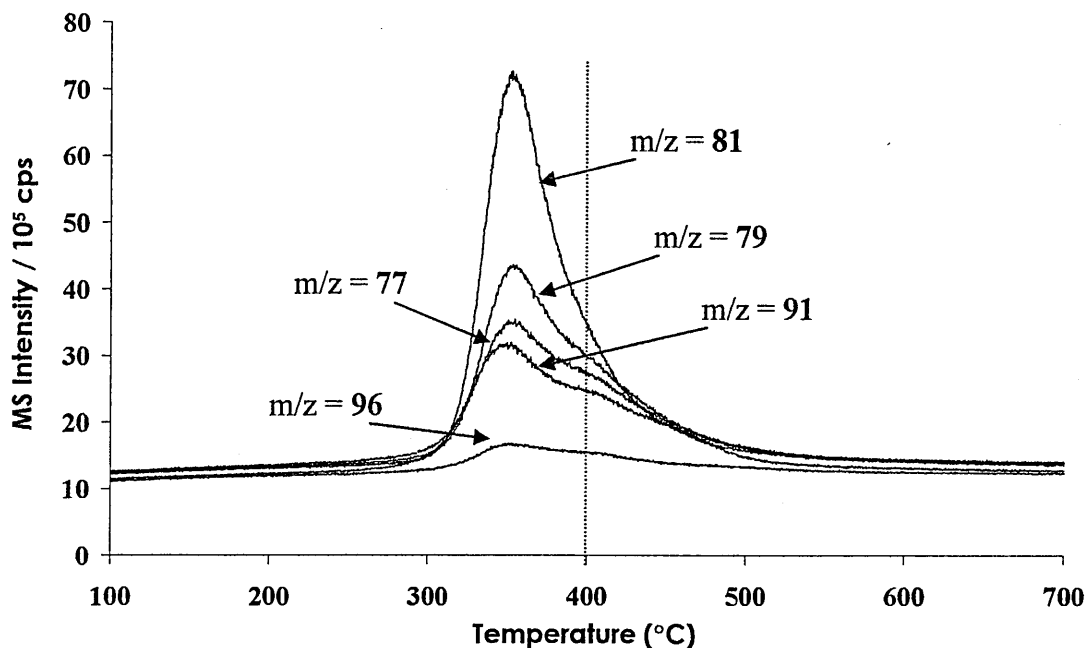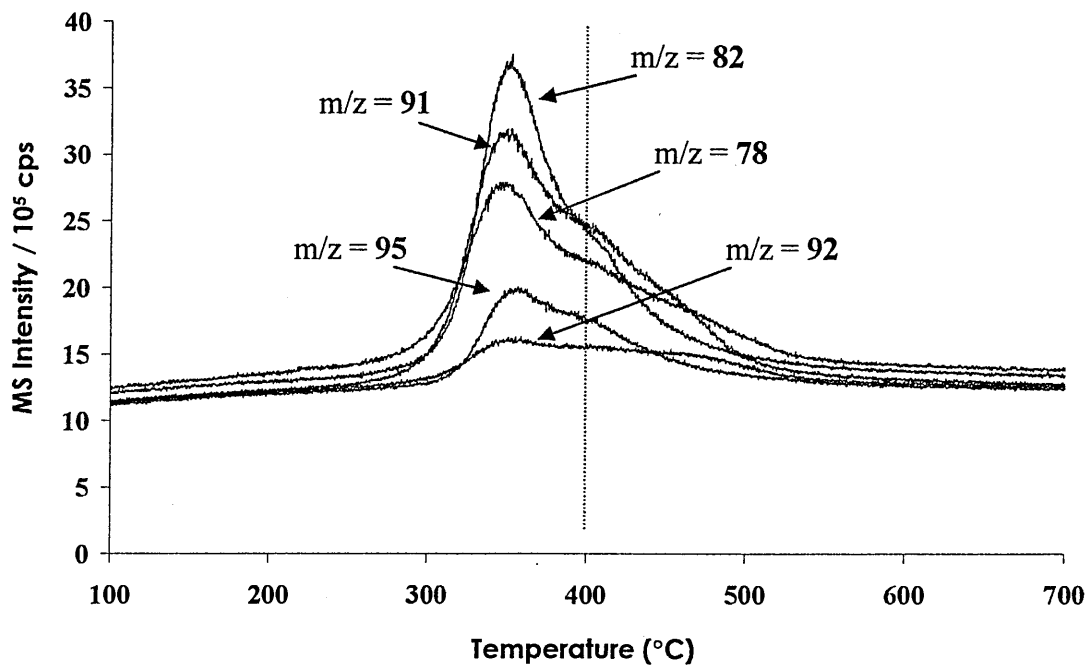Figure 3.27   RT-TG-MS ion chromatograms for the desorption of the following ring
compounds: benzyl (m/z = 78), cyclohexenyl (m/z = 82), tolyl (m/z = 91 &
92) and 1,6 dimethylcyclohexenyl or 3,5 dimethylcyclohexenyl (m/z = 95)
from SWa-1-C_{16}.

The temperature at which ring compounds were next desorbed was 363 °C, which showed an inflection in the positive gradient of toluene [m/z = 91] and was the main desorption maxima for toluene [m/z = 92] and methylcyclohexene [m/z = 96]. At 380 °C, methylcyclohexene [m/z = 81] and cyclohexene [m/z = 82] were desorbed, followed by 1,6 dimethylcyclohexene/3,5 dimethylcyclohexene [m/z = 95] at 391 °C. This was followed by cyclohexadiene/methylcyclohexene [m/z = 77], benzene [m/z = 78], cyclohexadiene/ methylcyclohexene [m/z = 79], toluene [m/z = 91] and a second event in the release of methylcyclohexene [m/z = 96] at 430 °C. The relative intensities of the evolved species remained the same as for the C_n = 8 samples.

Generally, as was seen with SAz-1, the shift to higher temperatures was again represented by an asymmetric shape in the TIC. In the C_n = 16 samples (fig. 3.26 & 3.27), benzene [m/z = 78] was again desorbed at lower temperatures than other ring compounds, in these samples it was desorbed as two very distinct maxima, the first of which showing significant intensity at 338°C. This was followed by the release of cyclohexadiene/methylcyclohexene [m/z = 77] at the first of two maxima, the first occurring at relatively low intensity at approximately 350°C, with respect to the second maximum. This was followed by a maximum for methylcyclohexene [m/z = 81] and 1,6 dimethylcyclohexene/3,5 dimethylcyclohexene [m/z = 95] at 420°C, cyclohexadiene [m/z = 79] and cyclohexene [m/z = 82] at 427°C, another for cyclohexadiene/methylcyclohexene [m/z = 77] and methylcyclohexene [m/z = 96] at 430°C, benzene [m/z = 78] (2nd maximum) at 435°C, and toluene [m/z = 91] / [m/z = 92] showed asymmetrical plots with a bias towards 445°C.

As with the SAz-1 samples, the RT-TG-MS results for SWa-1-CnNH3 correlated well with those results obtained from the Mettler TG50 thermograms. The thermally desorbed species could be transposed from one set of data to the other.

3.4.5 Summary of Analysis of SWa-1-C_nNH$_3$

i) XRD - SWa-1-C_nNH$_3$

The basal spacings for SWa-1-C_nNH$_3$, shown in table 3.15, indicated that expansion of the interlayer occurred when SWa-1 was exchanged with alkylammonium cations with alkyl chains ranging C_n = 8-13.

C_n	6	7	8	9	10	11	12	13	14	15	16
d_{001} (Å)	13.6	13.6	13.6	14.1	14.3	15.6	16.1	17.8	17.8	17.8	17.8

Table 3.15 Comparison of d_{001} for different alkyl chain lengths (C_n) exchanged onto SWa-1.

ii) TGA - SWa-1-C_nNH$_3$

The total weight loss from standard 10 mg samples increased as the length of the alkylammonium cation increased (table 3.16), but the maximum total weight loss for C_n = 16 was approximately 6 wt% less than was desorbed from the corresponding SAz-1 organoclay.

Cn	6	7	8	9	10	11	12	13	14	15	16
Total % wt loss	17.5	17.8	19.0	19.3	20.5	21.4	23.1	23.7	23.9	24.2	26.6

Table 3.16 Comparison of d_{001} for different alkyl chain lengths (C_n) exchanged onto SWa-1.

Weight loss at < 150 °C, which was believed to be due to loss of water associated with the surfactants cationic head groups, decreased steadily from 1.0 wt% at C_n = 6 to 0.4 wt% at C_n = 16. The alkylammonium cations were desorbed within the same temperature range as for SAz-1 (i.e. between 150 and 500 °C). As the length of the alkyl chain increased, the profile of the thermal events changed. At C_n = 6, the majority of the weight loss occurred at a maxima of 310 °C, as the alkyl chain length increased the majority of the thermally desorbed products were being evolved at increasingly higher temperatures until at C_n = 16 where the majority of the desorption products were under a maximum at 390 °C. The majority weight loss and therefore the products of thermal desorption from SWa-1 were

shown to have shifted to higher temperatures (i.e. approximately 25 °C) than SAz-1. Weight loss at temperatures > 500 °C was believed to be due to dehydroxylation of the clay, CO_2 formation and the release metal carbonates, remained constant throughout the series of samples, at ~2.6 wt%.

iii)   **RT-TG-MS - SWa-1-C_nNH_3**

     a.   **Water [m/z = 18] and CO_2 [m/z = 44]**

Water [m/z = 18] was shown to be released between 35-800 °C and the signal intensity was much lower, indicating lower overall concentrations. As the alkyl chain length of the organocation increased, a decrease in the loss of water below 200 °C and above 500 °C was shown. CO_2 [m/z = 44] was shown to be initially released at low intensities, with larger signal intensities at lower temperatures for shorter alkyl chain lengths. As the length of the alkyl chain was increased, the signal intensity increased and the signal maxima shifted to higher temperatures, but did not saturate the detector as seen with the SAz-1 samples.

     b.   **Aliphatic Hydrocarbons**

TG-MS results showed that alkyls [m/z = 43, 57, 71, 85] and alkenyls [m/z = 41, 55, 69, 83] were desorbed over different temperature ranges and showed successively higher thermal desorption maxima with increasing alkyl chain length (table 3.17).

C_n	Desorption Temp. Range (°C)	Alkyl Maxima (°C)	Alkenyl Maxima (°C)
8	250-500	358	400
12	300-525	400	400
16	325-550	425	435

Table 3.17   **Comparison of desorption characteristics with increasing alkyl chain length for SWa-1-C_n.**

c. Ring Compounds

A large number of ring compounds were thermally desorbed from the different SWa-1-C_nNH$_3$ samples. To summarise the pattern of ring compound desorption, the temperature ranges and maxima temperatures are shown in table 3.18 and the relative intensities of these maxima are shown in table 3.19.

	Thermal Desorption Maxima (°C)		
m/z	C$_8$	C$_{12}$	C$_{16}$
81	355/400	380	420
79	352/400	395	427
82	352/400	380	427
77	351/400	400	350/430
78	346/400	340/400	338/435
91	350/400/445	363	445
95	356/400	405	420

Table 3.18 Comparison of the thermal desorption maxima temperatures with increasing alkyl chain length for SWa-1-C_n. (results in order of decreasing relative MS intensity relative to SAz-1).

	MS Intensity / 10^6 cps		
m/z	C$_8$	C$_{12}$	C$_{16}$
81	7.3	10.1	7.0
79	4.3	8.2	6.1
82	3.7	6.7	2.6
77	3.5	7.6	4.9
78	2.8	5.0	2.1/2.3
91	3.2	6.0	3.0
95	1.9	5.2	2.5

Table 3.19 Comparison of the relative intensities of the major ring compound thermal desorption maxima with increasing alkyl chain length for SWa-1-C_n. (results in order of SAz-1 decreasing relative MS intensity).

The reason for the fluctuation in intensity between the signals recorded for C_8 - C_{12} samples was unknown. However, the relative intensities of the different species indicated subtle changes to the desorption profiles.

3.5   Na-MMT (MCBP) + N-Alkyltrimethylammonium Cations ($C_nN^+(CH_3)_3$)

3.5.1   Description/Reason for Use

Mineral Colloid British Pharmacopoeia (MCBP - Montmorillonite) clay is a smectite sourced from Wyoming, USA. This clay was exchanged with a range of alkyltrimethylammonium cations with chain lengths ranging from C_8 to C_{16}, at a concentration equivalent to 1 x CEC of MCBP (80 mEq/100g). In this section the XRD traces, TGA/DTG traces and comparative TG-MS data for the desorption/decomposition of the alkyltrimethylammonium cations are described and the specific trends are discussed below.

3.5.2   X-ray Diffraction (XRD) of MCBP-$C_nN(CH_3)_3$

The XRD traces of the different series of samples appeared to give constant d_{001} values for the different organic loadings at 0.5, 1.0, 2.0 and 3.0 x CEC (fig. 3.27).

C_n = 8 (OTAB) gave a d_{001} = 14.35 Å for the different organocation loadings, which indicated that an increase in the concentration of organocation led to no further expansion of the interlayer. According to the correlations made between the basal spacing of N-alkylammonium saturated clays, with an alkyl chain length of C_n = 8, these organocations had formed a monolayer within the clay gallery.

C_n = 12 (DTAB) gave a d_{001} = 16.14 Å for the different loadings. This indicated that the arrangement of the organocations in the gallery lay between a monolayer and a bilayer configuration. C_n = 14 (TTAB) showed a d_{001} = 18.34 Å for 1.0 x CEC, 18.73 Å for 2.0 x CEC and 18.15 Å for 3.0 x CEC. This slight variation, although insignificant, was probably due to slightly different amounts of water residing in the interlayer. When averaged, to a d_{001} of 18.41 Å, the configuration of the organocations was defined as a bilayer.

The d-spacings for the C_n = 16 (CTAB) samples were 19.30 Å at 1.0 x CEC, 20.37 Å at 2.0 x CEC and 20.37 Å at 3.0 x CEC. When the 2.0 and 3.0 x CEC samples were washed with i-

PrOH these d_{001} values were reduced from 20.37 Å to 19.20 Å, the new value resembled the 1.0 x CEC samples.

This indicated that the reduction may have been due to the removal of loosely bound material residing in the gallery. With a d_{001} of 19.30 Å the configuration of the organocations would be between a bilayer and a pseudotrilayer configuration. These samples adhered well to the expected pattern described by Jaynes & Boyd [1-29].
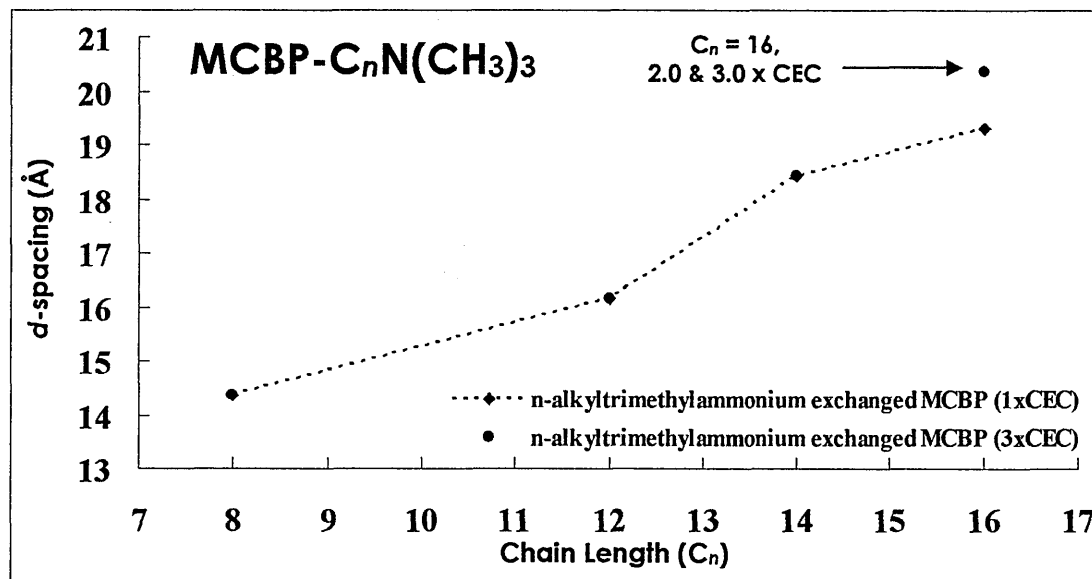
Figure 3.28   **Alkyltrimethylammonium exchanged MCBP. Effect of chain length of alkyltrimethylammonium ions on basal spacing.**

3.5.3   Thermo-Gravimetric Analysis (TGA) of MCBP-(C_8-C_{16})

The derivative thermograms for the MCBP series exhibited several thermal desorption maxima between 35 - 800 °C. A summary of the assignment of these maxima is shown in table 3.21.

As the length of the alkyl chain increased, the weight loss below 150 °C decreased. The charge density of MCBP was lower than SWa-1, but conversely, the cationic head group on the organocation was larger than those used previously, due to the replacement of hydrogen with methyl groups. At C_n = 8, the physisorbed water content was more than

double that present within organocation exchanged SAz-1 or SWa-1. As the alkyl chain length was increased, space within the galleries becomes extremely limited due to the intercalation of longer alkyl chain in addition to the bulky trimethylalkylammonium cations. The weight loss < 150 °C was seen to decrease rapidly with an increase in alkyl chain length and increases in organocation loading.

Desorption temperature	Assignment
35-150 °C	evolution of physisorbed water
150-500 °C	organocation decomposition events producing aliphatic, ring compounds, ammonia, water and CO_2
> 500 °C	clay dehydroxylation and CO_2

Table 3.20 **Assignment for thermal desorption maxima occurring within specific temperature ranges for MCBP-C_nN(CH$_3$)$_3$ TGA.**

Between 150 °C and 500 °C the DTG of MCBP-C_n showed two significant maxima that were readily identifiable as the desorption of organocation fragments. The TGA/DTG of C_n = 8 (OTAB) (fig.3.29/3.30) showed significant weight losses between 250-500 °C. The main peak was at 425 °C, with poorly resolved shoulders identifiable at 325, 370 and 470 °C. The appearance of the thermogram remained constant for each of three triplicate runs, also showing no change with an increase in the loading of organocation from 2.0 to 3.0 x CEC of MCBP. The overall weight loss for the 3 sets of thermograms remained the same at approximately 15 wt%. Fig. 3.29 shows that no change was shown relative to the loading of organocation, although the profile of the 0.5 x CEC weight loss showed less weight loss associated with alkyl fragments and more weight loss associated with the loss of physisorbed water.

The $C_n = 12$ (DTAB) TGA and DTG (fig. 3.31/3.32) displayed the maxima identified for the C_n = 8 (OTAB) sample, at the same temperatures. A large maximum at 425 °C showed a near constant weight loss at the four different organocation loadings, the adjacent maximum at 370 °C remained unchanged and the maxima at 325 and 470 °C were more prominent than in the OTAB samples. As well as those maxima that were previously reported, for the 1.0, 2.0 and 3.0 x CEC samples a new, broad maximum was observed at 240 °C. The absence of this lower temperature maximum in the 0.5 x CEC samples, could indicate that because the net negative charge at the surface of the clay was not fully satisfied, these organocations were attracted much more strongly than subsequent higher loadings. Therefore, the maximum at 240 °C appeared to have been fragmented to produce less stable decomposition products. The thermograms showed that as the organocation loading increased, weight loss associated with the maximum at 425 °C increased and losses above 500 °C were decreased. The overall weight loss from the samples increased with increased organocation loading, particularly between the 0.5 x CEC and 1.0 x CEC samples (fig. 3.31).

The $C_n = 14$ (TTAB) samples again displayed the most intense maximum at 425 °C. At a loading of 0.5 x CEC, the 325 and 370 °C events could only be seen as shoulders to the maximum at 425 °C (fig. 3.33/3.34). As the organocation loading increased, a new maximum was shown to increase at 280 °C which obscured the smaller maxima previously seen at 240, 325 and 370 °C. The emergence of the maximum at 280 °C again appeared to suggest that less thermally stable organocation fragments were being desorbed and the less thermally stable portions were being released at lower temperatures. The overall weight loss increased significantly between 0.5 and 1.0 x CEC (fig. 3.33).

The $C_n = 16$ (CTAB) samples displayed very little weight loss below 300 °C from the 0.5 x CEC loading, the DTG showing the same profile as that seen with all previous shorter alkyl chain
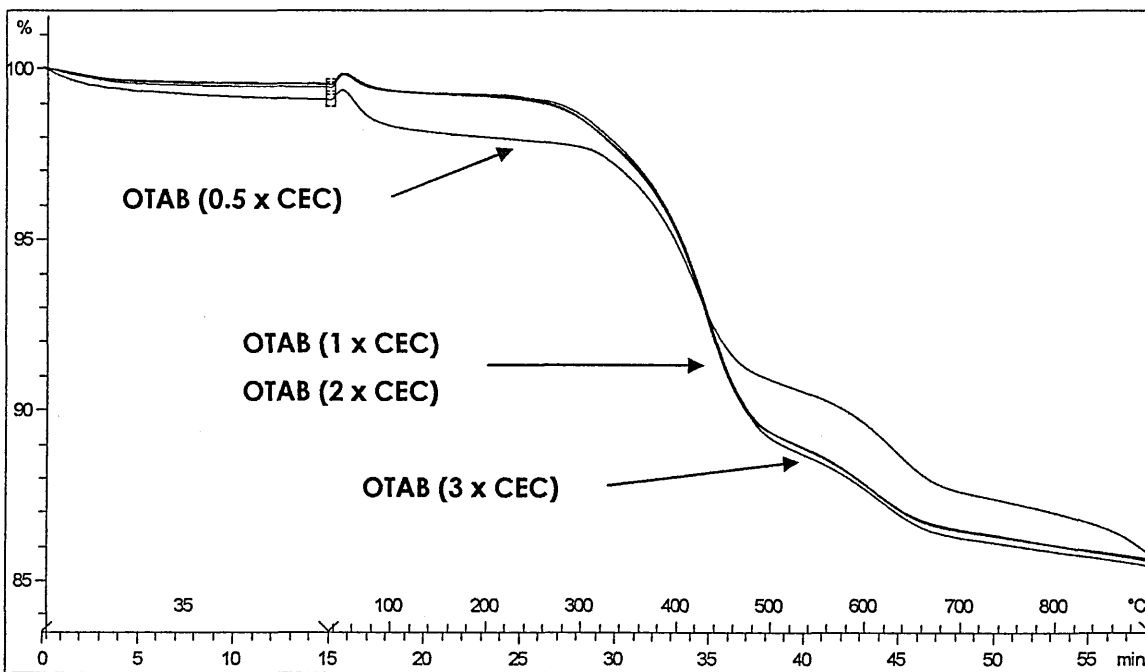
METTLER TOLEDO STAR® SW 7.01

Figure 3.29 Comparison of TG traces for MCBP-C$_8$(OTAB) with OTAB loadings of 0.5, 1, 2 and 3 x CEC (y-axis is relative % weight loss).
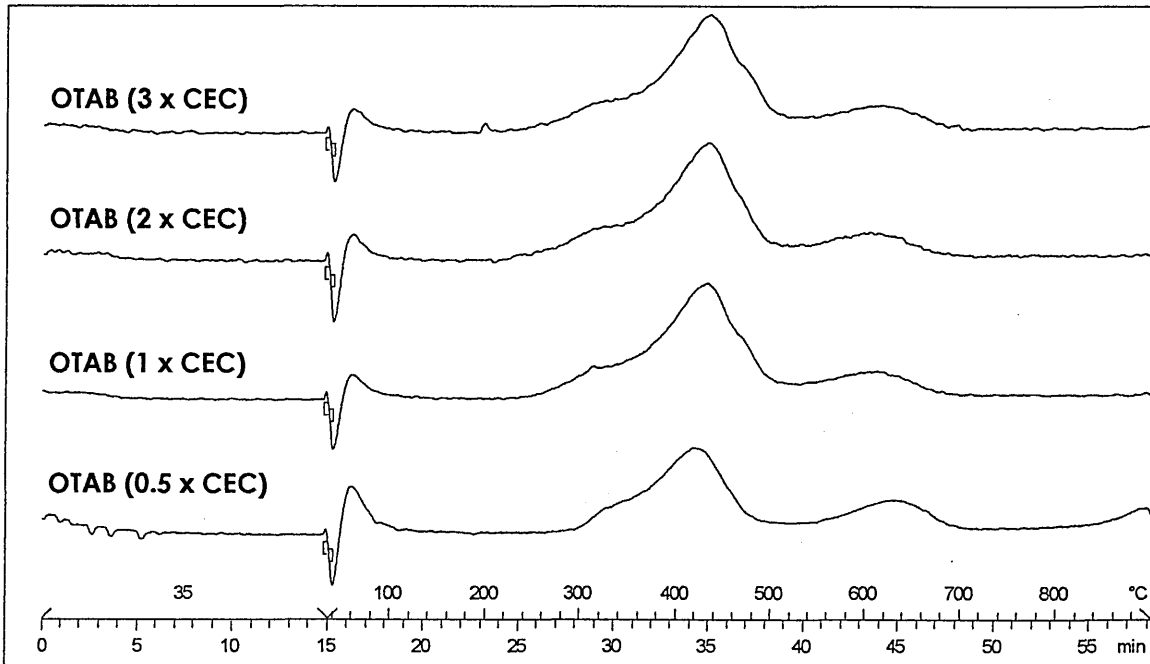
METTLER TOLEDO STAR® SW 7.01

Figure 3.30 Comparison of DTG traces for MCBP-C$_8$(OTAB) with OTAB loadings of 0.5, 1, 2 and 3 x CEC.

148
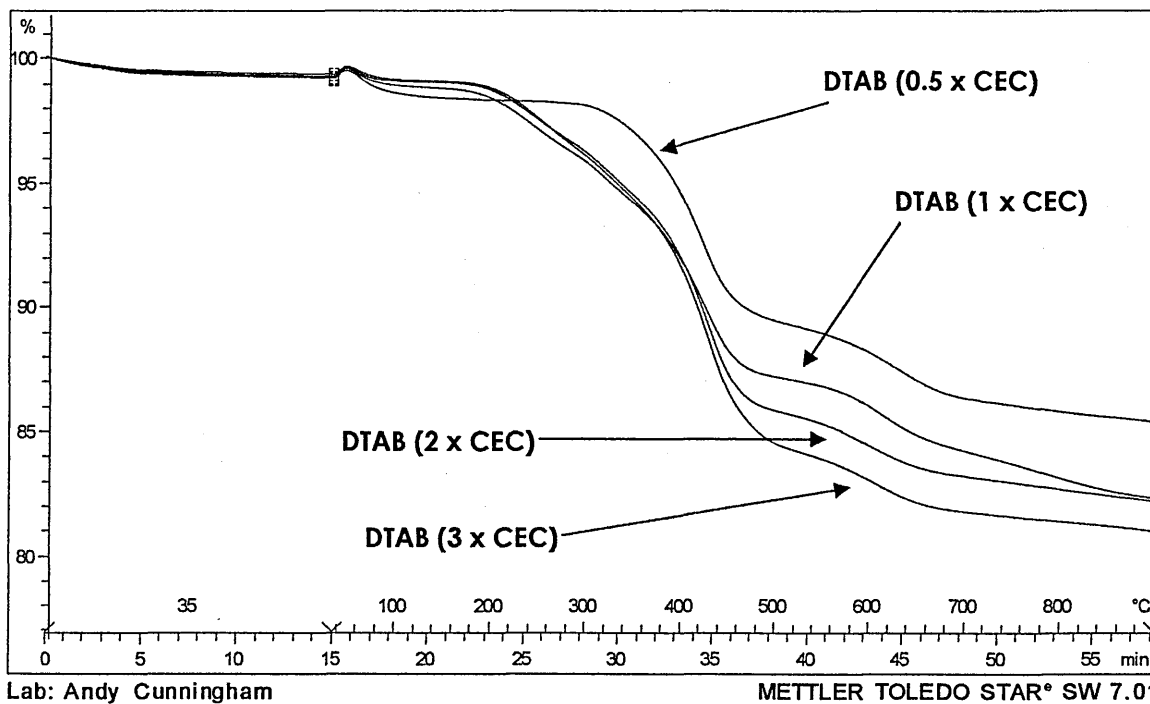
Figure 3.31   Comparison of TG traces for MCBP-C_{12} (DTAB) with DTAB loadings of 0.5, 1, 2 and 3 x CEC (y-axis is relative % weight loss).
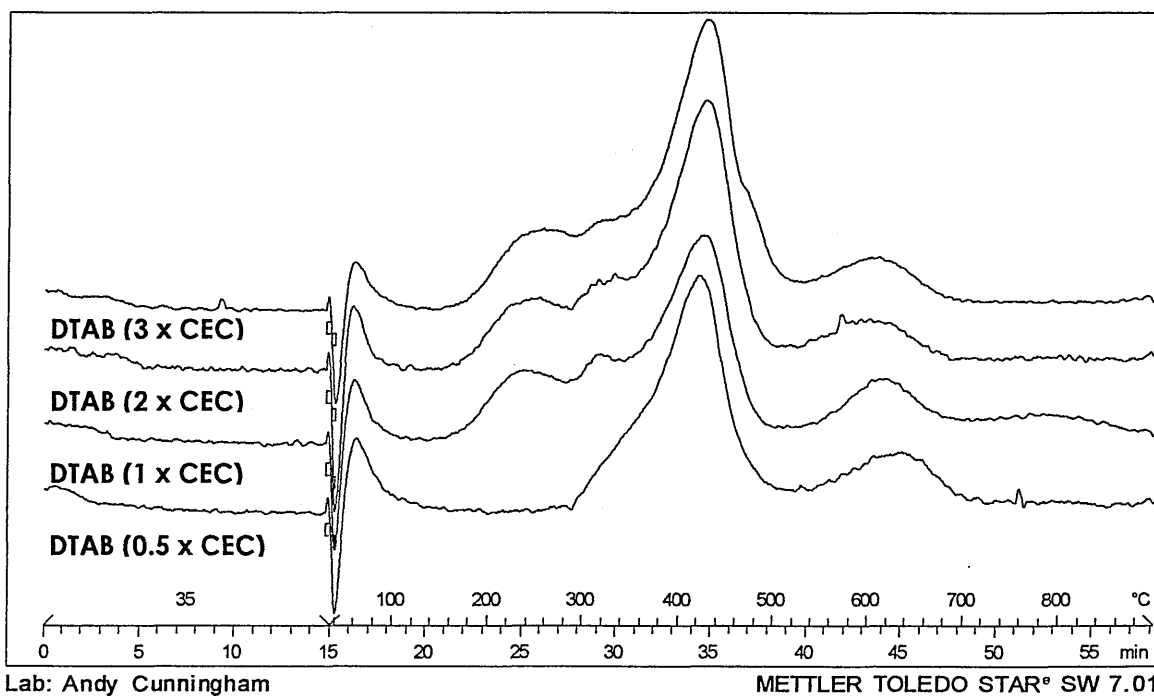
Figure 3.32   Comparison of DTG traces for MCBP-C_{12} (DTAB) with DTAB loadings of 0.5, 1, 2 and 3 x CEC.
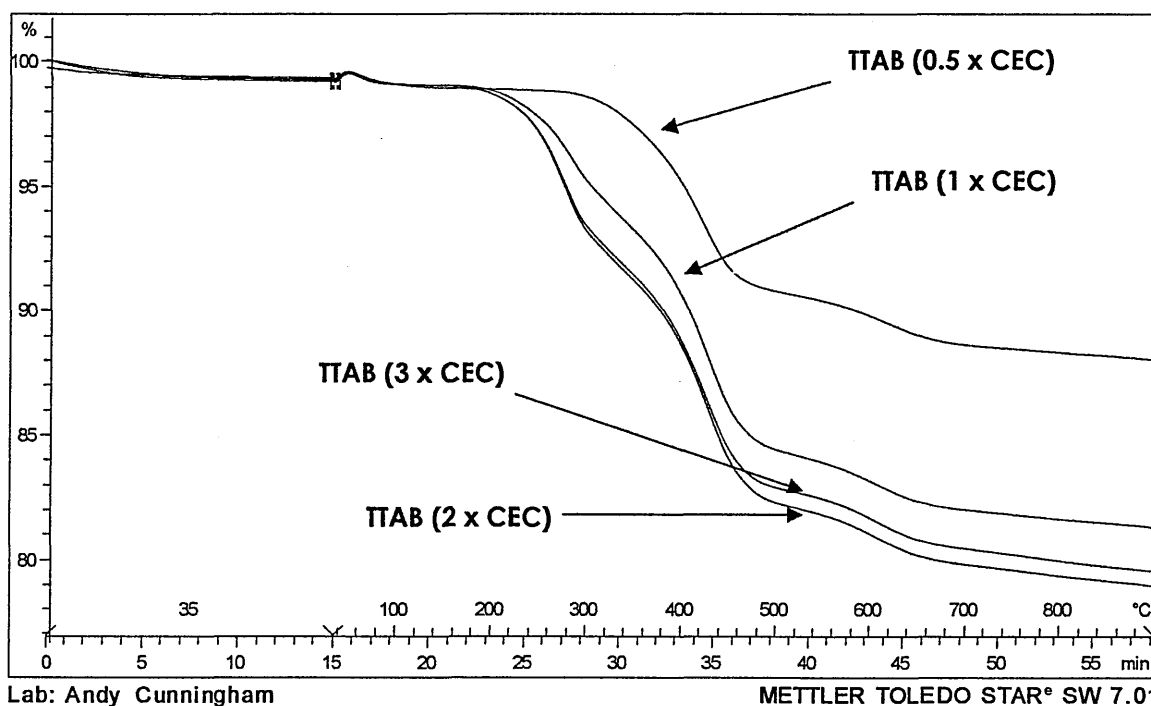
Figure 3.33 Comparison of TG traces for MCBP-C_{14} (TTAB) with TTAB loadings of 0.5, 1, 2 and 3 x CEC (y-axis is relative % weight loss).
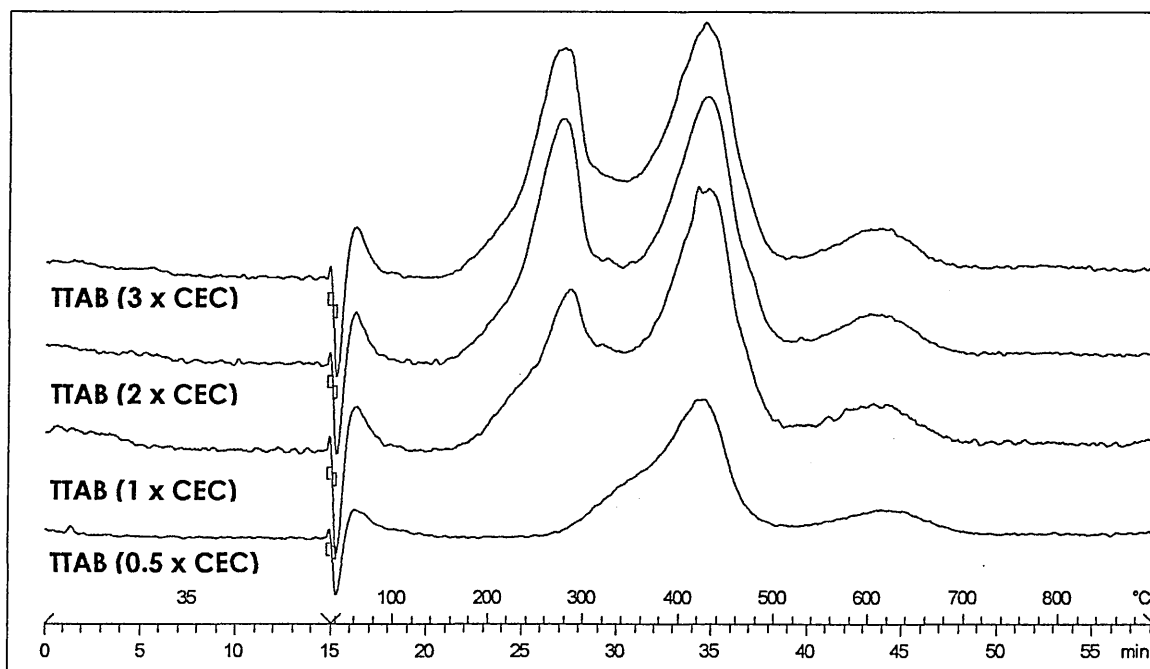
Figure 3.34 Comparison of DTG traces for MCBP-C_{14} (TTAB) with TTAB loadings of 0.5, 1, 2 and 3 x CEC.
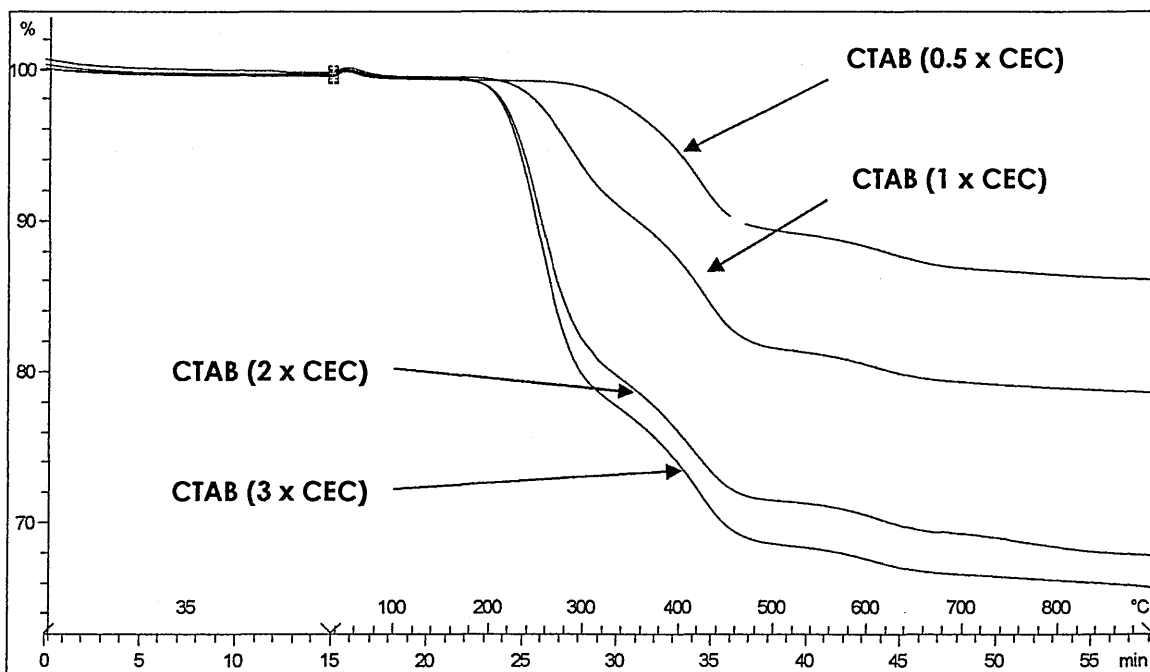
Figure 3.35   Comparison of TG traces for MCBP-C$_{16}$ (CTAB) with CTAB loadings of 0.5, 1, 2 and 3 x CEC (y-axis is relative % weight loss).
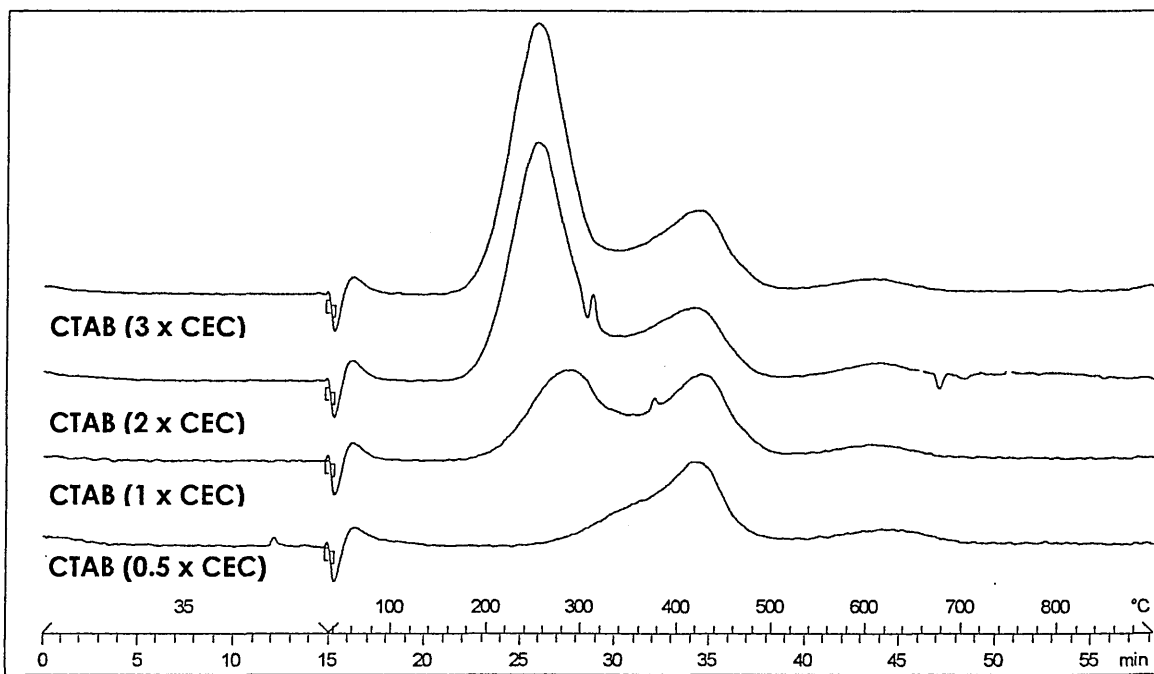
Figure 3.36   Comparison of DTG traces for MCBP-C$_{16}$ (CTAB) with CTAB loadings of 0.5, 1, 2 and 3 x CEC.

151

samples within this series (fig. 3.35/3.36). At 1.0 x CEC, the DTG showed prominent thermal desorption maxima at 280 °C (7 wt%) and 425 °C (9 wt%) when the total weight loss from the sample was approximately 19 wt% (fig. 3.35). As the organocation loading was increased to 2.0 x CEC of MCBP the weight loss associated with the maximum at 280 °C increased to 17.5 wt% and the maximum was shifted to the slightly lower temperature of 250 °C. The maximum at 425 °C remained constant at 9 wt% and the overall weight loss increased to 30 wt%. In the case of the 3.0 x CEC samples, a weight loss of 23.5 wt% was attributed to the 250 °C maximum, whilst the maximum at 425 °C still remained relatively unchanged at approximately 8 wt%. The overall weight loss was measured at 34 wt%. As the organocation loading of the C_n = 16 samples was increased, the lower temperature events became more prominent, this was the result of unintercalated material or that which was bound at the edges of the clay galleries.

The overall trends showed that the weight loss under the lower temperature maxima, in the temperature range of 200-300 °C, increased with alkyl chain length. This was the opposite of that observed with the alkylammonium exchanged SAz-1 and SWa-1 clays.

Further to this investigation, the 2.0 and 3.0 x CEC C_n = 16 samples were washed with 10ml *i*-PrOH in an attempt to remove any excess organic material. TGA results showed that by washing these samples the excess organic matter was easily removed, and the desorption profile reverted back to that which was previously seen at 1.0 x CEC. These results concur with the XRD data shown in section 3.5.2, fig. 3.28.

The broad maxima at approximately 600 °C (which ranged from 525-675 °C), represented the dehydroxylation of the clay and the loss of surface carbon. As the length of the alkyl chain increased the weight loss attributed to this region was successively reduced (table 3.21/fig. 3.37).

A summary of the weight losses at different temperatures is shown in table 3.21 and fig. 3.37.

MCBP	Weight Loss in the Temperature Range						Total %Wt loss
	35-150 °C	151-250 °C	251-310 °C	311-380 °C	381-500 °C	> 500 °C	
$C_8N^+(CH_3)_3$	2.3	0.3	0.7	2.2	6.8	3.4	15.7
$C_{12}N^+(CH_3)_3$	1.4	1.3	1.5	3.4	7.4	3.2	18.2
$C_{14}N^+(CH_3)_3$	0.9	1.6	3.4	3.7	6.7	2.8	19.1
$C_{16}N^+(CH_3)_3$	0.5	1.9	4.8	4.4	5.4	2.5	19.5

Table 3.21 Comparison of the weight loss at different temperature ranges, signifying different thermal events between 35 °C and 800 °C.
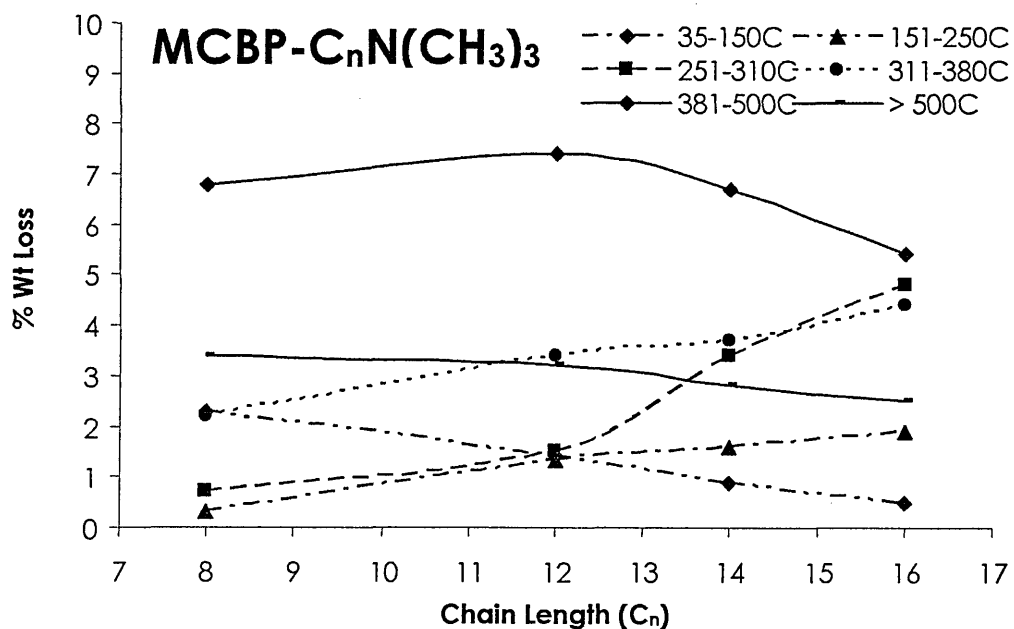
Figure 3.37 Alkyltrimethylammonium decomposition, a comparison of the weight loss (wt%) in different temperature ranges (outlined in table 3.22) with increased chain length.

Unless otherwise stated, the settings that were used for TG-MS were as previously reported. Also, the decomposition species were categorised as being the same as those evolved from both the alkylammonium exchanged clays, described in section 3.3.4.

3.5.4.1   Water [m/z = 18] and CO_2 [m/z = 44]

In the C_n = 8 (OTAB) samples, water [m/z = 18] was seen to be less intense than in previous samples and was released throughout the temperature profile. The C_n = 8 (OTAB) samples showed water being evolved as a shoulder at approximately 280 °C and a broad maximum at 340 °C. In the C_n = 12 (DTAB) traces, the baseline intensity of the water signal had decreased by 50 % to approximately 1.0×10^6 cps. Minor events were shown to occur at approximately 350 °C, 430 °C and 560 °C.
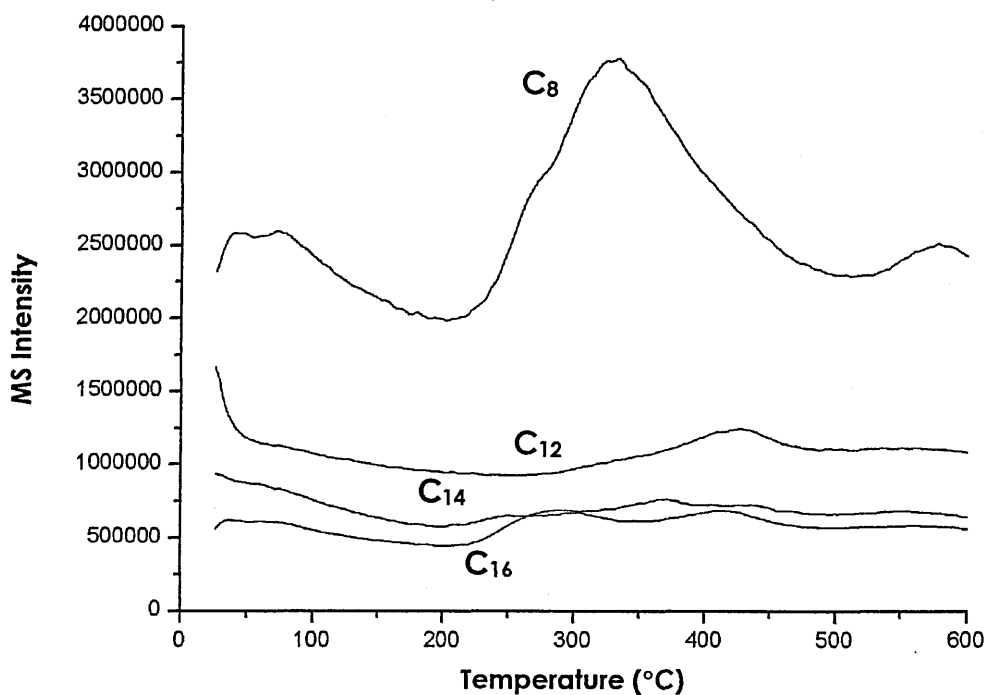
Figure 3.38   Shape of water [H_2O - m/z = 18] evolution with the increase in
alkylammonium chain length from C_8 to C_{16} for MCBP.

$C_n = 14$ (TTAB) showed similar trends to those seen in previous samples (i.e. an increase in the number of events at lower temperatures). Water [m/z = 18] was evolved with maxima at 250, 375, 440 and 560 °C. The TIC reflected these maxima as an asymmetric maxima at 410 °C with a bias towards temperatures >410 °C, but still reflecting the increase in species evolved between 200-410 °C. This trend continued with the $C_n = 16$ sample, water [m/z = 18] showed a broad maximum at 280 °C, another at 440 °C and a broad maximum at 580 °C. The TIC showed events at 250 °C, 325 °C and 415 °C, with the 415 °C event showing less intensity relative to the 250 °C and 325°C maxima.
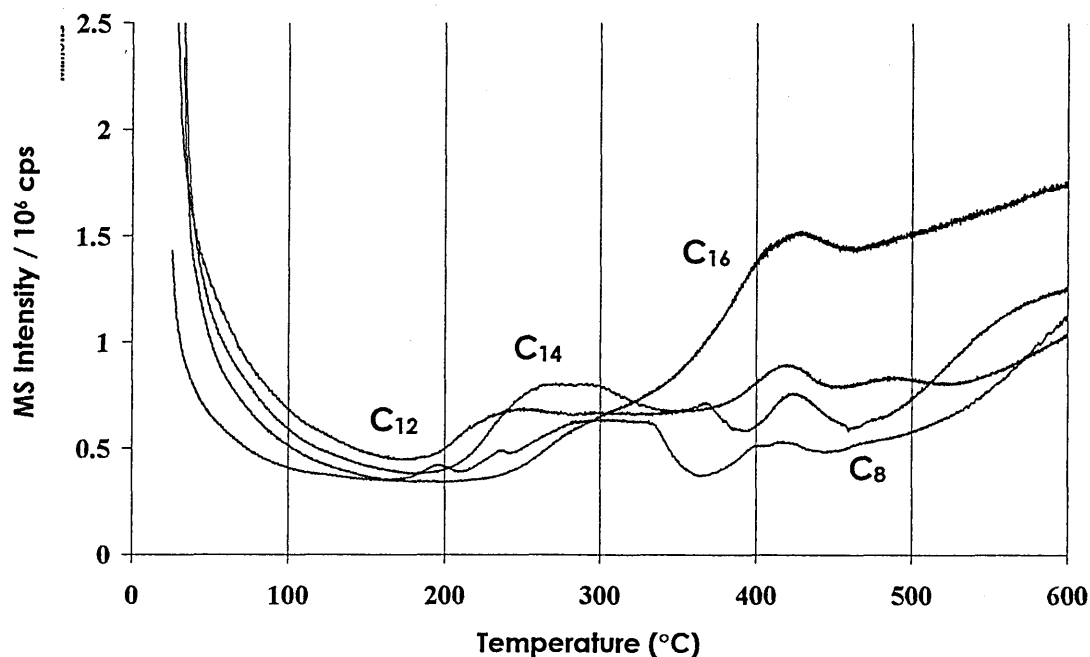
Figure 3.39   **Evolution of CO_2 [m/z = 44] for MCBP samples exchanged with alkyltrimethylammonium ions of increasing alkyl chain length.**

CO_2 [m/z = 44] was again released throughout the entire temperature profile. In the $C_n = 8$ samples, a broad maximum appeared at 280 °C (temp. range 200-350 °C), followed by events at 400 and 415 °C and 600 °C before the intensity continually increased until 800 °C. In the $C_n = 12$ (TTAB) samples, maxima were present at 200 °C, 240 °C, 300 °C, 405 °C, 430 °C and 600 °C from where the intensity increased steadily. The $C_n = 14$ samples showed maxima at 250, 370, 430 and 600 °C, with the signal intensity increasing steadily until 800 °C This trend was continued in the $C_n = 16$ (CTAB) samples, with maxima at 325, 430 and 600

155

°C. The general trend for the desorption of CO_2 in the region denoted for alkyl fragment desorption showed a shift to higher temperatures, and an increase in relative intensity with increased alkylammonium chain length. This was reflected in the TIC as an event at 350 °C followed by a second much more intense event with a maximum at 400 °C.

3.5.4.2 Aliphatic Hydrocarbons,

Alkyls [m/z = 43, 57, 71, 85] and Alkenyls [m/z = 41, 55, 69, 83]

The C_n = 8 (OTAB) samples showed that alkyls and alkenyls were desorbed at a main maximum at approximately 400 °C and a second lower temperature event that appeared as a shoulder at approximately 350 °C (fig. 3.40). It appeared that of the two types of species, the linear alkenyls desorbed at higher temperatures more favourably than the linear alkyls, which lead the lower temperature event in alkenyls appearing as more of an insignificant shoulder to the main maxima.
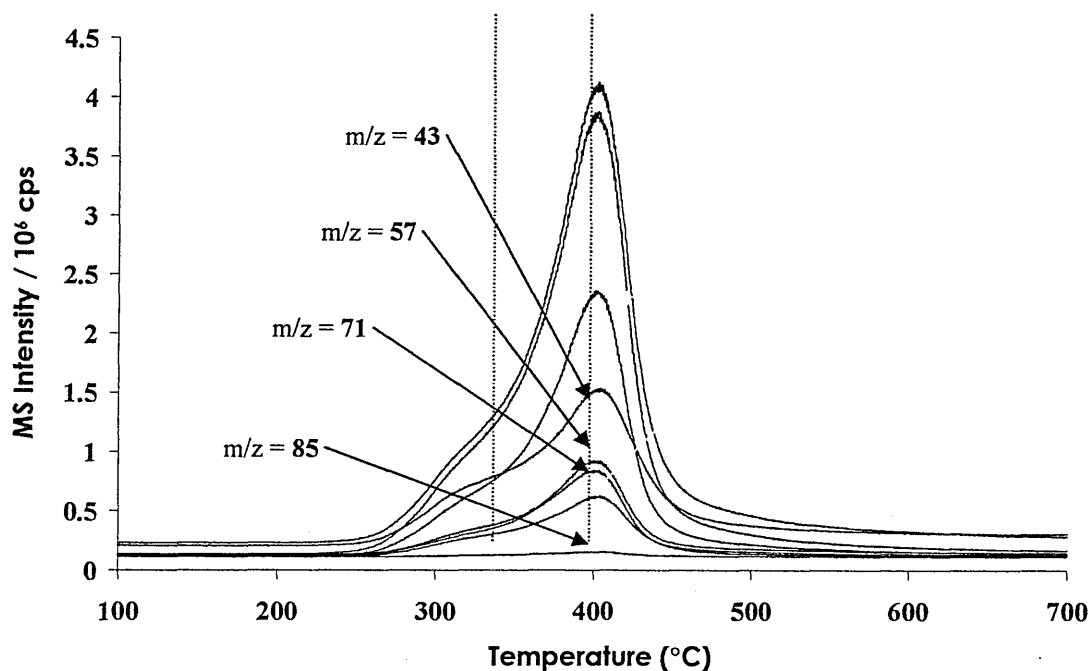
Figure 3.40   RT-TG-MS ion chromatograms for the desorption of linear alkyls (i.e. propanyl (m/z = 43), butanyl (m/z = 57), heptanyl (m/z = 71) hexanyl (m/z = 85)) and linear alkenyls (i.e. propenyl (m/z = 41), butenyl (m/z = 55), heptenyl (m/z = 69) hexenyl (m/z = 83)) from C_n = 8 (OTAB).

The $C_n = 12$ (DTAB) sample exhibited maxima at similar temperatures (348 °C and 412 °C) as seen with $C_n = 8$ (OTAB), and over the same temperature range. The differences in the intensity between alkyls and alkenyls remained the same as in $C_n = 8$ (OTAB), with the exception of the increase in the intensity of [m/z = 69] relative to [m/z = 55].

As the alkyl chain length was increased again to $C_n = 14$ (TTAB), both maxima were shifted to the slightly higher temperatures of 410 °C and 415 °C. The intensity of the shorter chain alkyls was also greatly increased relative to the corresponding fragments from saturated species.

In $C_n = 16$ (CTAB), as the alkyl chain length increased again, the linear alkyl and alkenyl fragments were desorbed at the same temperatures as with $C_n = 14$ (TTAB). However, the shape of these traces had changed. The alkenyl fragments (i.e. [m/z = 41, 55, 69] in particular) exhibited a greater intensity at 350°C relative to the corresponding maximum at 410 °C. Also, the 350 °C maximum for the alkyl fragments appeared to shift to progressively higher temperatures as the chain length of the evolved species increased. This was shown by a low temperature maximum for [m/z = 43] which evolved at 315 °C.

The spectrum of these desorbed species appeared much narrower than previously seen with alkylammonium exchanged SAz-1 and SWa-1. The species that were desorbed under the higher temperature maxima were approximately 30 °C more stable than those desorbed from SAz-1 samples and the intensity under the 405 °C maximum was ten times that which was previously seen with the SWa-1 samples.

3.5.4.3   Ring Compounds

Even with short chain length cations (i.e. $C_n = 8$ (OTAB)), there were a wide variety of secondary species desorbed from the organically modified MCBP, these ring compounds were evolved as a result of the Hoffman degradation process and subsequent

157

isomerisation reactions (see chapter 1). The secondary species that were desorbed were identified as being the same as those in the alkylammonium exchanged SAz-1 and SWa-1 series (table 3.7), however, the desorption profiles were different. This was because the evolution temperatures of the different species were different.

The C_n = 8 (OTAB) samples (fig. 3.41/3.42) desorbed these secondary species under a maximum at 405 °C which was asymmetric towards temperatures at < 405 °C. The shape of this maximum closely resembled the shape of the TIC for this sample. Cyclohexadiene / methylcyclohexene [m/z = 77], Benzene [m/z = 78], cyclohexadiene [m/z = 79] methylcyclohexene [m/z = 81] and cyclohexene [m/z = 82] were shown to have the greatest intensity in the MS at temperatures up to 316 °C. Above this temperature the intensity of methylcyclohexene [m/z = 81] and to a lesser degree cyclohexadiene [m/z = 79] dominated the desorbed output. Also, Toluene [m/z = 91] / [m/z = 92] was evolved at a relatively low intensity. Benzene [m/z = 78] and cyclohexene [m/z = 82] showed indications of a lower temperature event at 316 °C, and to a lesser extent toluene [m/z = 91] at approximately 350 °C.

The desorption of ring compounds from the C_n = 12 (DTAB) sample (see fig. 3.43/3.44) reflected the slight intensity increase in lower temperature events that were seen in the corresponding TIC. Benzene [m/z = 78] had the highest intensity of any evolved ring compounds between 200 and 280 °C (maxima ~250 °C). The benzene [m/z = 78] signal indicated that three significant events were probably occurring throughout its desorption, the first around 250 °C, a possible second event at approximately 325 °C and the main event, in line with the TIC maximum at 410 °C. The presence of these three events was confirmed by similar events at lower intensity being shown in cyclohexadiene/methylcyclohexene [m/z = 77] 1,6 dimethylcyclohexene/3,5 dimethylcyclohexene [m/z = 95] and methylcyclohexene [m/z = 96]. Above 280 °C, The relative intensities of the various desorbed species resembled those shown by C_n = 8
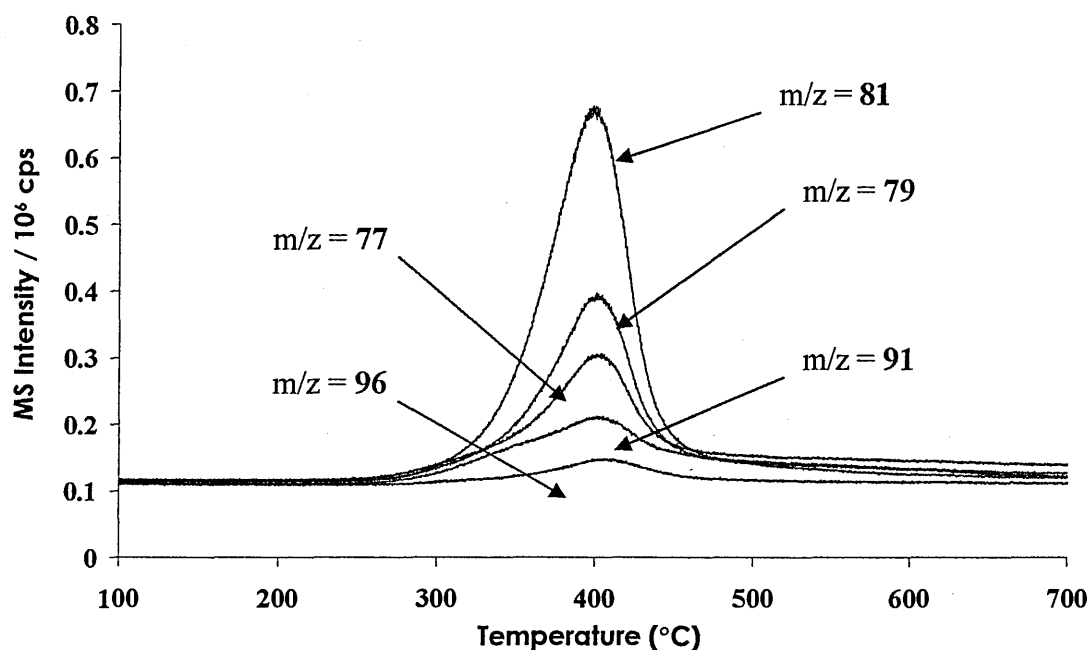
Figure 3.41   Cₙ = 8 (OTAB ~ 1 x CEC) RT-TG-MS ion chromatograms for the desorption of the following ring compounds: cyclohexadienyl / methylcyclohexenyl (m/z = 77), cyclohexadienyl (m/z = 79), methylcyclohexenyl (m/z = 81), toluenyl (m/z = 91) and methylcyclohexenyl (m/z = 96).

Figure 3.42   Cₙ = 8 (OTAB ~ 1 x CEC) RT-TG-MS ion chromatograms for the desorption of the following ring compounds: benzyl (m/z = 78), cyclohexenyl (m/z = 82), toluenyl (m/z = 91 & 92) and 1,6 dimethylcyclohexenyl or 3,5 dimethylcyclohexenyl (m/z = 95).

Figure 3.43 C_n = 12 (DTAB ~ 1 x CEC) RT-TG-MS ion chromatograms for the desorption of
the following ring compounds: cyclohexadienyl / methylcyclohexenyl (m/z
= 77), cyclohexadienyl (m/z = 79), methylcyclohexenyl (m/z = 81), toluenyl
(m/z = 91) and methylcyclohexenyl (m/z = 96).
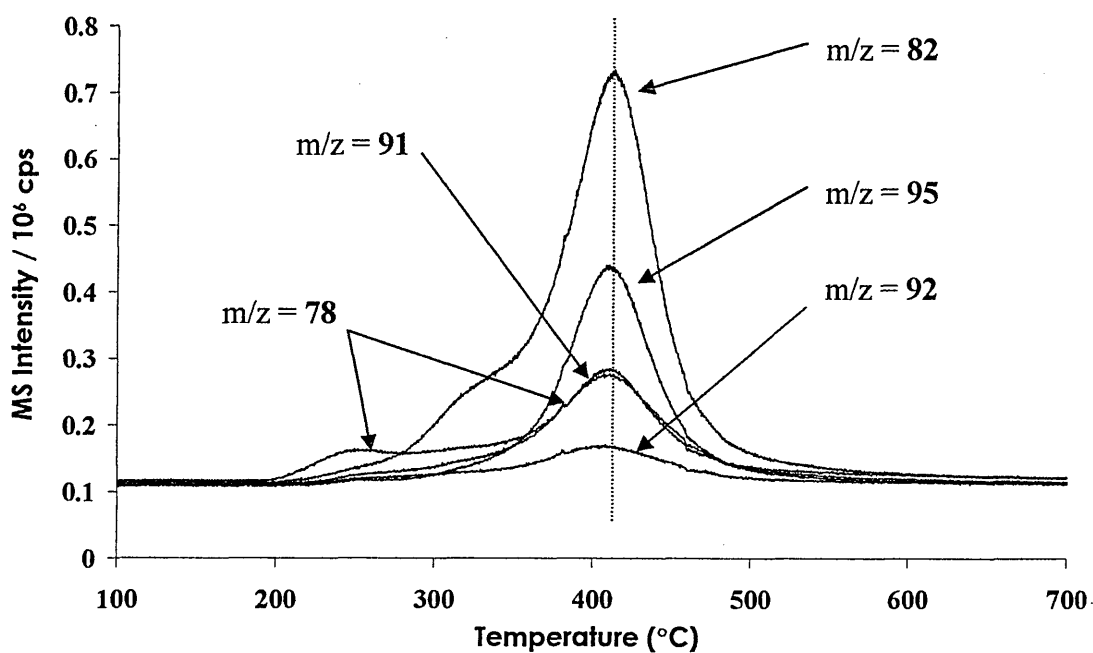
Figure 3.44 C_n = 12 (DTAB ~ 1 x CEC) RT-TG-MS ion chromatograms for the desorption of
the following ring compounds: benzyl [m/z = 78], cyclohexenyl [m/z = 82],
toluenyl [m/z = 91 & 92] and 1,6 dimethylcyclohexenyl or 3,5
dimethylcyclohexenyl [m/z = 95].
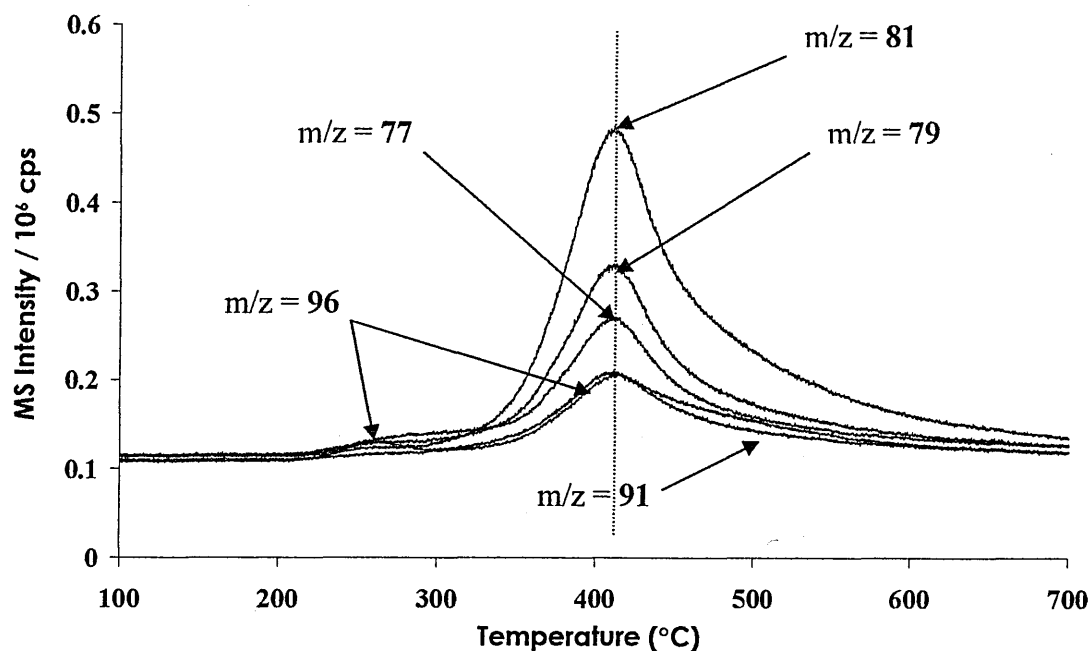
Figure 3.45 C_n = 14 (TTAB ~ 1 x CEC) RT-TG-MS ion chromatograms for the desorption of the following ring compounds: cyclohexadienyl / methylcyclohexenyl (m/z = 77), cyclohexadienyl (m/z = 79), methylcyclohexenyl (m/z = 81), toluenyl (m/z = 91) and methylcyclohexenyl (m/z = 96).
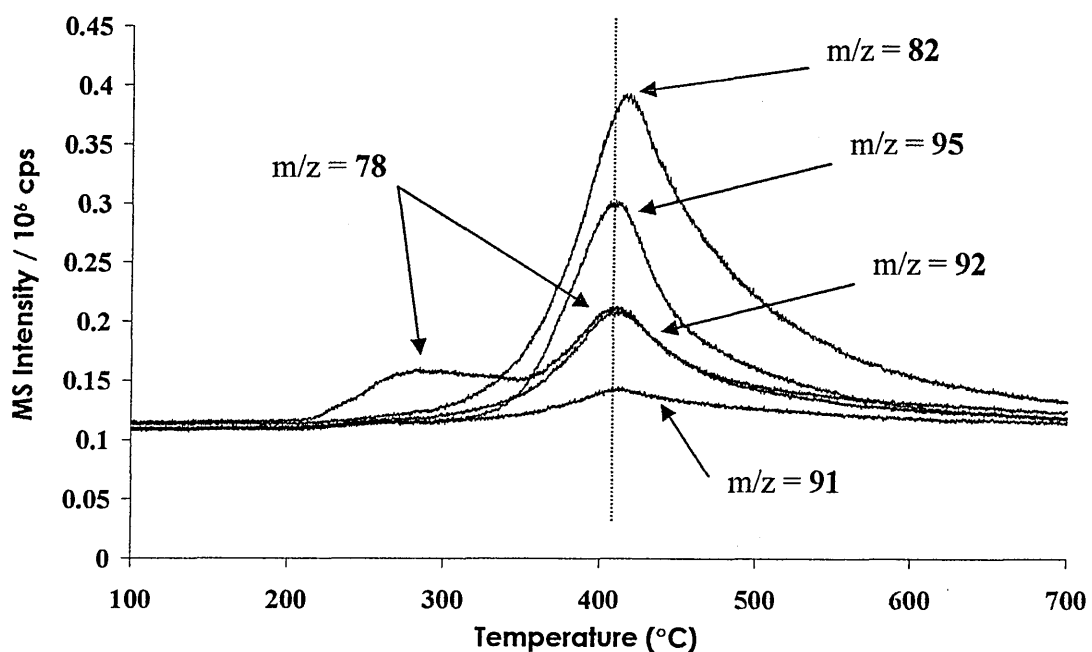
Figure 3.46 C_n = 14 (TTAB ~ 1 x CEC) RT-TG-MS ion chromatograms for the desorption of the following ring compounds: benzyl (m/z = 78), cyclohexenyl (m/z = 82), toluenyl (m/z = 91 & 92) and 1,6-dimethylcyclohexenyl or 3,5-dimethylcyclohexenyl (m/z = 95).
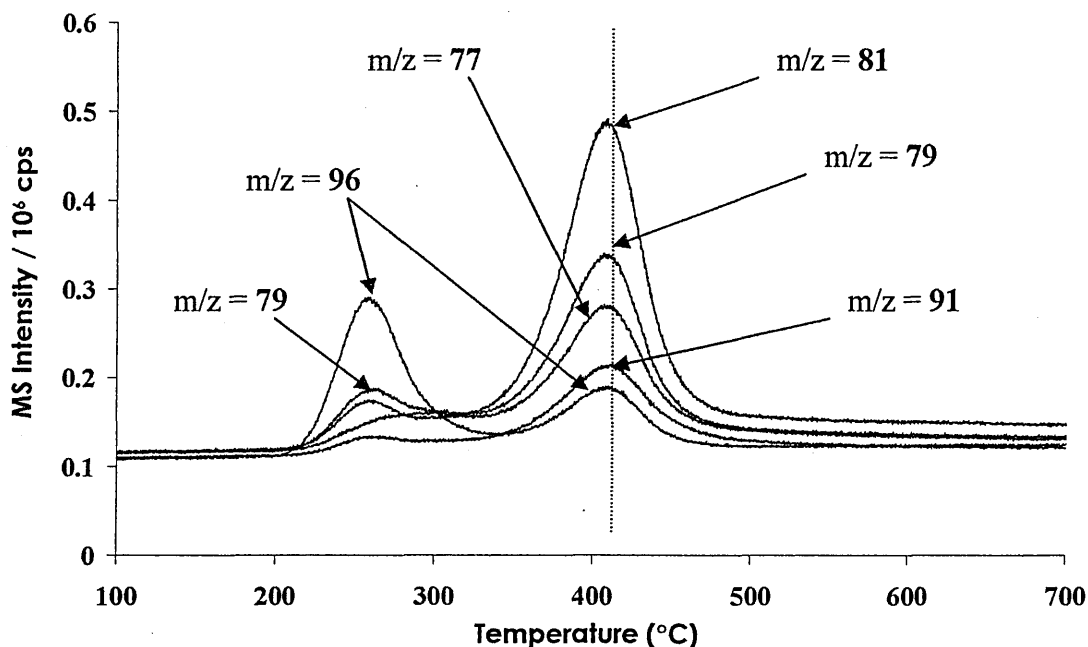
Figure 3.47   Cₙ = 16 (CTAB ~ 1 x CEC) RT-TG-MS ion chromatograms for the desorption of
the following ring compounds: cyclohexadienyl / methylcyclohexenyl (m/z
= 77), cyclohexadienyl (m/z = 79), methylcyclohexenyl (m/z = 81), toluenyl
(m/z = 91) and methylcyclohexenyl (m/z = 96).
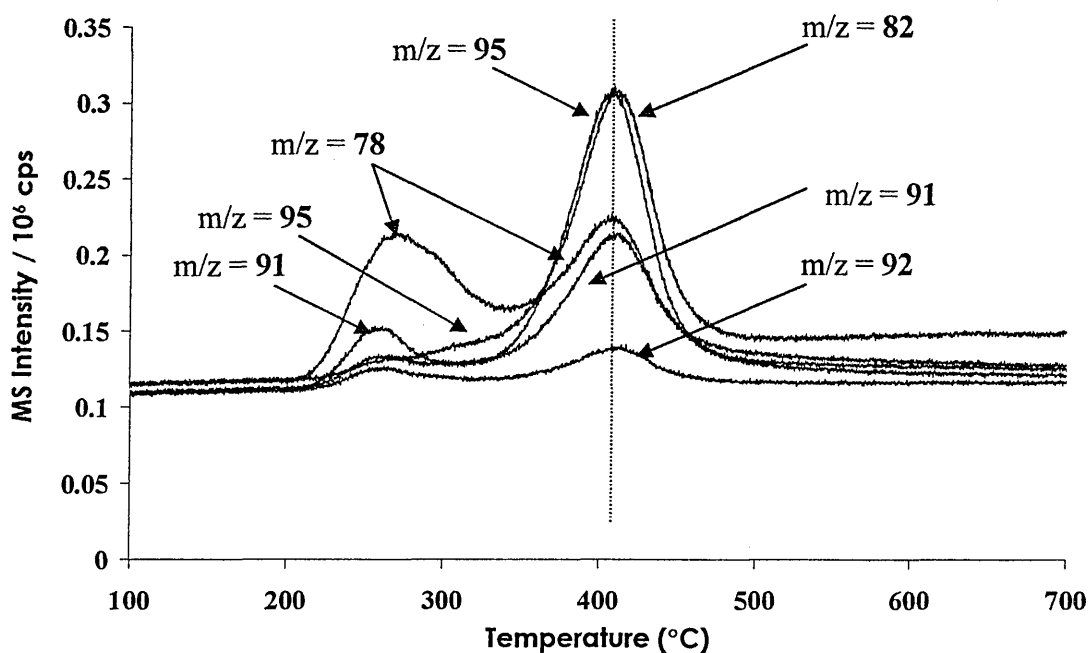
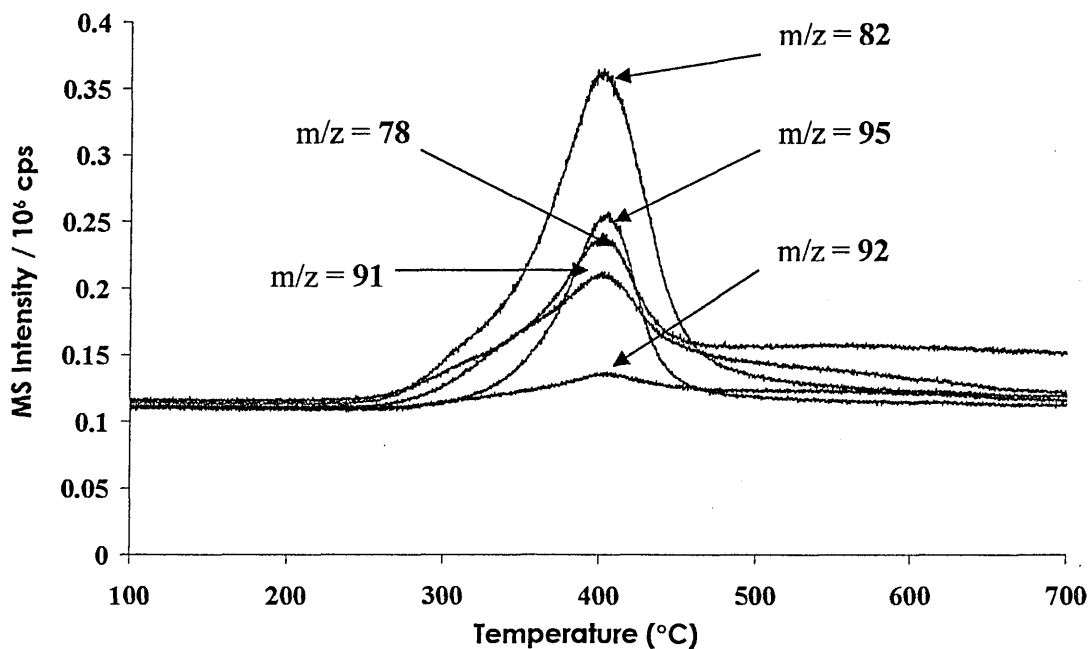Figure 3.48   Cₙ = 16 (CTAB ~ 1 x CEC) RT-TG-MS ion chromatograms for the desorption of
the following ring compounds: benzyl (m/z = 78), cyclohexenyl (m/z = 82),
toluenyl (m/z = 91 & 92) and 1,6-dimethylcyclohexenyl or 3,5-
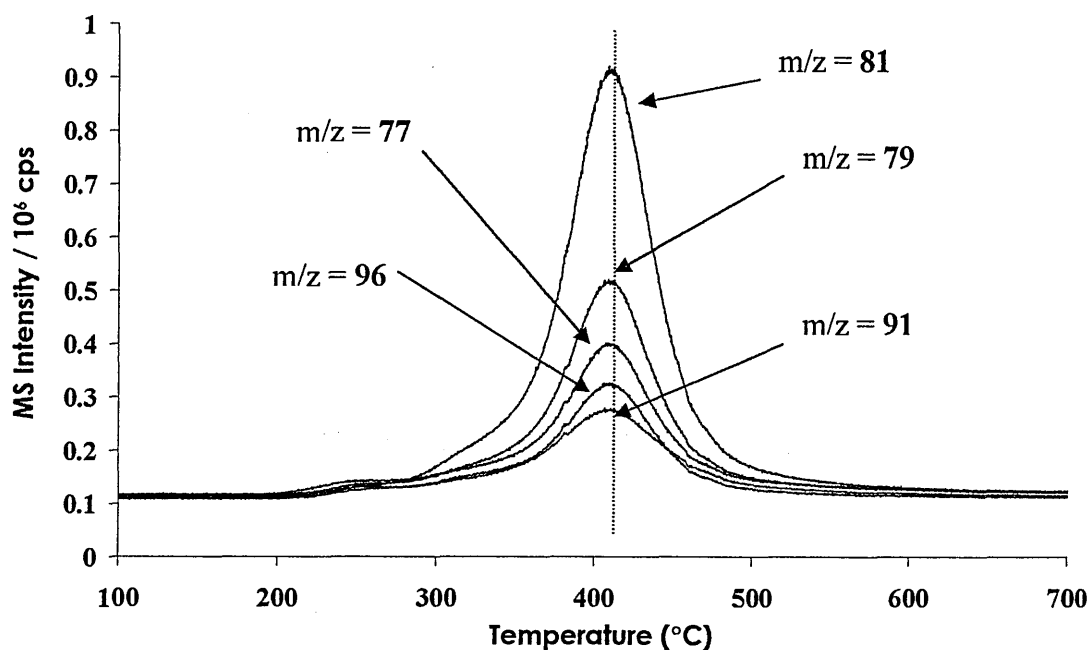dimethylcyclohexenyl (m/z = 95).

(OTAB), with all the aforementioned species possessing a main maximum at 410 °C; these were accompanied by asymmetric peak with a bias to temperatures < 410 °C for cyclohexadiene [m/z = 79], methylcyclohexene [m/z = 81], cyclohexene [m/z = 82] and toluene [m/z = 91] / [m/z = 92], also at 410 °C.

In $C_n = 14$ (TTAB) (fig. 3.45/3.46) the intensity of all the different species at temperatures > 410 °C was increased, this is not fully understood, specific ion chromatograms all exhibited a marked asymmetry with respect to higher temperatures. The trends that were shown in $C_n = 12$ (DTAB) (i.e. the shift to desorption at lower temperatures) were continued. Benzene [m/z = 78] showed a low temperature event of increased intensity between 200-340 °C, and displayed maxima at 280 °C and 410 °C, but no sign of a maximum at 325 °C. This was again confirmed by lower intensity events being present in cyclohexadiene/methylcyclohexene [m/z = 77], but only at approximately 260 °C in methylcyclohexene [m/z = 96].

$C_n = 16$ (CTAB) (fig. 3.47/3.48) again showed a continuation of these trends, but reflected the major shift in weight loss that was observed when using TGA (fig. 3.35). The most dramatic difference between $C_n = 16$ (CTAB) and the previous $C_n = 14$ (TTAB) sample was the significant increase in the maximum for methylcyclohexene [m/z = 96] at 260 °C, which was shown to be twice as intense as the maximum at 410 °C. The lower temperature event of Benzene [m/z = 78] now combined multiple events in a broad maximum of equal intensity to that at 410 °C. The increased intensity of lower temperature events was also shown in cyclohexene [m/z = 82], toluene [m/z = 91] and [m/z = 92] at 255 °C. The main desorption maximum, which for most species was at 410 °C, showed that there was a general decrease in intensity for most species, e.g. cyclohexene [m/z = 82] decreased in intensity until it was equal to 1,6-dimethylcyclohexene/3,5-dimethylcyclohexene [m/z = 95].

3.5.5 Summary of Analysis of MCBP-$C_nN(CH_3)_3$

i) XRD - MCBP-$C_nN(CH_3)_3$

The basal spacings for MCBP-$C_nN(CH_3)_3$, shown in table 3.22, showed that d-spacings for the alkyltrimethylammonium exchanged clay were larger than either SAz-1 or SWa-1 when exchanged with N-alkylammonium cations with the same alkyl chain length. Also, with the surface charge density of MCBP (80 mEq/100g) being less than both SAz-1 (120 mEq/100g) and SWa-1 (102 mEq/100g) the methyl groups on the quaternary ammonium head group must have significantly added to the organic bulk within the galleries or provided a more wholly organophilic environment for inward migrating surfactant molecules. The maximum d_{001} value of 19.3 Å for an exchange at 1.0 x CEC was swollen to 20.4 Å when the concentration of exchange species was increased to 2.0 and 3.0 x CEC.

C_n	8	→	12	14	16
d_{001} (Å)	14.4	→	16.1	18.4	19.3

Table 3.22 **Comparison of d_{001} for different alkyl chain lengths (C_n) exchanged onto MCBP.**

ii) TGA - MCBP-$C_nN(CH_3)_3$

The total weight loss from standard 10 mg samples increased as the length of the alkyltrimethylammonium cation increased (table 3.23). The maximum total weight loss for C_n = 16 was 19.5 wt%, which was 7 wt% less than SWa-1-$C_{16}NH_3$ and 13 wt% less than SAz-1-$C_{16}NH_3$. Weight loss due to loss of physisorbed water at < 150 °C was shown to be reduced rapidly from 2.3 wt% at C_n = 8 to 0.5 wt% at C_n = 16. The alkyltrimethylammonium cations were desorbed between 150 and 500 °C. As the length of the alkyl chain increased, the weight loss under the lower temperature maximum (i.e. 280 °C), in the temperature range of 200-300 °C, increased with alkyl chain length. The weight loss under a higher temperature maximum at 425 °C remained relatively constant. This was the reverse of that observed with the alkylammonium exchanged SAz-1 and SWa-1 clays.

When MCBP samples were swollen with $C_n = 16$ at 2.0 and 3.0 x CEC the quantity of material desorbed under the lower temperature maximum was increased. When washed with 10ml i-PrOH this was returned to the 1.0 x CEC level.

The broad maxima at approximately 600 °C (which ranged from 525-675 °C), represented the dehydroxylation of the clay and the loss of surface carbon. As the length of the alkyl chain increased the weight loss attributed to this region was successively reduced from 3.4 wt% at $C_n = 8$ to 2.5 wt% at $C_n = 16$.

C_n	8	→	12	14	16
Total % wt loss	15.7	→	18.2	19.1	19.5

Table 3.23   **Comparison of total percentage weight losses for different alkyl chain lengths (C_n) exchanged onto MCBP.**

iii)   **RT-TG-MS - SWa-1-C_nNH_3**

    a.   **Water [m/z = 18] and CO_2 [m/z = 44]**

Water [m/z = 18] was shown to be released between 35-800 °C. At $C_n = 8$ a significant maximum at approximately 340 °C was shown, but the signal intensity decreased rapidly with increased alkyl chain length indicating lower overall concentrations. The most significant decrease in the loss of water was between 150 and 500 °C. CO_2 [m/z = 44] was shown to be released at lower intensities overall as the alkyl chain length increased. This was most significant in the region from which alkyl fragments were desorbed.

    b.   **Aliphatic Hydrocarbons**

TG-MS results showed that alkyl fragments [m/z = 43, 57, 71, 85] and alkenyls [m/z = 41, 55, 69, 83] were desorbed over the same temperature range, but showed slightly higher peak maxima with increasing alkyl chain length

(table 3.24). The majority of aliphatic fragments desorbed by MCBP samples were evolved at slightly higher temperatures than the aliphatic fragments desorbed from SWa-1 and the intensity of the signals was 10 times stronger.

C_n	Desorption Temp. Range (°C)	Alkyl Maxima (°C)	Alkenyl Maxima (°C)
8	250-500	405	400
12	250-500	412	408
16	250-500	415	410

Table 3.24   Comparison of desorption characteristics with increasing alkyl chain length for MCBP-C_n.

c.   **Ring Compounds**

A large number of ring compounds were thermally desorbed from the different MCBP-C_nN(CH$_3$)$_3$ samples. To summarise the pattern of ring compound desorption, the temperature ranges and maxima temperatures are shown in table 3.25 and the relative intensities of these maxima are shown in table 3.26.

m/z	Thermal Desorption Maxima (°C)		
	C_8	C_{12}	C_{16}
81	405	410	260/415
79	405	410	260/415
82	320/405	320/410	260/415
77	350/405	410	260/410
78	320/405	250/320/410	260/310/415
91	350/405	340/410	260/415
95	350/405	410	260/415

Table 3.25   Comparison of the thermal desorption maxima temperatures with increasing alkyl chain length for MCBP-C_n. (results in order of decreasing relative MS intensity relative to SAz-1).

	MS Intensity / 10^6 cps		
m/z	C_8	C_{12}	C_{16}
81	0.7	0.9	0.5
79	0.4	0.5	0.3
82	0.4	0.7	0.3
77	0.3	0.4	0.3
78	0.2	0.3	0.2
91	0.2	0.3	0.2
95	0.3	0.4	0.3

Table 3.26   **Comparison of the relative intensities of the major ring compound thermal desorption maxima with increasing alkyl chain length for MCBP-C_n. (in order of decreasing relative MS intensity to SAz-1).**

3.6   Discussion - Thermal Stability of Organoclays

3.6.1   X-ray Analysis

XRD analysis of the N-alkylammonium exchanged SAz-1 and SWa-1 series showed that the main difference between the two organo-clays was that SAz-1 reached alkylammonium-gallery saturation at a lower organocation concentration than SWa-1, which attained a maximum d_{001} = 17.8 Å at C_n = 12, whereas SWa-1 did not attain this maximum d-spacing until C_n = 14. The clay with the higher surface-charge density attained a greater d-spacing with shorter alkyl chain lengths because, as with all organoclays, the d-spacing was determined by congestion in the gallery.   These results resemble molecular dynamic simulations conducted by Hackett *et al.* [3-18], however, this data predicted that with surface charge densities $\geq$ 102 mEq/100g the d-spacings for alkyl chain lengths between C_n = 10-16 would be much greater.

When the area to be occupied by the organocation lying flat on the surface was less than the area per unit negative charge on the clay surface, the organocations were adsorbed as a monolayer [3-9]. The incomplete organic saturation of the gallery space by the C_n = 8 alkyl chains prevented the creation of a wholly organophilic environment. As the length of the alkyl chains was increased, they formed a flat bilayer and then became increasingly

167

tilted. These bilayer complexes, for clays with a homologous series of N-alkylammonium cations, showed a regular increase in the spacing per carbon atom [3-9, 3-19].

Alkyl (Cn)	SAz-1-CnNH3 (N-alkylammonium)	SWa-1-CnNH3 (N-alkylammonium)	MCBP-CnN(CH3)3 (N-alkyltrimethylammonium)
8	13.6	13.6	14.4
10	15.5	14.2	-
12	17.8	16.0	16.1
14	17.8	17.8	18.3
16	17.8	17.8	19.3

(Leftmost column, rotated label: d_{001} spacing (Å))

Table 3.27 d_{001} **spacing (Å) for Na-SAz-1, Na-SWa-1 and Na-MCBP organoclays with increasing alkyl chain length (C_n).**

At C_{12} (SAz-1) and C_{14} (SWa-1) the length of the alkyl chains forced a bilayer conformation within their respective gallery spaces creating a completely organophilic environment (table 3.27).

The N-alkyltrimethylammonium exchanged MCBP series showed that the cation exchange process had been successful. These organoclay species showed a distinct increase in gallery spacing (d_{001}) over the N-alkylammonium exchanged species, from 14.4 Å at $C_n = 8$ to 19.3 Å at $C_n = 16$. This is likely to be due to the increased quantity of gallery alkyl species due to the associated methyl groups on the quaternary ammonium cations.

X-ray analysis of the four series of samples showed constant d-spacings for the different organic loadings. At $C_n = 8$ (OTAB) the $d_{001} = 14.35$ Å for organocation loadings of 0.5, 1.0, 2.0 and 3.0 x CEC, indicating that with an increase in the concentration of organocation no further expansion of the gallery occurred. According to correlations between the d_{001} of alkylammonium saturated clays (compiled by Jaynes & Boyd [3-20], fig. 3.30), with an alkyl chain length of C_8, the intercalated organocations had formed a monolayer arrangement between the aluminosilicate layers of the clay. $C_n = 12$ (DTAB) samples

showed a d_{001} = 16.14 Å for all the organocation loadings, correlating to an monolayer/bilayer arrangement with a bias toward a bilayer configuration.
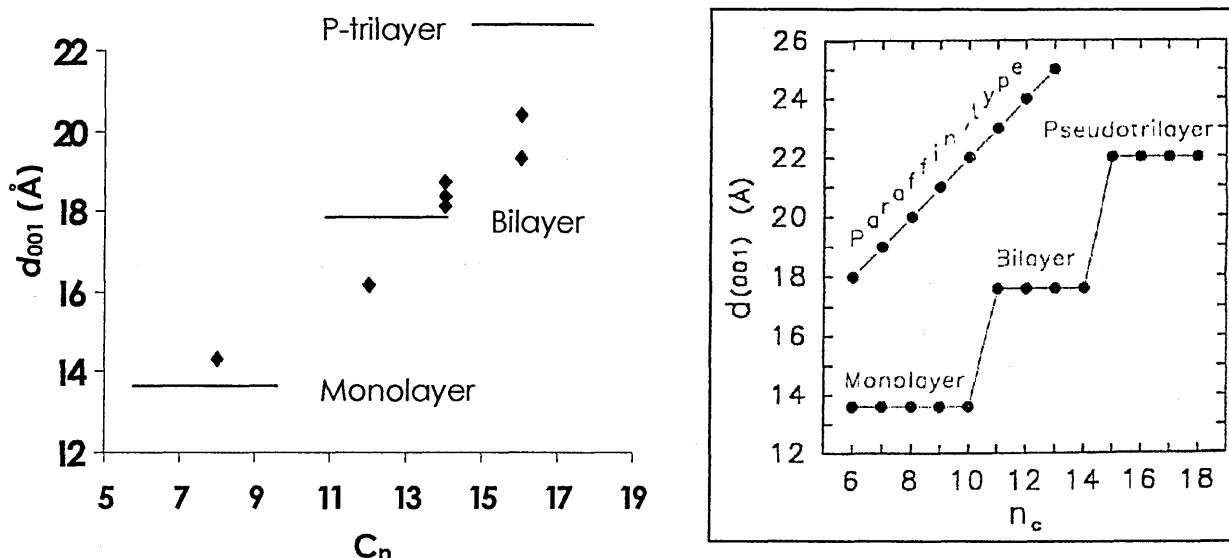
Figure 3.49   Comparison of d_{001}-spacings of the OTAB-CTAB exchanged Na-MCBP in relation to the schematic pattern of Jaynes & Boyd [3-20].

In the C_n = 14 (TTAB), d_{001} spacings of 18.3 Å at 1.0 x CEC, 18.7 Å at 2.0 x CEC and 18.6 Å at 3.0 x CEC were shown. The slight variation in d_{001} values was deemed insignificant and was attributed to accompanying water residing in the interlayer. For an average d_{001} of 18.5 Å and an alkylammonium chain length of C_{14} the gallery organocations were definitely arranged as a bilayer.

C_n = 16 (CTAB) showed d_{001} spacings of 19.3 Å at 1.0 x CEC, 20.4 Å at 2.0 x CEC and 20.4 Å at 3.0 x CEC. When the 2.0 and 3.0 x CEC samples were washed with i-PrOH the increased d-spacings were reduced from 20.4 to 19.2 Å which closely matched the d_{001} of the more strongly attracted 1.0 x CEC concentration. The reduction in d_{001} was due to the removal of loosely bound matter. A d_{001} = 19.2 - 19.3 Å indicated that the organocations were arranged in a bilayer / pseudotrilayer configuration or as a significantly hydrated bilayer. The configurations that the four series of alkyltrimethylammonium cations adopted did not

present any unexpected patterns and adhered well to that described by Jaynes & Boyd [3-20] (fig. 3.49).

Vaia *et al.* [3-21] believed these idealised structures to be too rigid. Using FTIR, they showed that the alkyl chains within organoclays vary from liquid-like to solid-like structures, with the liquid-like structure dominating as the interlayer density or chain length decreased, or as the temperature increased. This was attributed to the small energy differences between the trans and gauche conformers of the alkyl chain; the idealised models described in [3-20] assume an all-trans conformation. Also, for longer chain length surfactants, the surfactants in the layered silicate showed thermal transitions akin to melting or liquid-crystalline to liquid-like transitions upon heating. The fluidity of the alkyl chains, as described in Vaia *et al.*'s model, may account for the shortfall in expected *d*-spacings in the different samples (according to Boyd's diagram) and adds weight to the reasons why the alkyltrimethylammonium exchanged clays showed larger *d*-spacings.

Factors other than the length of the surfactant alkyl chain which would affect the cationic exchange of these clay species would be:

A.   *Charge density* at the surface of the different clay species would play a significant role; this is measured using alkylammonium ion exchange:

surface charge density / surface area per unit dry weight clay = CEC = mEq/100g

(N.b. 1 mEq = 1×10^{-3} g)

Clay species	CEC (mEq/100g)
SAz-1	120
SWa-1	102
MCBP	80

Table 3.28   Exchange clay species and relative cation exchange capacities (CEC).

The decrease in charge density is most probably the reason why SWa-1 does not go to a bilayer conformation until $C_n = 14$ (table 3.28).

However, the uptake and greater d_{001} shown by alkyltrimethylammonium exchanged cations on MCBP with a significantly lower CEC (80 mEq/100g) shows that other factors need to be addressed (see further work).

B.   *Grain size of the clay* would determine, the total surface area accessible to moisture within a mass of clay (Barshad [3-22]). The total surface area, and so the swelling potential, increases as the grain size decreases. Although the different clays were sieved to ensure a grain size of less than 200 μm, variations in the size of particles below this threshold were not controlled. Therefore, if the MCBP had a considerable concentration of particles below this grain size threshold, the surface area of these exchangeable clays would be greater. This would lead to a decrease in the number of gallery exchange sites and an increase in the number of edge sites. This may result in larger d_{001} spacings due to increased competition for gallery exchange sites.

3.6.2   Thermo-Gravimetric Analysis

The TGA of *N*-alkylammonium exchanged SAz-1 and SWa-1 both showed a shift to a higher thermal desorption maximum with increased alkylammonium chain length (see fig. 3.3 and 3.17). The degradation onset temperatures for SAz-1 and SWa-1 samples started below 200 °C and increased with increasing chain length to approximately 200 °C. The SWa-1 series showed greater weight loss < 300 °C than the SAz-1 series, and the major loss under a maximum for 390 °C at $C_n = 6$ gradually shifted to 400 °C at $C_n = 16$. The weight loss within this temperature range for SAz-1 became much more prominent, but as the major weight loss shifted towards the higher temperature peak, the maximum temperature decreased slightly from 390 °C at $C_n = 6$ to 370 °C at $C_n = 16$. SWa-1 was also shown to be evolving increasingly larger amounts of species at higher temperatures (> 400 °C). The thermal

desorption profiles of these two series of samples appeared to be very different, but a reasonable generalisation of the thermal events occurring underneath, was that with increased alkyl chain length, there was a shift towards greater weight loss at higher temperatures.

The TGA of the $C_n = 8$ (OTAB) - $C_n = 16$ (CTAB) samples showed that the majority of weight loss from alkyltrimethylammonium cations was much more thermally stable when intercalated than the N-alkylammonium cations (see fig. 3.29-3.36). These results also provided evidence for alkyl chain 'cracking' due to the catalytic activity of the acid sites on the clay surface. For example, this would explain why when $C_n = 12$ (DTAB) was analysed by TGA in its virgin state it decomposed giving a sharp maximum at 260 °C, but when it was intercalated in MCBP, it was desorbed under a series of different maxima (E.g. 225, 300, 355, 400 and 450 °C). The longer alkyl chains were believed to be releasing larger alkyl species under the weight loss at approximately 425 °C. These larger organocations may have been bulky enough to protrude out of the galleries, and so, may have easily been removed from the surface and the edges of the galleries.

The TGA and DTG traces for $C_n = 8$ (OTAB) - $C_n = 16$ (CTAB) showed that as the alkyl chain length increased the concentration of species evolved between 200 and 300 °C increased relative to the main desorption at ~425 °C. By exchanging the different organocations at 0.5, 1.0, 2.0 and 3.0 x CEC it was possible to determine whether the gallery was fully occupied by the relative organocation. These samples showed evidence that the clay galleries were fully occupied at 1.0 x CEC (i.e. at $\geq C_n = 12$). The addition of higher loadings of organocation at $C_n = 14$ (DTAB) and more evidently at $C_n = 16$ (CTAB) was thought to be the result of undissociated surfactant (i.e. $Me_3N^+RBr^-$) slightly swelling the organically saturated galleries with loosely associated matter. This swelling effect was reversed when the 2.0 x and 3.0 x CEC CTAB samples were washed with i-PrOH. The i-PrOH readily dissolved excess organocation content, and so, reduced the amount of species desorbed

at lower temperatures, the TGA and DTG traces of the *i*-PrOH washed samples being similar to the traces obtained for the 1.0 x CEC CTAB sample.

The Cahn TGA/DTG data obtained from the synergy system reflected and reinforced the data obtained from the Mettler TGA.

3.6.3 Thermogravimetry-Mass Spectrometry (TG-MS)

The decomposition temperature of organoclays controls the upper processing temperature and subsequent thermal stability of polymer-clay nanocomposite materials. A sound knowledge of the decomposition pathway is important because desorption products evolved at lower temperatures in an organoclay's thermal desorption profile may have a role in the thermal decomposition of the hybrid material.

The thermal decomposition of the different organoclay series may be briefly summarised in three distinct regions: (region I) < 150 °C, the evolution of adsorbed water, (region II) 150-500 °C, the desorption of organic species, (region III) 500-800 °C, dehydroxylation of the aluminosilicate layer and the evolution of products associated with residual organic carbonaceous residue.

3.6.3.1 TG-MS Study of Physisorbed and Interlayer Water [m/z = 18] Desorbed From SAz-1-C_nNH_3, SWa-1-C_nNH_3 & MCBP-$C_nN(CH_3)_3$ - (Region I)

Water desorption from the large internal surfaces of the pristine clays corresponded to previous reports [3-23, 3-24]. The general trends were, a high initial weight loss from 25 °C with a thermal desorption maximum at approximately 65 °C, from where weight loss due to water decreased rapidly until a small weight loss at approximately 300 °C. These different rates of thermal desorption have been attributed to weakly bound, physisorbed and free water pockets within the structure being desorbed at the lower temperatures (i.e. < 150 °C). Whilst water desorbed at higher temperatures (i.e. > 150 °C → ≤ 450 °C) was attributed

to water residing within the clay galleries and any associated with the cationic head groups of the intercalated surfactants [3-25].

The SAz-1-C_nNH_3 series of organoclays showed a high signal intensity for water [m/z = 18] for C_n = 8, across the temperature range 25-800 °C, which was saturated at temperatures < 500 °C (fig. 3.6). As the alkyl chain length was increased the relative intensity of the signal appeared to decrease and the regions of water desorption became more resolved. The SWa-1-C_nNH_3 series gave a lower signal intensity for C_n = 8, which was the result of the lower surface-charge density of the clay (fig. 3.19). The wholly organophillic environment had less water associated with organocations than the SAz-1-C_nNH_3 series. As the length of the alkyl chain was increased to C_n = 12 and then 16, relative weight losses could be seen to substantially decrease at temperatures > 150 °C.

The MCBP- $C_nN(CH_3)_3$ series gave a MS signal profile at C_n = 8, that was similar to that described above (fig. 3.38). As the alkyl chain length was increased the relative intensity of the water signal decreased and the signal intensity associated with water residing in the gallery fluctuated, but generally shifted towards a maximum at 280 °C. The alkyltrimethylammonium cations would have been relatively bulky compared to the alkylammonium cations. However, water which was H-bonded to methyl groups would have been less likely than that associated with alkylammonium cations. As a result of water being loosely attracted to the alkyltrimethylammonium head group and the lower surface charge density of MCBP, any gallery hydration would have been less physically hindered towards desorption, as shown in fig. 3.38 with increasing alkyl chain length.

3.6.3.2   TG-MS study of the aliphatic species and ring compounds desorbed from SAz-1-C_nNH_3, SWa-1-C_nNH_3 & MCBP-$C_nN(CH_3)_3$ - (Region II).

The decomposition products of the different organoclays were seen to be a mixture of aliphatic and aromatic species, as in [3-25, 3-26]. The SAz-1-C_nNH_3 series showed aliphatic

hydrocarbon species being evolved under a maximum at 344 °C for C_n = 8, which shifted to 377 °C for C_n = 16 (fig. 3.8). The accompanying ring compounds were desorbed at similar temperatures to the different alkyl chain lengths, but over a slightly narrower temperature range (fig. 3.9 - 3.14).

The different SWa-1 organocation fragments were shown to be evolved at a lower intensity than in the SAz-1 samples, but at a much higher desorption temperature. The C_n = 8 aliphatic species were all desorbed at a maximum of 400 °C with a lower temperature shoulder at approximately 360 °C, shifting to a single broad maxima for alkanes at 425 °C and alkenes at 435 °C when C_n = 16 (fig. 3.21 and fig. 3.50.iii). The C_n = 8 ring compounds were desorbed at a maximum at 345 °C and a higher temperature shoulder at 400 °C. This signal maximum shifted to higher temperatures with increased alkyl chain length, until most of the aromatic species were desorbed under a maximum at 435 °C. However, there were exceptions to this thermal desorption shift, for C_n = 16, benzene [m/z = 78] evolved at two distinct maxima at 338 and 445 °C, whereas methylcyclohexene [m/z = 77] and toluene [m/z = 91 / 92] showed evidence of competing desorption mechanisms (fig. 3.27 and fig. 3.50.iv).

The MCBP samples exchanged with C_n = 8 (OTAB) showed that aliphatic species were desorbed at a maximum of 405 °C and a lower temperature/intensity shoulder at approximately 350 °C (fig. 3.51.iii). As the alkyl chain length increased the higher temperature maximum shifted to increased temperatures, until at C_n = 16 (CTAB) the maximum was at approximately 415 °C. Moreover, the lower temperature maximum at 350 °C, increased in intensity with respect to the desorption of alkenes, and decreased with respect to the desorption of alkanes.

The ring compounds desorbed from C_n = 8 (OTAB) (fig. 3.51.iv) at approximately 400 °C with a bias towards a lower temperature shoulder, only partially revealed in cyclohexene [m/z =

Figure 3.50   Comparison of SAz-1 and SWa-1 (C$_8$ & C$_{16}$) selected desorbed aliphatic and aromatic species.

i. SAz-1: Alkanes (E.g. [m/z = 71]) / Alkenes (E.g. [m/z = 69])

ii. SAz-1: Aromatics (E.g. [m/z = 78, 95 & 96])

iii. SWa-1: Alkane (E.g. [m/z = 71]) / Alkene (E.g. [m/z = 69])
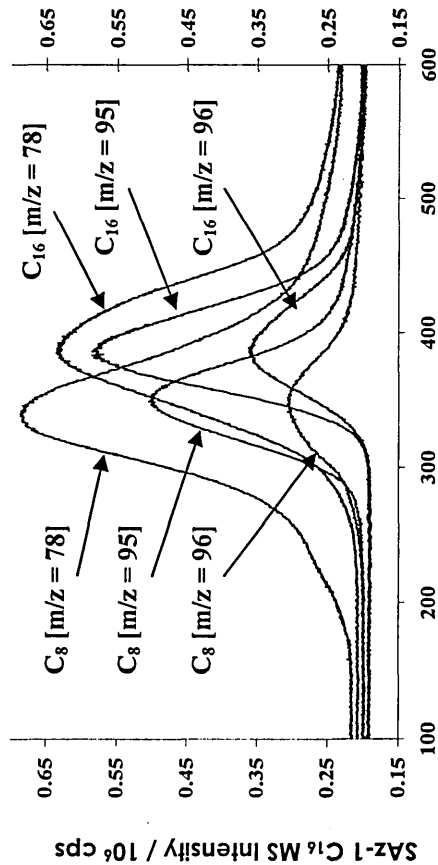
iv. SWa-1: Aromatics (E.g. [m/z = 78, 95 & 96])

176
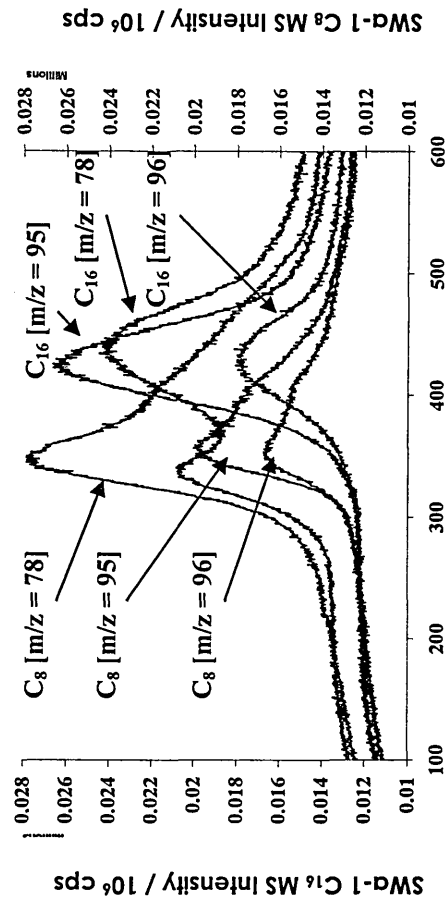
Figure 3.51   Comparison of SWa-1 and MCBP (C$_8$ and C$_{16}$) selected desorbed aliphatic and aromatic species.

i. SWa-1: Alkanes (E.g. [m/z = 71]) / Alkenes (E.g. [m/z = 69])

ii. SWa-1: Aromatics (E.g. [m/z = 78, 95 & 96])
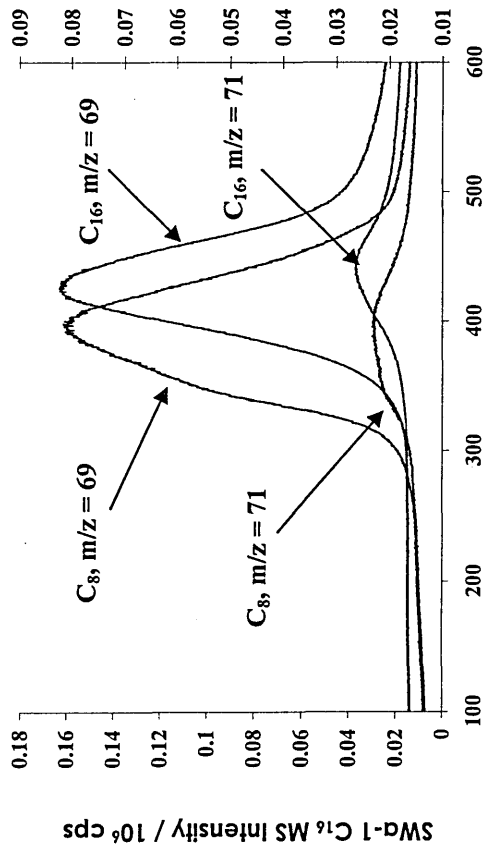
iii. MCBP: Alkanes (E.g. [m/z = 71]) / Alkenes (E.g. [m/z = 69])
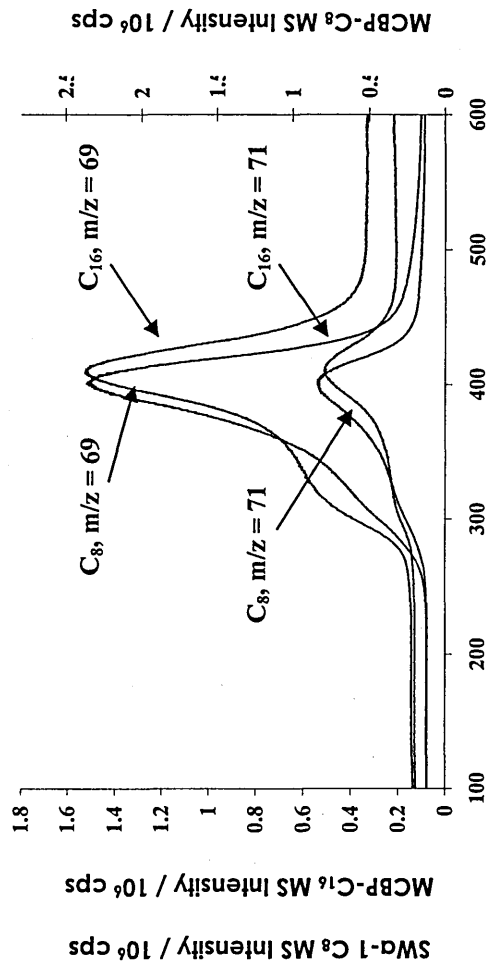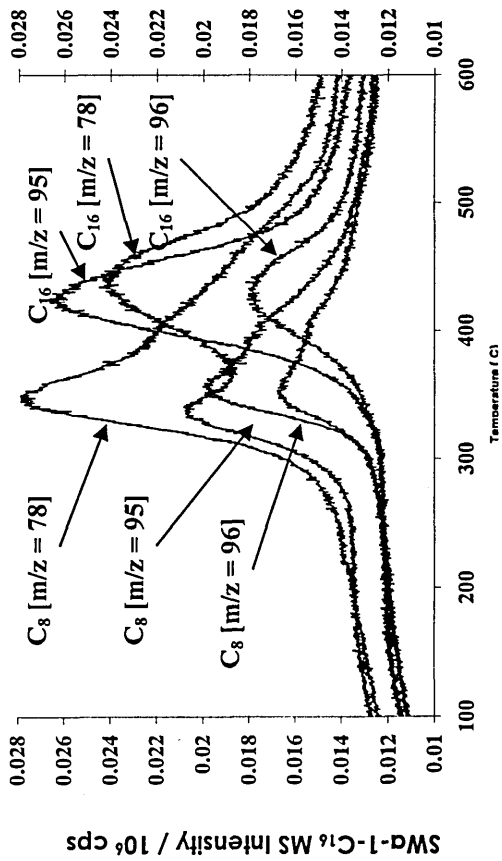
iv. MCBP: Aromatics (E.g. [m/z = 78, 95 & 96])

177
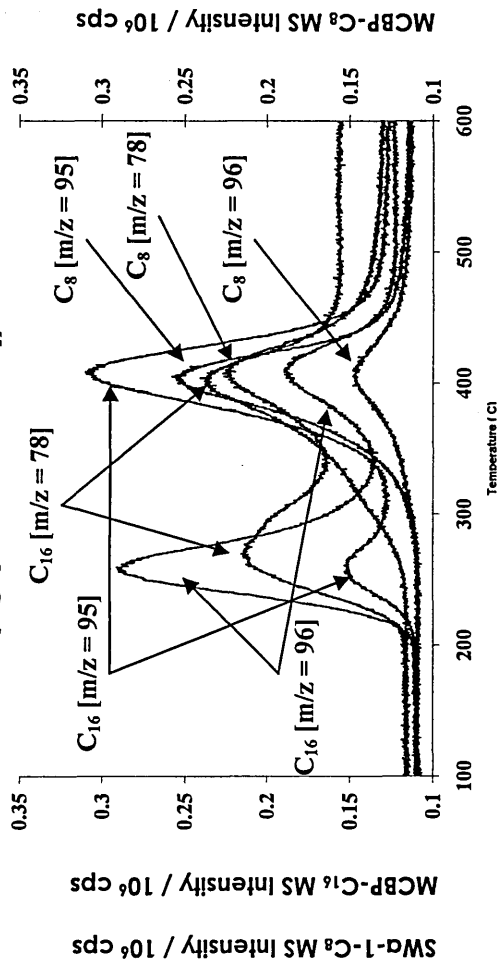
82], benzene [m/z = 78] and toluene [m/z = 91 / 92] at 320 °C. As the alkyl chain length of the organocation increased the unresolved maximum at 320 °C diminished whilst the development of a lower temperature maximum (250-275 °C) was seen to increase for all the different samples, most notable was the higher intensity of the methylcyclohexene [m/z = 96] signal and the broader, desorption of benzene [m/z = 78] signal at lower temperatures of equal intensity to the higher temperature desorption (fig. 3.51.iv).

This trend was shown through conventional TGA and TG-MS, suggesting that a large proportion of the species evolved at higher temperatures were aliphatic fragments and ring compounds. But as the organic content of the gallery space was increased (as is required in a nanocomposite precursor) weakly bound material was easily expelled and increasingly catalytically transformed into aromatic species at lower temperatures.

A comparison of the TG-MS results for the SAz-1, SWa-1 and MCBP organoclay series indicated that the decomposition products were similar.

In an attempt to resolve the amine and carbonyl (predominantly aldehyde) species which have been previously reported by Xie *et al.* [3-25 - 3-27], TD-GC-MS was conducted on the C_n = 16 (CTAB) - 1 x CEC samples. Selected species from the results of these analyses are shown in table 3.29, indicating some of the species that were anticipated but not resolved in the TG-MS.

Temperature range: 200 - 500 °C			
	Species	Formula	M.W.
CTAB (1 x CEC)	1,3-pentadiene, (E)-	C_5H_8	68
	cyclopentene	C_5H_8	68
	2-propenal, 2-methyl-	C_4H_6O	70
	2-butene, 2-methyl-	C_5H_{10}	70
			Continued over...

cyclopropane, 1,1-dimethyl-	C_5H_{10}	70
benzene	C_6H_6	78
1,3-hexadien-5-yne	C_6H_6	78
1H-pyrrole, 3-methyl-	C_5H_7N	81
1,5-hexadiene	C_6H_{10}	82
toluene	C_7H_8	92
cyclohexanone	$C_6H_{10}O$	98
benzene, 1,3-dimethyl-	C_8H_{10}	106
1-octene	C_8H_{16}	112
1-propene, 3-bromo	C_3H_5Br	120
benzene, 1,3,5-trimethyl-	C_9H_{12}	120
nonane	C_9H_{20}	128

Table 3.29 **Selection of the organic species identified by TD-GC-MS, desorbed in the 200-500 °C temperature range.**

These results showed that the carbonyl species and complex aromatic and ring compounds previously reported were present in the minority. Amines were not shown in the TD-GC-MS results, but there was evidence of nitrogen complexes (i.e. 1H-pyrrole, 3-methyl-).

3.6.3.3 TG-MS Study of Aluminosilicate Dehydroxylation (i.e. Water [m/z = 18]) and the Desorption of Carbonaceous Residue (i.e. CO_2 [m/z = 44]) from SAz-1-C_nNH_3, SWa-1-C_nNH_3 & MCBP-$C_nN(CH_3)_3$ - (Region III)

The different organoclay series all showed that the signal intensity for water [m/z = 18] decreased steadily at temperatures > 500 °C and decreased in intensity with increased alkyl chain length. Whereas, the signal intensities for CO_2 [m/z = 44] desorption were shown to shift to higher temperatures and increase in intensity with increased alkyl chain length.

The XRD, TGA and TG-MS results showed differences for the different aluminosilicate hosts, alkyl chain lengths and surfactant types.   TG-MS analysis showed that the major decomposition products were a mixture of alkanes, alkenes and ring compounds and showed that different thermal desorption mechanisms occurred on the different organoclay species.

3.6.4.1   TG Analysis

The TGA data for the SAz-1-C_nNH_3 series showed that as the length of the alkyl chain increased, weight loss at higher temperatures was increased. This shift of the desorption products was mirrored by the TG-MS data which showed alkanes, alkenes and aromatic species being desorbed at successively higher temperatures.   Although there was increased weight loss at higher temperatures, the T_{max} shifted from 390 °C at C_n = 6 to 370 °C at C_n = 16 (fig. 3.3). This was shown by the TG-MS data to be due to the alkanes and alkenes being desorbed at slightly lower temperatures than the aromatic species, but having a much higher relative intensity (especially the shorter chain fragments, i.e. [m/z = 41, 55]). Also, as the length of the alkyl chain was increased the intensity of the signal from water [m/z = 18] decreased at higher temperatures, whilst the intensity of the signal from CO_2 [m/z = 44] was increased. These showed that whilst water was becoming less of a contributory factor to the weight loss in the region > 370 °C, CO_2 concentrations were becoming more prominent.

The TGA data for the SWa-1-C_nNH_3 series showed that as alkyl chain length increased the weight loss was again shifted to successively higher temperatures, with the majority of thermal desorption products residing above and below the T_{max} = 390 °C. The desorption temperature of alkyl and alkenyl species was shown to increase until at C_n = 16, the alkyl T_{max} = 425 °C and the alkenyl T_{max} = 435 °C. The aromatic species showed a shift from the

major desorption products being evolved at a lower t_{max} at $C_n = 8$ (approximately 350 °C), to higher temperature maxima at $C_n = 16$ within the temperature range 420-445 °C. In most cases, the relative intensity of the aromatics was greater than the aliphatic species. The relatively constant weight loss under the lower temperature maximum shown in the TGA at 310 °C would have been due to release of water from the interlayer, with possible contributions from increased CO_2 and the lower temperature maximum from benzene [m/z = 78]. The maximum at 405 °C would have been due to the additive effect of high intensity/concentrations of water, CO_2, aliphatic and aromatic species. The staggered desorption of these species being shown as much higher weight loss up to 500 °C in the C_n = 16 samples.

TGA analysis of the MCBP-$C_nN(CH_3)_3$ organoclay series showed that at $C_n = 8$ the onset of organocation decomposition occurred at approximately 230 °C, followed by two unresolved thermal events at 325 °C and 370 °C and the major weight loss at a maximum of 425 °C. As the alkyl chain length was increased, a shift to greater concentrations of decomposition products at lower temperatures was shown. At $C_n = 16$, the onset of decomposition had shifted down to approximately 150 °C and prominent thermal desorption maxima were shown at 280 and 425 °C respectively, accounting for 7 and 9 wt% loss of the 19 wt% overall loss.

Many studies have been conducted on the thermal desorption of organic species from clays. The earliest work conducted on alkylammonium ions in zeolites was conducted by Fripiat. Yariv et al. [3-28 – 3-32] have previously studied the thermal desorption large number of dye complexes adsorbed on clays, but the results are not of particular relevance to this thesis.

Yariv et al., conducted a study of the thermal stability of sepiolite and palygorskite exchanged with butylamine under air and N_2, Sepiolite DTG T_{max} at 300 °C (broad diffuse

maximum 275 to 310 °C). Palygorskite DTG T_{max} at 280 and 390 °C [3-32]. The temperature of the principle exothermic peak was lower for sepiolite than for palygorskite. The fact that the peak temperatures are dependent on the mineral type may serve as evidence for the existence of interactions between butylamine and the clays.

TG and DTA curves showed that the amounts of zeolitic and bound water become very small due to the penetration of the amine into the pores as a result of the adsorption of the organic molecules by both clays. Adsorbed butylamine molecules were held by the clays up to temperatures far above the boiling point of butylamine. In the presence of butylamine, the dehydroxylation of both clays was shifted to higher temperatures compared to the untreated clays, again possibly due to the presence of the organic molecule inside the pores. The penetration of butylamine molecules into the pores requires some flexibility of the silicate planes, and such flexibility in organo-MMTs has previously been reported by Suito *et al.* (1969) using electron microscopy.

In other studies conducted by Xie *et al.* [3-25 – 3-27], analysing the thermal stability of various quaternary ammonium exchanged MMT's. From extrapolation of the published DTG data, a T_{max} at 380 °C and lower temperature maxima at 210 and 300 °C were shown for cocotrimethyl ammonium surfactants (n.b. Coco, composed of a variety of alkyl chain lengths ranging C_n = 8-18, approximately 50% C_n = 12). As the concentration of longer alkyl chains was increased, shown in tallowtrimethylammonium surfactants (n.b. *Tallow*, alkyl range C_n = 8-18, approximately 50% C_n = 16), the thermal desorption maxima at 210 and 375 °C were of equal intensity, with maxima at 290 and 320 °C indicating that the majority of the weight loss was still occurring at higher temperatures. As the overall alkyl chain length and consistency of the surfactant were increased by the exchange of octadecyltrimethylammonium surfactant, the majority weight loss appeared to have shifted to the T_{max} at 210 °C, which was followed by maxima at 280, 320 and 370 °C. Although not identified within the publication, as the loading of organic species was

increased, the majority weight loss was increasingly desorbed at a lower temperature maximum (i.e. shifting to approximately 200 °C from 400 °C). This trend appears to support the results obtained from the N-alkyltrimethylammonium exchanged-MMT analysed within this thesis.

Suter *et al.* [3-33] used both conventional and high resolution TGA to analyse the thermal decomposition of octadecyltrimethylammonium surfactant from a Na-bentonite host under air. These results showed a marked shift of a low temperature maximum from 210 °C (as had been previously seen under N_2) to approximately 300 °C.

3.6.4.2 TG-MS Analysis

NH_3 was known to be evolved during the decomposition process, but could not be resolved by TG-MS, because the peak for NH_3 ($m/z = 17$) overlapped with that for water. However, IR spectra from a previous study by Xie *et al.* [3-27] showed that the desorption of ammonia occurred across the same temperature range at which other organic fragments were being desorbed (i.e. 200-500 °C).

TG-MS showed that water [$m/z = 18$] shifted from a maximum at approximately 350 °C to a profile which indicated maxima at 280 and 425 °C at $C_n = 16$, although the intensity was greatly reduced. CO_2 [$m/z = 44$] showed a shift towards higher temperature with increased chain length and showed a maximum at 425 °C at $C_n = 16$. Alkenes and to a lesser extent alkanes would have contributed to the increase in the lower temperature maximum. However, the most dramatic shift was shown by most ring compounds (fig. 3.32). A lower temperature was shown to be particularly significant for benzene [$m/z = 78$] and methylcyclohexene [$m/z = 96$]. Benzene [$m/z = 78$] showed two maxima of equal intensity with a broader range of events occurring underneath the lower temperature maximum, whilst methylcyclohexene [$m/z = 96$] was shown to be desorbed at 280 °C in at least three times the intensity as at 425 °C.

Previously, TG-MS analysis on the decomposition products of alkyltrimethylammonium cations, was conducted by Xie *et al.*[3-27]. The organic species were stated as being desorbed between 200 and 500 °C and were only identified as being the products of decomposition, i.e. water, CO_2, $NCH_2(CH_3)_2$, alkenes and alkanes. There was no indication of any catalytic reforming reactions which are thought to have resulted in the branched, cyclic and aromatic species identified in this thesis.

Also, a comparison may be drawn between the results in this thesis and the results reported by Taylor [3-34] regarding the catalytic transformation of polymer waste. In his work, a gas stream resulting from the pyrolysis of high density polyethylene (HDPE) was activated by various clay species. The result was a high yield conversion, through DHC of the polyolefinic plastic, to various transalkylated aromatic compounds, principally trimethylbenzene.

3.6.4.3 The Effect of Increased Iron Content in Clays

Oxide	SAz-1	SWa-1	MCBP
SiO_2	67.72	43.75	70.80
Al_2O_3	19.74	7.95	19.04
MgO	7.24	1.75	2.38
Fe_2O_3	1.59	25.25	4.19
TiO_2	0.27	0.54	0.10
CaO	3.16	2.05	0.88
Na_2O	0.07	0	2.37
K_2O	0.21	0.03	0.14

Table 3.30   XRF data showing the elemental composition of the natural clays and the exchanged form (Na-MCBP). Only the major oxides are shown and values are given as wt%.

As the alkyl chain length of the SAz-1 and SWa-1 series increased, the relative concentration of desorption products at higher temperatures was shown to be increased. With approximately 36% of desorption products being from SAz-1-C_{16} after 380 °C

compared with 43% desorbed from SWa-1-C_{16}. It was thought that this shift of thermal desorption products to higher temperatures was the result of the greater concentration of structural iron (i.e. Fe^{3+}) in the octahedral sheet of SWa-1 (table 3.30).

It is currently thought the structural iron acts as a radical trap, which significantly reduces the catalytic activity of the clay's acid sites until higher temperatures. Zhu *et al.* [3-35] reported that clays containing structural iron exhibit enhanced thermal stability when measured by TGA and identified the structural iron site as being the operative site for radical trapping within the clay.

3.7   Conclusions

The results of this study have lead to a number of important findings:

The release of organic compounds from the decomposition of alkyl chains with increasing lengths was shown to occur in stages. These stages appeared to be related to the increasing length of the alkyl chain in the clay gallery. For *n*-alkylammonium cations these stages were shown to increase in number and shift to higher temperatures as C_n increased. Whilst for *N*-alkyltrimethylammonium cations, the increasing number of stages was shown to shift to increase the concentration of compounds desorbed at temperatures between 200 and 300 °C.

The desorption of organic compounds at higher temperatures in the iron containing SWa-1 organoclays may be evidence of a radical trapping mechanism, which has been reported as offering a possible additive advantage in flame retardant polymers.

A large number aromatic species were shown to be desorbed at lower temperatures from the C_n = 16 (CTAB) organoclays, which could have structural implications for the production of polymer-clay nanocomposites (particularly by melt processing).

Chapter 3 - References

[3-1]   Lagaly, G., Clay-organic reactions, interactions, *Phil. Trans. R. Soc.*, London, 1984, A-311. 315.

[3-2]   Cowan, C.T. & White, D., *Trans. Faraday Soc.*, 1958, **54**, 691.

[3-3]   Theng, B.K.G., Greenland, D.J. & Quirk, J.P., *Clay Miner.*, 1967, **7**, 1.

[3-4]   Jones, T.R., The properties and uses of clays which swell in organic solvents. *Clay Miner.*, 1983, **18**, 399.

[3-5]   Lagaly, G. and Weiss, A., *Determination of the layer charge in mica type silicates*, 61-80 in: *Proc. Int. Clay Conf.*, Tokyo (Heller, L., ed.) Isreal Univ. Press, 1, 1969.

[3-6]   Lagaly, G., *Layer charge determination by alkylammonium ions.* 1-46 in: Layer charge characteristics of 2:1 silicate clay minerals. (Mermut, A.R., ed.) Clay Minerals Society Workshop Lectures 6, Boulder, CO, USA, 1994.

[3-7]   Maes, A., Stul, M.S. & Cremers, A., *Clays Clay Miner.*, 1979, **27**, 387.

[3-8]   Malla, P.B. & Lowell, A.D., *Soil Sci. Soc. Am. J.*, 1987, **51**, 1362.

[3-9]   Jordan, J.W., *Jour. Phys. Colloid Chem.*, 1949, **53**, 294.

[3-10]   Street, G.B. & White, D., *J. Appl. Chem.*, 1963, 288.

[3-11]   Slabough, W.H. & Hanson, D.B., *J. Coll. & Int. Sci.*, 1969, **29**: 3, 460.

[3-12]   Boyd, S.A., Jaynes, W.F. & Ross, B.S., *Immobilisation of organic contaminants by organoclays: application to soil restoration and hazardous waste contaminants.* In: Baker, R.A. (ed.), *Organic substances and sediments in waters*, 1. Chelsea, MI: Lewis, 1991, 181-200, 2619.

[3-13]   Brixie, J.M. & Boyd, S.A., *J. Environ. Qual.*, 1994, **23**, 1283.

[3-14]   Qutubuddin, S., Fu, X. & Tajuddin, Y., *Polymer Bulletin*, 2002, **48** (2), 143.

[3-15]   Weichert, M.W., Chen, H., Giannelis, E.P. & Sogah, D.Y., *J. Am. Chem. Soc.*, 1999, **121**, 1615.

[3-16]   Theng B.K.G., *Formation and Properties of Clay-Polymer Complexes*, Elsevier Science, 1979.

[3-17]   Komadel, P., Janek, M. and Lagaly, G., *Clay Minerals* 32, 623-632, 1997.

[3-18]   Hackett, E., Manias, E. & Giannelis, E.P., *J. Chem. Phys.*, 1998, **108**, 7410.

[3-19]   Walker, G.F., *Clay Miner.*, 1969, **7**, 129.

[3-20]   Jaynes, W.F. & Boyd, S.A., *Soil Sci. Soc. Amer. J.*, 1991, **55**, 43.

[3-21]   Vaia R.A., Teukolsky R.K. & Giannelis E.P., *Chem. Mater.*, 1994, **6**, 1017.

[3-22]   Barshad, I., 1955, Adsorptive and swelling properties of clay-water system, in Pask, J. A., & Turner, M. D. (eds), Clays and clay technology: National Conference on Clays and Clay Technology, 1st, Berkeley, California, July 21-25, 1952, Proceedings, California Division of Mines Bulletin 169, p. 70-77.

[3-23]   Brindely, G.W. & Brown, G., *Crystal Structure of Clay Minerals and their X-ray identification*, Mineralogical Society: London, 1980.

[3-24]   Greene-Kelly, R., The differential thermal investigation of clays, Mineralogical Society: London, 1957.

[3-25]   Xie, W., Gao, Z., Pan, W-P., Hunter, D., Singh, A. & Vaia, R., *Chem. Mater.*, 2001, **13**, 2979.

[3-26]   Xie, W., Gao, Z., Pan, W-P., Hunter, D., Singh, A. & Vaia, R., *Chem. Mater.*, 2002, **14**, 4837.

[3-27]   Xie, W., Gao, Z., Liu, K., Pan, W-P., Vaia, R., Hunter, D. & Singh, A., *Thermochimica Acta*, 2001, 339, 367.

[3-28]   Grauer, Z., Grauer, G., Avnir, D. & Yariv, S., *J. Chem. Soc., Faraday Trans*, 1987, **83**, 1685.

[3-29]   Yariv, S., Kahr, G. & Rub, A., *Thermochemica Acta*, 1988, **135**, 299.

[3-30]   Yariv, S., Muller-Vonmoos, M., Kahr, G., & Rub, A., *Thermochemica Acta*, 1989, **148**, 457.

[3-31]   Shuali, U., Steinberg, M., Yariv, S., Muller-Vonmoos, M., Kahr, G. & Rub, A., *Clay Minerals*, 1990, **25**, 107.

[3-32]   Yariv, S., *J. Therm. Anal.*, 1990, **36**, 1953.

[3-33]   Osman, M.A., Ploetze, M. & Suter, U.W., *J. Mater. Chem.*, 2003, **13**, 2359.

[3-34]   Taylor, S., PhD Thesis, Sheffield Hallam University, September 2002.

[3-35]   Zhu, J., Uhl, F.M., Morgan, A.B. & Wilkie, C.A., *Chem. Mater.*, 2001, **13**, 4649.

4

Thermal Analysis of Polystyrene-Clay Nanocomposites

"The rapidly developing classes of composite and nanostructured materials

will dominate the industrial landscape of future centuries"

4.1 Introduction

Most commercial interest in nanocomposites has focused on thermoplastics. Thermoplastics can be broken into two groups: less expensive commodity resins (e.g. polystyrene, poly (vinyl chloride), polyethylene and many others) and more expensive (and higher performance) engineering resins (e.g. polycarbonate, polyimide). One of the goals of nanocomposites is to allow substitution of more expensive engineering resins with a less expensive commodity resin nanocomposite. The substitution with a nanocomposite resin which shows equivalent performance should yield overall cost savings.

Polymer nanocomposites are a class of materials that have properties with significant commercial potential. A polymer nanocomposite is generally defined as the combination of a polymer matrix resin and inorganic particles that have at least one dimension (i.e., length, width, or thickness) in the nanometre size range. A typical inorganic filler/polymer nanocomposite is the commercial use of silica fillers in rubber and other polymers, although most reports on commercial systems indicate that silica has an agglomerated structure, which has dimensions in the micron range. Several benefits of these nanocomposites have been identified to include [4.1 - 4.3]:

- increased reinforcement and impact strength
- increased thermal stability
- increased flame resistance
- improved gas/liquid barrier properties
- reduced shrinkage and residual stress
- improved abrasion resistance
- altered electronic and optical properties

4.1.1 Polystyrene (PS)

The polymer selected to be the host matrix for the production of polymer-clay nanocomposites is polystyrene (PS). PS already offers the advantages of good dimensional stability, was inexpensive, relatively easy to mould and formed rigid solids, however, it has the disadvantages of brittleness, poor thermal stability and shows relatively poor resistance to chemicals [4-4].

PS is formed by the addition polymerisation of styrene monomers and was first commercially manufactured by BASF in the 1930's. It is a thermoplastic polymer that is currently produced in many different forms. Some examples of these forms, apart from pure cast PS mold and sheet products, are *expanded PS* (EPS) which is its most common use (a mixture of about 5% PS and 95% air), *high impact PS* (HIPS), modified with a rubber additive and as general purpose PS. Consequently, PS is used in a variety of commercial and consumer applications from appliance housing and electronics to medical supplies, with the largest end use being packaging [4.5].
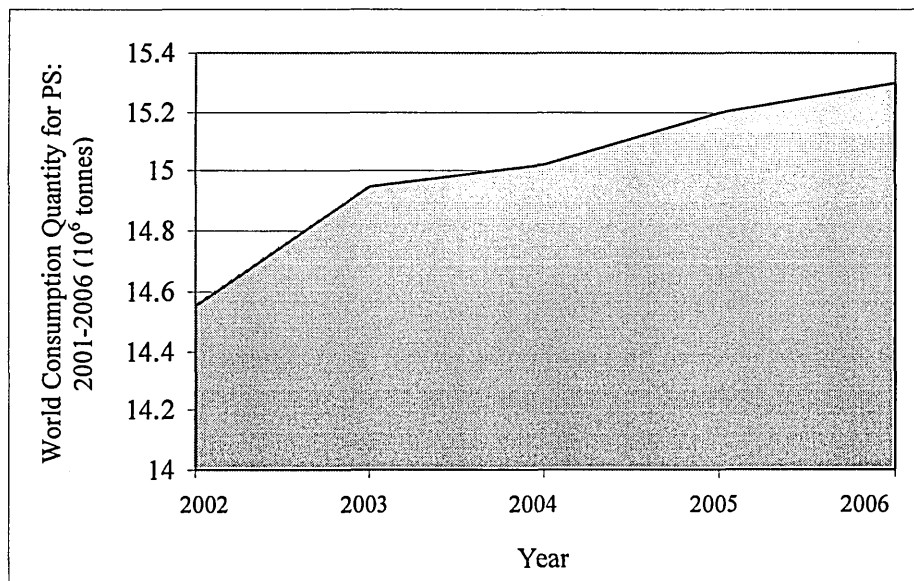
Figure 4.1   Actual and future estimated world PS consumption [4.6].

It has been estimated that the world polystyrene market will grow 5% over the next three years, with world consumption rising to 15.3 million tonnes by 2006. The USA is the largest PS manufacturer (producing over 2.8 million tonnes annually), and the largest PS consumer is Asia (accounting for 40% of total world consumption) [4.6].

These studies incorporated PS in its primary form, the aim being to investigate how the thermal stability of PS was affected by the interaction of a specified range of organoclays.

4.1.2 Polystyrene-Clay Nanocomposites

The intercalation of organoclays by vinylic monomers such as styrene [4.7-4.11], methyl methacrylate [4.12-4.15] and acrylonitrile [4.16, 4.17] followed by free-radical polymerisation have previously been reported.

Several attempts to produce polystyrene-clay nanocomposites have been reported in the literature. Early attempts by Friedlander & Grink [4.18] and Blumstein [4.19] to impregnate clay with styrene monomer followed by polymerisation, showed little or no expansion of the basal spacing of the clay, which led to confusion over the state of the polystyrene within the clay layers. Kato et $al.$ [4.20] reported the intercalation of styrene into stearyltrimethyl-ammonium (C_n = 18) cation exchanged MMT and noted an increase in the basal spacing.

Alternative methods for the inclusion of polymers into the gallery spaces have been reported. The modification of MMT by a variety of functional groups was reported by Kelly et $al.$ [4.21] in their study of epoxy composites, to effectively anchor the polymer chains to the surface. Akelah & Moet [4.22] prepared polystyrene nanocomposites from acetonitrile using Na$^+$ exchanged MMT and a vinylbenzyltrimethylammonium chloride which contained a reactive vinyl group that could take part in the polymerisation. Using this method a maximum basal spacing of 24.5 Å was reported for the hybrid material.

Similarly, Fu & Qutubuddin [4.23] further developed the process of *in-situ* polymerisation by using VDAC (vinylbenzyldimethyldodecylammonium chloride), which again included a vinyl group, to make the organoclay more stable to inclusion in the bulk polymer. Because of the solubility of the VDAC's vinyl group within the styrene monomer, this process lead to the production of an exfoliated PS-clay nanocomposite. This polymer-clay nanocomposite was prepared by dispersing the organoclay in styrene monomer followed by free-radical polymerisation using AIBN at 60 °C/48 hr.

Another process for fabricating PS-clay nanocomposites was developed and reported by Giannelis [4.24] who used polymer melt intercalation. Problems associated with this were similar to those mentioned earlier, i.e. those of organophilic-organophobic interactions, and as such, the diffusion of molten polymer into the interlayers is very slow, depending on factors such as temperature, molecular weight of polymer and organocation-chain length [4.25, 4.26]. A more recent example was a study by Doh & Cho [4.11], who prepared PS-clay intercalated nanocomposites by polymerisation in the presence of organophilic clay. This intercalated polystyrene-clay nanocomposite showed a greater thermal stability than pure polystyrene.

Nanocomposites may also be formulated by using an emulsion polymerisation process, in which the clay would be dispersed in an aqueous solution that contained surfactant, monomer and initiator. In an aqueous environment the interlayer will expand and the presence of surfactant would stabilise the monomer, and so, reduce its hydrophobicity, allowing it to enter the clay galleries more readily. Polymerisation is achieved using a radical initiator and the resulting polymer-clay composite is precipitated using a metal salt of high ionic strength, e.g. Al(III) salts. The resulting latex would then require treatment with organic solvents to extract the included water. Examples of this have been reported using polystyrene and polymethylmethacrylate [4.27, 4.28].

4.2 Free-Radical Polymerisation of Styrene

The free-radical polymerisation of vinylic monomers is initiated by the formation of radical monomer molecules from which the polymer chains grow by the successive addition of monomer molecules. This growth may be terminated when two growing chains collide, producing one or two stable molecules. Growth may also stop when the radical nature of a growing chain is transferred to a monomer molecule.

4.2.1 Kinetic Model of Free-Radical Polymerisation

Styrene monomer readily enters into free radical vinyl polymerisation when in the presence of a strong oxidising agent (e.g. AIBN, 2,2 -azo-bis-isobutyronitrile), see fig. 4.2.
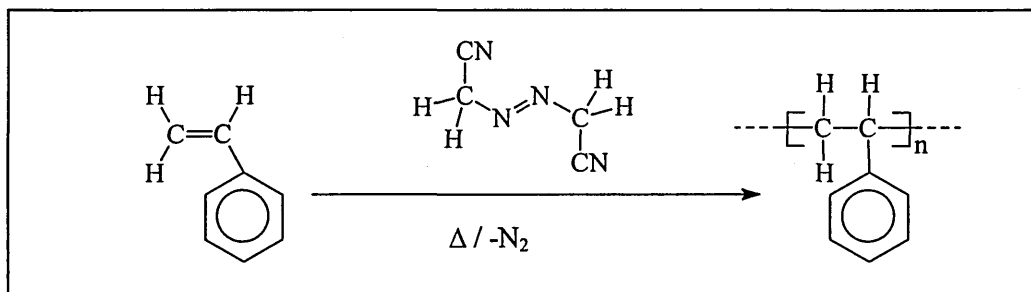
Figure 4.2   General styrene polymerisation equation.

4.2.1.1 Initiation

Step 1: Initiator decomposition kinetics:

$$I \xrightarrow{k_d} 2R\bullet$$

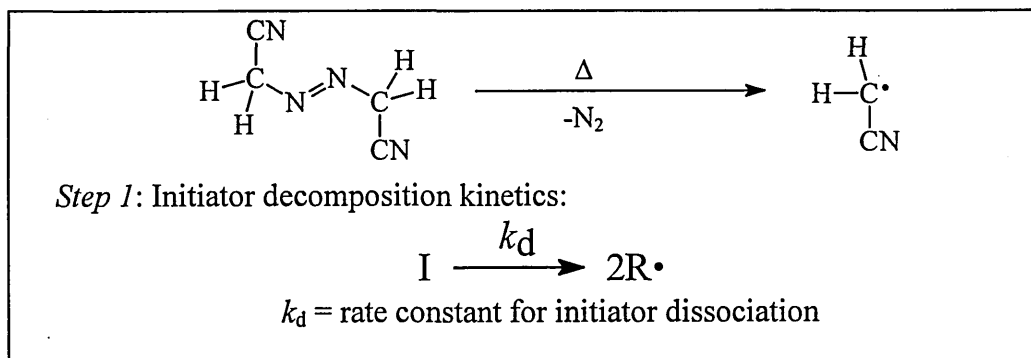k_d = rate constant for initiator dissociation

Figure 4.3   Initiator decomposition (E.g. AIBN).

This step is usually involves two reactions, the first is the production of free radicals (fig. 4.3), which in this case come from the homolytic dissociation of an initiator species (I) to form a pair of radicals (R·).

The second initiation step results from the addition of the initiator radical to the first monomer molecule to produce the chain initiating species M_1 (fig. 4.4).

Step 2: Formation of chain initiating polymer growth:

$$R^\bullet + M_1 \xrightarrow{k_i} M_1^\bullet$$

k_i = rate constant for initiation step
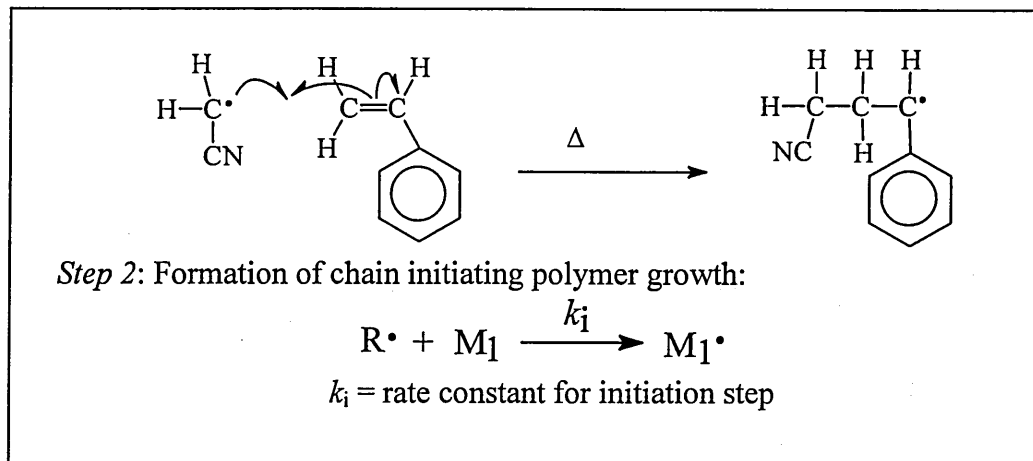
Figure 4.4   **Initiation of polystyrene chain growth through radical formation.**

4.2.1.2   Propagation

As propagation continues and each monomer unit is added (fig. 4.5), the radical has the same identity as the radical before except that it is larger by one unit.

Step 3: Chain propagation kinetics:

$$M_n^\bullet + M \xrightarrow{k_p} M_{n+1}^\bullet$$

k_p = rate constant for propagation step
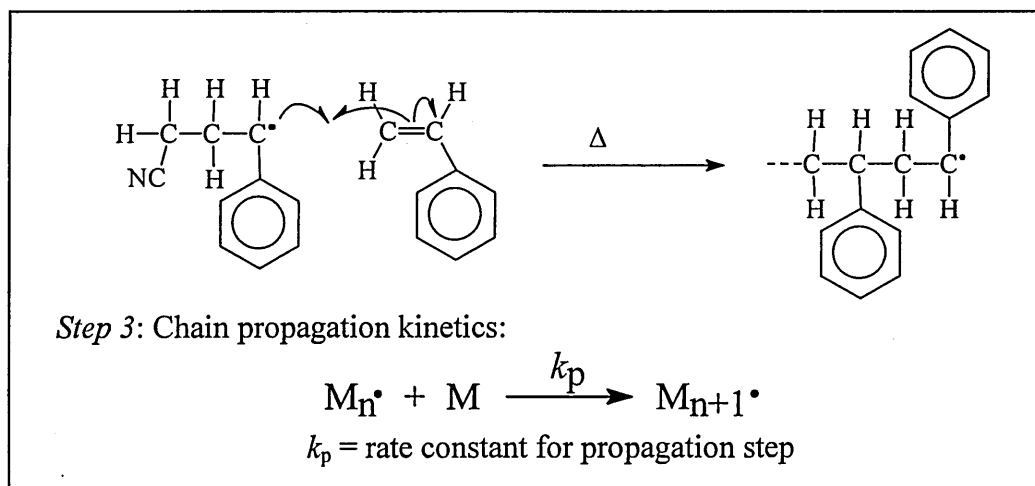
Figure 4.5   **Propagation of polystyrene chain growth.**

The formation of a high molecular weight polymer occurs very rapidly. However, at some point the propagating radicals at the end of the polymer chain stops growing and terminate.

4.2.1.3 Termination

Propagation will terminate as a result of two radicals colliding. This termination reaction may be the outcome of two possible processes (fig. 4.6 and 4.7).

Step 4a: Coupling termination kinetics:

$$M_n^\bullet + M_m^\bullet \xrightarrow{k_{tc}} M_{n+m}$$

k_{tc} = rate constant for coupling termination step
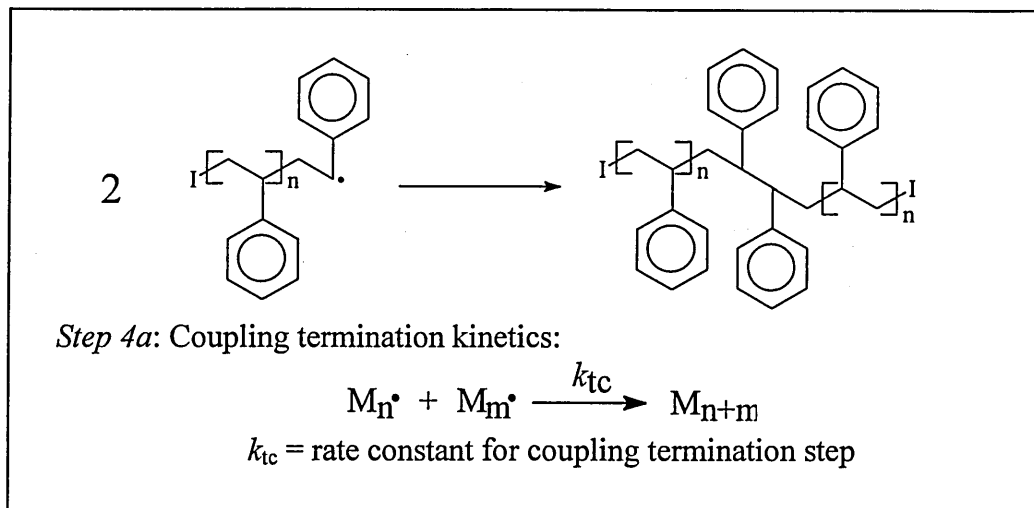
Figure 4.6 *Coupling* **termination process of two propagating polystyrene radical chains.**

Step 4b: Disproportionation termination kinetics:

$$M_n^\bullet + M_m^\bullet \xrightarrow{k_{td}} M_n + M_m$$

k_{td} = rate constant for disproportionation termination step

Figure 4.7 *Disproportionation* **termination process of two propagating polystyrene radical chains.**

In general, the termination step would be described without specifying the mode of termination.

$$k_t = k_{tc} + k_{td}$$

k_t is generally assumed to be independent of the size of the propagating chain.

4.2.2 Initiator Efficiency (f)
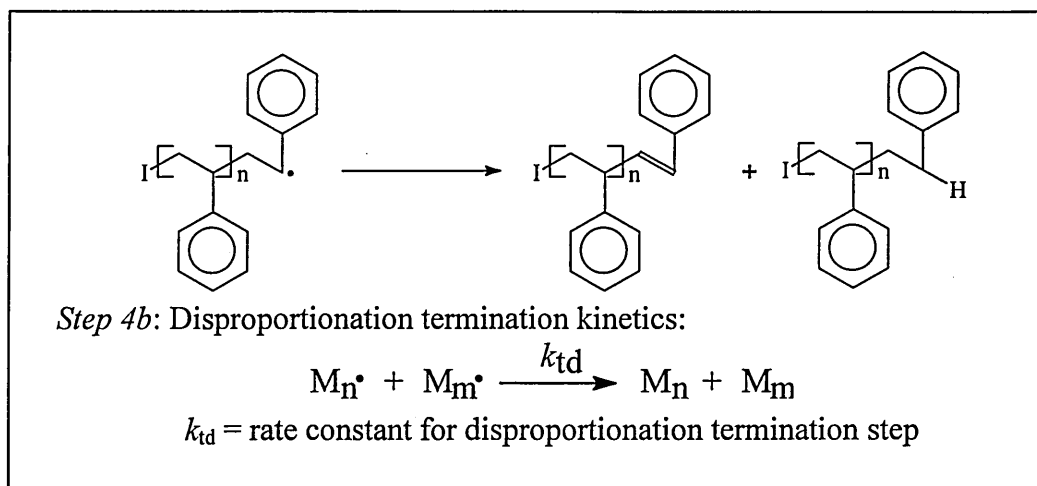
f is the ratio of growing chains to radicals generated initially. $f = 1$ if all initially generated radicals start a chain-growth reaction. In reality, f would be of the range 0.1-0.8.

4.2.3 Rate of Polymerisation

To derive kinetic equations for these reactions certain assumptions are made:

The 1st assumption is that the rate of initiation (R_i) is the same as the rate of initiator decomposition (R_d), and with reference to these respective equations:

$$Eq^n\ 4.1 \qquad R_i = R_d = 2fk_d[I] = k_i[I^\bullet][M]$$

f = mole fraction of initiator radicals which actually initiate polymerisation, i.e. the *initiator efficiency*.
2 = accounts for two $I^\bullet$ being derived from each initiator molecule.

The *second assumption* is that the rate of termination can be expressed kinetically by:

$$Eq^n\ 4.2 \qquad R_t = 2k_t[M^\bullet]^2$$

2 = two radicals combining in the termination step.

The next assumption in this derivation assumes that the concentration of free radicals quickly reaches a value which does not change substantially. This assumption is known as the steady state assumption, and can be expressed as:

$$R_i = R_t$$

or

$$Eq^n\ 4.3 \qquad 2fk_d[I] = 2k_t[M^\bullet]^2$$

The concentration of radical needs to be expressed in terms of measurable quantities:

$$Eq^n\ 4.4 \qquad [M^\bullet] = (fk_d[I] / k_t)^{1/2}$$

The overall rate of polymerisation (R_{poly}) can be considered as the rate of disappearance of monomer with respect to time, $-d[M]/dt$. This is due to the reaction between the initiator-monomer and the propagation reaction:

$$Eq^n\ 4.5 \qquad R_{poly} = -d[M]/dt = k_i[I^\bullet][M] + k_p[M^\bullet][M]$$

$$Eq^n\ 4.6 \qquad R_{poly} = k_p[M^\bullet][M]$$

By substituting the radical concentration term into this equation, the following equation could be derived:

$$\text{Eq}^n \ 4.7 \qquad R_{poly} = k_p[M](fk_d[I] / k_t)^{\frac{1}{2}}$$

Therefore, the rate of polymerisation would be dependent on the concentration of monomer and the square root of the initiator concentration. According to this equation if the concentration of monomer was doubled, the rate would double, but if concentration of initiator was doubled, the rate of polymerisation would only increase by a factor of $2^{1/2} = 1.414$.

4.2.4 Molar Mass

The kinetic chain length, v, of a free radical polymerisation is defined as the average number of monomer molecules polymerised per radical that initiates a polymer chain. This is a measure of the average molar mass of the polymer produced. The kinetic chain length is given by the ratio of the polymerisation rate to the initiation or termination rate, the last two being equal if the steady state assumption of the total concentration [M$^\bullet$] of all the radical species $M_n^\bullet$ is made.

$$\text{Eq}^n \ 4.8 \qquad v = R_{poly} / R_t = R_{poly} / R_i$$

Substitution of previous equations (4.1 and 4.2) for R_i and R_t in equation 4.8 produces:

$$\text{Eq}^n \ 4.9 \qquad v = k_p[M] / 2k_t[M^\bullet]$$

or

$$\text{Eq}^n \ 4.10 \qquad v = k_p^2[M]^2 / 2k_t R_{poly}$$

Further substitution of R_{poly} into equation 4.10 produces:

$$\text{Eq}^n \ 4.11 \qquad v = k_p[M] / 2(fk_d k_t[I])^{\frac{1}{2}}$$

The final equation shows a very significant peculiarity of free-radical polymerisation. The kinetic chain length, and therefore the average molar mass, decreases when the initiator concentration is increased. Therefore, by trying to increase the rate of polymerisation by

increasing the initiator concentration the result would be the production of a polymer with a lower average molar mass.

4.2.5   Chain Transfer

Chain transfer is the termination of a growing polymer chain by transfer of the active centre to a monomer molecule. This transfer marks the start of growth for a new polymer chain, the result of this process is a decrease of the average molar mass.

Chain transfer may occur by two different mechanisms:

i.   *Spontaneous chain transfer*, where the rate of re-initiation is considered comparable to that of the growth of the original propagating chain, and so, has no influence on the rate of polymerisation with $R_{poly} = k_p[M]($f$k_d[I] / k_t)^{1/2}$ remaining valid.

ii.   *Addition of chain transfer agents*, are used to allow control of the average molar mass of the polymer obtained. An agent which is commonly used is dodecyl mercaptan. This readily transfers a hydrogen from its sulphur to a carbon radical. Depending on the agent used this addition may also result in a decrease of the rate of polymerisation. No chain transfer agents were added in this work.

4.2.6   The Trommsdorf-Norrish Effect

Equation 7 suggests that upon depletion of the monomer at the end of the polymerisation reaction the rate of polymerisation will decrease. In reality, the polymerisation rate increases with conversion or with the reaction time, this is because of the Trommsdorf-Norrish effect (also referred to in relevant literature as the *gel effect*).

This can cause an auto-acceleration of the polymerisation reaction and complicate a kinetic study of polymer formation. This involves an increase in viscosity which leads to a decrease in the rate of termination, since the bulky growing polymer radical cannot diffuse easily through the medium. So, the possibility for two polymer radicals to interact and

participate in a termination process is reduced. Conversely, the mobility of small monomer molecules is not affected by the increasing viscosity of the reacting fluid; therefore, the limited mobility of macromolecules affects the rate of propagation to a much smaller extent.

From Eq^n 7, it may be concluded that the decreased mobility of growing macromolecules results in a decrease of k_t at constant k_p, which results in an increase in the rate of polymerisation, and Eq^n 11 predicts that the Trommsdorf effect causes an increase in the average molar mass. Furthermore, the polydispersity of the molar mass distribution curve usually increases.

This auto-acceleration has been observed for many monomers including styrene and many acrylates [4.29-4.39] and is considered to be normal behaviour during free-radical polymerisation. According to O' Driscoll and Huang [4.40], the polymerisation rate for a styrene homopolymerisation may be as high as x15 the theoretical rate, expressed by Eq^n 7.

The Trommsdorf effect is undesirable in industrial applications; it occurs when the viscosity is already high and therefore when heat and mass transfer are hindered. It can lead to the development of 'hot-spots' and erratic behaviour, which reduces the quality of the end product [4.41, 4.42]. In a review by Neil & Torkelson [4.29], it was determined that the best way to avoid the Trommsdorf effect would be to reduce the possibility of entanglements of macromolecules by performing the polymerisation in the presence of relatively large volumes of solvent. However, the addition of a solvent has many negative consequences and is not the most desirable solution to the problem.

Reduction of the Trommsdorf effect was reported by Chen *et al.* [4.43] when using mixtures of initiators, tailored to balance the decrease of k_t with a corresponding decrease of k_d. Saban *et al.* [4.44] have performed bulk free-radical polymerisation of styrene in the

presence of nitroxide-stable free radicals, resulting in the suppression of the conventional termination reaction (Eq^n k_{tc}/k_{td}) and therefore the Trommsdorf effect did not occur. These studies show that in some specific cases the Trommsdorf effect can be reduced or eliminated, however, in general, it remains an unsolved problem.

4.2.7 Thermal Self-Initiation of Styrene

Styrene monomer can be initiated solely by heat without the addition of initiators. This is unique to PS, which is the only polymer that polymerises without some form of initiator [4.45]. The mechanism for self-initiation, known as the Mayo mechanism (fig. 4.8 [4.46]) is a complex reaction where three monomer molecules form 2 radicals and can be summarised as:

$$\text{Eq}^n\ 4.12 \qquad 3[M] \xrightarrow{k_i} 2[I^\bullet]$$

where the rate of initiation can be defined as,

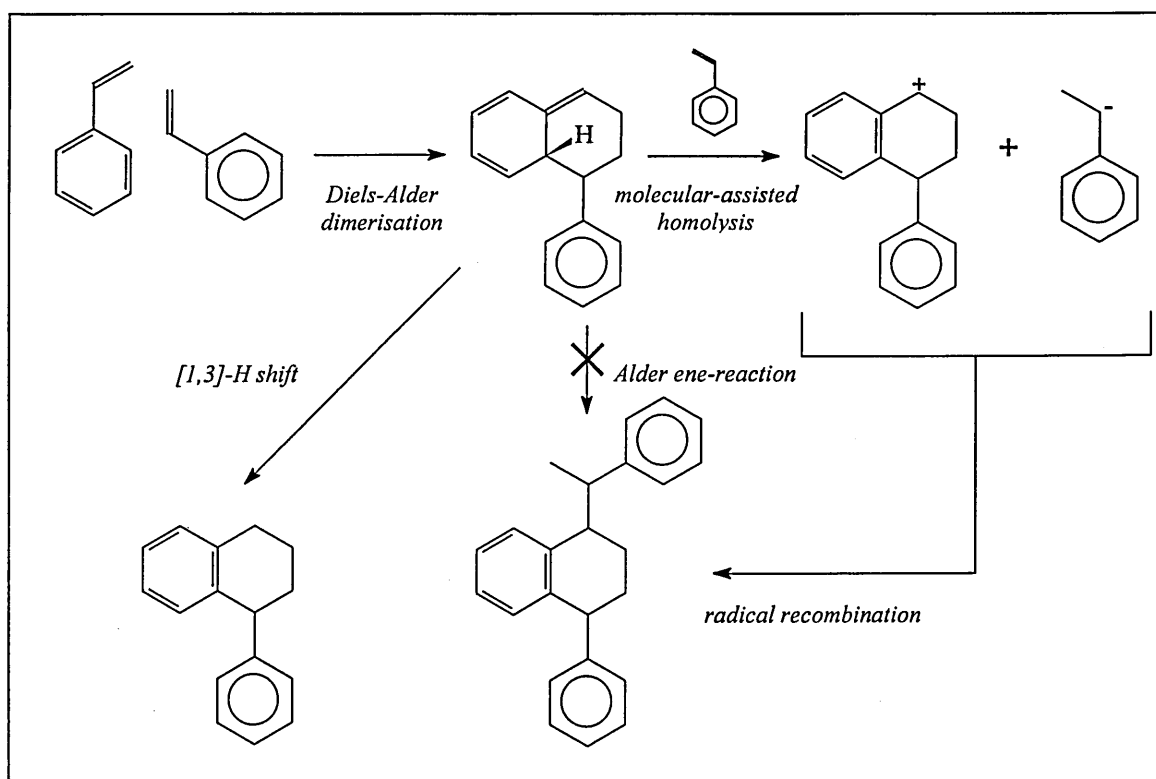$$\text{Eq}^n\ 4.13 \qquad R_i = k_i[M]^3$$

Figure 4.8 Self-initiation mechanism for styrene [4.46].

However, this process is reported as occurring at 0.1 % per hour at 60 °C and, 2 % per hour at 100 °C, James *et al.* [4.45]. The low rate of thermal self-initiation of styrene ensured that the addition of different initiator species would lead to a reasonable polymerisation rate without self-initiation having much effect on polydispersity.

4.2.8 Molecular Weight (MW)

All polymers made by traditional polymerisation processes are polydisperse, i.e. they are made up of a mixture of different molecular weight (MW) chains.

The MW of a polymer is an important determinant of its physical properties [4.47].

- As MW increases, strength increases to a maximum at very high MW (in the millions).

- Specific MW ranges are optimum for a particular application.

- Typically, a polymerisation is not industrially useful unless very high MW can be reached.

These may be characterised by an average MW; two methods for defining this are:

4.2.8.1 Number Average Molecular Weight, M_n

This is equivalent to the total mass of the polymer divided by the total moles in the polymer. Mathematically, the number average molecular weight is defined as:

$$\text{Eq}^n \ 4.14 \qquad M_n = \Sigma N_i M_i \ / \ \Sigma N_i$$

N = number of moles in the sample, M = mass, N*M = mass of the sample

Each chain contributes equally to the number average molecular weight.

4.2.8.2 Weight Average Molecular Weight, M_w

Weight average molecular weight is an absolute method of measuring molecular weight. It differs from M_n by being dependent on the mass of the polymer rather than on the end groups or colligative properties. This is apparent in the equation for M_w which is:

$$\text{Eq}^n \ 4.15 \qquad M_w = \Sigma_i N_i M_i^2 \ / \ \Sigma_i N_i M_i$$

When compared with the equation for M_n, it can be seen that in M_w it is divided by the mass sum rather than the mole sum. Also, M in the numerator is squared where as in M_n it is not [4.48].

4.2.9 Polydispersity and the Polydispersity Index (PDI)

The average MW of a polymer can be very misleading; to this effect the polydispersity of a polymer sample can be a key parameter in a sample's description.

The polydispersity index (PDI) is the ratio of the weight average molecular weight to the number average molecular weight, it is a measure of the breadth of a molecular weight distribution, equal to the ratio:

$$\text{Eq}^n \ 4.16 \qquad PDI = M_w \ / \ M_n$$

Usually, the narrower the polydispersity, the more homogeneous the polymer sample. Narrow distributions have PDI's near 1 while a very broad distribution can have a PDI of 10. Step growth polymers and free radical chain growth polymers usually have a PDI near 2 [4.49].

4.3 Various Organoclay and Initiator Species

The role of an organoclay within a nanocomposite-hybrid material is to reduce the surface energy of the clay surface, thus improving the wetting characteristics by the desired monomer/polymer [4.50, 4.51]. The successful production of a nanocomposite material (whether intercalated or exfoliated) is dependent on the miscibility of the individual components and the extent of their interactions. Due to the importance of this material compatibility between the exchanged organic species (i.e. on the surface of the clay) and the monomer [4.52, 4.53], it was an objective of this study to investigate the effect that the

chemical structure of various organophilic MMT clays had on the process of PS-clay nanocomposite formation.

The PS-clay nanocomposites produced in this study were prepared from mixtures of styrene monomer with various weight percentages of organophilic MMT. After blending the material's components, the styrene monomers were allowed to diffuse into the galleries of the organoclays, the process was followed by *in-situ* polymerisation with different initiators. These hybrid mixtures were blended at varied concentrations and under different curing profiles (see ch.2, section 2.2.3).

4.3.1   Organoclay Species

The organocations are shown in table 4.1, for specific details refer to 2.1.2.1/2.1.2.2.

Organoclay	Organic cation structure
MCBP-C_8 - C_{16}	CH_3—$\overset{\underset{\displaystyle CH_3}{\vert}}{\underset{\underset{\displaystyle CH_3}{\vert}}{N}}{}^{+}$—R R----►$C_8$-$C_{16}$
C15A	CH_3—$\overset{\underset{\displaystyle CH_3}{\vert}}{\underset{\underset{\displaystyle HT}{\vert}}{N}}{}^{\pm}$HT
C20A	CH_3—$\overset{\underset{\displaystyle CH_3}{\vert}}{\underset{\underset{\displaystyle HT}{\vert}}{N}}{}^{\pm}$HT
C10A	CH_3—$\overset{\underset{\displaystyle CH_3}{\vert}}{\underset{\underset{\displaystyle HT}{\vert}}{N}}{}^{\pm}CH_2$—⬡

Table 4.1   Comparison of quaternary ammonium cations exchanged into MMT.

4.3.2   Initiator Species

The initiator species used to promote radical initiation were AIBN, BPO, AIBA, SPS and APS (see table 4.2). By heating the different initiators in styrene monomer, the initiator molecules are homolytically cleaved, in the case of AIBN / AIBA, cleavage of the C-N bonds, and formation of two t-butyl radicals. The radical species then adds to a styrene

monomer, initiating polymerisation. The polymerisation ends when one of the radicals does something other than add to another monomer. The differences between the initiator species are presented in table 4.2. As well as the structural differences between species, these different species were blended into the different hybrid mixtures at concentrations equivalent to 0.5, 1 and 2 wt% of the styrene monomer.
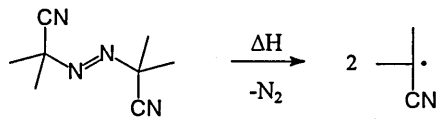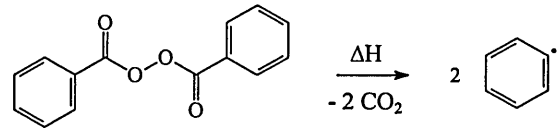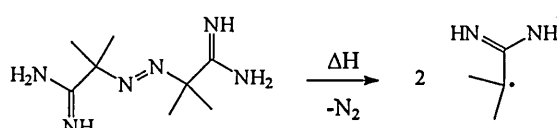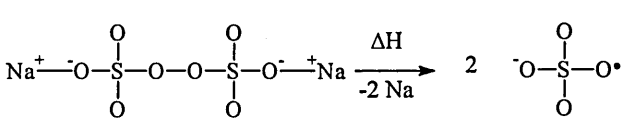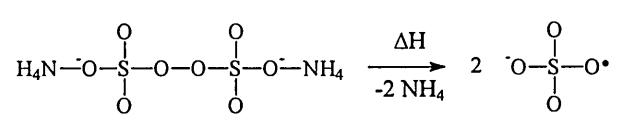
Initiator	Chemical Name	Chemical Structure and degradation path	Mpt
AIBN	2,2-azo-bis-isobutyronitrile		103-105 °C
BPO	Dibenzoyl peroxide		104-106 °C
AIBA	2,2-azo-bis-isobutyramidine		~110 °C
SPS	Sodium peroxodisulphate		Decomposes ~100°C
APS	Ammonium peroxodisulphate		Decomposes ~110°C

Table 4.2   The different initiator species used and schematic diagrams of their decomposition mechanisms.

4.4   **Results/Discussion**

4.4.1   **Polystyrene-Clay Nanocomposites (PSCN) ~ PS - MCBP-Cₙ Initiated with**

AIBN, BPO, AIBA, SPS, APS

Initial experiments were conducted using the range of initiators shown in table 4.2. The experimental procedure for this batch of experiments is described in section 2.2, ch. 2.

4.4.1.1   **PSCN - AIBN, BPO, AIBA, SPS, APS - Results**

The PS-MCBP-C_n mixtures which were initiated with AIBN and BPO were easily suspended by using overhead mixing and ultrasonification. The ease with which the initiator was homogeneously dispersed within these samples (i.e. relative to other mixtures with different initiator types) was observed as a good indicator of the initiators intimacy within the system. The good dispersal and homogeneity of these mixtures meant that the free-radicals which were generated would continuously react with the vinyl groups of styrene throughout the bulk of the styrene. An example DTG for a PSCN is shown in fig. 4.9a. The differences between the DTG T_{max} (i.e. highest temperature of maximum weight loss) for PS-MCBP-C_n samples initiated with AIBN, BPO, AIBA, SPS and APS are shown in fig. 4.9b. Also, the corresponding data and associated values and observations are displayed in table 4.3.
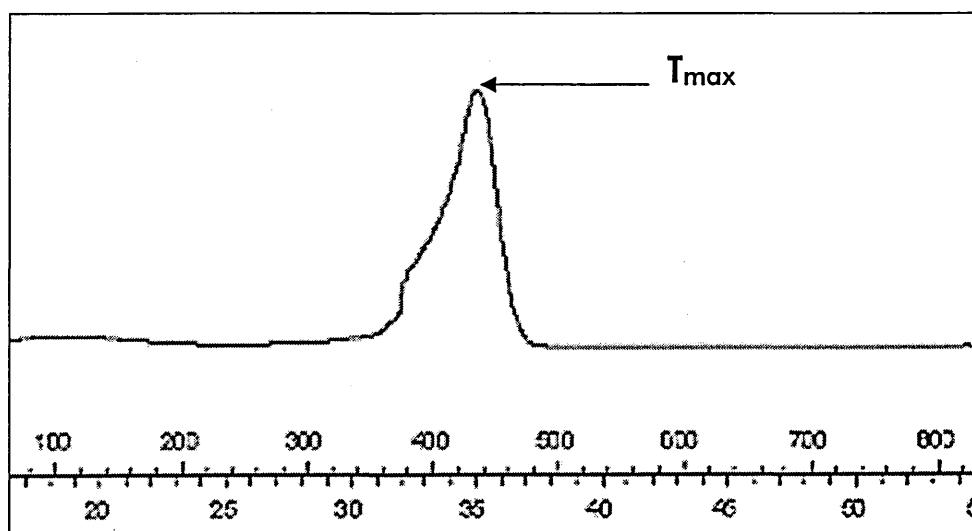

Figure 4.9a   Example DTG trace, indicating temperature specific derivative weight loss maxima and the T_{max} (asymmetric < 430 °C).

Organo-cation	CEC of clay (mEq/100g)	Init. type	[Init.] (wt%)	T_{max} (°C)	d_{001} (Å)	Cure time at 60 °C (Hrs)	Notes on peak shape
OTAB	90	AIBN	1	438	> 43.3	72	Asymmetric < 438 °C
DTAB	"	"	"	440	"	"	Asymmetric < 440 °C
TTAB	"	"	"	440	"	"	Asymmetric < 440 °C
CTAB	"	"	"	442	"	"	Asymmetric < 450 °C
PS		"	"	405	n/a	"	n/a

OTAB	90	BPO	1	431	> 43.3	72	Asymmetric < 431 °C
DTAB	"	"	"	432	"	"	Asymmetric < 432 °C
TTAB	"	"	"	438	"	"	Asymmetric < 438 °C
CTAB	"	"	"	439	"	"	Asymmetric < 439 °C
PS		"	"	404	n/a	"	n/a

OTAB	90	AIBA	1	423	> 43.3	120	Asymmetric < 423 °C
DTAB	"	"	"	425	"	"	Asymmetric < 425 °C
TTAB	"	"	"	425	"	"	Asymmetric < 425 °C
CTAB	"	"	"	430	"	"	Asymmetric < 430 °C
PS		"	"	409	n/a	"	n/a

OTAB	90	SPS	1	439	> 43.3	120	Asymmetric < 439 °C
DTAB	"	"	"	440	"	"	Asymmetric < 440 °C
TTAB	"	"	"	441	"	"	Asymmetric < 441 °C
CTAB	"	"	"	448	"	"	Asymmetric < 448 °C
PS		"	"	415	n/a	"	n/a

OTAB	90	APS	1	432	> 43.3	120	Asymmetric < 432 °C
DTAB	"	"	"	441	"	"	Asymmetric < 441 °C
TTAB	"	"	"	443	"	"	Asymmetric < 443 °C
CTAB	"	"	"	445	"	"	Asymmetric < 445 °C
PS		"	"	412	n/a	"	n/a

Table 4.3   Comparison of sample characteristics for PSCN nanocomposites initiated with 1wt% AIBN, BPO, AIBA, SPS and APS initiators. Note that asymmetric < 425 °C means that the maximum in the DTG was asymmetric on the low temperature side.
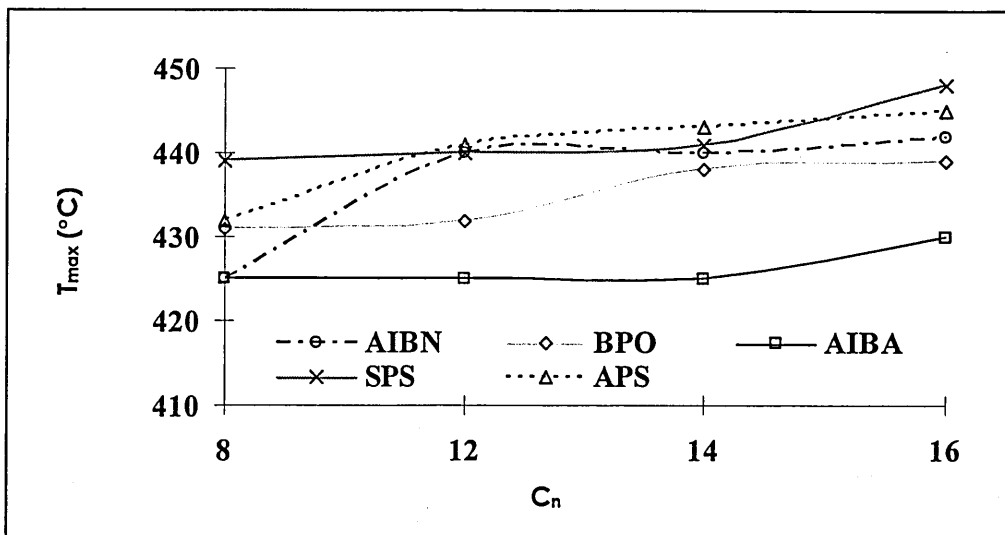
Figure 4.9b Plot of DTG T_{max} vs. alkyltrimethylammonium chain length for PSCN initiated with 1 wt% AIBN, BPO, AIBA, SPS and APS.

4.4.1.2 Discussion of PS-MCBP-C_n Initiated by AIBN, BPO, AIBA, SPS, APS

TG analysis of the AIBN and BPO free-radical initiated PSCN-C_{16} samples showed T_{max} temperatures at 442 °C and 439 °C (Table 4.3), which in turn showed relative increases in thermal stability of about 38 °C and 35 °C when compared with the pure PS samples. Both of these initiators were easily dispersed in styrene monomer and the respective PSCN-C_{16} samples were fully cured in a relatively short time period (72 h/50 °C), the result of which were discoloured (i.e. due to clay content), translucent and visually homogeneous products. The d_{001} could not be determined using a Cu-kα x-radiation because no peak was visible below the detection limit of 43.3 Å (e.g. 1 wt%, fig. 4.14). This combination of reactants and procedures had formed homogeneous PSCNs with an exfoliated org-MMT content, showing an approximate 35°C increase in thermal stability.

The ease of initiator dispersal within these samples would have lead to the migration of the initiator with the styrene monomer into the expanded gallery spaces of the org-MMT. Then, as the temperature was increased, polymerisation would have occurred throughout the gallery spaces and in the bulk as the radical species were generated *in-situ*. This mechanism would have first delaminated the clay layers and then spread them

throughout the growing polymer matrix. The result of which was believed to have been the production of exfoliated PS-clay nanocomposites.

The AIBA free-radical initiated PSCN-C_{16} sample exhibited a T_{max} in the DTG at 430 °C, showing an increase of 21 °C over pure PS. XRD analysis revealed a d_{001} for PSCN-C_{16} = 20.4 Å, which represented a negligible increase over MCBP-C_{16} (19.3 Å), but the clay appeared to be well dispersed throughout the samples. The AIBA-PSCN-C_{16} samples took 96 h/50 °C to cure (i.e. 24 h longer than AIBN/BPO samples) and produced opaque, homogeneous samples. As a result, the AIBA initiated PSCN-C_{16} was characterised as having a well-dispersed intercalated organoclay content, which imparted a 20 °C increase in thermal stability.

The AIBA-PSCN-C_{16} samples required an increased mixing duration (i.e. + 5 h), were slow to cure and the initiator was relatively bulky, with a higher decomposition temperature. All these factors would have lead to the slower thermal initiation of styrene and poor intercalation of the monomer within the clay galleries. This would have lead to the vast majority of polymerisation occurring in the bulk. Consequently, little polymerisation took place in the galleries, hence an intercalated nanocomposite was formed.

The SPS and APS initiated PSCN-C_{16} (i.e. mixture of free-radical/ionic in solution) showed T_{max} values of 448 °C and 445 °C, respectively, an increase of 33 °C over pure PS. SPS showed a d_{001} = 22.9 Å (i.e. increase of 2.6 Å), whereas APS initiated samples showed a much less significant increase to 19.9 Å (i.e. ~ 0.6 Å). The SPS and APS-PSCN-C_{16} samples took 120 h/50°C to cure (i.e. 48 h longer than AIBN/BPO samples), the products of these polymerisations were opaque solids with slight clay sedimentation visible in both samples, but most prominent in the APS samples. Consequently, SPS and APS-PSCN-C_{16} were characterised as being poorly-dispersed, phase separated micro-composites, with partial

intercalation of the org-MMT additive in the SPS samples. Both mixtures imparted a 33 °C increase in thermal stability.

When the SPS and APS samples were subjected to a pre-polymerisation temperature (i.e. 110 °C) the nanocomposite mixture became highly viscous. This was most probably the result of auto-acceleration of the polymerisation process. This phenomenon is known as the Trommsdorf-Norrish effect (gel effect), initially leading to a significant increase in the rate of bulk radical polymerisation. It is related to the increasing concentration of propagating radicals as a result of the decreasing rate constant of termination with increasing viscosity of the system (see section 4.2.6). With this increase in the viscosity of the nanocomposite, the growing polymer chains diffuse poorly, which strongly effects the termination process. Radical species and terminal end monomers have restricted mobility within the system leading to a greater degree of termination by disproportionation, rather than coupling reactions. The increasing chain lengths within these samples could be the main reason for the increase in the polymers thermal stability, with chain length being directly proportional to melting point.

In the different series of samples, the T_{max} was shown to increase as the length of the alkyl chain increased. This trend showed that a greater alkyl concentration in the gallery led to a greater intimacy between the PS and organoclay, imparting greater thermal stability.

4.4.2 Effect of Initiator Concentration on PSCN Containing 1 wt% of Various Organoclay Species

Due to the relative ease of their dispersal and the rapidity of cure that they imparted, AIBN and BPO were chosen as the most suitable initiators for continued use in further experiments. In this series of experiments, the concentration of initiator was varied from 0.5 to 2.0 wt% to observe the effects that lower and higher concentrations of free-radical

species may have on the thermal stability of the cured materials and the *d*-spacing in the XRD of the PSCN product.

4.4.2.1 Results for varying AIBN and BPO concentrations in PSCN-MCBP-C_n

AIBN						
Organocation	[Init.]	T_{max} (°C)	[Init.]	T_{max} (°C)	[Init.]	T_{max} (°C)
OTAB	0.5 wt%	440	1.0 wt%	439	2.0 wt%	430
DTAB	"	442	"	440	"	432
TTAB	"	442	"	440	"	435
CTAB	"	447	"	442	"	436

Table 4.4   Comparison of the DTG T_{max} values for PSCN initiated with AIBN at 0.5, 1.0 and 2.0 wt% of styrene.
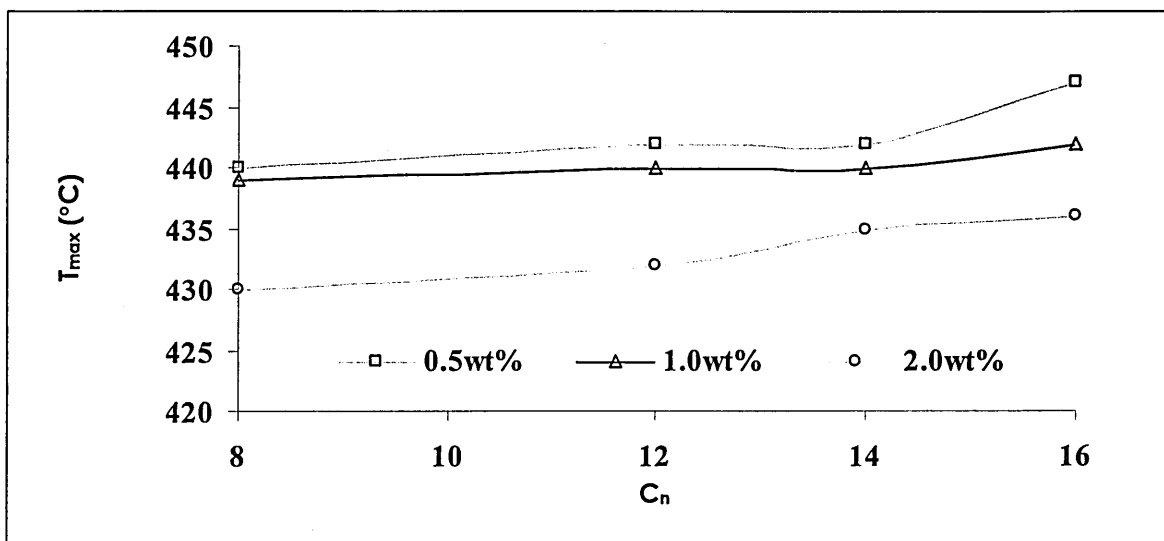

Figure 4.10   Plot of DTG T_{max} values for PSCN-C_n initiated with AIBN.

BPO						
Organocation	[Init.]	T_{max} (°C)	[Init.]	T_{max} (°C)	[Init.]	T_{max} (°C)
OTAB	0.5 wt%	436	1.0 wt%	431	2.0 wt%	429
DTAB	"	438	"	432	"	430
TTAB	"	439	"	438	"	436
CTAB	"	440	"	439	"	439

Table 4.5   Comparison of DTG T_{max} values for PSCN initiated with BPO at 0.5, 1.0 and 2.0 wt% of styrene.
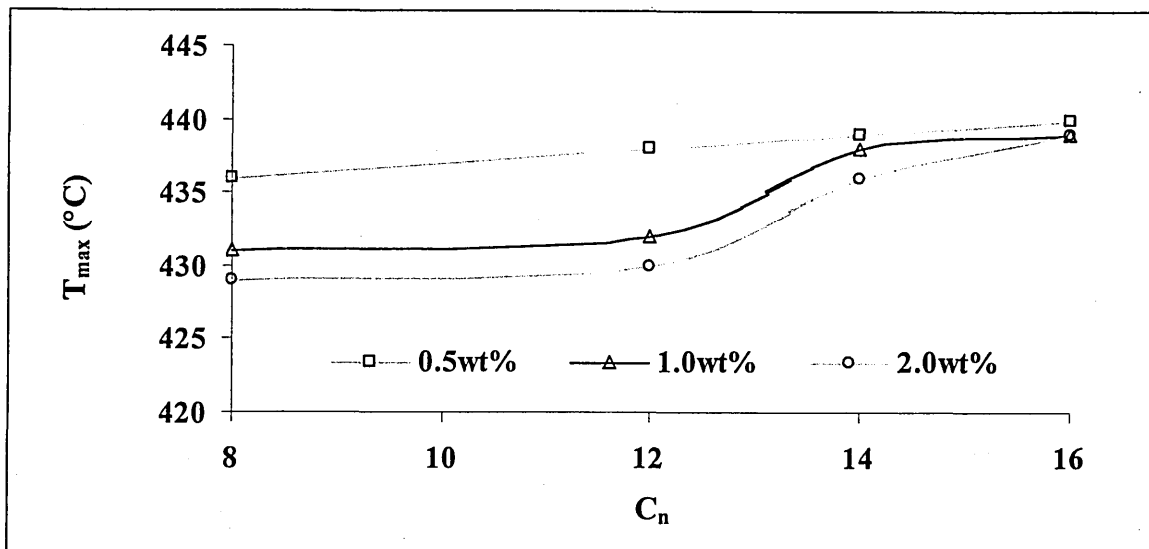
209

Figure 4.11 Plot of the DTG T_{max} values for PSCN initiated with BPO.

All samples that were studied here were XRD silent and therefore deemed to be exfoliated. The use of AIBN as the initiator and lower initiator concentrations resulted in higher T_{max} values, this was most significant for organoclays with shorter alkyl chains.

4.4.2.2 Results for Varying AIBN and BPO Concentrations in PSCN which Incorporated C15A, C20A and C10A Organoclays

In this series of experiments, the concentration of initiator was varied slightly to observe what effects lower and higher concentrations of free-radical species may have on the properties of the PSCN product. The organoclays used here were commercially available, organically modified MMTs (outlined in ch.2, section 2.1.2.2).

	AIBN					
4° OLS	[Init.]	T_{max} (°C)	[Init.]	T_{max} (°C)	[Init.]	T_{max} (°C)
C15A	0.5 wt%	443	1.0 wt%	439	2.0 wt%	429
C20A	"	438	"	431	"	425
C10A	"	432	"	427	"	425

Table 4.6 Comparison of DTG T_{max} values for PSCN initiated with AIBN (0.5, 1.0 and 2.0 wt%) with Cloisites 15A, 20A and 10A (loaded at 1.0 wt%).
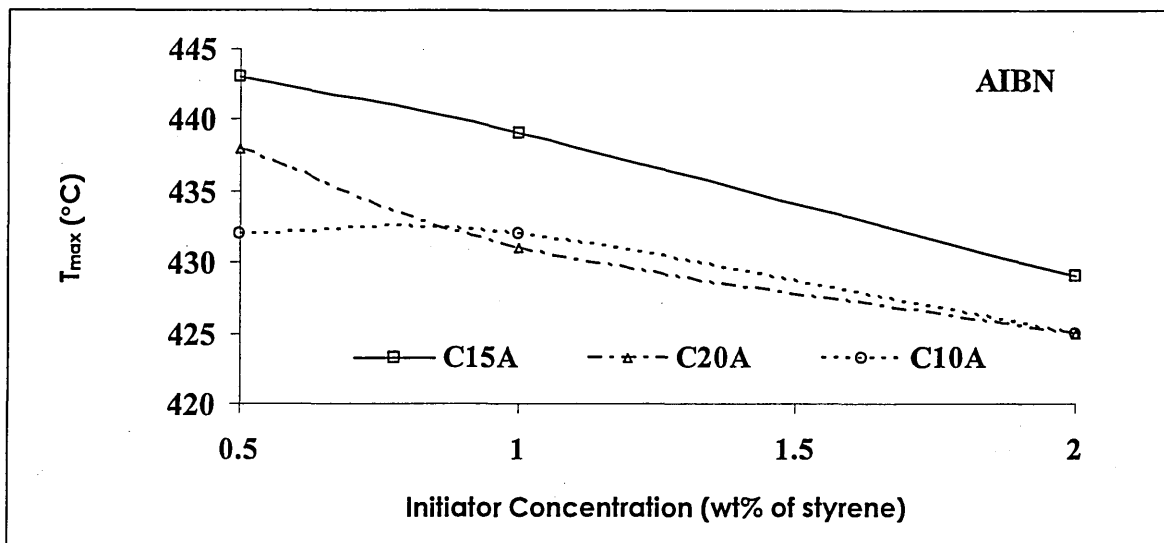
Figure 4.12   Plot of DTG T_{max} values for PSCN initiated with AIBN (0.5, 1.0 and 2.0 wt%) with Cloisites 15A, 20A and 10A (loaded at 1.0 wt%).

BPO						
4° OLS	[Init.]	T_{max} (°C)	[Init.]	T_{max} (°C)	[Init.]	T_{max} (°C)
C15A	0.5 wt%	439	1.0 wt%	430	2.0 wt%	426
C20A	"	437	"	430	"	423
C10A	"	429	"	425	"	422

Table 4.7   Comparison of DTG T_{max} values for PSCN initiated with BPO (0.5, 1.0 and 2.0 wt%) with Cloisites 15A, 20A and 10A (loaded at 1.0 wt%).
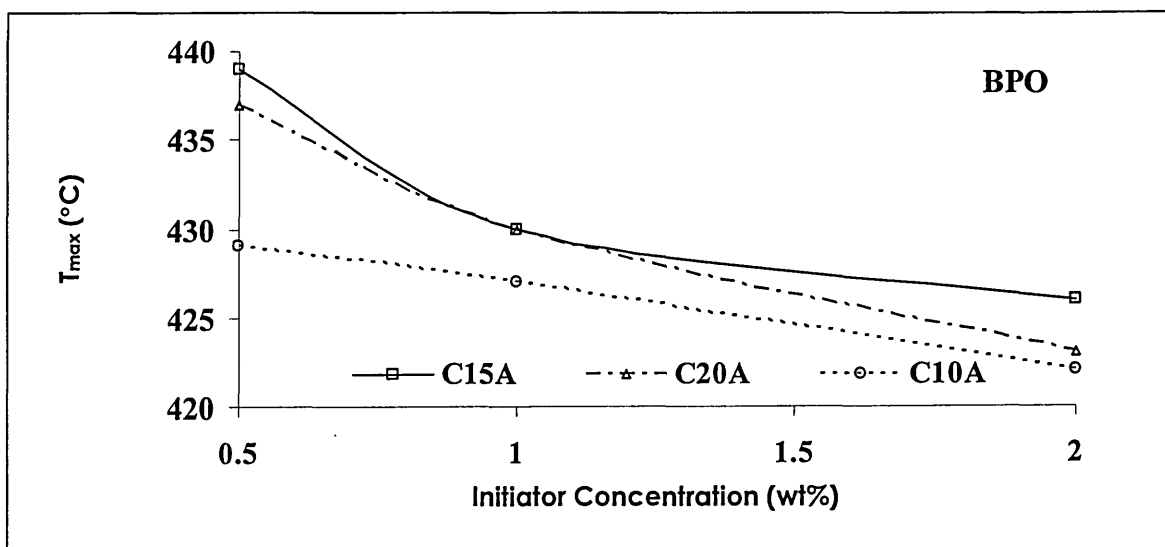

Figure 4.13   Comparison of DTG T_{max} values for PSCN initiated with BPO (0.5, 1.0 and 2.0 wt%) with Cloisites 15A, 20A and 10A (loaded at 1.0 wt%).

211

Again, all the 1 wt% organoclay PSCN samples that were studied were exfoliated, the use of AIBN and lower initiator concentrations resulted in higher T_{max} values.

4.4.2.3 PSCN - AIBN/BPO - MCBP-C_n, C15A, C20A and C10A - Discussion

The initiator concentration was varied with respect to the concentration stated in Doh & Cho's *in-situ* polymerisation mechanism (1 wt%) [4.11] to observe the effect that this would have on the thermal stability of various PSCNs. The MCBP-C_n samples showed increased T_{max} values as the alkyl chain length was increased and the commercially available organoclays gave relative Tmax values of the order of C15A > C20A > C10A. The T_{max} values of all the samples initiated with AIBN were slightly higher than for those initiated with BPO in all cases (table 4.8), including C15A, C20A and C10A.

Initiator type: AIBN / BPO						
4° OLS	[Init.]	T_{max} (°C)	[Init.]	T_{max} (°C)	[Init.]	T_{max} (°C)
MCBP-C_{16}	0.5 wt%	447	1.0 wt%	442	2.0 wt%	436
	"	440	"	439	"	439
C15A	"	443	"	439	"	429
	"	439	"	430	"	426
C20A	"	438	"	431	"	425
	"	437	"	430	"	423
C10A	"	432	"	427	"	425
	"	429	"	425	"	422

Table 4.8   Comparison of T_{max} with increasing [AIBN] for MCBP-C_{16}, C15A, C20A and C10A samples.

The reason for the decrease in T_{max} with increasing initiator concentration resulted from increased concentrations of initiator having hindered the propagation of the polymer chain by increasing the quantity of radical species available to terminate the chain growth. This would have led to smaller chains being formed, and consequently, a decrease in the thermal stability of the composite matrix (table 4.8).

This supports the kinetic model of chain length, which in a free radical polymerisation is defined as "*the average number of monomer molecules polymerised per radical that initiates a polymer chain*". It is, a measure of the average molar mass of the polymer produced. The kinetic chain length is given by the ratio of the polymerisation rate to the initiation or termination rate, the last two being equal if the *steady state* assumption of the total concentration [M•] of all the radical species M_n• is made.

$$\text{Eq}^n \ 4.11 \qquad\qquad v = k_p[M] / 2(f k_d k_t[I])^{\frac{1}{2}}$$

Equation 4.11 shows that the kinetic chain length, and therefore the average molar mass, decreases when the initiator concentration is increased. Therefore any attempt to increase the rate of polymerisation by increasing the initiator concentration results in the production of polymer with a lower average molar mass.

4.4.3 PSCN initiated by AIBN and BPO, with Increased Organoclay Concentration

In this series of experiments, the concentration of initiator was kept constant at 1 wt% whilst the concentration of organoclay was increased to observe the effects that higher concentrations may have on the properties of the PSCN products.

4.4.3.1 PSCN - AIBN/BPO (1wt%), with Increasing MCBP-C_{16} Organoclay Concentration - Results

MCBP-C_{16}				
Organoclay loading/wt%	[AIBN]/wt%	T_{max} (°C)	[BPO]/wt%	T_{max} (°C)
1	1	442	1	439
3	"	443	"	441
5	"	450	"	445

Table 4.9   Comparison of DTG T_{max} values for PSCN initiated with 1wt% AIBN and BPO with increasing organoclay loading.
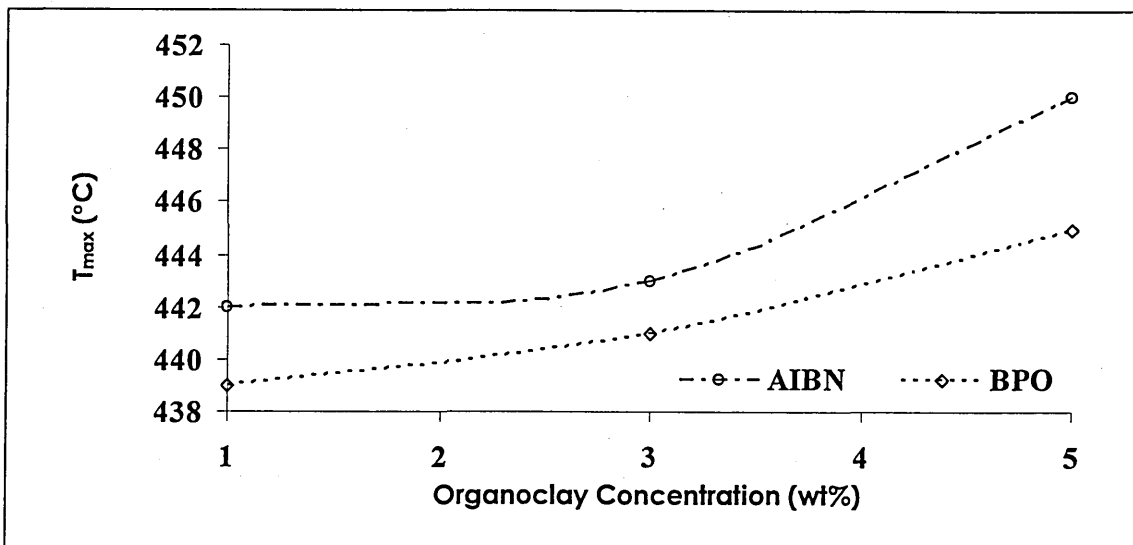
Figure 4.14   Plot of DTG T_{max} values for PSCN initiated with AIBN and BPO with increasing organoclay loading.
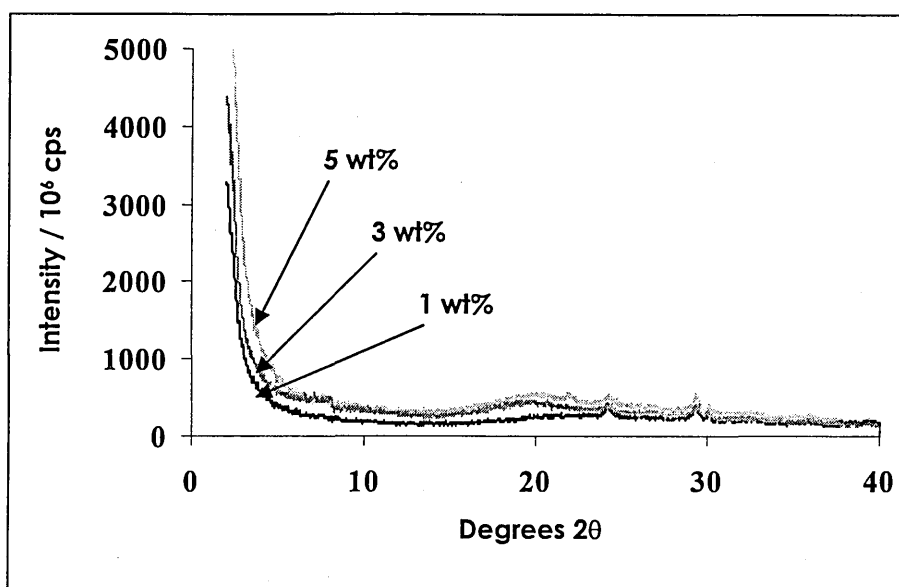

Figure 4.15   Comparison of XRD traces for PSCN loaded with 1, 3 and 5 wt% MCBP-C_{16} organoclay (1 wt% AIBN). Both AIBN and BPO showed similar exfoliated traces.

As the concentration of MCBP-C_{16} organoclay was increased, samples initiated with AIBN and BPO both showed T_{max} values shifted to successively higher temperatures, until reaching a value for 1 wt% AIBN of 450 °C at 5 wt% (fig. 4.14). All samples were shown to be XRD silent, i.e. they showed no silicate crystalline structure (fig. 4.15).

214

PSCN-C15A				
[C15A]/wt %	[AIBN]	Tmax (°C)	[BPO]	Tmax (°C)
1	1	439	1	427
3	"	440	"	430
5	"	442	"	432

Table 4.10   Comparison of Tmax values for PSCN nanocomposites initiated by 1 wt% AIBN and BPO with 1.0, 3.0 and 5.0 wt% C15A organoclay.
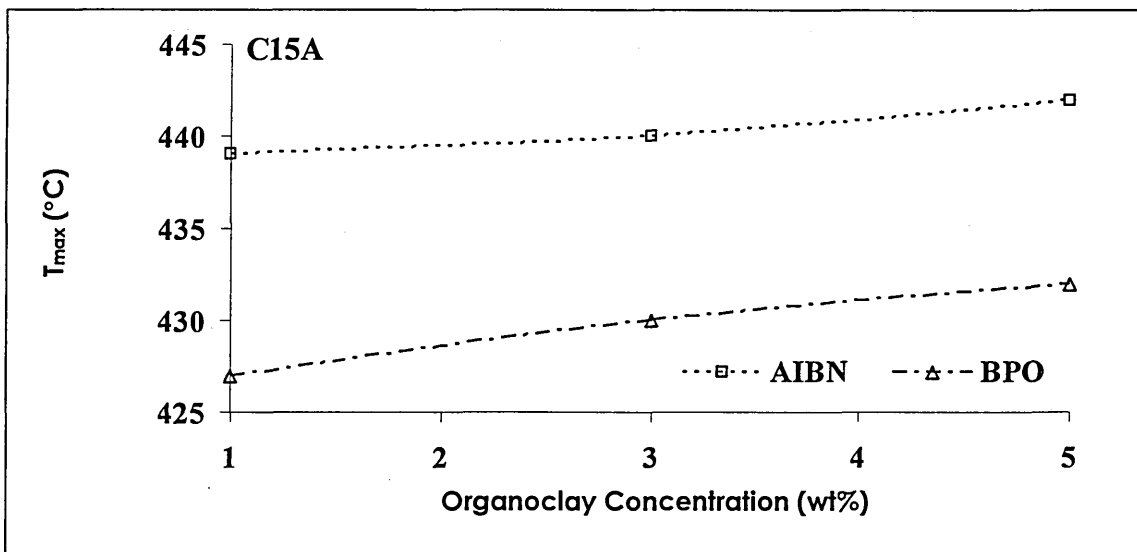

Figure 4.16   Plot of DTG Tmax values for PSCN initiated with AIBN and BPO with increasing C15A organoclay loading.
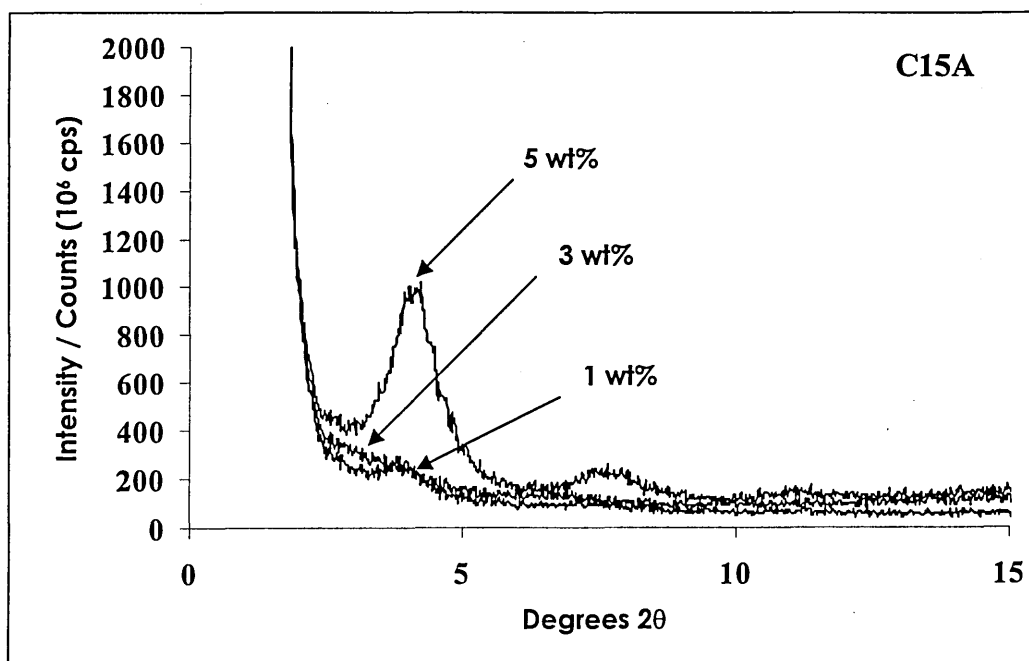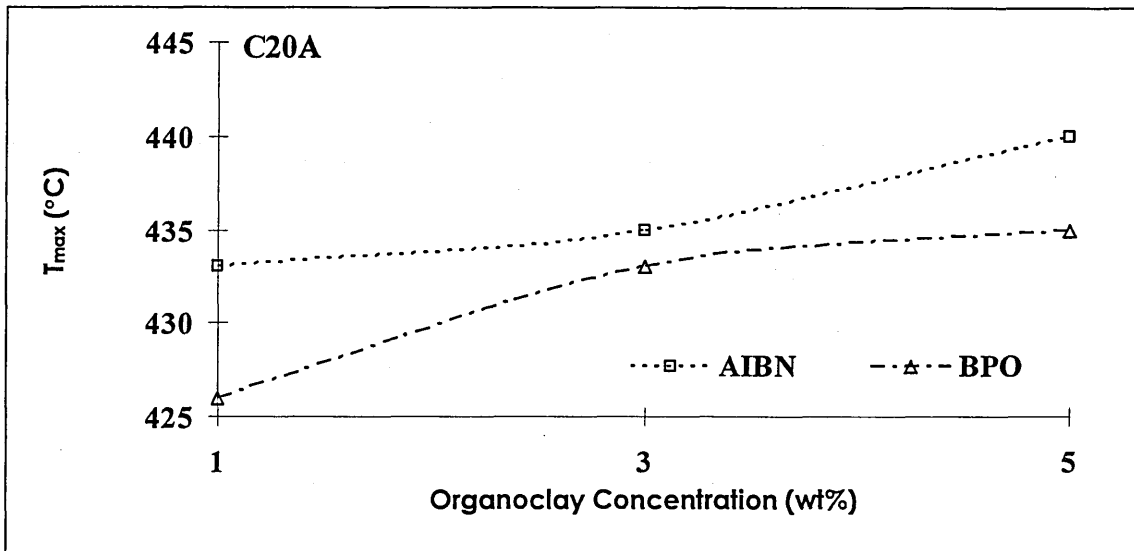

Figure 4.17   XRD traces for styrene/AIBN nanocomposites containing 1, 3 and 5wt% C15A.

215

PSCN-C20A				
[C20A]/wt %	[AIBN]	Tmax (°C)	[BPO]	Tmax (°C)
1	1	433	1	426
3	"	435	"	433
5	"	440	"	435

Table 4.11   Comparison of Tmax values for PSCN nanocomposites initiated by 1 wt% AIBN and BPO with 1.0, 3.0 and 5.0 wt% C20A organoclay.

Figure 4.18   Plot of DTG Tmax values for PSCN initiated with AIBN and BPO with increasing C20A organoclay loading.
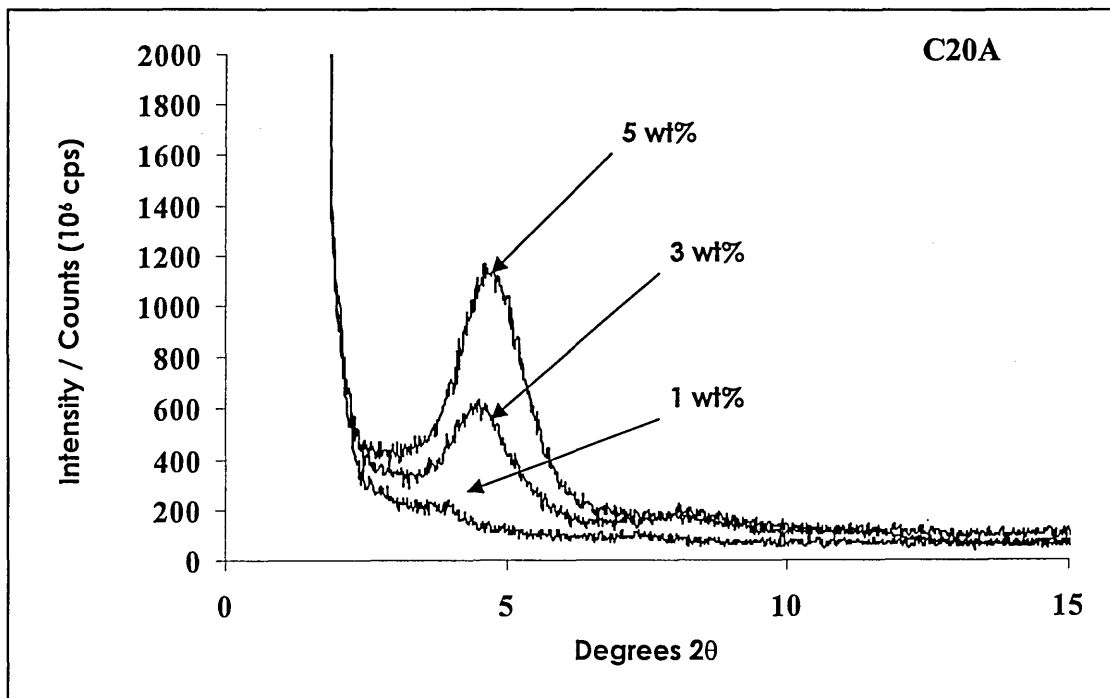

Figure 4.19   XRD traces for styrene/AIBN nanocomposites containing 1, 3 and 5wt% C20A.

216

PSCN-C10A				
[C10A]/wt %	[AIBN]	Tmax (°C)	[BPO]	Tmax (°C)
1	1	427	1	425
3	"	432	"	428
5	"	437	"	432

Table 4.12   Comparison of Tmax values for PSCN nanocomposites initiated with 1 wt% AIBN and BPO at 1, 3 and 5 wt% of styrene.
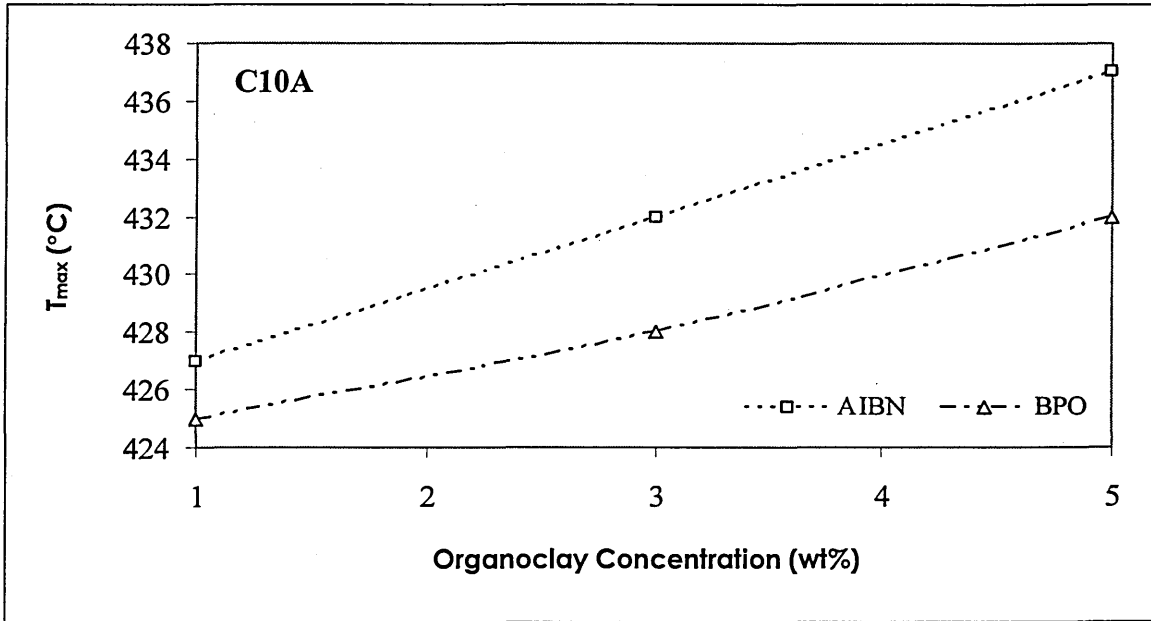

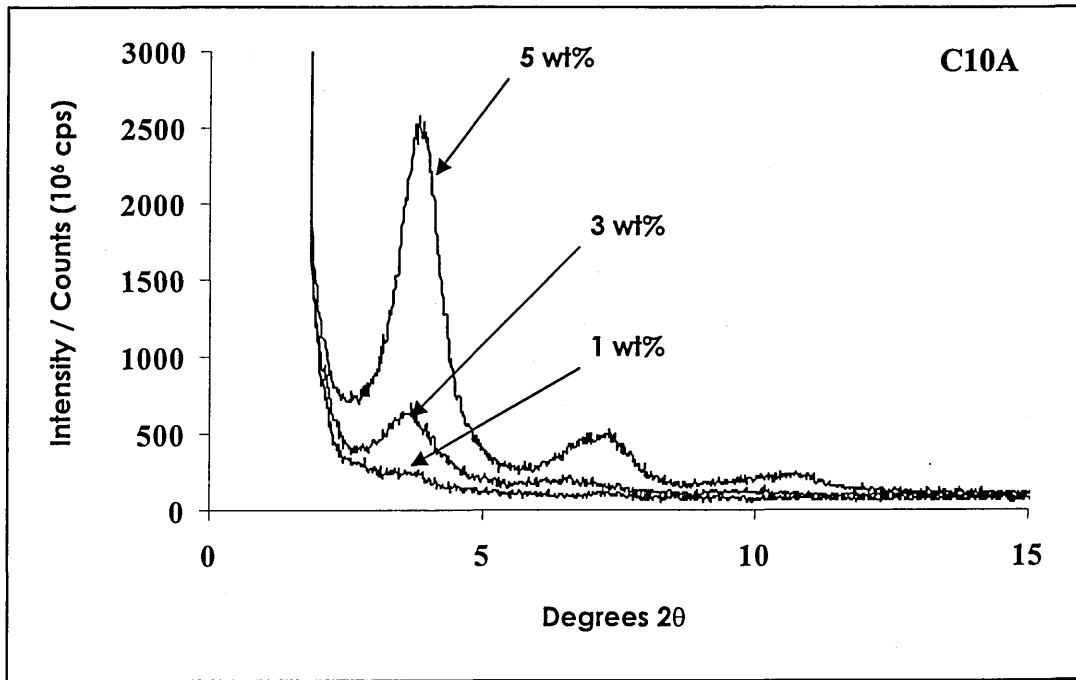Figure 4.20   Plot of DTG Tmax values for PSCN initiated with AIBN and BPO with increasing C10A organoclay loading.

Figure 4.21   XRD traces for styrene/AIBN nanocomposites containing 1, 3 and 5wt% C10A.

217

The increase in the concentration of organoclay from 1 to 5 wt% of styrene monomer increased the T_{max} values of all PSCN samples (table 4.13), this was attributed to the increased barrier to thermal decomposition. Any differences between the T_{max} values for the various series of samples and the PS/AIBN T_{max} = 405 and PS/BPO T_{max} = 404 were attributed to the dispersal of the initiators and organoclays within the PSCN systems. The MCBP-C$_{16}$ samples showed the highest T_{max} values of any PSCN series. The organoclays incorporated in these samples had the lowest modifier concentration (i.e. CEC = 80 meq/100g clay) of all the series examined. The increased T_{max} was attributed to the structure of the organic modifier (3Me, Hexadecyl), but the reason for this increase is largely unknown. The C15A organoclay (structure 2Me2HT, where HT is Hydrogenated Tallow (~65% C$_{18}$; ~30% C$_{16}$; ~5% C$_{14}$)) showed a relatively large d_{001} = 31.5 Å, and had a higher organic modifier concentration (i.e. 125 mEq/100g clay) than MCBP-C$_{16}$, however, the DTG of the C15A-PSCN showed lower T_{max} values, more evident with BPO (table 4.13). The C20A organoclay, which was intercalated with the same organic modifier as C15A, but reported to have a lower organic modifier concentration (i.e. 95 mEq/100g clay), showed a d_{001} = 24.2 Å.

Initiator type: AIBN / BPO			
Organoclay Concentration	**1wt% [org-MMT]** T_{max} (°C)	**3wt% [org-MMT]** T_{max} (°C)	**5wt% [org-MMT]** T_{max} (°C)
MCBP-C$_{16}$	442	443	450
	439	441	445
C15A	439	440	442
	427	430	432
C20A	433	435	440
	426	433	435
C10A	427	432	437
	425	428	432

Table 4.13   Comparison of DTG T_{max} for PSCN with increasing organoclay concentrations for MCBP-C$_{16}$, C15A, C20A, C10A samples.

The reduction in d_{001} and organic modifier concentration in the gallery spaces of C20A, relative to C15A, should have lowered the affinity of the styrene monomer to migrate into these organophilic environments. This was most evident between the AIBN initiated PSCN series which showed higher T_{max} values than corresponding BPO values. As the organoclay concentration was increased to 3 and 5 wt% a slight reversal occurred as the BPO initiated C20A samples gave slightly higher T_{max} values than C15A.

The C10A organoclay showed a d_{001} = 19.2 Å, and had an organic modifier concentration of 125 mEq/100g clay, the structure of which was 2MeBzHT (i.e. as in C15A, but with a HT group replaced by a -CH$_2$-Bz substituent). According to the producer's literature, C10A had a lower surface hydrophobicity rating than C20A, which in turn was lower than C15A. These values are relative to the surface accessibility of the different organoclay species. The aromaticity of the benzyl substituent would mean that its presence would not alter the overall organophilicity of the gallery spaces, however, the relatively low d_{001} and high modifier concentration may indicate a high degree of order in the arrangement of organic modifiers in C10A. Although, registering the lowest T_{max} values throughout the PSCN series, the T_{max} values was increased by 20-25 °C, relative to PS.

The optimum organoclay content, which gave the best improvements in thermal stability was 5 wt% for the various PSCNs. The thixotropic effects of greater concentrations of organoclay hindered the production process and stopped the creation of PSCN by in-situ polymerisation with organoclay concentrations that were > 5wt%. But, in an attempt to identify the profile of increased thermal stability as the concentration of organoclay was increased in the PS matrix, lower concentrations of C15A were added at 0.2, 0.4, 0.6 and 0.8 wt% of the styrene monomer (fig. 4.21). When plotted (fig. 4.23), the T_{max} of these samples levelled off at 0.8 wt%, and increased very little up to 5.0 wt%. This may be evidence that the additive thermal stability offered by these organoclay dispersions may be reaching their material limit at around 1.0 wt%. This may be due to a reduction in the

concentration of exfoliated clay platelets, with greater organoclay concentrations increasing the likelihood of platelets remaining as stacks.
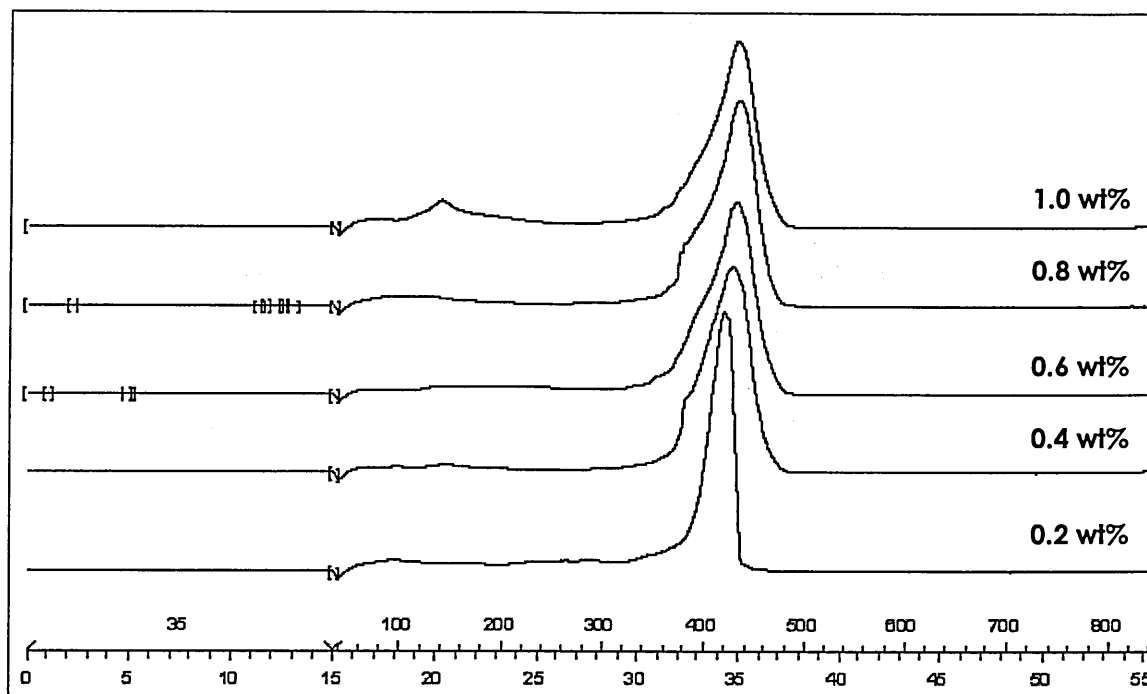

Figure 4.22   DTG traces for PSCN, initiated with AIBN, with the concentration C15A organoclay increased from 0.2-1.0 wt%.
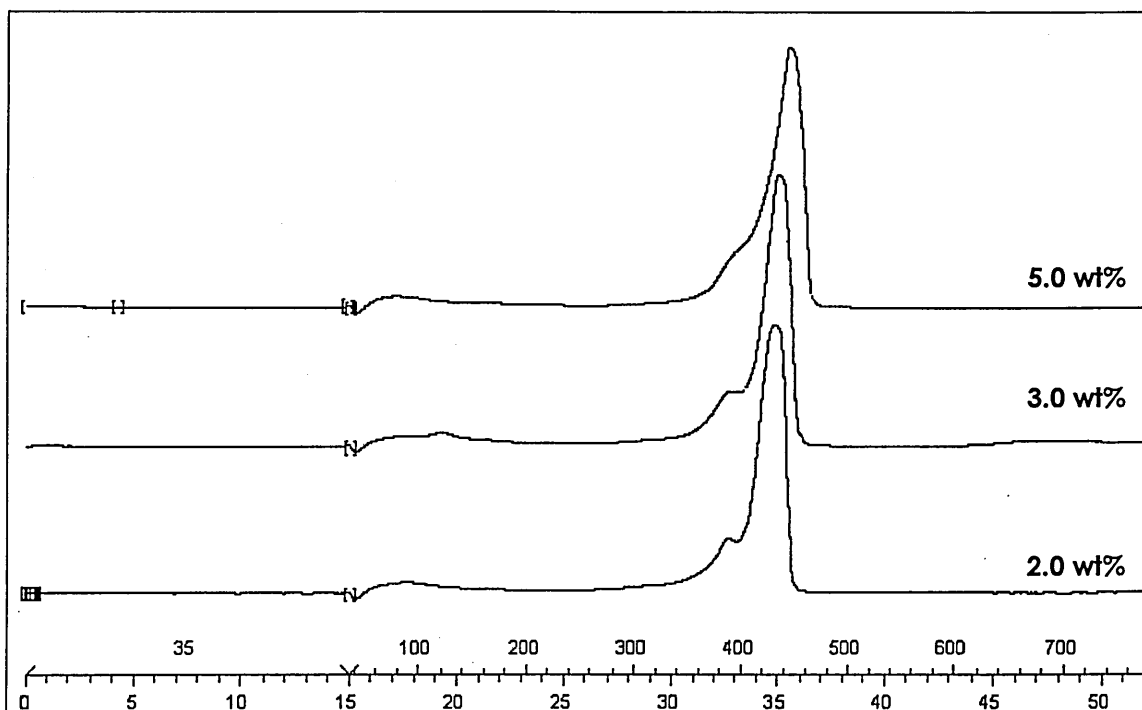

Figure 4.23   DTG traces for PSCN, initiated with AIBN, with the concentration C15A organoclay 2.0, 3.0 and 5.0 wt%.

The DTG traces in fig. 4.21 and 4.22 exemplified the previous data sets that were shown as plots. These traces show the Tmax as the apex of an asymmetric maximum which had a bias towards other thermal events occurring at temperatures closer to the Tmax of styrene.
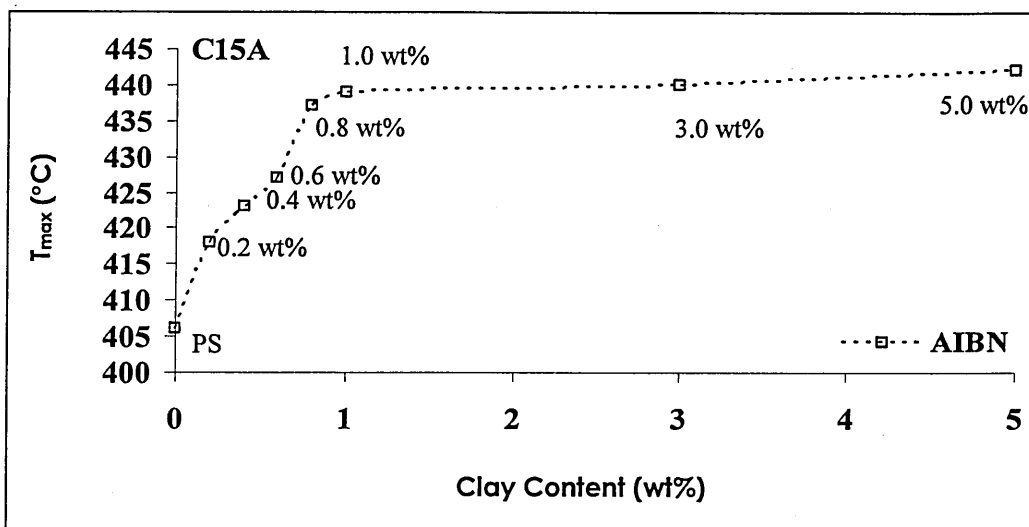

Figure 4.24 **Plot of DTG Tmax values for PSCN initiated with AIBN with C15A organoclay loading increasing from 0 - 5.0 wt%.**

4.4.4 General Discussion

All experiments and analysis within these studies were conducted with the aim of gaining a better understanding of the thermal stability offered by these nanocomposite materials. These studies also aimed to clarify any differences between the different polymer-clay suspensions and subsequent preparation techniques. This knowledge would be fundamental in a process attempting to control the nanoscale structure of these materials.

Within the first series of experiments, where the initiator type and quaternary ammonium alkyl chain length were varied a general decrease in Tmax was observed between the initiators of the order of AIBN>BPO>SPS=APS>>AIBA. The Tmax of SPS and APS initiated PSCN were slightly higher than samples initiated by AIBA, but this increase was attributed to longer PS chains being formed by the less reactive SPS and APS initiators over a longer cure duration. The AIBN initiated the polymerisation of the mixture rapidly and any decrease in polymer chain length may have been compensated by a better platelet dispersion.

In studies by Kornmann *et al.* [4.54] on epoxy-clay nanocomposites, three curing agents (a polyoxyalkylene diamine, Jeffamine D-230, and two cycloaliphatic diamines: Amicure bisparaaminocyclohexylmethane (PACM) and 3,3'-dimethylmethylene-di(cyclohexylamine) (3DCM)) were used to produce samples for dynamic mechanical thermal analysis (DMTA). They concluded that the reactivity and the diffusion rate of the curing agents had a direct influence on the balance between the intragallery polymerisation and the extragallery (bulk) polymerisation. The more reactive Jeffamine D-230 produced PS with a lower glass transition (Tg) temperature (100 °C) compared with PACM with a Tg of 179 °C and 3DCM which had a Tg of 187 °C. When they increased the curing temperature to balance the reactivity order of the initiators, the octadecylammonium compatibiliser was thought to have degraded. They also noted that as the organoclay concentration was increased between 5-12 wt% in the 3DCM samples, the Tg gradually decreased due to a reduction in polymer mobility, which may have been the result of agglomeration of clay platelets, but no XRD analysis was shown in support.

Measurements performed on two epoxy systems showed that the largest improvements in modulus with clay content are obtained for an epoxy resin cured with a an aliphatic curing agent with relatively low reactivity. In such an epoxy system, the largest extent of exfoliation was observed. The corresponding larger degree of silicate layer dispersion correlated with a higher modulus of the material [4.54].

During this and previous studies Kornmann *et al.* [4.55, 4.56] have also reported that the use of excess initiator species had no effect on the Tg. However, when initiator concentrations were increased in the PSCN of this study, decreases were observed relative to the increased concentration.

Doh & Cho [4.11] mixed 1 wt% equivalents of Na-MMT, C15A, C25A (dimethyl, hydrogenated tallow, 2-ethylhexyl quaternary ammonium) and C10A organoclays with PS

to create hybrid composite materials. They reported an increased d_{001} for all organoclays (table 4.14), however, these results contrast with those reported here in many ways, because at 1 wt% it was possible to expand the clay layers in all but Na-MMT to > 43.3 Å, in samples prepared for this thesis.

org-MMT	d_{001} of org-MMT	d_{001} of PS/org-MMT hybrids	Δd
C10A	19.1 Å	34.0 Å	14.9 Å
C25A	20.4 Å	28.5 Å	8.1 Å
C15A	32.7 Å	32.9 Å	0.2 Å
Na-MMT	11.8 Å	14.2 Å	2.4 Å

Table 4.14   XRD results reported by Doh and Cho [4.11].

As was seen during Doh & Cho's study, the addition of higher loadings of Na-MMT to PS showed very little change in the thermal desorption onset temperature (i.e. ~ 410 °C). The decomposition onset temperature for C15A and C25A showed a dependency on the org-MMT loading (i.e. as seen in the relationship between T_{max} and clay loading (fig. 4.23)). TGA analysis of Doh & Cho's samples with organoclay loadings in the range of 0.2-3.0 wt% showed that the decomposition onset temperature increased markedly with clay loading to 0.5 wt%/430 °C from where the increase in onset of thermal desorption was gradual. In this thesis, a similar type of effect was shown, but not until approximately 1.0 wt%/~440 °C (fig. 4.23).

Doh & Cho's results also showed the C10A samples to have much higher decomposition onset temperatures at a clay loading of 0.3 wt% when compared with C15A. This does not necessarily contradict the results found in this thesis, however the T_{max} for C10A occurred at slightly lower temperatures than all the other samples reported here. Which suggested that the similarity of the benzene ring on the C10A cation to the PS monomer had no beneficial effect on the exfoliation of the organoclay, as was stated by Doh & Cho.

Wilkie *et al.* [4.57] showed a 50 % weight loss from PS-C10A (3 wt%) nanocomposites produced by *in-situ* polymerisation with AIBN to be approximately 40 °C higher than the thermal desorption onset at 396 °C (i.e. 435 °C). This equated to approximately the same value as that seen in table 4.13, but Wilkie did state that the particular preparative technique that is used has a large effect on the type of material that is produced and the results obtained from it.

4.4.5 Summary of Results for PSCN

- AIBN was shown to be the best initiator from the series of different types of initiators chosen. The relative effectiveness of these various initiators for the production of the most thermally stable PSCNs was AIBN > BPO > SPS > APS >>AIBA. This was thought to be due to the less bulky and more reactive AIBN being intercalated more easily, leading to intimate polymerisation within the galleries.

- Lower initiator concentrations were shown to be most effective at producing PSCNs with higher thermal stability. 0.5 wt% of initiator and concentrations above and below this may have been better amounts to use for this study, however, the results obtained in this thesis still give a strong indication of the effect of changing associated PSCN variables.

- Lower organic modifier concentrations in combination with less bulky organocations (i.e. single linear alkyl chain) showed higher T_{max} values. The relative effectiveness of these various organoclays for the production of more thermally stable PSCNs was MCBP-C_n > C15A > C20A >> C10A. A possible reason for the lower efficacy of the commercially available organoclays may have been the congestion of the MMT galleries with alkyl chains, which may lead to them being relatively inflexible. This physical state may have reduced the migration of monomer into the gallery spaces.

- The preparation method appeared to be effective at producing exfoliated nanocomposites, up to 1 wt% of the various organoclays using AIBN and BPO as initiators. The MCBP-C_n PSCNs remained exfoliated up to 5 wt%, they also showed higher thermal stability when compared with the commercial products, which XRD results showed to remain stacked at organoclay loadings > 1 wt%.

4.5 **One-pot synthesis of PSCN produced from the reaction of Na-MMT, Decanamide and Styrene Monomer**

4.5.1 Introduction

This study aimed to report on the preparation of nanocomposites from an original "one-pot" reactive process which started with the Na+-form of MMT. An efficient one-pot synthesis method would encapsulate all PSCN components simultaneously in a mixture which would then be chemically or physically driven towards the formation of a PSCN. Such a method would potentially provide an economic advantage through cost reduction, be more efficient and reduce environmental impact through reduced process manufacture.

This particular study aimed to produce a nanocomposite via a one-pot synthesis in which an alkylamide was used to bind to the gallery cations of Na-MMT, when dispersed in styrene monomer with the layered material. The carbonyl groups of Dimethylformamide (DMF) [4.58] and *N*-Methylformamide (NMF) [4.59] molecules adsorbed within the galleries of MMT have been shown to bind with increasing strength to gallery cations with increasing charge, which was indicated as the thermal stability decreased as Mg > Ca > Na. It was thought that when sufficient intercalated alkylamide was adsorbed between amide swollen platelets, the distance between the gallery surfaces would expand (between 5-100 Å), preferably in the range 10-45 Å, so that the clay platelets could be delaminated into individual platelets when polymerisation occurred throughout the gallery spaces [4.60]. Due to decanamide's a high melting point (i.e. range 95.5 - 99.2 °C) and insolubility, a method for dispersion of decanamide within the clay gallery needed to be formulated.

4.5.2 Physical Characterisation - Decanamide
Structure:
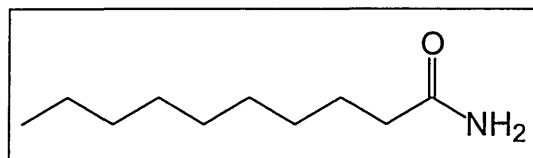
Synonyms: *n*-decanamide, capramide, decylamide, decanoic acid amide.

Formula: $C_{10}H_{21}NO$ **Mw:** 171.28   **CAS:** 2319-29-1

4.5.3 Experimental Method

Due to the nature of the *in-situ* polymerisation process being used to produce PSCNs, the formation of a pre-polymer required that the styrene-organoclay mixture would be heated to temperatures in excess of 100 °C, above the melting point of decanamide. The OPS reaction mixture consisted of styrene, Na-MMT (1 wt%), decanamide (1 wt%) and AIBN (0.5 wt%). These components were mixed together in the dark for 5 min/200 rpm at 110 °C/N_2, were then cooled to RT, and then heated for 5 min/80 °C/N_2 before curing for 48 h/60 °C in an oven.

The composite products were translucent and showed no visible trace of clay agglomerates, however, there was a slight yellowing of the sample which could have been due to decanamide content. Although compensated by polymerisation in the dark, it is well known that polystyrene undergoes light-induced yellowing, the origin of this colouration is not clear, but is variously attributed to conjugated polyene, the formation of various oxygenated species, or the products of ring-opening reactions [4.61].

4.5.4 Results

4.5.4.1 XRD Analysis

Multiple XRD traces showed that although the MMT was uniformly dispersed, the *d*-spacing of the MMT interlayer had been expanded from 11.8 Å to between 36.2-> 43.3 Å. This expansion was evidence that decanamide had preferentially entered the gallery spaces of the clay (fig. 4.25).

The greatest increase in *d*-spacing appeared to occur when the decanamide and Na-MMT concentrations were similar (fig. 4.26). When the concentration of the clay was increased the d_{001} could be seen to gradually decrease as there was a deficit in the concentration of decanamide for intercalation at the collectively much larger gallery surface area.
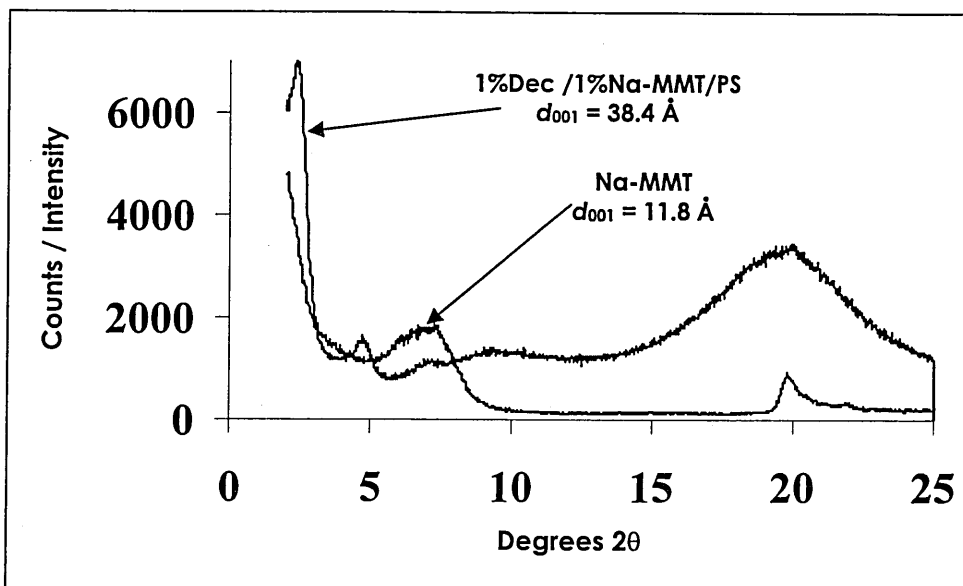
Figure 4.25   Comparison of XRD traces for Na-MMT before (d_{001} = 11.8 Å) and after (d_{001} = 38.4 Å) dispersal in the one-pot synthesis/decanamide mixture.
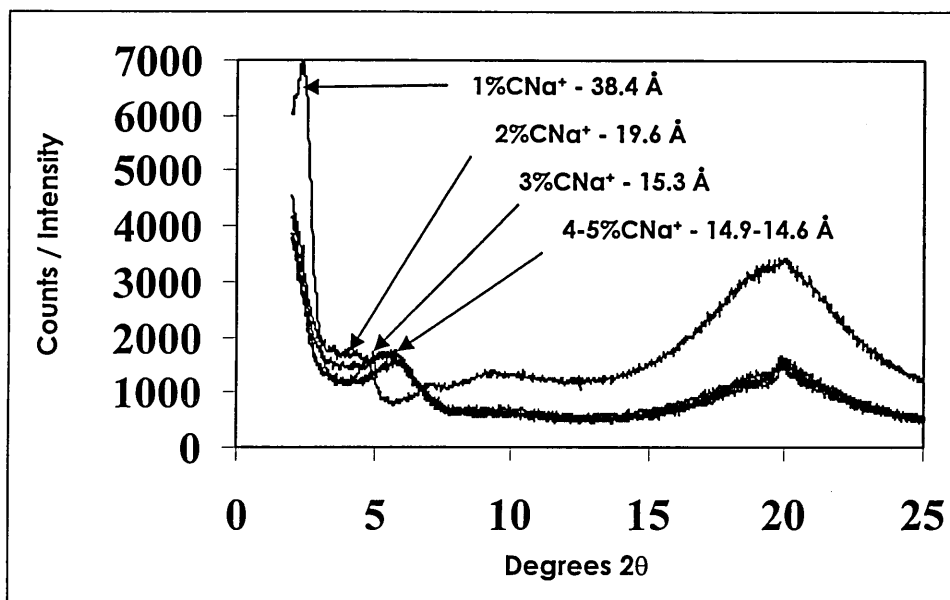

Figure 4.26   Comparison of XRD traces for one-pot synthesis/decanamide (1 wt%) samples with increasing Na-MMT concentrations, with d_{001} decreasing from 38.41 Å to 14.63 Å (Cu-XRD).

Experiments to identify further d_{001} increases with increased concentrations of decanamide (i.e. 2-5 wt%) were obstructed by the limitations of the x-ray diffractometer. No signals were seen above 43.3 Å, but as the concentration of decanamide was increased a precipitate deposited at the bottom of the polymer mould with increasing depth. This indicated that

when 1 wt% of Na-MMT and decanamide were dispersed in PS the gallery cations were satiated. When the concentration of decanamide in the one-pot synthesis mixture was increased to >1 wt%, the greater the concentration of alkylamide within the system the less well dispersed it appeared within the one-pot synthesis mixture and the subsequent composites that were formed.

4.5.4.2 TG Analysis

TGA/DTG analysis showed that when the concentrations of Na-MMT and decanamide were equivalent, that the composite materials showed a 15 °C shift from a $T_{max} = 405$ °C for PS to a $T_{max} = 420$ °C. As the concentration of Na-MMT was increased, the T_{max} decreased until at 5 wt% Na-MMT the T_{max} was less than that of PS (i.e. $T_{max} = 395$ °C) (fig. 4.27/4.28). This would have been due to the increased presence of agglomerated Na-MMT, and so, the clay platelets would not have been in intimate contact with the PS matrix, which led to a decrease in the PSCN thermal stability.
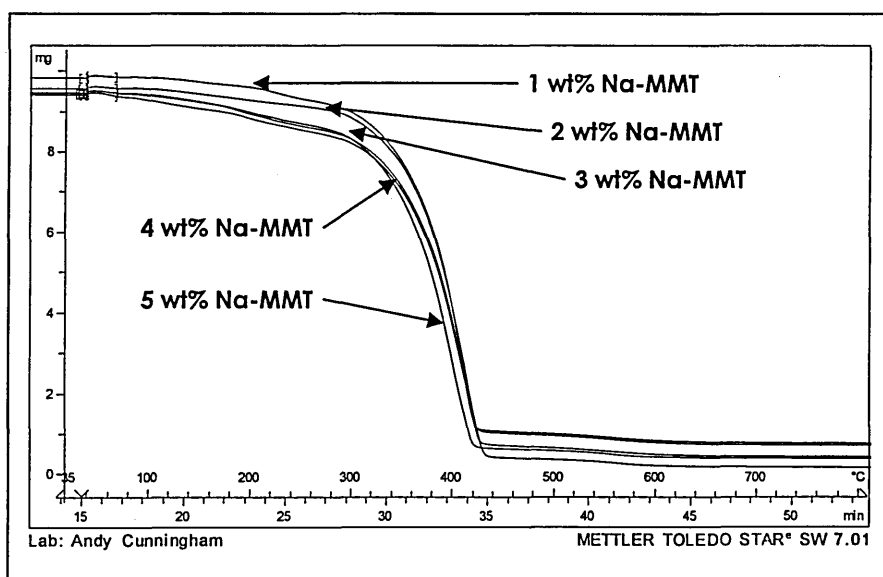

Figure 4.27 One-pot synthesis/decanamide TGA traces for samples with increasing [Na-MMT], showing most evidently increasing weight loss at the 5 % level.
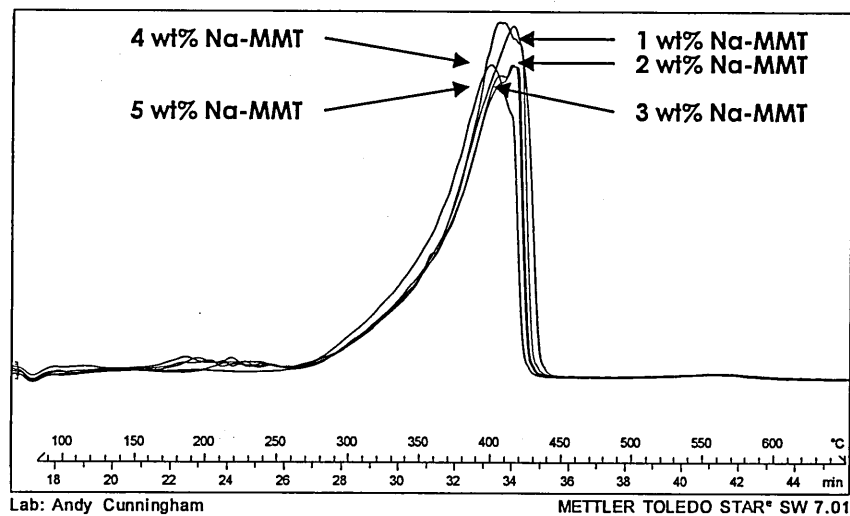
Figure 4.28   DTG traces of one-pot synthesis/decanamide (relative to fig. 4.26).

The onset of sample decomposition (i.e. approximately 275 °C) started much earlier for this set of samples than in the samples studied in section 4.4 which generally showed a thermal desorption onset temperature of between 325-350 °C. Lower concentrations of alkylamide would need to be exchanged with future samples to see what effect this ratio of alkylamide to Na-MMT would have on d_{001}, T_{onset}, T_{max} and T_{end}.

4.5.5   Discussion

The expansion of Na-MMT by decanamide in a PS matrix appeared to have been successful in these preliminary one-pot synthesis experiments. The XRD and TGA analysis showed the need for a balance between the concentration of Na-MMT and the adsorbed alkylamide. It was also shown that the presence of agglomerated clay platelets tended to decrease the thermal stability of the matrix, as can be seen specifically by the T_{max}, but also by the T_{end} values in fig. 4.29.

Like a previous example to formulate a one-pot synthesis procedure [4.62], this study has demonstrated the ability to prepare PS-based nanocomposites by *in-situ* polymerisation from Na-MMT in a one-pot reactive process. However in this study, decanamide (an

uncharged surfactant) was used to compatibilise Na-MMT with the PS matrix, whereas in the previous study, an organocation was used.
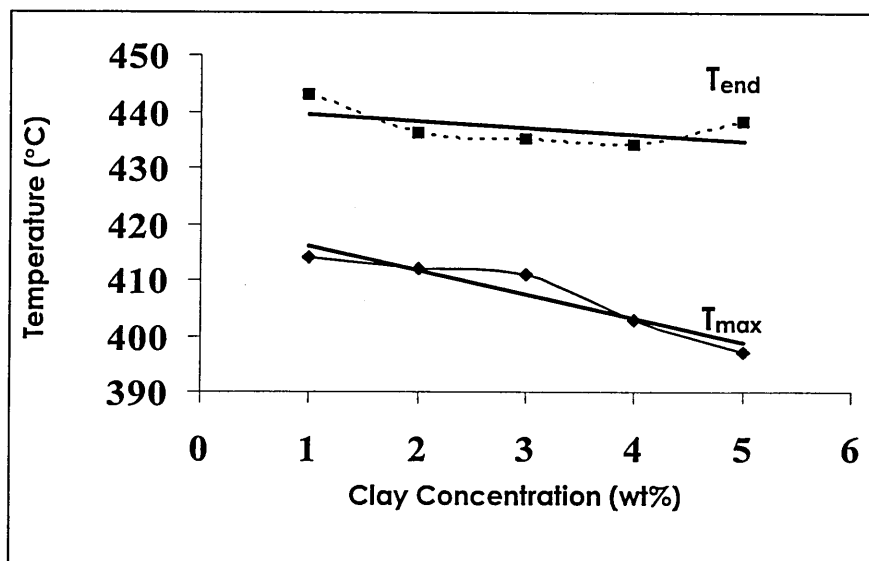

Figure 4.29 T$_{max}$ and T$_{end}$ temperatures for the one-pot synthesis/decanamide samples with increasing [Na-MMT].

4.6 **The production of PSCN from MMT compatibilised with**

N-vinylformamide (NVF)

4.6.1 **Introduction**

In previous studies conducted by Breen *et al.*, vapour phase DMF [4.58] and NMF [4.59] were shown to expand the gallery spaces of MMT (SWy-2) exchanged with different interlayer cations. This work showed that intercalating amide molecules would bind strongly to different exchange cations and that the configuration of the amide molecules changed with the type of cation and the duration of exposure.

The aim of this study was to intercalate N-vinylformamide (NVF) within the galleries of Na-MMT as a liquid phase amide molecule, with the vinyl group adding molecular functionality. Because NVF is miscible with water at RT the probability of the adsorption of NVF into the clay galleries was thought to be high. When sufficient NVF was adsorbed to the cations in the gallery, the interlayer space would expand slightly, but not as much as with alkylammonium surfactants. The prospective view of this pre-polymer mixture was that

the functional vinyl group would be incorporated in the bulk polymerisation of PS and possibly encourage the polymer matrix to penetrate into the gallery spaces.

4.6.2   Physical Characterisation - *N*-vinylformamide (NVF)
Structure:
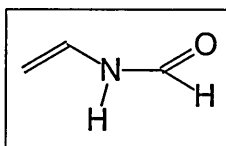
Formula: C_3H_5NO **Mw:**   71.1   **CAS:**   13162-05-5

4.6.3   Experimental Method

NVF is a liquid at RT (i.e. Mpt -15 °C) and is readily soluble in water. The production of PSCN was attempted by using two methods. Firstly, the formation of an NVF intercalated Na-MMT organoclay prior to the addition of styrene monomer was attempted. Na-MMT and NVF were mixed overnight in de-ionised water at RT, then vacuum filtered, dried and ground, before being analysed. Secondly, a one-pot synthesis method was applied; in this method styrene monomer, Na-MMT, NVF, 0.5 wt% AIBN were mixed together at high speed for 1, 8 and 24 hrs and were subjected to the polymerisation, and cure profiles established with standard PSCN.

4.6.4   Results

Following the intercalation of NVF, any excess space filling NVF had to be thermally desorbed from the propped MMT galleries to create 'free space' for any styrene monomer that could subsequently be intercalated into the organoclay (fig. 4.30).

When Na-MMT was intercalated with NVF at a loading of 0.8 mmol g^{-1}, a solid waxy clay product was formed, which was easily miscible with water. The XRD spectra for the Na-MMT intercalated with NVF, at 0.8 mmol g^{-1}, showed a d_{001} = 23.2 Å; this indicated an interlayer expansion of 11.5 Å (fig. 4.31). XRD analysis of this organoclay after heating,

showed a *d*-spacing of approximately 23.0 Å, which indicated that the MMT galleries were propped by NVF associated with sodium cations.
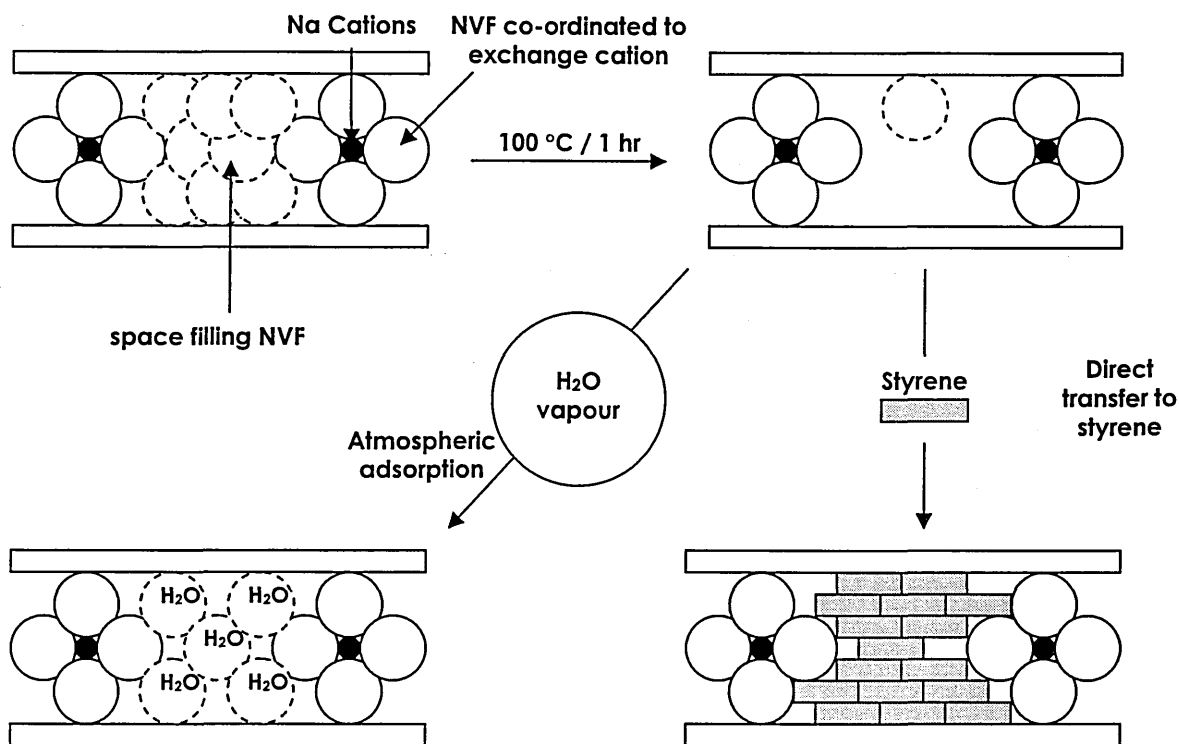

Figure 4.30 Schematic diagram of the relationship between NVF, H_2O and styrene within the gallery spaces of NVF-MMT propped by NVF associated with interlayer cations.
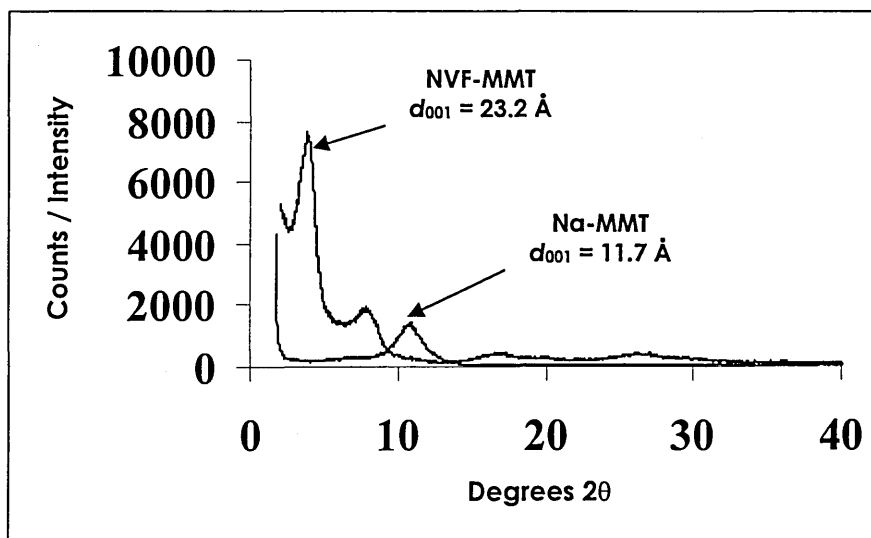

Figure 4.31 XRD traces for MMT before (d_{001} = 11.7 Å) and after intercalation by NVF at a loading of 0.8 mmol g^{-1} (d_{001} = 23.2 Å).

Thermal analysis (TGA) of these samples identified two distinct thermal maxima, at 130 °C

and 260 °C. The material constituting the first maximum at 130 °C was partially, and then

fully removed by heating at 60 °C/1hr and 100 °C/1hr, respectively (fig. 4.32).
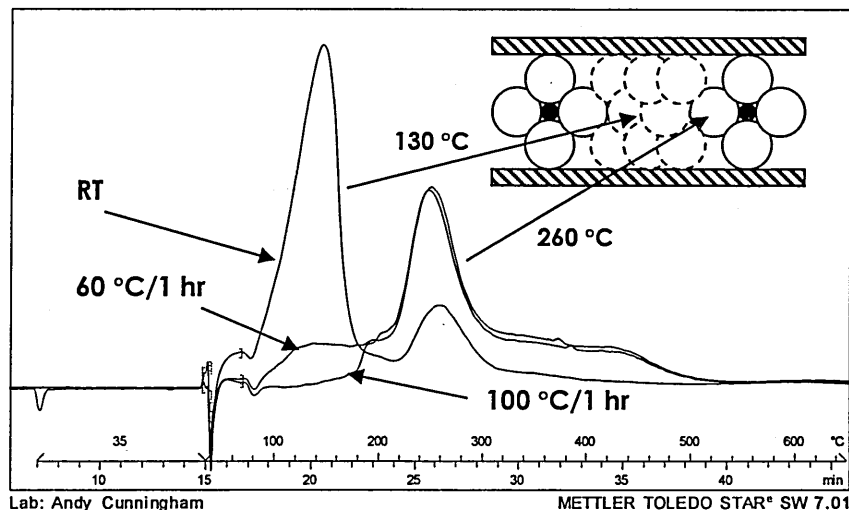

Lab: Andy Cunningham   METTLER TOLEDO STAR^e SW 7.01

Figure 4.32   **DTG traces for Na-MMT/NVF [0.8 mmol g^{-1}] and samples heated at 60°C/1hr and 100°C/1hr.**

From correlations with the XRD data of the intercalated clay, before and after heating, the

first thermal event was thought to be due to the loss of the space filling NVF not associated

with cationic centres, whilst the second thermal event was due to the loss strongly

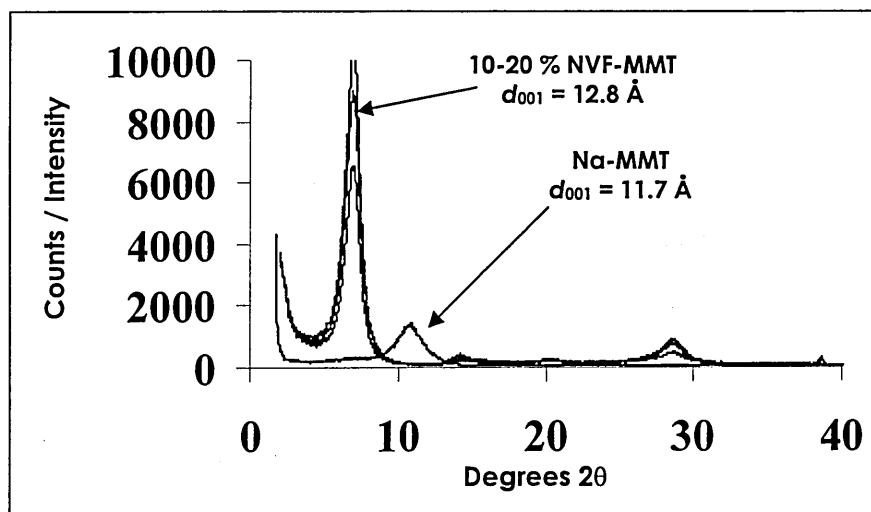attracted NVF from around the exchange cations.

Figure 4.33   **Comparison of XRD traces for Na-MMT before (d_{001} = 11.7 Å) and after (d_{001} = 12.8 Å) dispersal in the NVF-one-pot synthesis mixtures.**

With excess NVF being easily removed, it was thought it may be possible to expand the clay galleries with an NVF concentration similar to that which was lost at the second event (260 °C), between 10-20 %. Na-MMT was exchanged in deionised water with 10, 15 and 20 % of NVF [0.8 mmol g⁻¹]. The XRD traces showed that the gallery spaces of the MMT were only slightly expanded (approx. 1 Å), indicating that very little had entered the gallery (fig. 4.33).
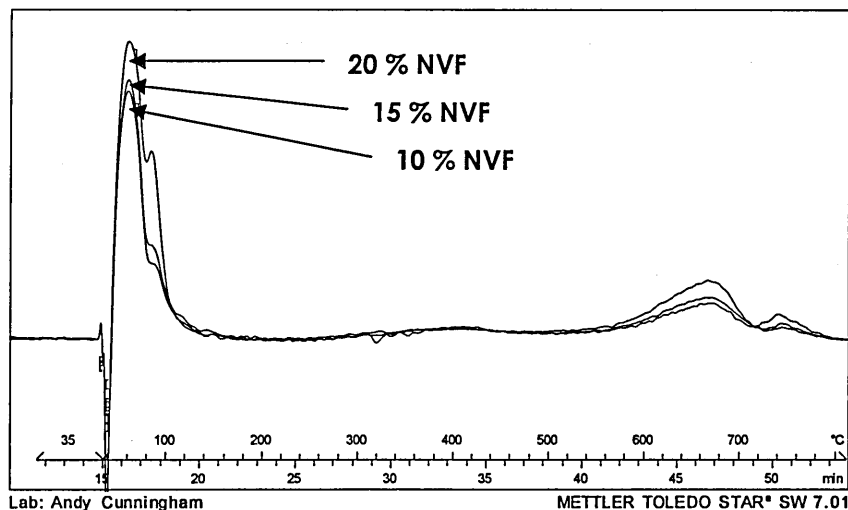

Figure 4.34   DTG traces for NVF-MMT (10, 15, 20 %).

This was confirmed by TGA which saw the majority of weight loss from the three samples occurring around and below 100 °C, however, there were traces of NVF being evolved between 350-450 °C (fig. 4.34). This seemed to confirm that the extent and speed of intercalation was on one level dependent on the concentration of free amide molecules in solution.

All initial attempts to produce a dispersed PS/Na-MMT/NVF nanocomposite were unsuccessful, with the MMT agglomerating within the host matrix. This agglomeration occurred when the MMT and NVF were added directly to the styrene monomer, and when MMT pre-expanded with NVF was added as organoclays before and after heat treatment (at 100 °C/1 hr) to remove space filling NVF.

The TGA analysis of the Na-MMT exchanged with NVF at a loading of 0.8 mmol g^{-1} had previously shown two significant thermal events. To remove any space filling NVF and associated water from the samples, they were heated at 100 °C/1 hr. Then the heat treated NVF exchanged sample was transferred directly into PS (to significantly reduce water adsorption) (fig. 4.30). The components were then mixed together in the dark for 5 min/200 rpm at 110 °C/N$_2$, were then cooled to RT, then heated for 5 min/80 °C/N$_2$ before curing for 48 h/60 °C in an oven. The clay was well dispersed throughout the sample but faintly visible. The XRD data (fig. 4.35) showed a d_{001} at 25.7 Å, which indicated that the galleries had been slightly swollen when they were mixed with styrene.
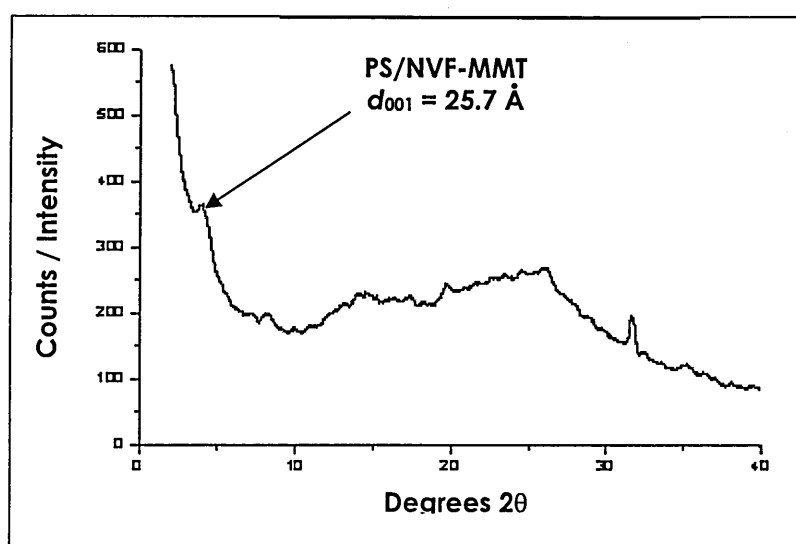

Figure 4.35   XRD trace for PS/NVF-MMT nanocomposite, formulated after heating NVF-MMT at 100 °C/1 hr (d_{001} = 25.7 Å).
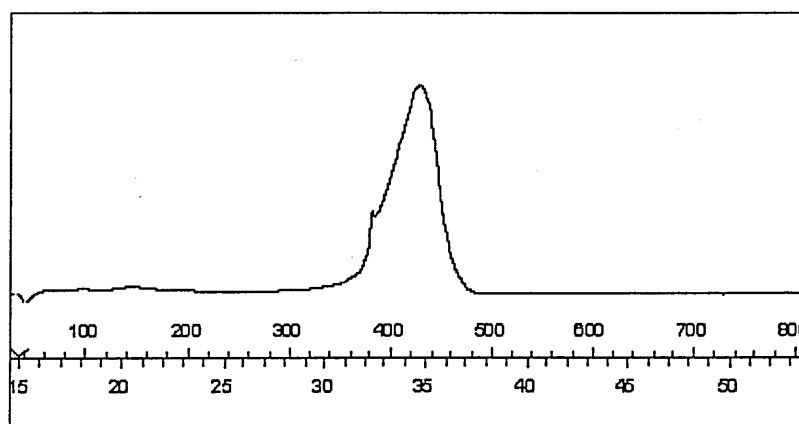

Figure 4.36   DTG trace for PS/NVF-MMT nanocomposite (T_{max} = 427 °C).

Although this process did not lead to the production of an exfoliated PSCN, it did produce a well dispersed intercalated clay phase in the PS and transposed a certain degree of thermal stability on the PS host matrix seen by shifting the T_{max} > +20 °C (fig. 4.36).

4.6.5 Discussion/Conclusions

The expansion of the MMT gallery was shown to be promising in the NVF-MMT samples, with a possibility that the functional NVF molecules inserted in the interlayer would participate in the polymerisation process with the styrene monomers. The initial attempts to produce a PSCN were disappointing, with the reason for the agglomeration of clay platelets in the PS matrix being attributed to space filling NVF and water being present in the MMT gallery, hence styrene could not penetrate the gallery. In the additive organoclay experiments, this leads to hindrance of the polymerisation throughout the gallery spaces which would have driven an increased rate of polymerisation in the bulk rather than through the clay galleries, where the NVF was held (in one phase) to be thermally stable until approximately 260 °C.

The production process then aimed to remove this space filling matter for the creation of a clear homogeneous environment for the polymerisation of NVF with PS. This process is outlined in fig. 4.30. The removal of the space filling NVF and water led to a uniform dispersal of the NVF-MMT throughout the PS matrix. However, the lack of a substantially increased *d*-spacing in the PSCN may have been an indication that the concentration of PS within the galleries was limited. This led to the assumption that the polymerisation throughout the galleries was predominantly between NVF molecules which were bonded to the PS matrix at the gallery edges and homogeneously dispersed as the PS chains were propagated.

4.7   **The formulation of PSCN from MMT compatibilised by the amphoteric surfactant - Foamtaine Scab**

4.7.1   **Introduction**

The premise was that an amphoteric surfactant (i.e. Foamtaine SCAB (FS)) would migrate to cation exchange sites at the gallery surfaces of Na-MMT. The quaternary ammonium molecule would be preferentially adsorbed to the gallery surface of the MMT, displacing the sodium cations. When sufficient intercalated monomer was adsorbed between the adjacent platelets, the distance between the gallery surfaces would expand, preferably in the range 10-45 Å, so that the organoclay could be exfoliated into individual platelets when polymerisation occurred through the gallery spaces.

Amphoteric surfactants possess both cationic and anionic groups, they form cations in acidic solutions, anions in alkaline solutions, and in the mid-pH range they become zwitterions. The associations between amphoteric surfactants and saponite clays have been previously reported [4.63, 4.64] and showed that the hydroxyls on the surface of the clay galleries lead to the surfactants being attracted in both cationic and zwitterionic states.

Because the properties of amphoteric surfactants are often used for foaming, wetting and emulsification they have numerous applications in cosmetic and personal hygiene products. The amphoteric surfactant that was exchanged with MMT was Foamtaine SCAB (FS) (see section 4.7.2), which is commonly used in many of the applications previously described. To exchange MMT with such a surfactant would have led to the possible production of PSCN materials which would have many legislative and financial advantages for commercial plastics applications.
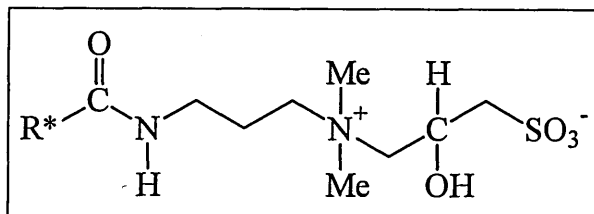
Structure: R* = 'coco' radical

Chem. name: N-[3-(cocamido)-propyl]-N-(2-hydroxy-3-sulfopropyl)-N,N-di-methyl

quaternary ammonium compounds, hydroxide, inner salts

Synonyms: cocamidopropyl hydroxy sultaine, cocamidopropyl betaine

Formula: $C_{20}H_{42}N_2O_5S$ **Mw:**   422.62   **CAS:**   68139-30-0

4.7.3   Results

4.7.3.1   XRD Analysis

When Na-MMT was exchanged with FS at 1 x CEC the resulting product was a soft, off-white solid, which was easily miscible with water.

The XRD traces for MMT expanded with FS at a loading of 1 x CEC showed an increase in d_{001} of approximately 10.6 Å, to 22.32 Å (fig. 4.37).
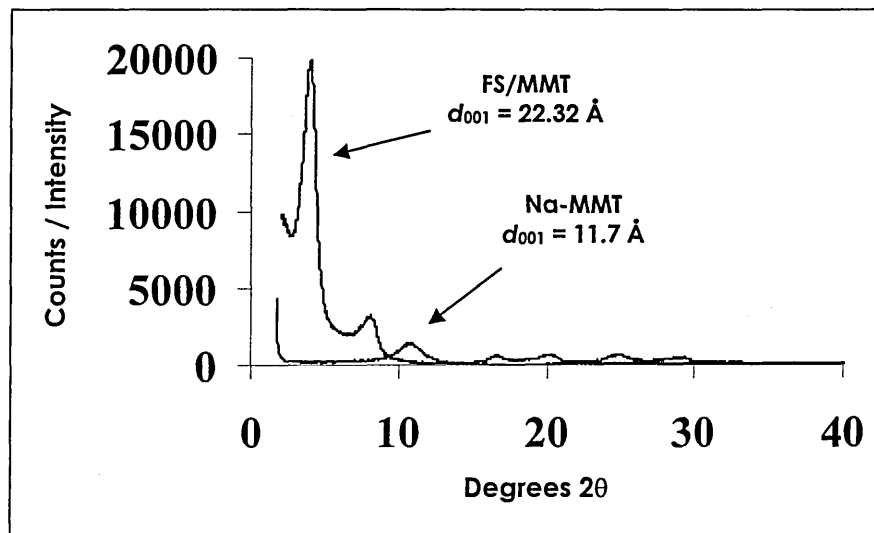

Figure 4.37   XRD traces for Na-MMT before (d_{001} = 11.7 Å) and after dispersal in FS at [1 x CEC] (d_{001} = 22.32 Å).

4.7.3.2 TG Analysis

TG analysis of the FS/MMT organoclays identified weight loss events at approximately 320 °C which appeared to conceal two maxima at 320 °C and 340 °C (appearing as a shoulder in the DTG, fig. 4.38).

All attempts to produce a FS-PS-clay nanocomposite were not successful, with the MMT agglomerating in all samples. This agglomeration occurred when the FS and MMT were added directly to the styrene monomer, and when the FS/MMT organoclays were added after being pre-formulated.
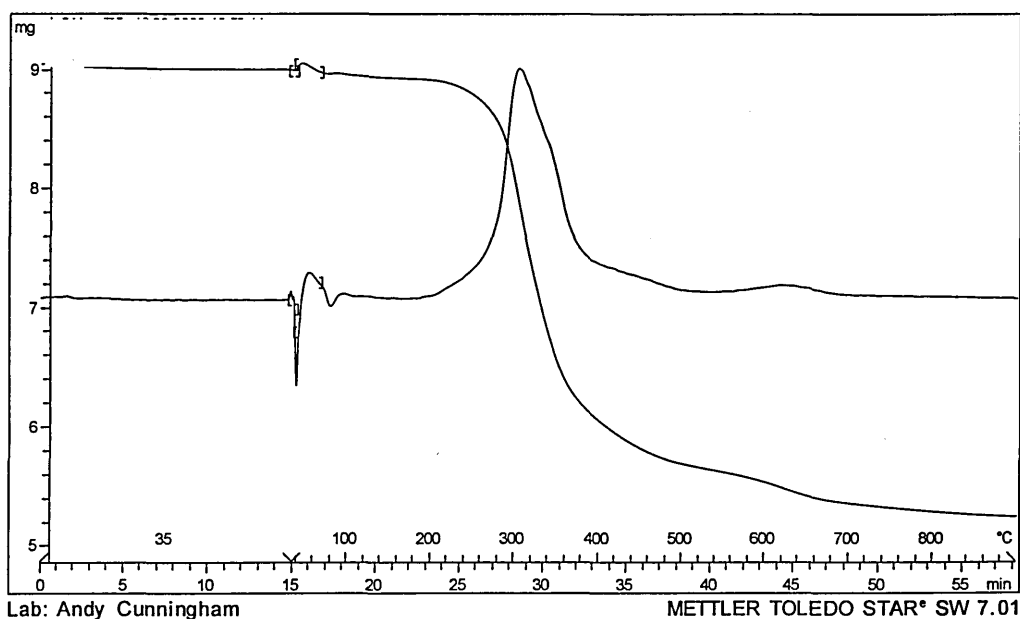

Lab: Andy Cunningham   METTLER TOLEDO STAR® SW 7.01

Figure 4.38   TGA/DTG traces for FS/Na-MMT [1 x CEC].

4.7.4   Discussion/Conclusions

The expansion of the MMT gallery in the FS/MMT samples was comparable with that of the NVF samples. The relatively high thermal stability of the FS amphoteric surfactant showed promise for the application of the organoclay with various processing methods and polymeric systems. The lack of a dispersed MMT phase in all attempts to produce PSCNs may have been due to many reasons:

- The large molecular weight of the surfactant may have hindered monomer and initiator migration into the galleries, increasing the rate of polymerisation in the bulk rather than through the clay galleries.

- The variety of charge carried on the surfactant molecules may have attracted associated water until higher temperatures, or may lead to a variety of phases within the galleries.

- The FS in FS/MMT was held thermally stable until approximately 300 °C, which was much higher than the production process used.

The presence of the agglomerated MMT platelets was again shown to decrease the thermal stability of the PS material.

4.8   Summary of Results for PSCN Formulated by OPS and Novel Methods

- A one-pot method for the production of PSCN, by the *in-situ* polymerisation of PS in the presence of decanamide (an uncharged surfactant) and Na-MMT, was shown to be successful.   When mixed, the alkylamides preferentially migrated to bind with the inorganic cations in the galleries of Na-MMT.

- XRD and TGA analysis of these PSCN showed the need for a balance between the concentrations of alkylamide and Na-MMT to optimise the *d*-spacing ($\geq$ 38.4 Å) and T_{max} (shifted +15-20 °C). An imbalance was seen to lead to the presence of agglomerated clay platelets which decreased the thermal stability of the PSCN matrix.

- A one-pot method for the production of PSCN incorporating NVF molecules, has to date been less successful than the study incorporating alkylamide. In parallel experiments, attempts to produce PSCNs from NVF-MMT organoclays resulted in MMT remaining stacked in the PS matrix. This lack of dispersion was attributed to space-filling NVF and water being present in the

241

MMT gallery, and so, styrene monomer could not penetrate the congested gallery. XRD and TG analysis identified the slight expansion of the MMT galleries by NVF and the presence of two states within the galleries, with NVF directly associated with the Na cations held thermally stable until 260 °C and interstitial space-filling NVF which was thermally stable until approximately 130 °C.

- The removal of the space filling NVF and water led to a uniform dispersal of the NVF-MMT throughout the PS matrix (n.b. shifting the T_{max} > +20 °C). However, the lack of a substantially increased d-spacing in the PSCN (i.e. 25.7 Å) may have indicated that the concentration of PS within the galleries was limited. It was thought that polymerisation throughout the galleries was predominantly between NVF molecules bonded at the gallery edges to the PS matrix and homogeneously dispersed as PS chain growth propagated.

- The one-pot method for the production of FS-MMT PSCNs has so-far been unsuccessful. In parallel experiments, the expansion of the MMT gallery in FS-MMT organoclays was shown to be comparable with that of the NVF samples (i.e. expanded by 10.6 Å, to 22.32 Å). These samples also showed that the FS amphoteric surfactant had a relatively high thermal stability (i.e. T_{max} = 320 °C) which showed promise for its application with various processing methods and polymeric systems. However, in all attempts to produce PSCNs the organoclay phase failed to disperse in a PS host matrix. This may have been due to the large molecular weight of the surfactant, the variety of charge carried on the surfactant molecules or the thermal stability of FS in the MMT galleries, which was higher than the production process used.

Chapter 4 - References

[4.1]   Dubois P. & Alexandre M., *Mat. Sci. Eng.*, 2000, **28**, 1.

[4.2]   Gilman J., *App. Clay Sci.*, 1999, **15**, 31.

[4.3]   NIST (National Institute of Standards and Technology): Building and Fire Research Laboratory, last accessed 02/28/2001, URL: http://www.bfrl.nist.gov/objectives/fsm/FSM_od2000.htm.

[4.4]   Odian, G., *Principles of Polymerization 3rd Ed.*, Chapters 1 & 3, John Wiley & Sons, Inc., New York, 1993.

[4.5]   Ring, K-L., .Polystyrene., *Chemical Economics Handbook*, 580.1500B . 580.1502C, Menlo Park, Ca., 1998.

[4.6]   Polystyrene - The International Market 2003, Gobi International Report (2003), Last accessed 21.2.2003, URL: http://www.gobi.co.uk/pdfs/Polystyrene.PDF

[4.7]   Kato, C.; Kuroda, K.; Takahara, H., *Clays Clay Miner.*, 1981, **29**, 294.

[4.8]   Moet, A.; Akelah, A., *J. Mater. Sci.*, 1996, **28**, 3589.

[4.9]   Moet, A.; Akelah, A., *Mater Lett.*, 1993, **18**, 97.

[4.10]   Akelah, A., Rehab, A., Selim, A. & Agag, A., *J. Mol. Cat.*, 1994, **94**, 311.

[4.11]   Doh, J. G.; Cho, I., *Polym. Bull.*, 1998, **41**, 511.

[4.12]   Dong, C. L.; Lee, W. J., *J. Appl. Polym. Sci.*, 1996, **61**, 1117.

[4.13]   Claudia, F., Marco, G., Silvia, G., Giacomo, R., Carlo, A. V. & Bernardo, M., *Polymer*, 1998, **39**, 2651.

[4.14]   Luca, B., Mauro, A., Giacomo, R. & Francesco, C., *Polymer*, 1994, **35**, 3296.

[4.15]   Al-Esaimi, M. M., *J. Appl. Polym. Sci.*, 1997, 367.

[4.16]   Sugahara, Y., Satokawa, S., Kuroda, K. & Kato, C., *Clays Clay Miner.*, 1988, **36**, 343.

[4.17]   Bergaya, F. & Kooli, F., *Clay Miner.*, 1991, **26**, 33.

[4.18]   Friedlander H.Z. & Grink C.R., *J. Poly. Sci., Poly. Lett.*, 1964, **2**, 475.

[4.19]   Blumstein A., *J. Polym. Sci.*, Part A 3, 1965, 2653.

[4.20]   Kato C., Kuroda K. & Takahara H., *Clays Clay Miner.*,1981, **29**, 294.

[4.21]   Kelly P., Moet A. & Qutubuddin S., *J. Mater. Sci.*, 1994, **29**, 2274.

[4.22]   Akelah A. & Moet A., *J. Mater. Sci.*, 1996, **31**, 3189.

[4.23]   Fu X. & Qutubuddin S., *Mat Lett.*, 2000, **42**, 12.

[4.24]   Giannelis E.P., Vaia R. & Ishii H., *Chem. Mater.*, 1993, **5**, 1694.

[4.25]   Vaia R.A., *Chem. Mater.*, 1996, **8**, 2628.

[4.26]   Vaia R.A., *Macromolecules*, 1997, **30**, 8000.

[4.27]   Doh J.G. & Cho I., *Poly. Bull.*, 1998, **41**, 511.

[4.28]   Lee D.C. & Jang L.W., *J. Appl. Polym. Sci.*, 1996, **61**, 1117.

[4.29]   Noh M.W. & Lee D.C., *Poly. Bull.*, 1999, **42**, 619.

[4.30]   O'Neil, G.A. & Torkelson, J.M., *Trends in Polym. Sci.*, 1997, **5**, 349.

[4.31]   Abuin, E. & Lissi, E.A., *J. Macro. Sci. Chem.*, 1977, **A11**, 287.

[4.32]   Balke, S.T. & Hamielec, A.E., *J. Appli. Polym. Sci.*, 1973, **17**, 905.

[4.33]   Cardenas, J.N. & O'Driscoll, K.F., *J. Polym. Sci., Polym. Chem.*, 1976, **14**, 883.

[4.34]   Cardenas, J.N. & O'Driscoll, K.F., *J. Polym. Sci., Polym. Chem.*, 1977, **15**, 1883.

[4.35]   Cardenas, J.N. & O'Driscoll, K.F., *J. Polym. Sci., Polym. Chem.*, 1977, **15**, 2097.

[4.36]   Small, P.A., *Adv. Polym. Sci.*, 1975, **18**, 1.

[4.37]   Turner, D.T., *Macromolecules*, 1977, **10**, 221.

[4.38]   Yamamoto, K. & Sugimoto, M., *J. Macromol. Sci. Chem.*, 1979, **A13**, 1067.

[4.39]   Jongbloed, H.A., Mulder, R.K.S. & Janssen, L.P.B.M., *Polym. Eng. Sci.*, 1995, **35**, 587.

[4.40]   Jongbloed, H.A., Kiewit, J.A., Van Dijk, J.H. & Janssen, L.P.B.M., *Polym. Eng. Sci.*, 1995, **35**, 1569.

[4.41]   O'Driscoll, K.F. & Huang, J., *Eur. Polym. J.*, 1990, **26**, 643.

[4.42]   Epstein, I.R. & Pojman, J.A., *Chaos*, 1999, **9**, 255.

[4.43]   Janssen, L.P.B.M., *Polym. Eng. Sci.*, 1998, **38**, 2010.

[4.44]   Chen, C.Y., Chen, C.S. & Kuo, J.F., *Polymer*, 1987, **28**, 1396.

[4.45]   Saban, M.D., Georges, M.K., Veregin, R.P.N., Hamer & G.K., Kazmaier, P.M., *Macromolecules*, 1995, **28**, 7032.

[4.46]   James, D. H.; Gardner, J. B.; Mueller, E. C., .*Styrene Polymers.*, *Encyclopedia of Polymer Science and Engineering*, 2nd ed., Mark, H. F.; Bikales, N. M.; Overberger, C. G.; Menges, G. Eds., 16, 1-246, Wiley, New York, 1989.

[4.47]   Tien, N. K., Flaschel, E. & Renken, A., *Chem. Eng. Comm.*, 1985, **36**, 251.

[4.48]   Odian, G., *Principles of Polymerisation*, 3rd Ed., Chapters 1 & 3, John Wiley & Sons, Inc., New York, 1993.

[4.49]   Elias, H.G., *An Introduction to Polymer Science*, VCH, Weinheim, 1997.

[4.50]   Sperling, L.H., *Introduction to Physical Polymer Science*, 2nd ed., Wiley, New York, 1992.

[4.51]   Giannelis, E.P., *Adv. Mater.*, 1996, **8**, 29.

[4.52]   Krishnamoorti, R., Vaia, R.A. & Giannelis, E.P., *Chem. Mater.*, 1996, **8**, 1728.

[4.53]   Akelah A. & Moet A., *J. Mater. Sci.*, 1996, **31**, 3589.

[4.54]   Kato C., Kurado K. & Takahara H., *Clays Clay Miner.*, 1981, **29**, 294.

[4.55]   Kornmann, X., Lindberg, H. and Berglund, L.A., *Polymer*, 2001, **42**, 41, 1303.

[4.56]   Kornmann, X., Lindberg, H. and Berglund, L.A., *Polymer*, 2001, **42**, 10, 4493.

[4.57]   Wang, D. and Wilkie, C.A., *Polymer Degradation and Stability*, 2003, **80**, 1, 171.

[4.58]   Breen, C., Clegg, F., Hughes, T.L. and Yarwood, J., *Langmuir*, 2000, **16**, 16, 6488.

[4.59]   Breen, C., Clegg, F., Hughes, T.L. and Yarwood, J., *J. Phys. Chem. B.*, 2001, **105**, 21, 4872.

[4.60]   Beall, G.W., Tsipursky, S. and Vinakour, E., US Patent # 5849830, "*Intercalates and exfoliates formed with N-alkyl amides and/or acrylate-functional pyrrolidone and allylic monomers, oligomers and copolymers and composite materials containing same*", 1998.

[4.61]   Rabek J., *Photodegradation of Polymers: Characteristics and Applications*, Springer Verlag, 1996.

[4.62]   Kojima, Y., Usuki, A., Kawasumi, M., Okada, A., Kurauchi, T. and Kamigaito, O., *J. Polym. Sci. A*, 1993, **31**, 1755.

[4.63]   Navdeep Chemicals PVT Ltd., amphoteric surfactant chemical company product information.

[4.64]   Guo, B., Ouyang, X., Cai, C. and Jia, D., *J. Polym. Sci. B: Polymer Physics*, 2003, **42**, 7, 1192.

5

Unsaturated Polyester-Clay Nanocomposites

—

5.1 Introduction

Unsaturated polyesters are widely used as matrix for composites because of their low cost and excellent chemical resistance. It was suggested by Lee & Giannelis [5-1] that unsaturated polyester resins were not suitable to form polymer-clay nanocomposites because they have a 3-dimensional structure that would hinder intercalation, even before cross-linking. Recently, Kornmann *et al.* [5-2] reported partially exfoliated MMT nanocomposites of unsaturated polyester. Unsaturated polyester nanocomposites were prepared by bulk polymerisation in the presence of vinylbenzyldimethyl-alkylammonium chloride. The XRD results suggested the formation of an exfoliated polyester-clay nanocomposite and mechanical analysis showed that these nanocomposites displayed a higher dynamic modulus compared with pure polyester. Literature relevant to this chapter relates to work conducted by Bharadwaj & Boyd (1999) [5-3], Suh *et al.* (2000) [5-4] and Bharadwaj *et al.* (2002) [5-5].

Although being acknowledged in the relevant literature very little has been reported about the thermal degradation / stability and solvent resistance degradation of unsaturated polyester-clay nanocomposites (UPCN). This section aims to elucidate any enhancements offered by UPCNs.

5.2 Background and Preparation Theory

5.2.1 Unsaturated Polyester Resins (UPR)

The molecular chains of the polyester can be represented as follows (fig. 5.1), where 'B' indicates the reactive sites in the molecule.
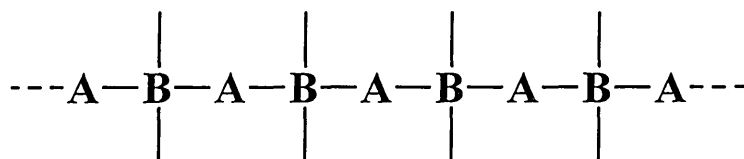
$$---A-B-A-B-A-B-A-B-A---$$

Figure 5.1 Two component polyester chain structure.

For the following samples, the idealised reaction mechanism is represented in fig. 5.2.

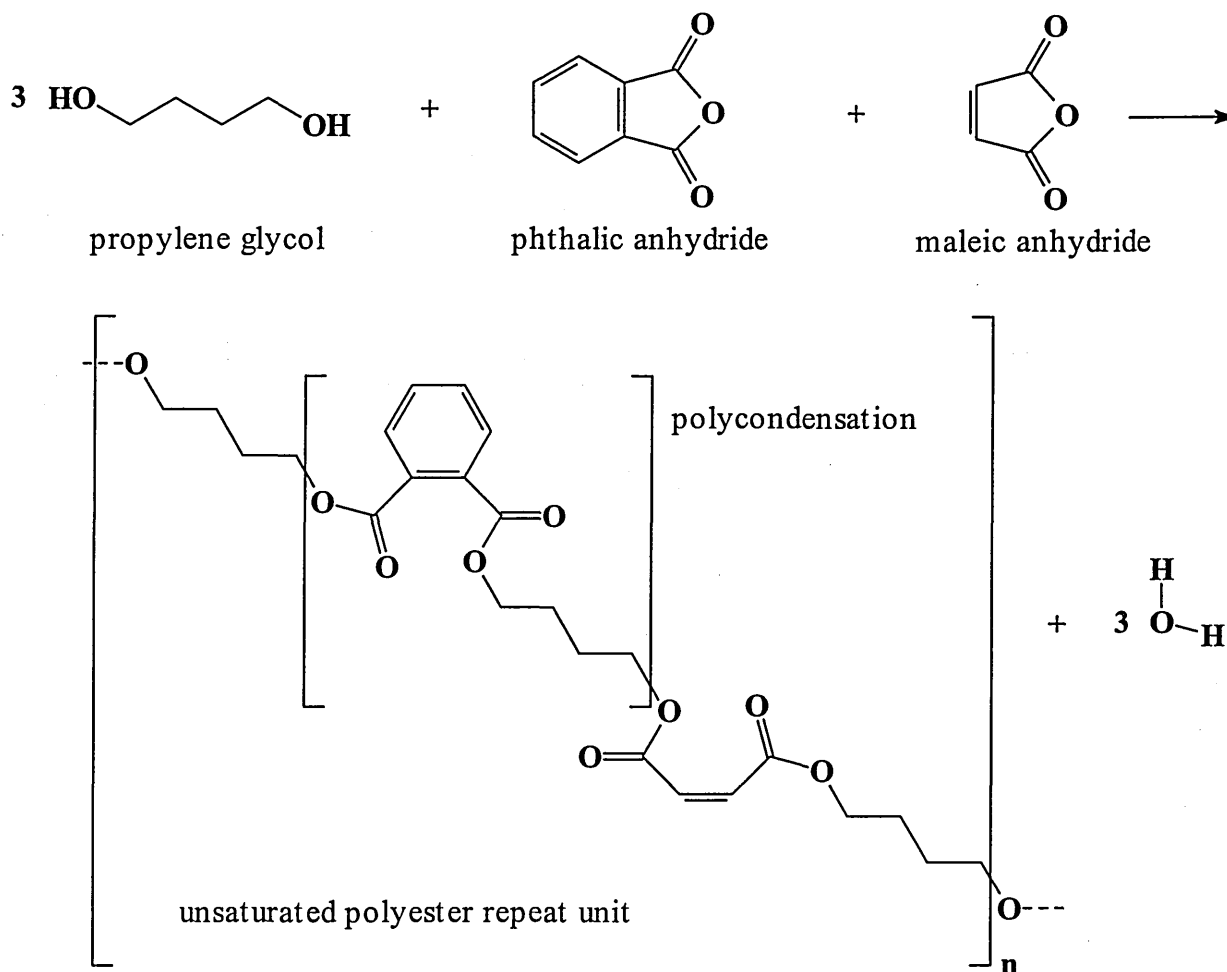propylene glycol   phthalic anhydride   maleic anhydride

Figure 5.2   **Schematic of unsaturated polyester resin mechanism, incorporating phthalic anhydride, maleic anhydride and propylene glycol.**

Unsaturated polyesters can be dissolved in a polymerisable monomer such as styrene. Unsaturated polyester is a long-chain polymer containing a number of reactive vinyl groups. The styrene, which also contains a vinyl group, acts as a curing agent by bridging adjacent polyester molecules at their unsaturated loci (fig. 5.3). During the styrene–unsaturated polyester co-polymerisation, an initiator is decomposed by an accelerator/promoter to create free radicals in the system. The free radicals initiate the growth of styrene oligomers that react with the polyester pre-polymer. A schematic of the growth of these free radicals is shown in fig. 5.4 [5-6].
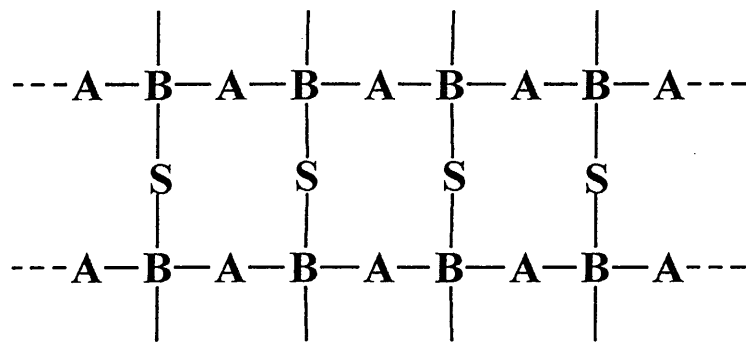
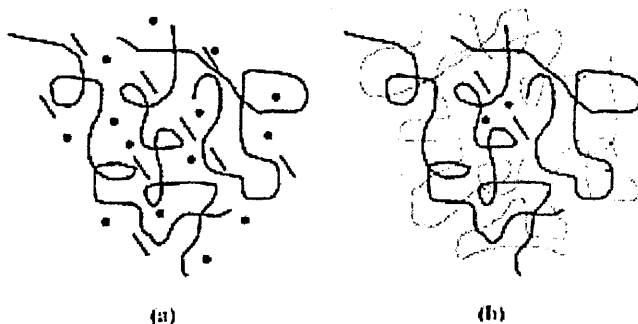**Figure 5.3**   Cross-linked two component polyester chain structure.

Figure 5.4   Curing mechanism of UPR: (a) styrene–UP solution mixture before curing; and (b) after curing. (• = styrene monomer; — = uncured unsaturated polyester chain; — = polymerised-styrene chain connecting the unsaturated points of unsaturated polyester) [5-6].

5.2.2   Curing Process

Unsaturated polyester resins can be formulated so that the rate of polymerisation is rapid enough for practical purposes. Catalysts and accelerators are used to achieve resin polymerisation within a practical time period. Dibenzoyl peroxide (BPO) was added as a catalyst for the resin system shortly before use (i.e. to initiate the copolymerisation reaction), the purpose being not to take part in the chemical reaction, but simply activate the process. An accelerator, i.e. N,N-dimethylaniline, was added to the catalysed resin to enable the reaction to proceed at room temperature. Accelerators have little influence on the resin in the absence of a catalyst, and so, are sometimes added to the resin to create 'pre-accelerated' resins. The accelerator binds to the initiator, forming an unstable ionic species. This at first, leads to the production of one radical, before dissociating, to release the second radical.

On addition of the curing agent and initiator a polyester resin becomes more viscous, until it reaches a state when it is no longer a liquid and has lost its ability to flow, forming a gel structure. The resin will continue to harden after it has gelled, until it has obtained its full hardness and properties. The reaction is exothermic and the heat generated accelerates the reaction. The whole process is known as the 'curing' of the resin. The speed of cure is controlled by the amount of accelerator in a UPR.

It is possible to accelerate the cure process by the application of heat, so that the higher the temperature the faster the final hardening will occur. This would be most useful when the cure would otherwise take several hours or even days at RT. *Note*: the accelerating effect of heat on a resin is that 10 °C increases in temperature will roughly double the reaction rate. Therefore if a resin gels in a laminate in 25 minutes at 20 °C it will gel in about 12 minutes at 30 °C.

Curing at elevated temperatures has the added advantage that it actually increases the final mechanical properties of the material, and many resin systems will not reach their ultimate mechanical properties unless the resin is given this 'post-cure'. The post-cure involves increasing the laminate temperature after an initial room temperature cure. This increases the amount of cross-linking. To some degree this post-cure will occur naturally at warm room temperatures, but improved properties and shorter post-cure times are obtained when elevated temperatures are used. This is particularly true of the material's melting point or glass transition temperature (T_g), which is known to increase with increasing post-cure temperature.

5.2.3 Synthesis of an UPR with Org-MMT

Scott-Bader Company Ltd. is a multi-national commonwealth company which provides specialised polymer, resin and composite solutions to the construction, chemical, marine,

piping and transport sectors, also high value-added, speciality niche markets. Scott-Bader's Wellingborough plant specialises in:

- unsaturated polyester resins (UPR) and dicyclopentadiene (DCPD)

- UPR gel coats, pigments and casting

- glass fibre moulding materials

During a four day visit, the industrial development and formulation process of resins and composites within Scott-Bader was thoroughly explained. The visit also afforded the opportunity to produce a number of samples which could be analysed later (table 5.1). The nanocomposite and resin materials were sent to the MRI, Sheffield Hallam University, to be characterised in order to gain physical data about their composition and to investigate what effect the different post-cures had on the final product.

The procedure for the formulation of these materials was outlined in *chapter 2, section 2.3.* Scott-Bader required results regarding the advantages that these nanocomposites would offer. The objective of this study was to characterise the materials listed in table 5.1 and investigate their structural and thermal properties.

Code	Material	Post-cure/temp.
Std LDS	Styrenated orthophthalic UPR	LDS/Low
Std SB	Styrenated orthophthalic UPR	SB/High
Nano LDS	UPR containing 4wt% silane modified MMT Clay	LDS/Low
Nano SB	UPR containing 4wt% silane modified MMT Clay	SB/High

N.B. *Std refers to a standard orthophthalate resin and Nano refers to a Std resin/silane modified clay Nanocomposite, SB = Scott-Bader, LDS = Lloyds (both standard post-cures used at Scott-Bader)*

Table 5.1   The different UPR materials produced at Scott-Bader, corresponding codes and different post-cure temperatures.

5.3 Results and Discussion

5.3.1 XRD Analysis

The XRD traces of the MMT incorporated in unsaturated polyester at Scott-Bader, before and after silane modification (S-MMT), showed that the treatment had expanded the layers by 7.3 Å (fig. 5.5).
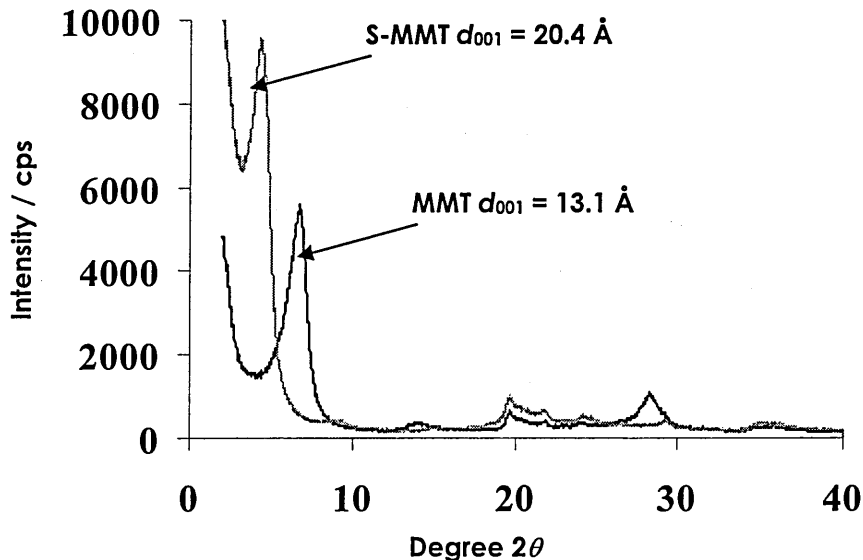

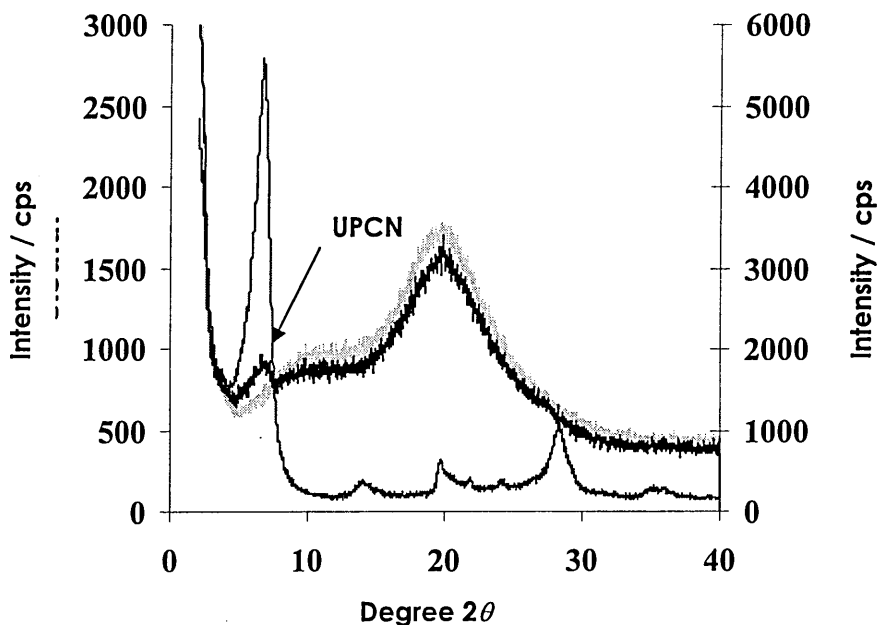**Figure 5.5** XRD traces for MMT and S-MMT.

Figure 5.6 XRD traces for LDS post-cured UP, UPCN together with the trace for MMT.
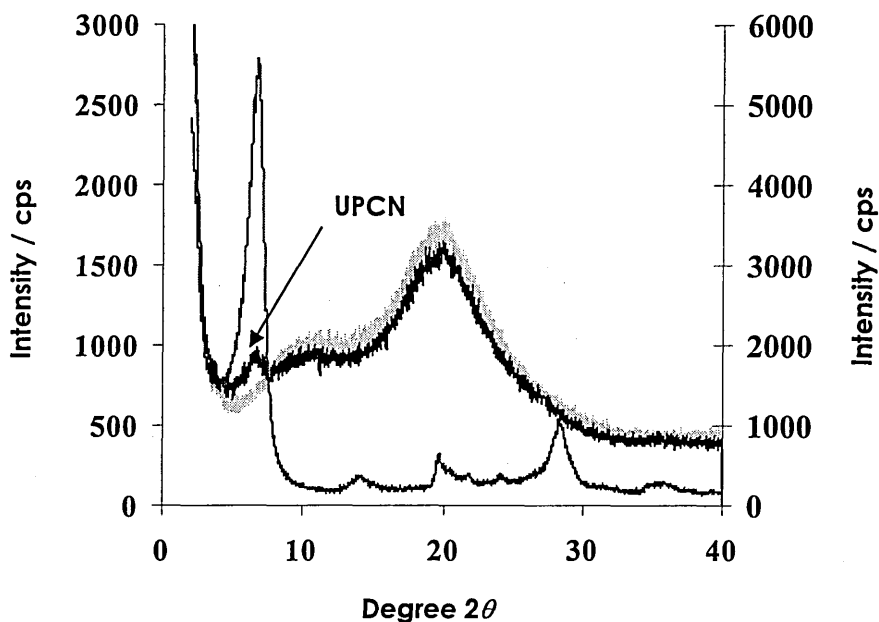
251

Figure 5.7   XRD traces of SB post-cured UP, UPCN together with the trace for MMT.

Multiple XRD sampling of the Scott-Bader samples showed that good dispersion of the silane treated-MMT had been achieved throughout the UP matrices by blending. XRD results showed that S-MMT was present within the polymeric matrix, but not intercalated or exfoliated, expressing the same d_{001} spacing that was shown by Na-MMT (see fig. 5.6 / 5.7). The UPCNs showed a reduction in the d_{001} of the incorporated S-MMT from 20.4 Å to 13.2 Å (- 7.2 Å). The surface compatibilisers appeared to have been drawn out of the gallery spaces by the UPR components rather than leading to the delamination of the clay platelets.

This analysis of the silane-MMT and the subsequent nanocomposite formation indicated that the silanes (e.g. $SiRH_2OH$) which had been used to react with the clay gallery hydroxyls may have, for the majority, spontaneously condensed to form ethers (e.g. disilyl ether, $(SiRH_2)_2O$) or had reacted with water in the galleries to form disiloxanes. It was apparent from the XRD traces that the silane treatment had not been tethered to the clay surface as was expected.

The production of partially delaminated aluminosilicate structures has previously been reported by Kornmann et al. (1998) [5-2] dispersing Na^+ MMT and Bharadwaj et al. (2002) [5-5] dispersing quaternary ammonium exchanged MMT. However, Bharadwaj et al. [5-5] found that dispersion of the organoclay was relative to local orientational ordering, i.e. at lower magnifications TEM showed the global morphology of the UPCN samples to be exfoliated and well dispersed, but at higher magnification the aluminosilicate sheets were shown to be dispersed between regions of clustered platelets, in which a regular stacking arrangement was maintained with a layer of polymer between the sheets; and, regions where the platelets were completely delaminated (fig. 5.8).
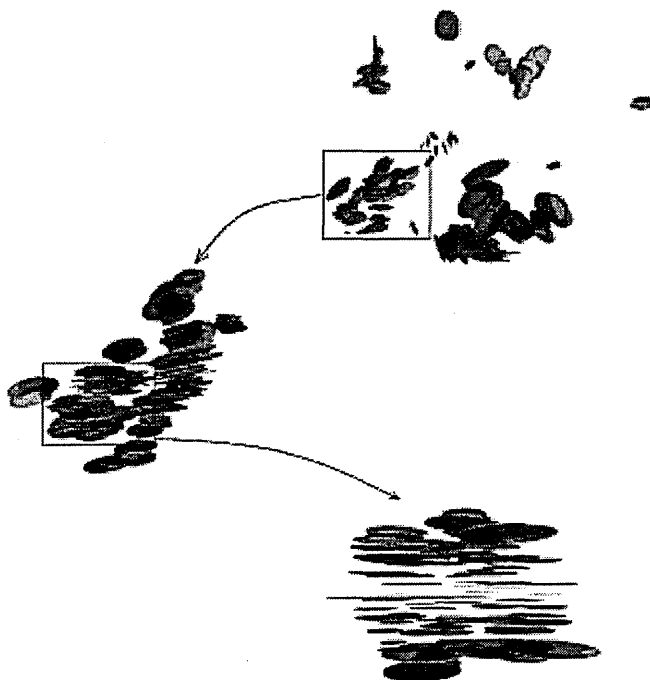

Figure 5.8   Schematic diagram of the morphological hierarchy in Bharadwaj et al.'s UPCN showing the dispersion of intercalated/exfoliated platelets throughout the matrix and local orientational ordering of sheets (agglomeration) [5-5].

Suh et al. (2000) [5-4] noted that the concentrations of styrene in the gallery spaces of a quaternary ammonium organoclay increased with the duration of mixing, with styrene migrating more easily than uncured UP chains into the gallery spaces. This was indicated by the lower degree of crosslinking of samples that were mixed for shorter durations. Hence, the styrene monomers, which act as a curing agent, are much more dispersed

253

inside and outside of the silicate layers as mixing time increases. Therefore, the cross-linking reaction takes place homogeneously inside and outside of the silicate layers, and the degree of cross-linking density would ideally reach that of the cured pure UP.

However, the loss of the silane modification (i.e. removing the compatibilising agent from the gallery spaces) and the comparatively short mixing time (i.e. 15 mins) of the silane-MMT with styrene monomer may not have afforded the styrene monomer the opportunity to enter the MMT gallery spaces.

5.3.3 TGA Analysis
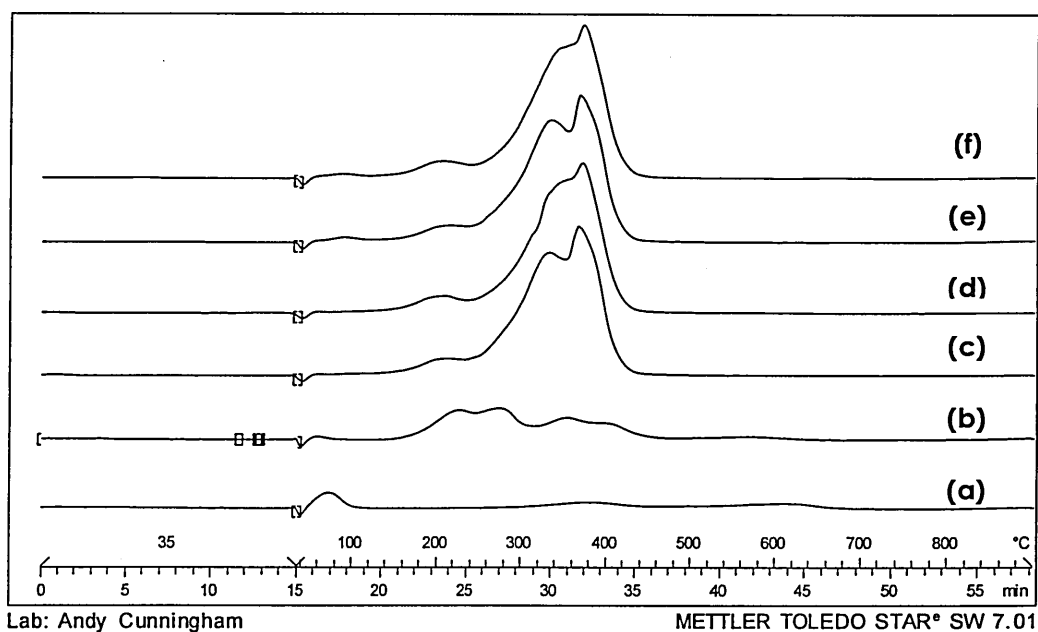

Figure 5.9   DTG traces collected under nitrogen for (a) MMT, (b) S-MMT, (c) StdLDS, (d) NanoLDS, (e) StdSB and (f) NanoSB.

The TG analysis under N_2 showed that the silane compatibiliser was thermally desorbed from MMT as a series of events between 150-460 °C (Fig. 5.9 (b)), over the same range as the total mass loss from the standard resins and nanocomposite materials. The UPCN samples showed a slight increase of the higher temperature thermal decomposition maxima (T_{max}) from 362 °C for resins to 374 °C for the nanocomposites (Fig. 5.9 (d & f). This

was accompanied by a shift of largest mass loss to higher temperatures, which can be seen as a larger area under the higher temperature maxima.
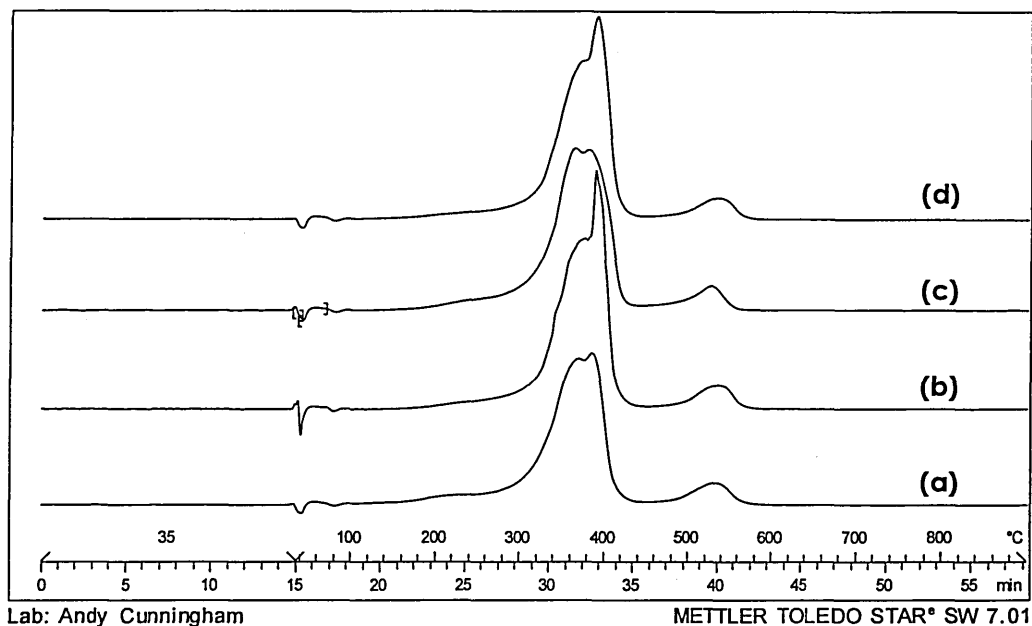

Figure 5.10   DTG traces collected under air for (a) StdLDS, (b) NanoLDS, (c) StdSB and (d) NanoSB.

Under N_2 the TGA data showed little increase in thermal stability for both the resins and the nanocomposites under both post cures. However, when TGA were conducted under air their appeared a marked shift of mass loss to the higher temperature maxima (fig. 5.10).

These results contrast the results of previous work [5-5] which showed that the TGA of the crosslinked polyester nanocomposites displayed exactly the opposite behaviour. The onset of degradation for the nanocomposites was progressively shifted to lower temperatures with increased addition of clay with respect to the pure polymer. This increase in the rate of degradation in the nanocomposites was reportedly due to the presence of increasing amount of hydroxyl groups in the organic modifier that provided a supply of oxygen.

The Scott-Bader UPCNs displayed two thermal desorption maxima in the DTG of all the materials, this was most probably due to the differentiation of the polyester backbone at 340 °C / N_2 - 370 °C / Air and the polystyrene cross-linker at 385 °C / N_2 - 395 °C / Air [5-6].

255

The UPCN samples show a shift towards the high temperature thermal desorption maxima, which shows as a stabilising effect on the entire system until an upper thermal limit of the material which happens to coincide with the styrene maxima.

For the Scott-Bader UPCNs it was believed that this shift was due to the formation of a protective barrier layer due to the surface accumulation of clay platelets with a small quantity of carbonaceous char [5-6, 1-113]. This barrier would have thermally insulated the UP matrix. Also, a highly tortuous path to mass transport afforded by the layering of clay platelets would have created a diffusion barrier to gases and fumes [5-7]. These two mechanisms were the most likely to retard the combustion of the polymeric materials.

This increase in thermal stability is more impressive when it is understood that the thermal stability of polymeric material in air would have been prominently reduced by the oxidative dehydrogenation of the various organic species accompanied by hydrogen abstraction [5-7].

5.3.4   Solvent Resistance

To compare the solvent resistance imparted on each of the materials, equal sections of the materials were cut and weighed on a balance (5 d.p.). Sections of each sample were then immersed (in triplicate) in one of three different solvents:

1)   deionised water

2)   ethanol

3)   butanone

The samples were then pat-dried and weighed every 2 hours for the first day and then every 24 hours for 1 week.

The uptake of solvent by the various samples is based primarily on the free volume (i.e. the fraction of the volume that is not occupied by polymer) and the access which the

penetrant has to it, with hydrogen bonding being the main process of attraction between the polymer and penetrant species.

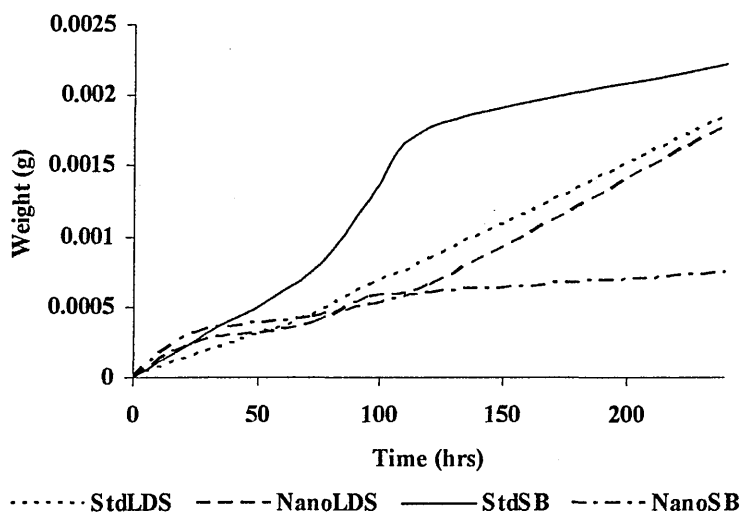## 5.3.4.1   Deionised Water (H₂O)

Figure 5.11   H₂O / 240 hr - Cumulative mass increase.

The ester linkages can participate in hydrogen bonding as H-bond acceptors, this ability to participate in H-bonding makes them water soluble to a certain extent. The increase in mass of materials which were immersed in water was attributed to the hydrolysis of ester linkages and the accompanying ingress of the solvent. The cumulative mass increase of the UP resins (fig. 5.11) could be seen to be greater than for the corresponding UPCN materials. This effect seemed to be enhanced for the higher temperature post-cure where the degree of cross-linking would be higher, and so, would more acutely hinder the passage of small water molecules. These results indicate that the presence of the clay in the UPCN samples hinders the passage of water into the material.

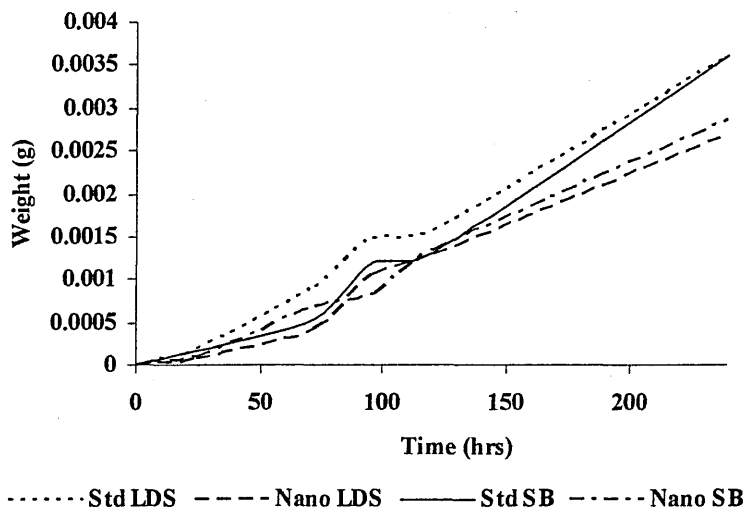## 5.3.4.2   Ethanol (CH$_3$CH$_2$OH)

Figure 5.12   Ethanol / 240 hr - Cumulative mass increase.

Ethanol is a polar solvent, but significantly less so than water; the ethanol molecule is also much bulkier. As ethanol diffused into the polyester structure it would have H-bonded with the polyester backbone. The concentration and proximity of the penetrant species may have also lead to esterification of the polyester backbone leading to scission as the alcohols reacted with carbonyl groups to form esters. The ethanol uptake can be seen to be hindered in UPCNs, but this effect is not as pronounced as with H$_2$O, the ingression of these bulkier molecules may have been slowed by size exclusion (fig. 5.12). The slightly higher cumulative mass increase was attributed to the increased molecular weight of the solvent molecules.

5.3.4.3   2-Butanone (CH$_3$(CH$_2$)$_2$CHO)

The rapidity with which 2-butanone solvated the polyester materials was believed to be evidence of the penetrant attacking the polymeric structure. The initial ingress of the penetrant would have proceeded in a similar way as with deionised water and ethanol, only much more rapidly, due to the increased polarity of the ketone functional group. 2-butanone would then have reacted with the polymeric structure via nucleophilic addition

to the carbonyl linkages. The 'active' diffusion of 2-butanone into the resin matrices was very rapid and complete by 24 hours, beyond this duration sample degradation occurred very rapidly.
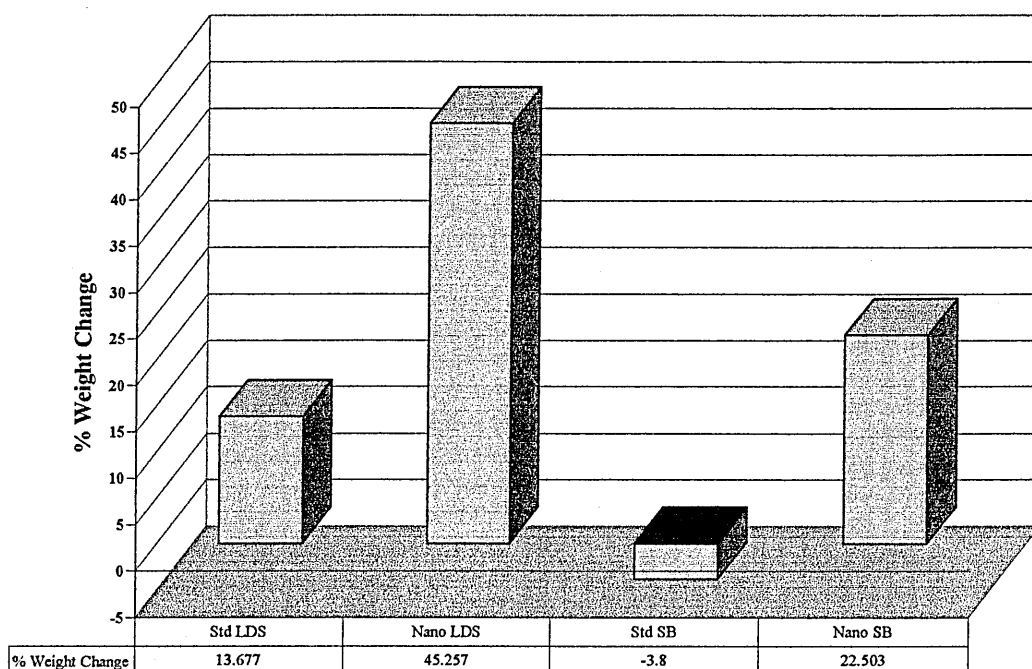

	Std LDS	Nano LDS	Std SB	Nano SB
% Weight Change	13.677	45.257	-3.8	22.503

Figure 5.13   **2-butanone / 24 hr - percentage weight change resulting from solvent absorption.**

The standard resins retained less solvent and fractured more easily than the nanocomposite resins. The loss of sample observed for the Std SB sample indicated the solvation of surface resin (fig. 5.13). The NanoLDS and NanoSB materials increased in mass relative to the corresponding resins and the higher temperature post-cure displayed 50% less solvent uptake. The clay appeared to have provided the function of structurally stabilising the material by providing a 'binding function' within the resin that underpinned the polymeric matrix. This was observed as a swollen structural appearance, more spherical than the original cubic samples.

5.3.5 Dimensional Stability and Observations

The four materials were then subjected to specific thermal treatments. Designated areas of the sheet materials were sectioned to produce several small cubes (i.e. ~ 5 mm^3). These cubes were then heated in the furnace of the TGA under a nitrogen atmosphere to prevent ignition. To observe any significant dimensional changes that may occur as the materials were heated, samples of the same material were heated for one hour at selected temperatures; room temperature (standard), 150, 200, 250, 300 and 320°C. A maximum temperature of 320°C was used because at 350°C the sample tended to vaporise in the furnace.

Temp. (°C)	Std SB	Nano SB	Std LDS	Nano LDS
150	Clear	Opaque	Clear	Opaque
200	Clear	Opaque	Clear	Opaque
250	Yellowing	Yellowing	Yellowing	Yellowing
300	Dark Yellow	Dark Yellow	Dark Yellow	Dark Yellow
320	Black	Dark Orange	Black	Dark Orange

Table 5.2   Table of observed colour changes at selected temperatures.

At temperatures < 250°C no physical change, discolouration (table 5.2) or dimensional change was observed. At temperatures ≥ 250°C there were noticeable differences, discolouration of the samples was accompanied by dimensional loss to a greater extent as the samples were heated to successively higher temperatures. Discrimination between the two different post-cures produced negligible results, and so, could not be defined as conclusive. Differences were observed between the resin and nanocomposite samples. The nanocomposites were recorded as having an average of 2.1% (NanoLDS) and 2.5% (NanoSB) less dimensional loss than their resin counterparts (table 5.3, fig. 5.17 & 5.18).

Axis	Std SB			Nano SB			Std LDS			Nano LDS		
	Before	After	Diff	Before	After	Diff	Before	After	Diff	Before	After	Diff
	250			250			250			250		
X	3.342	3.275	-2.01%	3.693	3.669	-0.65%	3.875	3.817	-1.50%	4.199	4.14	-1.41%
Y	3.14	3.135	-0.16%	2.815	2.788	-0.98%	3.088	3.086	-0.06%	2.926	2.894	-1.09%
Z	4.401	4.332	-1.57%	6.073	5.985	-1.45%	6.886	6.824	-0.90%	6.644	6.511	-2.00%
	300			300			300			300		
X	3.468	3.305	-4.70%	4.247	4.042	-4.83%	4.507	4.297	-4.66%	3.926	3.775	-3.85%
Y	3.122	3.079	-1.38%	2.903	2.823	-2.76%	3.088	3.028	-1.94%	2.981	2.884	-3.25%
Z	4.588	4.317	-5.91%	5.776	5.513	-4.55%	7.022	6.682	-4.84%	6.671	6.137	-8.00%
	320			320			320			320		
X	3.797	3.406	-10.30%	3.271	2.977	-8.99%	4.916	4.417	-10.15%	4.112	3.802	-7.54%
Y	3.108	2.912	-6.31%	2.864	2.728	-4.75%	3.132	2.991	-6.38%	2.886	2.702	-4.50%
Z	5.51	4.803	-12.83%	5.55	5.096	-8.18%	6.452	5.745	-10.96%	6.281	5.669	-9.74%

Sample Dimensions (as measured):
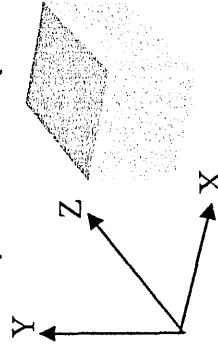
Table 5.3   Dimensional stability results for Scott-Bader UPR and UPCNs.

Std LDS and Nano LDS (320C)

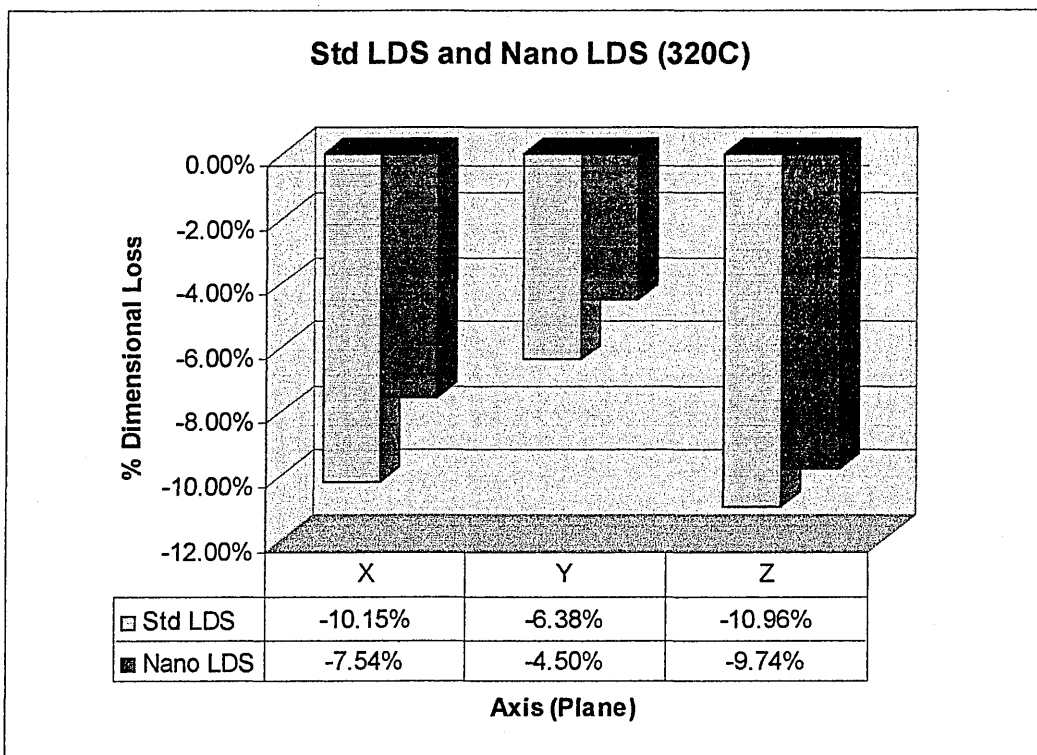|	X	Y	Z
☐ Std LDS	-10.15%	-6.38%	-10.96%
▨ Nano LDS	-7.54%	-4.50%	-9.74%

Axis (Plane)

Figure 5.14 Comparison of dimensional stability results for StdLDS and NanoLDS samples after heating to 320°C / N_2 (data taken from table 5.3).
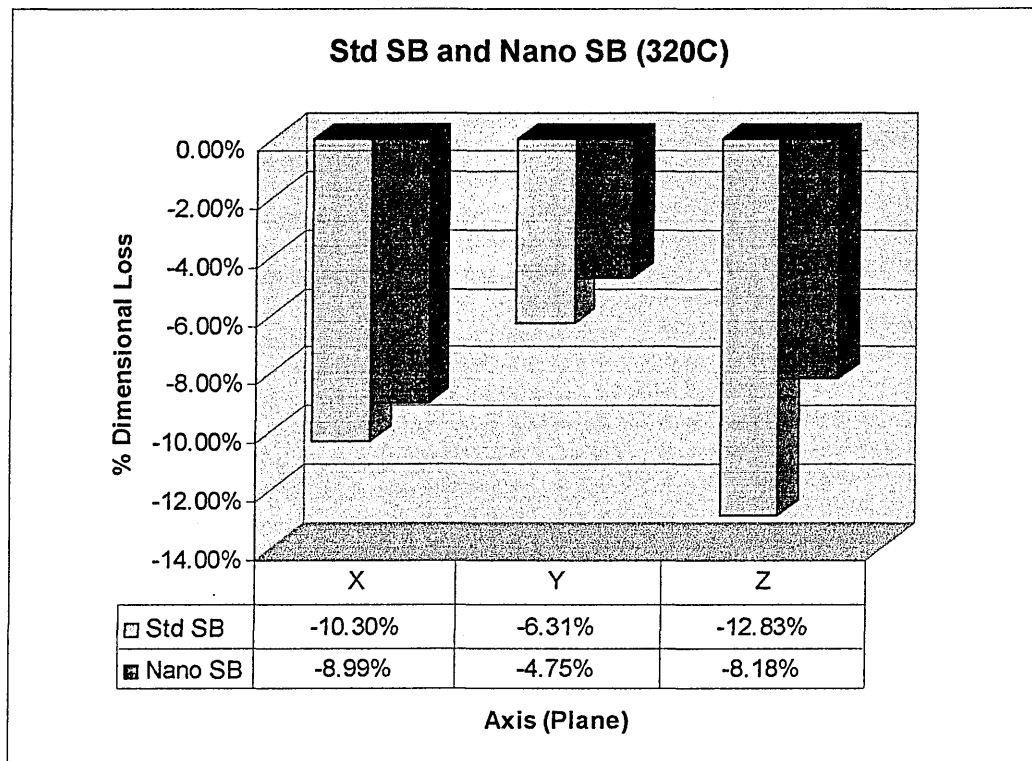

Std SB and Nano SB (320C)

	X	Y	Z
☐ Std SB	-10.30%	-6.31%	-12.83%
▨ Nano SB	-8.99%	-4.75%	-8.18%

Axis (Plane)

Figure 5.15 Comparison of dimensional stability results for StdSB and NanoSB samples after heating to 320°C / N_2 (data taken from table 5.3).

5.3.6   Topographical Analysis

5.3.6.1   ESEM Analysis

It was believed that ESEM would be useful for a cross-material comparison of surface effects. However, due to the usage constraints, scheduling enough time for a full analysis of the samples has been impossible to date. During the time that was allotted it seemed more beneficial to concentrate on one of the NanoLDS series of nanocomposite samples.

The surface of the Nano LDS/RT (fig. 5.19 (a)) displayed contrasting rough and smooth areas. The rough areas were most prone to being disrupted by irradiation from the electron beam, this was observed throughout the duration of the analysis. At first it was considered that these rougher areas could have been the regions within which clay layers were located in the nanocomposites. However, these surface deformations appeared to have larger proportions than the sub-micron layers of clay, and so, were taken as evidence for dispersed clay agglomerates.

The surface of the Nano LDS/200°C samples appeared much rougher and more stable than samples treated at lower temperatures (fig. 5.19 (b)). The samples' surfaces appeared to be more stable with respect to the heating effects of the electron beam, which after mapping, was more indicative of the surface morphology prior to analysis and was indicative of the EDX elemental analysis showing Al associated with Si in regions designated to be clay agglomerates.

With NanoLDS/300°C (fig. 5.19 (c)) the surface appears to be rougher than at 200°C. The surface artefacts appeared similar to when smectites were previously observed with ESEM [5-8]; showing a glassy, web-like texture. This could be near surface accumulation of clay platelets, possibly forming a kind of precursor of char layer. The surface was still slightly sensitive to radiation, seen by blistering of the surface during prolonged scans.
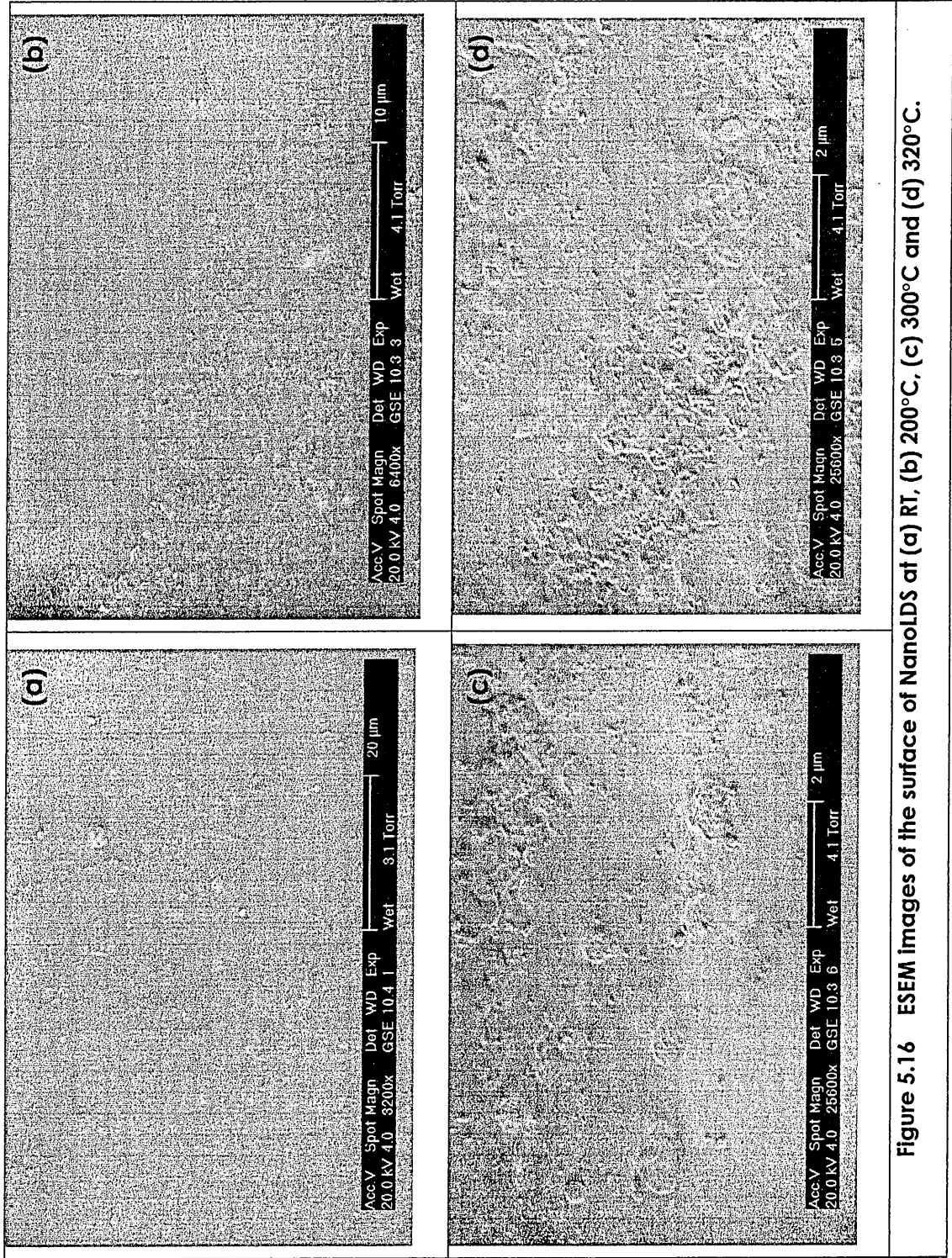
Figure 5.16 ESEM images of the surface of NanoIDS at (a) RT, (b) 200°C, (c) 300°C and (d) 320°C.
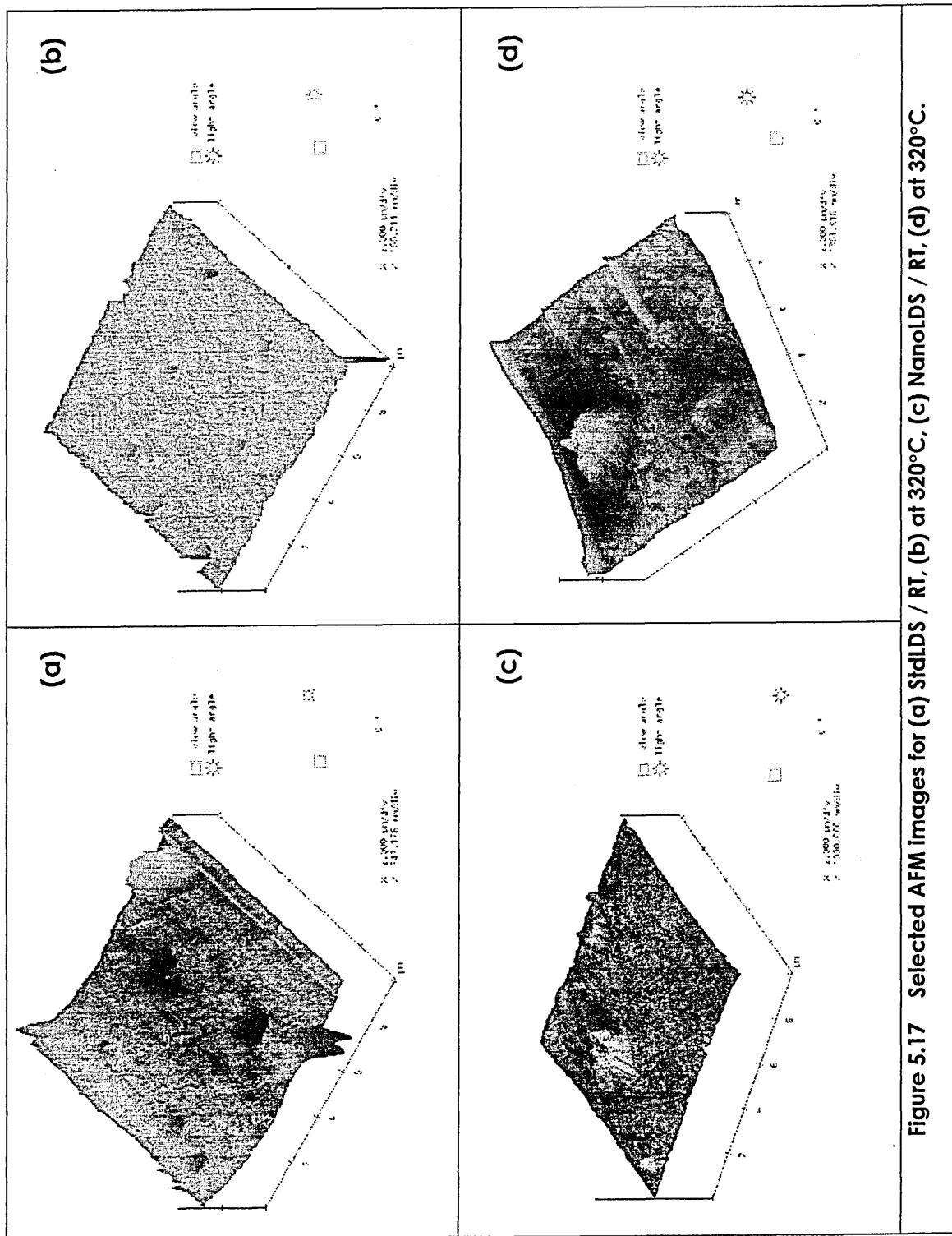
264

Figure 5.17   Selected AFM images for (a) StdLDS / RT, (b) at 320°C, (c) NanoLDS / RT, (d) at 320°C.

265

At 320°C (fig. 5.19 (d)), an apparent increase in surface stability was noticed, as less electron beam degradation was observed and the surface appeared to be rougher than with previous samples.

The ESEM images and analyses were taken at random surface locations on the samples, and so, the findings cannot be generalised as being representative of the entire surface.

5.3.6.2 Atomic Force Microscopy (AFM) Analysis

5.3.6.2.1 Tapping Mode Analysis

Tapping mode atomic force microscopy (AFM) was used to map and identify any differences in surface composition between the different materials at RT and 320 °C. For the standard resin materials the topography of the StdLDS/StdSB became visibly smoother at 320°C as surface material had been evolved and been permitted to flow. This was evident from the AFM micrographs of the UPR samples where surface smoothing occurred (fig. 5.20 a/b). However, the NanoLDS / NanoSB materials showed no pits, and a surface that had greatly increased in roughness between RT and 320 °C, this was attributed to the initial evolution of surface resin and the subsequent build-up of clay agglomerates at the surface-N_2 interface (Fig. 5.20 c/d).

Figure 5.18   Selected AFM images of NanoLDS 320°C - regions (a) and (b).
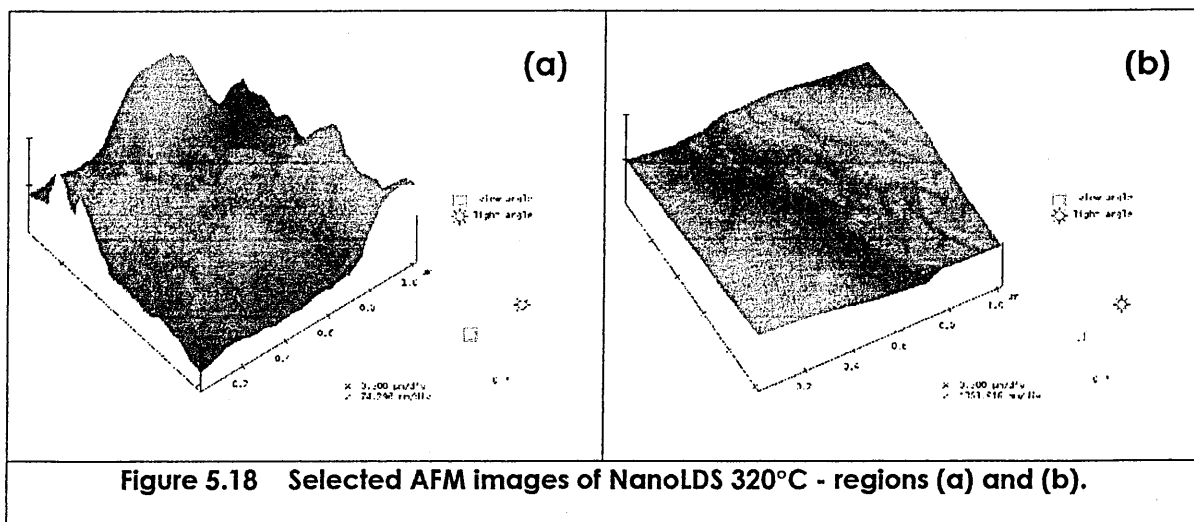
However, different regions identified on the samples surface (fig. 5.18 a/b) showed that the build-up of clay at the surface was not uniform, (a) shows a high-clay region and (b) shows a region of low-clay concentration which is topographically smooth due to the flowing of polymer.

5.3.6.2.2 AFM Roughness Analysis (i.e. RMS and Ra)

AFM was used to measure roughness of the sample surfaces. The units of measurement are usually given in values of roughness root mean squared (Rq) or roughness average (Ra).
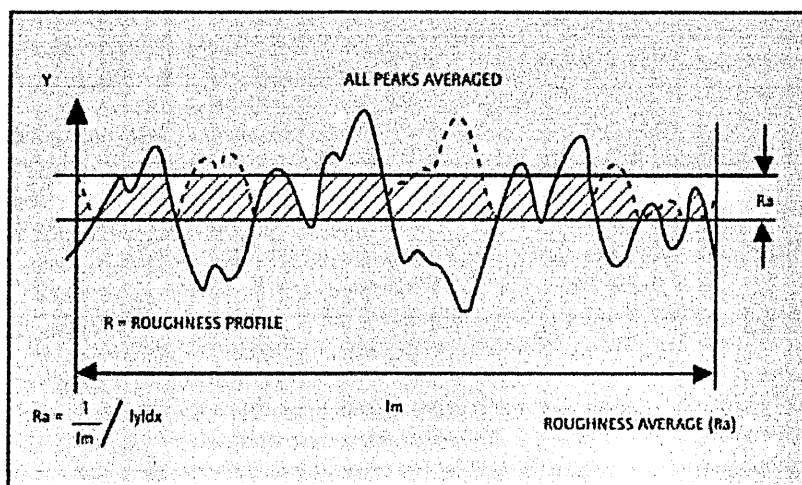

Figure 5.19   Schematic diagram of the roughness average (Ra) sample peaks [5-9].

Roughness root mean squared (referred to as RMS or Rq) has been the accepted standard in the past. It can be defined as the square root of the average deviation from the centreline squared. Ra has been designated by the International Standards Organizations (ISO) as the correct medium for measuring the roughness, but values for both have been collected in this work. Ra is established by finding an average centreline. Any valleys below the centreline would then inverted and counted as peaks. The average height of the peaks above the centreline, is the Ra (fig. 5.19). The meaningful difference between the two measurements is that RMS is sensitive to peaks and valleys on a surface and the

reading accounts for extreme peaks or valleys, whereas Ra averages them into the reading [5-9].

Ra values for the different samples were used to estimate the increase in the number of clay platelets at the surface of the material as the samples were heated. The Ra values were taken on the same samples at RT and after heating to 320°C.

Sample	Rq - RT	Ra - RT	Rq - 320°C	Ra - 320°C
StdLDS	87.96 nm	48.99 nm	44.81 nm	20.39 nm
NanoLDS	48.28 nm	33.31 nm	270.47 nm	212.92 nm
StdSB	78.48 nm	41.37 nm	37.53 nm	18.77 nm
NanoSB	56.23 nm	36.48 nm	237.64 nm	196.36 nm

Table 5.4   Rq and Ra values for Scott-Bader Materials.

The results in table 5.4 show that at 320°C, the standard resins appear to have undergone smoothing, whereas the nanocomposite resins show a greatly increased surface roughness, which could be evidence of clay accumulation at the resin surface.

5.3.6.2.3   Phase Imaging

Phase imaging was used to distinguish between the amorphous polymeric regions and dispersed crystalline clay platelets. The results showed the clay at the surface of the nanocomposite samples (i.e. with lighter contrast and blocky morphology) and no phase difference in the standard resins. The phase imaging data in fig. 5.20 shows that the clay platelets (with lighter contrast and blocky morphology) are randomly mixed within the polymer system, appearing mainly at the topographically high regions. This data suggests the formation of a char layer; but whereas the dispersion may be good on a macroscopic level, at the microscopic level there may have been regions where no clay was present, leading to discontinuity of the char layer, and so, unshielded regions which would be thermally degraded more rapidly. This can be seen in the topographically low regions with darker contrast in fig. 5.20.
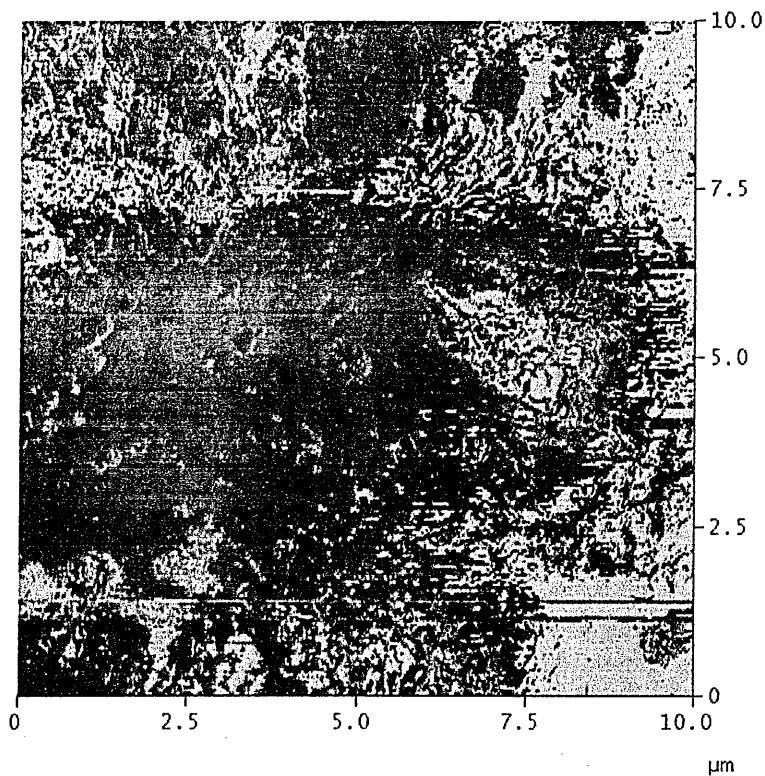
Figure 5.20 **A selected phase image of the surface of NanoLDS / 320 °C.**

This research follows work conducted by Bhushan & Qi [5-10 & 5-11], where the identification of a phase contrast in magnetic tapes was observed. This tentative study, using tapping mode and phase contrast microscopy, has shown that for the measurement of the surface composition of polymer nanocomposites AFM can provide information that cannot be obtained by other means.

5.3.7 ATR-FTIR Microscopy of Thermally Effected UP resins and UPCNs

5.3.7.1 Background and Experimental Method

When a polyester matrix is subjected to thermal energy, atmospheric oxygen or moisture, the polymeric backbone will be readily cleaved; as a result of which two radical species will be generated [5-12]. In the presence of thermal energy greater than the bond energy, spontaneous scission occurs. When this process is combined with atmospheric oxygen, polymers undergo thermo-oxidation, the oxidation reaction releasing carbonyl groups or crosslink . Alternatively, moisture absorption in polyesters leads to hydrolysis. Stabilisers may be used to reduce polymer degradation, for example antioxidants that can act as free-radical scavengers, hindering further reaction of radical polymer chains.

Almost every polymer needs to be protected from degradation, during processing and use, by one or more stabilisers. Development of stabilising and fire retardant additives over decades of research have been essential to the success of polymers. An understanding of the complex mechanisms of the degradation and stabilisation of polymers is fundamental to rational use of existing chemistry and to new product design. The thermal decomposition of polyesters produces a complex mixture of products [5-13]. To study the effects of different temperatures on specific UP resins and any stabilising effects in their corresponding UPCNs, ATR-FTIR was used to detect the increasing concentrations of degradation products being produced.

Sections of equal dimensions of the different UP materials were subjected to a range of specific temperatures ≤320°C, these were specified to be below the vaporisation temperature (325-350°C) as designated by TGA experiments. Seven sections of each material were exposed to RT (control), 100, 150, 200, 250, 300 and 320°C for 1 hr, under an N_2 atmosphere, to study the products of thermal degradation in the absence of sample oxidation or hydrolysis.

5.3.7.2   Results

The ATR-FTIR spectra of the four thermally treated Scott-Bader materials showed identifiable peaks associated with the bulk resin materials that were universal for the four materials (see table 5.5).

Band Position / cm⁻¹	Assignment	Identification	Reference
3400-3600	v(O-H)	alcohol mixture	[5-4]
3081	v_{ring}(C-H)	aromatic, styrene / phthalate residues	[5-6]
3067	v_{ring}(C-H)	aromatic, styrene / phthalate residues	[5-6]
2918	v_a(C-H)	styrene / phthalate residues	[5-6]
2851	v_s(C-H)	styrene / phthalate residues	[5-6]
1778	v(C=O)	high frequency carbonyl	[5-8]
1724	v(C=O)	ester carbonyl, phthalate / maleiate	[5-5]
1600	v_{ring}(C-C)	aromatic, styrene / phthalate	[5-6]
1576	v_{ring}(C-C)	aromatic, styrene / phthalate	[5-6]
1550	v_s(COO-)	ionised carboxylic acid	[5-7]
1545	v_{ring}(C-C)	conjugated aromatic	[5-7]
1495	$v_{conjugated}$(C-C=O)	o-di-sub. aromatic, phthalate	[5-6]
1452	δ(CH₂)	propyl	[5-6]
1400	v_a(COO-)	ionised carboxylic acid	[5-7]
1368	v(C=C) / w(CH₂)	polymerised maleic anhyride / propyl	[5-5]
1282	v(C-O-C)	polymerised anhydride	[5-5]
1260	v(C-O) / δ(C-H)	ester - multi-component band	[5-7]
1163	v_{ring}(C-H)	ester, phhalate	[5-7]
1116	v_{ring}(C-H)	ester, phthalate	[5-7]
1070	v_{ring}(C-H)	ester, phthalate	[5-7]
1040	v(CH₂-OH)	propylene glycol	[5-6]
1016	in-plane δ(C-H)	o-di-sub. phthalate	[5-6]
992	out-of-plane δ(C-H)	-CH=CH₂, styrene	[5-4]
965	out-of-plane δ(C-H)	CH=CH, styrene / phthalate	[5-6]
909	out-of-plane δ(C-H₂)	-CH=CH₂, styrene	[5-4]
840	out-of-plane δ(C-H)	CH=CH, styrene / phthalate	[5-6]
777	out-of-plane δ(C-H)	mono-sub. aromatic, styrene	[5-4]
741	$v_{conjugated}$(C-C=O)	o-di-sub. phthalate	[5-6]
704	out-of-plane δ(C-H)	mono-sub. aromatic, styrene	[5-4]
698	v_{ring}(C-H)	aromatic breathing mode, styrene	[5-7]

Table 5.5   ATR-FTIR assignments for Std/Nano LDS and Std/Nano SB [5-15 – 5-19].

The various materials showed similar spectra and trends that were observed as a function of different thermal treatments. The bands in the 1710-1750 cm⁻¹ region v(C=O) and in the 1250-1300 cm⁻¹ region v(C-O-) can be assigned to phthalate groups. The ortho-disubstituted phthalic anhydride has a very characteristic band at 740-745 cm⁻¹ and another at 1016 cm⁻¹ these bands are characteristic of unreacted phthalic anhydride. The dibasic acid components of polyesters were the easiest to identify by ATR-FTIR. Characteristic features are the bands at 1724 cm⁻¹ v(C=O), at 1282 cm⁻¹ v(C-O-C) and the

ring breathing bands at 1600 and 1575 cm⁻¹ (doublet), 1163, 1070, 741 and 704 cm⁻¹. The bands corresponding to the ring breathing modes of the resin are derived from both the phthalic anhydride and styrene components. In research conducted by Paauw and Pizzi [5-14] four bands were selected to follow the extent of cure within polyester systems by FTIR. They selected 745 cm⁻¹, free phthalic anhydride band, the 1116 cm⁻¹ band representing the polymerised phthalic anhydride residue, the 1354-1380 cm⁻¹ band of the polymerised maleic anhydride residues, and the 1630-1647 cm⁻¹ band representing free maleic anhydride. The presence of styrene was detected by its numerous characteristic sharp bands. These were at 698, 777, 909, 992, 1021, 1452, 1495, 1545, 1576 (1603, 1632 masked), 3030 and 3084 cm⁻¹. Also, propylene glycol has a strong characteristic band at 1040 cm⁻¹.
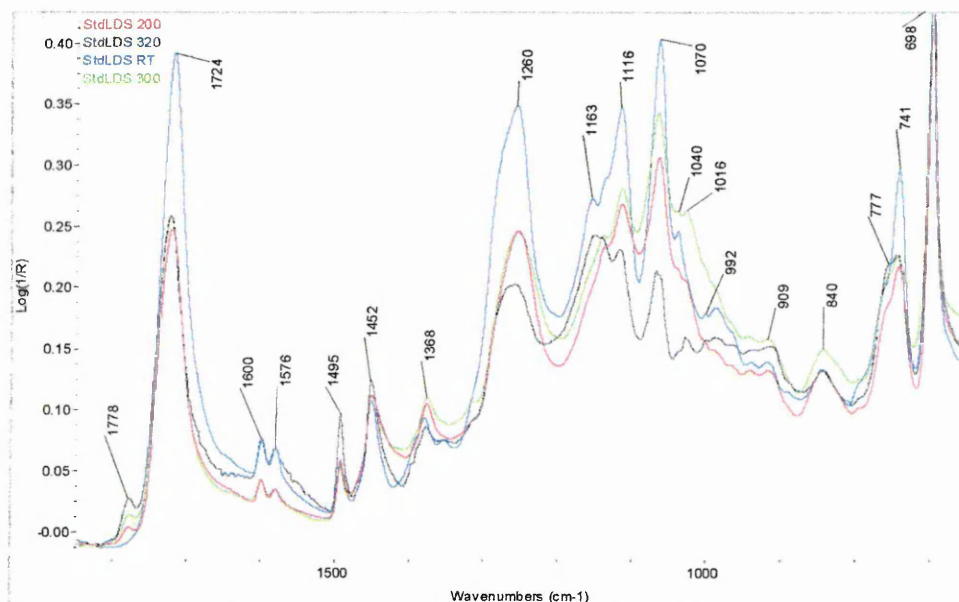
5.3.7.2.1 StdLDS and NanoLDS

Figure 5.21 StdLDS - RT, 200, 300 and 320°C (1850-650 cm⁻¹).

In the StdLDS (fig. 5.24) sample the following observations were made. With increased temperature, up to 175°C, no structural change (FTIR) and little physical discolouration could be observed. Between 200-320°C, bands at 741, 1070, 1116, 1260, 1368 and 1379 cm⁻¹ decreased in relative intensity, whereas the v_{ring}(C-C) band at 1600 cm⁻¹ increased in relative intensity and a band between 1778 cm⁻¹ (v(C=O)) developed with increasing

temperature. These band changes related to the thermal degradation of the polyester matrix with increased temperature.

In the NanoLDS sample (fig. 5.25) similar observations were made as StdLDS sample and the same bands were identified. Differences could be seen which related to the greater relative intensity of the band at 1116 cm^{-1} (v_{ring}(C-H)) and the slower rate (reflected by lower relative intensity) with which the band at 1778 cm^{-1} was seen to develop.
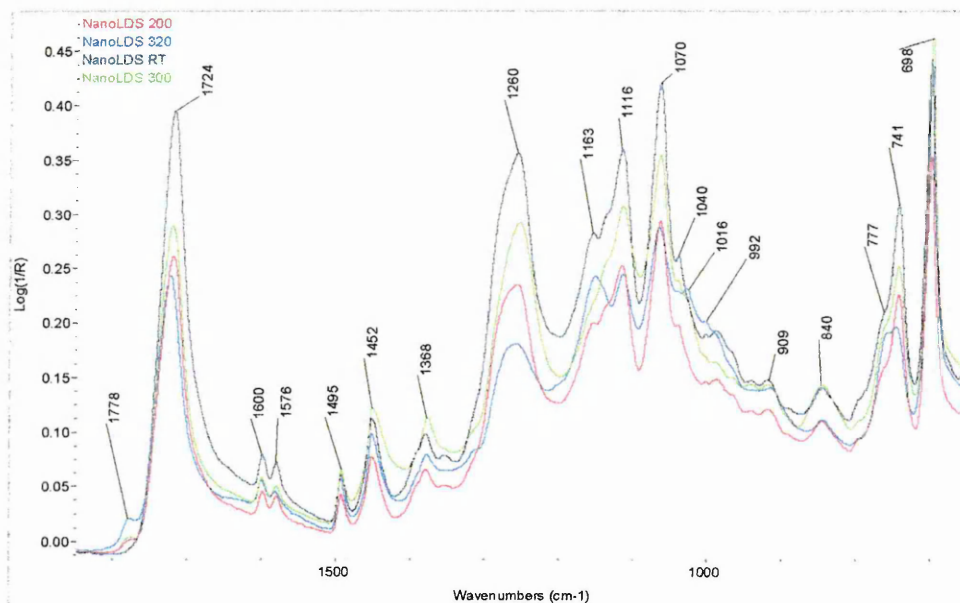

Figure 5.22   NanoLDS - RT, 200, 300 and 320°C (1850-650 cm^{-1}).

5.3.7.2.2   StdSB and NanoSB

The results for the materials subjected to the higher temperature Scott-Bader (SB) post-cure gave less reproducible readings than the previous samples, which could have been due to the higher degree of the cross-linking slowing the release of degradation products. The same bands were identified in both the standard resin (fig. 5.26) and the nanocomposite resin (fig. 5.27) samples that had been seen previously with the lower temperature Lloyds post-cure (LDS). The relative intensity of the band at 1116 cm^{-1} (v_{ring}(C-H)) was increased with increasing temperature to a reduced extent in the nanocomposite than in the

273

standard resin, and the high frequency carbonyl band (1778 cm⁻¹) showed a similar trend, but was not as evident as in the Lloyds post-cure.
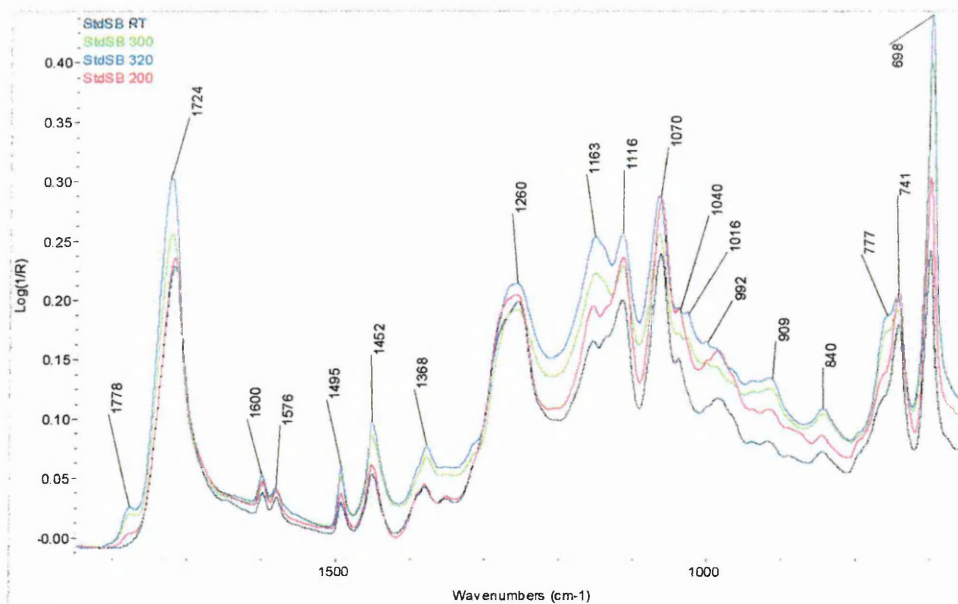

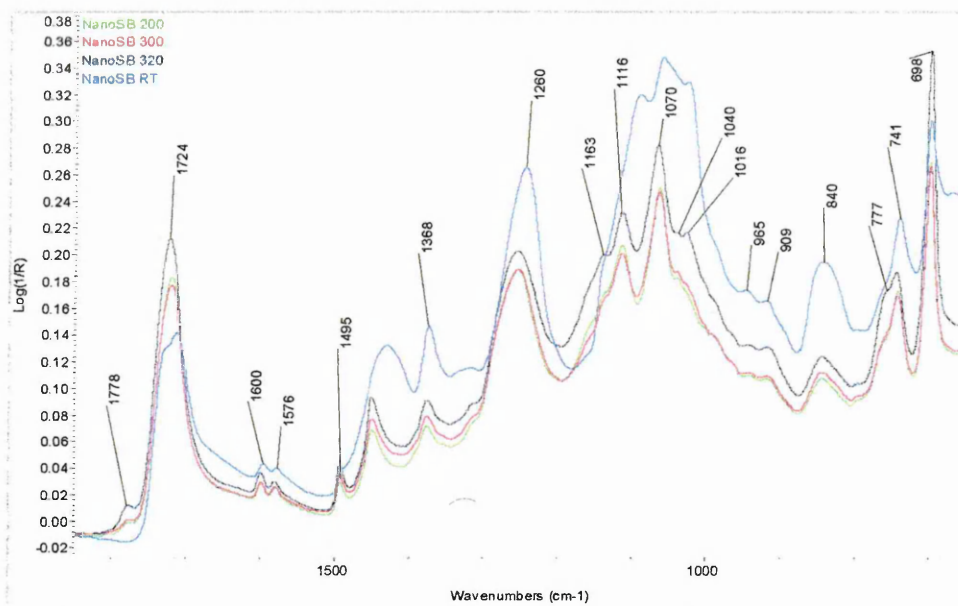Figure 5.23   StdSB - RT, 200, 300 and 320°C (1850-650 cm⁻¹).

Figure 5.24   NanoSB - RT, 200, 300 and 320°C (1850-650 cm⁻¹).

5.3.7.3   Discussion

All of the bands that were assigned were due either to the changing morphology of the polyester backbone or the reorganisation of the polymer chains. At the temperatures used

(i.e. ≤ 320°C), the degradation would not involve the physical degradation of the S-MMT. Although hydrolysis of polyesters does occur, it was not thought to be occurring at any significant rate due to the trace concentrations of water that would be enclosed in the clay galleries and the selected temperatures being significantly below the dehydroxylation of the clay. The data was normalised to elucidate any band changes and shifts, also, any reproducibility problems that were encountered with surface sampling were lessened with increased temperature, due to a decrease in roughness of the standard resins and a greater uniformity in the nanocomposite resins.

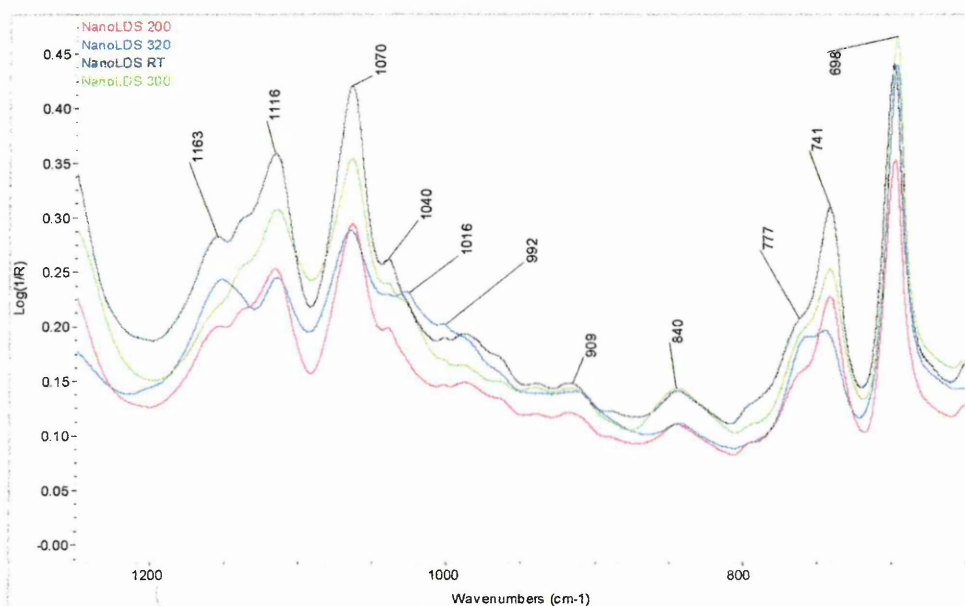Several regions showed characteristic changes:

Figure 5.25   Example - NanoLDS - RT, 200, 300 and 320°C (1250-650 cm⁻¹).

Spectral changes observed for the 1250-650 cm⁻¹ region are displayed in fig. 5.28, and are listed below:

- 741 cm⁻¹ decrease in relative intensity ($\nu_{conjugated}$(C-C=O)) indicating a possible rearrangement of the phthalate structure.

- 909 cm⁻¹ slight increase in relative intensity (out-of-plane δ(C-H$_2$)), indication of the scission of cross-linking polystyrene networks.

275

- 1016 cm^{-1} slight increase in relative intensity (in-plane δ(C-H)), free ester carbonyl resulting from scission of polyester structure.

- 1040 cm^{-1} decrease in relative intensity (ν(CH$_2$-OH)), free glycol units resultant of scission of polyester structure.

- 1070 cm^{-1} decrease in relative intensity (ν_{ring}(C-H)), disappearance of band due to scission of phthalate units from polyester structure.

- 1116 cm^{-1} decrease in relative intensity (ν_{ring}(C-H)), disappearance of band due to scission of phthalate units from polyester structure.
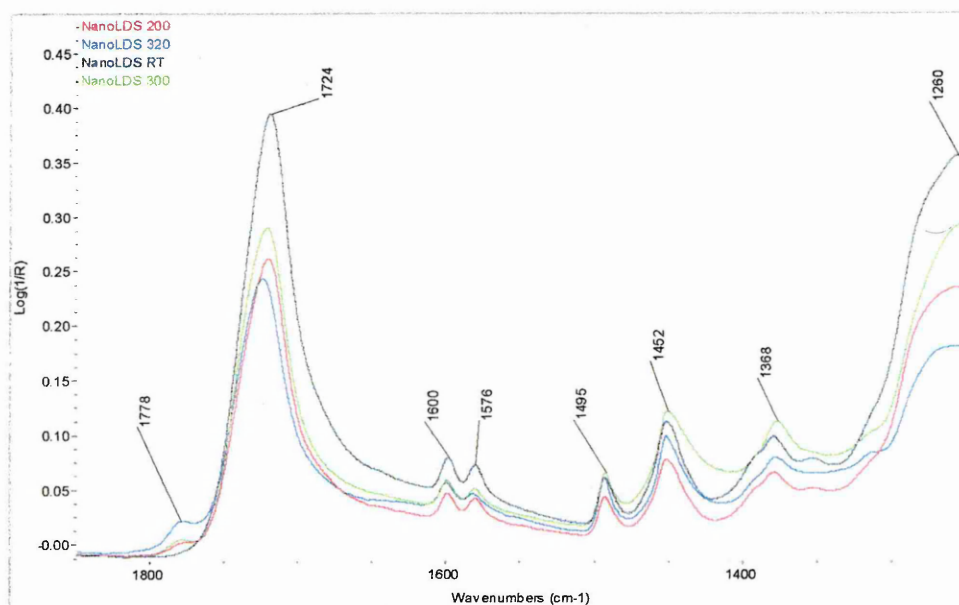

Figure 5.26   Example - NanoLDS - RT, 200, 300 and 320°C (1850-1250 cm^{-1}).

Spectral changes observed for the 1850-1250 cm^{-1} region are displayed in fig. 5.29, and are listed below:

- 1260 cm^{-1} decrease in relative intensity (ν(C-O) / δ(C-H)) and 1282 cm^{-1} decrease in relative intensity (ν(C-O-C)), scission of polyester structure.

- 1368 cm^{-1} slight decrease in relative intensity and shift to lower frequency (ν(C=C) / w(CH$_2$)), scission of maleic anhydride from polyester structure.

- 1576 cm^{-1} decrease in relative intensity (ν_{ring}(C-C) (doublet with 1600 cm^{-1})), possibly due to structural decomposition of low concentration of styrene monomers.

276

- 1778 cm^{-1} increase in intensity (ν(C=O), high frequency carbonyl), due to the formation of 7 and 8 member ring structures, leading to this unusually high position for a carbonyl band [5-19] (fig. 5.30). The slight shift to lower frequency of a band at 1368 cm^{-1} (ν(C=C) / w(CH$_2$)) indicated that the maleic anhydride residues may have been incorporated in the formation of the larger ring structures possibly through ring opening reactions with free glycol residues [5-20]. Phthalate and styrene residues may have also been degraded to form residues which may have become reactants.
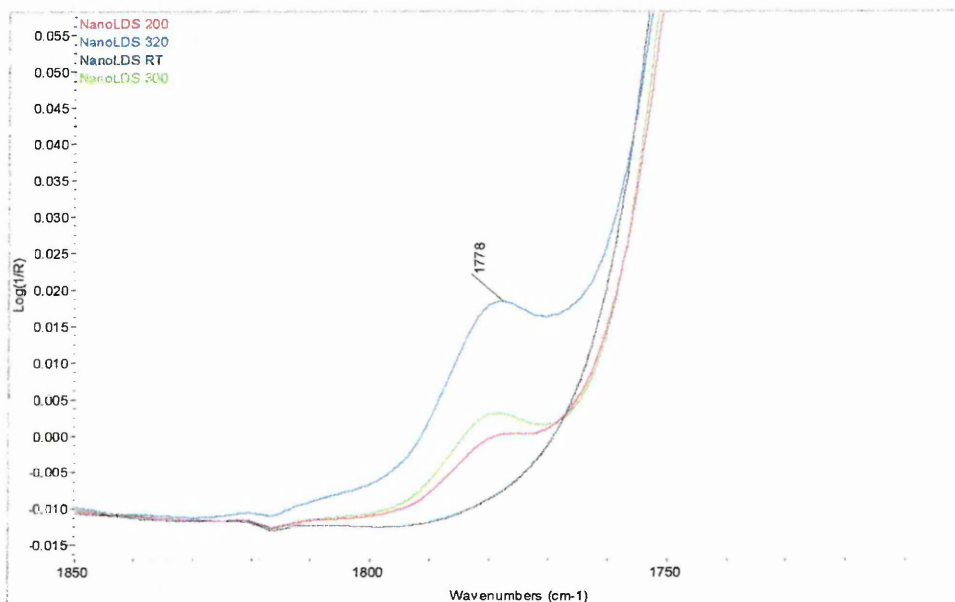

Figure 5.27   **Example - NanoLDS - RT, 200, 300 and 320°C (1850-1700 cm^{-1}).**

From the comparison of the results for the resins and nanocomposite resins, it was evident that the S-MMT had a good synergistic effect on the overall material. Under both post-cures, the addition of the organoclay reduced the decrease in intensity of the band at 1070 cm^{-1} (ν_{ring}(C-H)) and slightly reduced the increase in intensity of the band arising between 1778 cm^{-1} (ν(C=O), high frequency carbonyl).

Fig. 5.31 displays the difference in normalised intensity of the spectral band at 1778 cm^{-1} for the StdLDS and NanoLDS materials. Fig. 5.32 displays the difference in normalised intensity

277

of the spectral band at 1778 cm^{-1} for the StdSB and NanoSB materials. The RT intensity value was reduced to zero to display any increase in intensity with increased temperature.
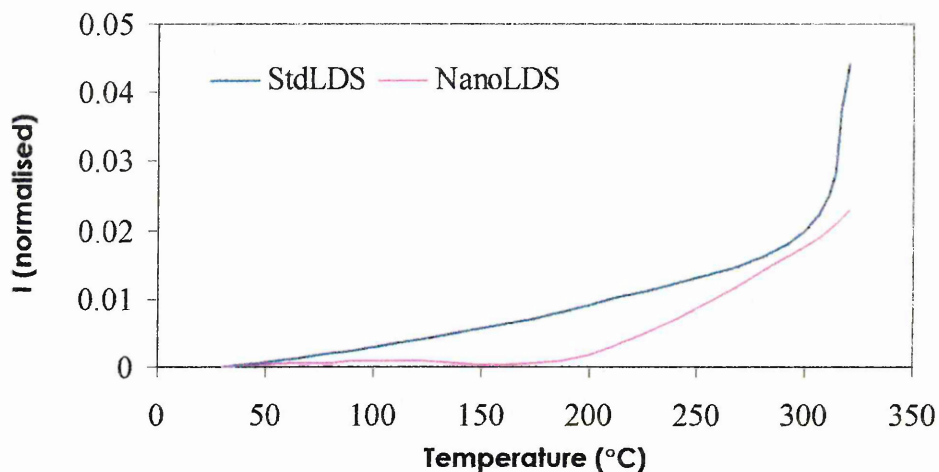

Figure 5.28 **Plot of normalised intensity vs. temperature for StdLDS and NanoLDS - ν(C=O) 1778 cm^{-1}.**
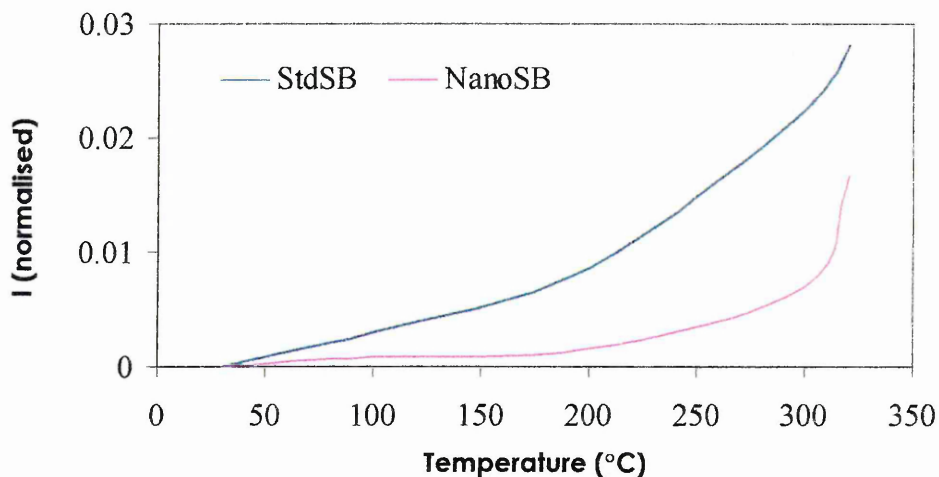

Figure 5.29 **Plot of normalised intensity vs. temperature for StdSB and NanoSB - ν(C=O) 1778 cm^{-1}.**

The intensity of the 1778 cm^{-1} band in the LDS materials (fig. 5.31) at 320 °C was seen to be reduced by 50%, by the inclusion of the 4 wt% S-MMT in the NanoLDS material relative to StdLDS. This effect was also seen in the SB materials (fig. 5.32) at 320 °C, but was

278

significantly less intense and the additive effect of the S-MMT appeared to have slightly less of an effect, reducing the intensity of the 1778 cm^{-1} band by 40 %.

Generally evidence of the degradation of the SB post-cured materials was more subtle than was seen with LDS post-cured materials. This may have been due to either a more complete cure or higher degree of cross-linking being imparted when post-curing at a higher temperature. The bands in the region > 1850 cm^{-1} did not show any change, and so, has been referred to, but not included in the study.

5.3.8   Summary of Results

- XRD showed that no exfoliation had occurred in the UPCN, but that the S-MMT was well dispersed. This was believed to have been due to an unsuccessful silanisation process.

- TGA of the UPCN samples showed a slight positive shift of T_{max} (i.e. from 362 °C for resins to 374 °C for the nanocomposites (~10 °C)), which was accompanied by a shift of greatest mass loss to higher temperatures, seen as greater area under higher temperature maxima. The increased thermal stability offered by the S-MMT was more effective under air than under a nitrogen atmosphere, which is could be evidence of char layer formation.

- Solvent resistance tests conducted on the different materials showed that the UPCN were more resistant to H_2O and ethanol than the virgin UPR. In all cases the SB post-cured materials were the most resistant to solvent diffusion, attributed to the higher degree of cross-linking. 2-butanone and hexane were seen to diffuse more quickly into the UPCN than the virgin UPR. The presence of the clay platelets in the UPCN may have caused micro-fissures and crazing that permitted the easier passage of the solvent into the material. This effect was most evident with the 2-butanone samples which had a swollen structural appearance, more spherical than the original cubic samples.

- The dimensional stability of the UPR and UPCN was recorded after heating to 250 °C, 300 °C and 320 °C. The UPCN were shown to have between 2.1-2.5 % less dimensional loss than the corresponding UPR.

- ESEM topographical analysis appeared to show an increase in the surface roughness of the UPCN relative to the UPR at increased temperature. The surface of the samples became rougher and more stable under the radiation emitted by the microscope after being exposed to higher temperatures.

- AFM tapping mode analysis gave roughness analysis data that showed the smoothing effect of higher temperatures on UPR and the increase in surface roughness in the UPCN (~5x). Phase imaging showed that the S-MMT was not uniformly dispersed (presence of UPR regions), but that in topographically high regions the crystalline clay phase was in abundance.

- ATR-FTIR analysis of the UPR and UPCN, showed that the S-MMT had a good synergistic effect on the overall material. Under both post-cures, the addition of the organoclay reduced the decrease in intensity of the band at 1070 cm^{-1} (ν_{ring}(C-H)) and slightly reduced the increase in intensity of the band arising at 1778 cm^{-1} (ν(C=O), high frequency carbonyl). This was seen as evidence of the well-dispersed clay agglomerates reducing the formation of combustion products, either by thermally stabilising the polyester structure through formation of a char layer or by slowing the mass transit of thermally degraded by-products from the polyester structure by acting as a tortuous path to diffusion.

Chapter 5 - References

[5-1]   Lee, JD, and Giannelis, E.P., *Polymer Preprints*, 1997, **38**, 688.

[5-2]   Kornmann X., Berglund, L.A., Sterte, J., and Giannelis, E.P., *Polym. Eng. & Sci.*, 1998, **38**, 1351.

[5-3]   Bharadwaj, R. K. and Boyd, R. H., *Polymer*, 1999, **40**, 4229.

[5-4]   Suh, D.J., Lim, Y.T. and Park, O.O., Polymer, 2000, **41**, 8557.

[5-5]   Bharadwaj, R. K., Mehrabi, A. R., Hamilton, C., Trujillo, C., Murga, M., Fan, R., Chavira, A. & Thompson, A. K., *Polymer*, 2002, **43, 3699.**

[5-6]   Yang, Y.S. and Lee, L.J., *Polymer*, 1998, **29**, 1793.

[5-7]   Gilman, J.W., *Appl. Clay Sci.*, 1999, **15**, 31.

[5-8]   *Private Communication* – Dr Steve Habesch, MRI, SHU, 2001.

[5-9]   B & G Inc., *Technical Articles*, Feb. 1995, Last accessed: 4.3.2003,
         URL: http://www.bandgmachine.com/technical/feb95.htm,

[5-10]   Bhushan, B. and Qi, J., *Nanotechnology*, 2003, **14**, 886.

[5-11]   Bhushan, B., Ma, T. and Higashioji, T., *J. Appl. Polym. Sci.*, 2002, **83**, 2225.

[5-12]   Seymour, R.B. Chemical Susceptibily, *Eng. Plastics*, Vol.II, 1988, 571.

[5-13]   A. Tidjani, R. Arnaud and A. DaSilva, *J. Appl. Polym. Sci.*, 1993, **47**, 211.

[5-14]   Paauw M. & Pizzi A., *J. Appl. Polym. Sci.*, 1993, **48**, 931.

[5-15]   Colthup, J., *Opt. Soc. Amer.*, 1950, **40**, 397.

[5-16]   Bellamy, L. J., The Infrared Spectra of Complex Molecules, Chapman & Hall, 3rd Ed., Vol. 1, 1975.

[5-17]   Paauw M. & Pizzi A., *J. Appl. Polym. Sci.*, 1991, **42**, 1377.

[5-18]   Silverstein, Bassler, Morrill, *Spectrometric identification of organic compounds*, 4th Ed., John Wiley and Sons, 1976.

[5-19]   Wilhelm C. & Gardette J-L, *J. Appl. Polym. Sci*, 1994, **51**, 1411.

[5-20]   Williams D.H. & Fleming I., *Spectroscopic Methods in Organic Chemistry*, 5th Ed., McGraw-Hill, 1997, 46.
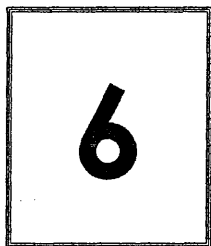
Kaolin-Phenylphosphonic Acid (KPPA)

Kaolin is a dioctahedral 1:1 layered clay mineral with the structural formula $Al_4Si_4O_{10}(OH)_8$. It is formed through the alteration of feldspar-rich parent rocks by either weathering or hydrothermal processes. Each layer of kaolin consists of two sheets: a tetrahedral sheet in which Si atoms are tetrahedrally co-ordinated by oxygen atoms; and an octahedral sheet where aluminium atoms are octahedrally co-ordinated to hydroxyl groups and shared apical oxygens from the silica tetrahedral sheet. One side of each kaolin layer presents a siloxane surface which arises from the bases of the silica tetrahedra whilst the other presents a surface of hydroxyl groups from the aluminium octahedra [6-1, 6-2]. Hydrogen bonding between these two surfaces imparts a significant cohesive energy between the layers which makes intercalation into kaolin difficult [6-1, 6-3 - 6-5].

Swelling of kaolin has previously been achieved by the intercalation of small polar molecules like dimethyl sulphoxide (DMSO) [6-6, 6-7], formamide [6-8, 6-9] and hydrazine [6-10, 6-11], which have been intercalated by hydrogen bonding to kaolin's aluminol surface. Intercalation of other molecules has been achieved by replacement of an entraining agent such as DMSO, water or acetone, for example water-expanded kaolin has previously been prepared using a DMSO intercalate which has then been used to intercalate molecules such as pyridine [6-12], amino acids [6-13] and alkylamines [6-14]. Wypych *et al.* [6-15] described a topotactic reaction that occurred between kaolin and phenylphosphonic acid (PPA) which resulted in the formation of covalent bonds between the acid and the clay surface according to the reaction:

$$Al_2Si_2O_5(OH)_4 + 3H_2O_3PPh \rightarrow Al_2Si_2O_5(OH)(HO_3PPh)_3.2H_2O + H_2O$$

This implied that PPA reacted with all three of the inner surface hydroxyls and the only OH group remaining after the process was the relatively inaccessible inner sheet hydroxyl. The aim of this study was to intercalate PPA in kaolin (KPPA) under reflux conditions, in a water-acetone mixture at elevated temperatures.
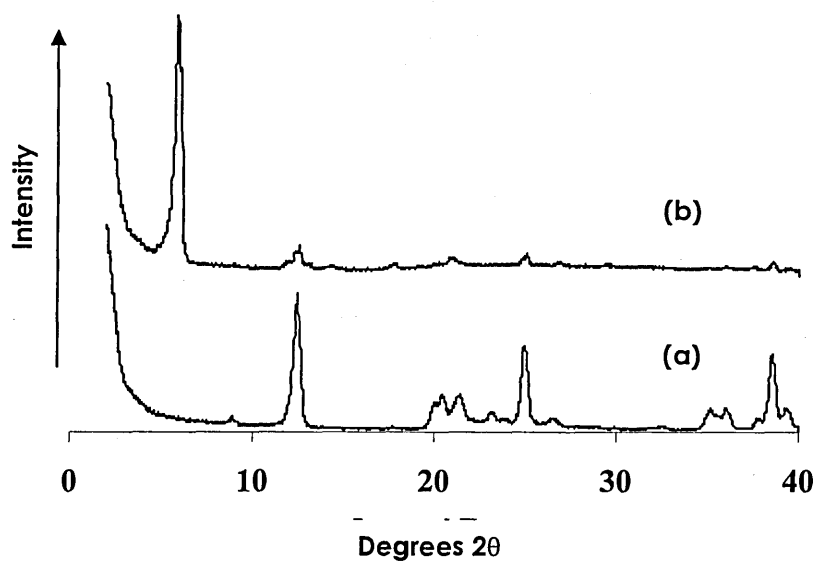
6.2.1   XRD Analysis

Figure 6.1   Comparison of XRD traces for (a) kaolin and (b) KPPA after 15-days under reflux in a water-acetone mixture.
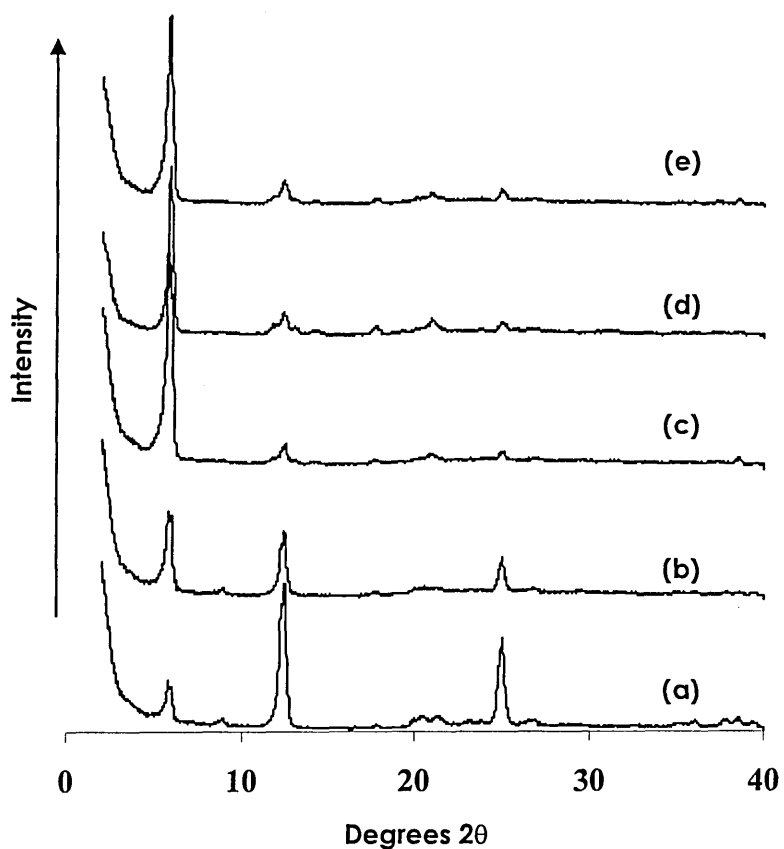

Figure 6.2   Comparison of XRD traces for KPPA samples refluxed for (a) 3, (b) 9, (c)15, (d) 21 and (e) 28 days in a water-acetone mixture.

The premise for these studies was that the greatly increased thermal stability being offered to PPA by kaolin, as was previously shown in [6-16, 6-17], could be investigated further before attempting to transfer this stability to a PS-KPPA hybrid.

The XRD traces in fig. 6.1 and 6.2 show that the kaolin had expanded (from 7 Å) when PPA was intercalated into the gallery increasing the interlayer spacing to 15.4 Å. The intensity of the d_{001} peak for the KPPA, increased steadily with reflux up to 15 days, after which the intensity did not increase further. The low intensity kaolin d_{001} peak at 12.3° 2θ remained present in the 15, 21 and 28-day reflux samples, the intensity of which fluctuated slightly beyond 15-days. This may have been the result of longer durations of reflux displacing some surface bound PPA.

6.2.2 TGA / DTG Analysis

The TGA traces in fig. 6.3, and DTG traces in fig. 6.4 clearly show the thermal stability being afforded to PPA through its intercalation into the kaolin gallery.
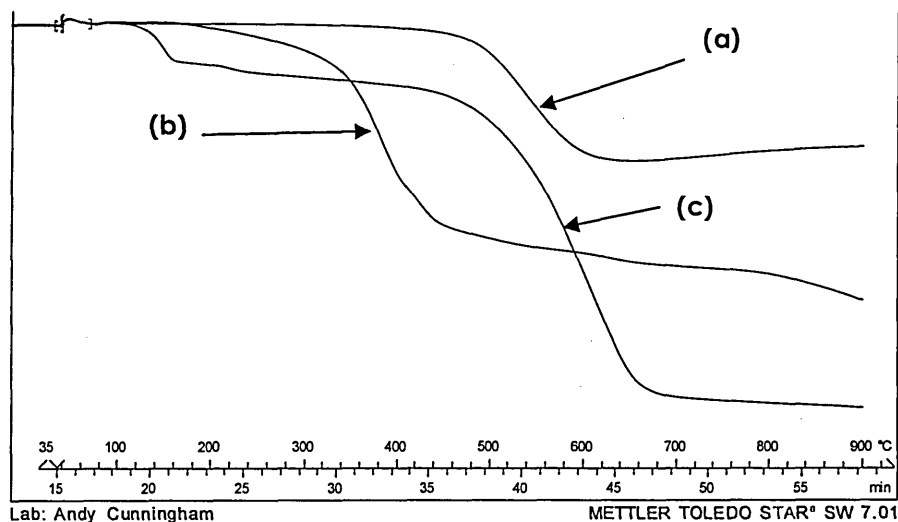

Figure 6.3   Comparison of TGA traces for (a) kaolin, (b) PPA and (c) KPPA (15-day reflux).

The TGA and DTG traces (fig. 6.3 and 6.4) show the extremely high thermal stability of the PPA intercalates. The DTG shows that decomposition of PPA reached a T_{max} value at ~350

°C and the dehydoxylation of kaolin occurred at a T_{max} = ~500 °C. The KPPA intercalates exhibited two major distinguishing maxima when compared to kaolin and PPA. The first was associated with a loss of ~4 wt% at 140 °C and the second occurred with the majority weight loss after the layer dehydroxylation at 585 °C.
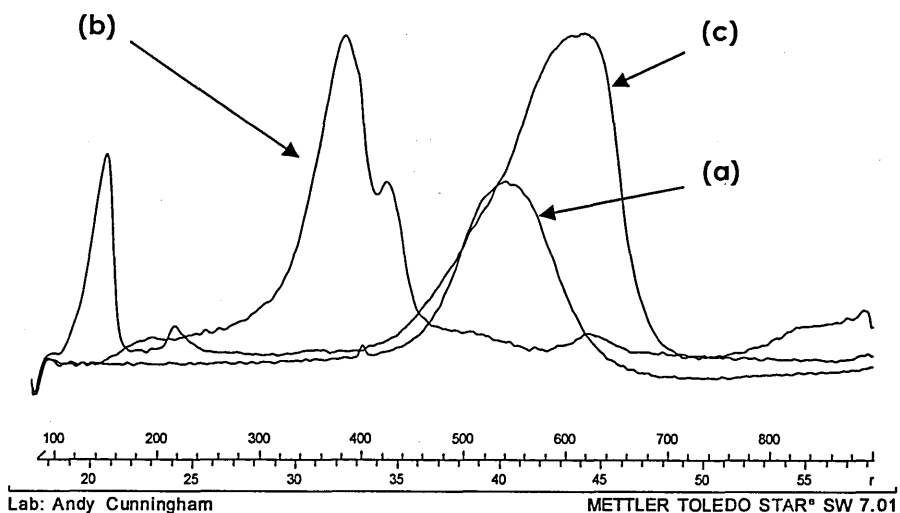

Figure 6.4   Comparison of DTG traces for (a) kaolin, (b) PPA and (c) KPPA (15-day Reflux).

Figure 6.5   Comparison of TGA traces for KPPA after refluxing in a water-acetone mixture for (a) 3, (b) 9, (c) 15, (d) 21 and (e) 28 days.

As the duration of the reflux increased the weight losses at 140 °C increased from 0.3 wt% at 3 days to 3 wt% at 21 and 28 days (fig. 6.5). This has been reported as adsorbed water by others [6-15] and was definitely confirmed by Breen et al. [6-18] using TG-MS. As well as

this increase, the maxima indicating events around the dehydroxylation of kaolin (> 500 °C) shifted to increasingly higher temperatures with increasing reflux duration (fig. 6.6). The T_{max} values ranged from 540 °C at 3 days to 660 °C at 21 days.
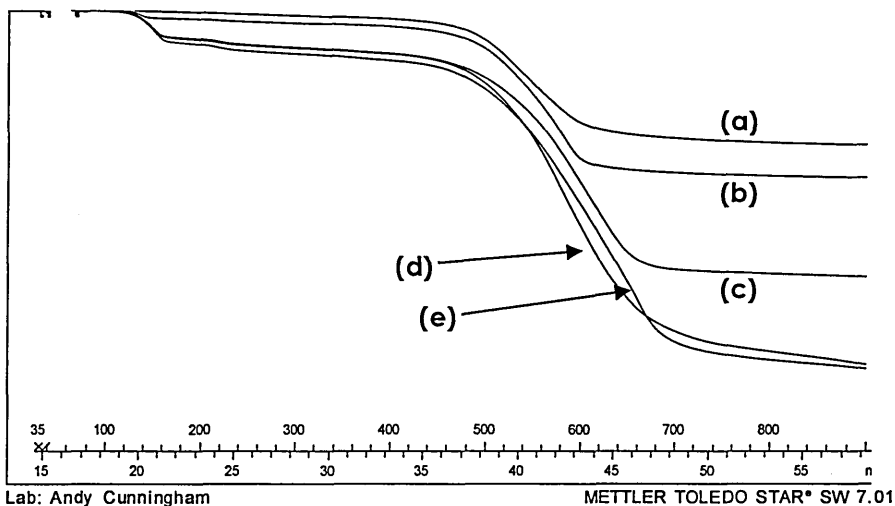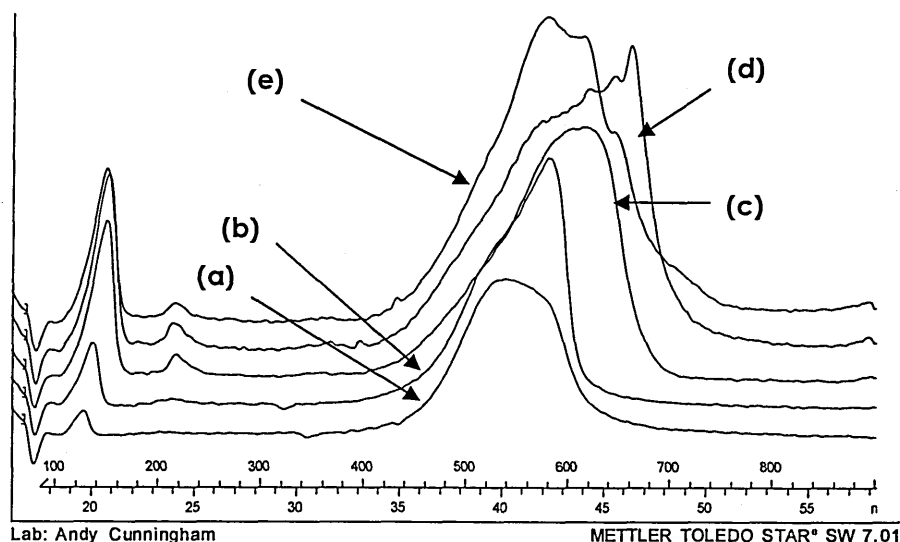

Figure 6.6   **Comparison of DTG traces for KPPA after refluxing in a water-acetone mixture for (a) 3, (b) 9, (c) 15, (d) 21 and (e) 28 days.**

The T_{max} in the 28-day reflux samples was decreased by 80 °C to 580 °C (fig. 6.6(e)) and evolved products were thermally desorbed over a slightly increased temperature range (i.e. 400-800+ °C) than previously shown in the 21-day samples (fig. 6.6(d)).

6.2.3   DRIFTS Analysis

The DRIFTS spectrum of each of the kaolin, PPA and KPPA samples (fig. 6.7) were obtained at RT. The spectra of these samples exhibited a range of bands most of which could be directly assigned to vibrations of the kaolin host or PPA.

Bands at 3698 cm^{-1} and 3625 cm^{-1} were assigned to the inner surface and inner sheet hydroxyls. Much broader bands at 3551 cm^{-1} and 3331 cm^{-1} were attributed to hydrogen bonded hydroxyls arising from either the interaction of water or PPA with the inner surface
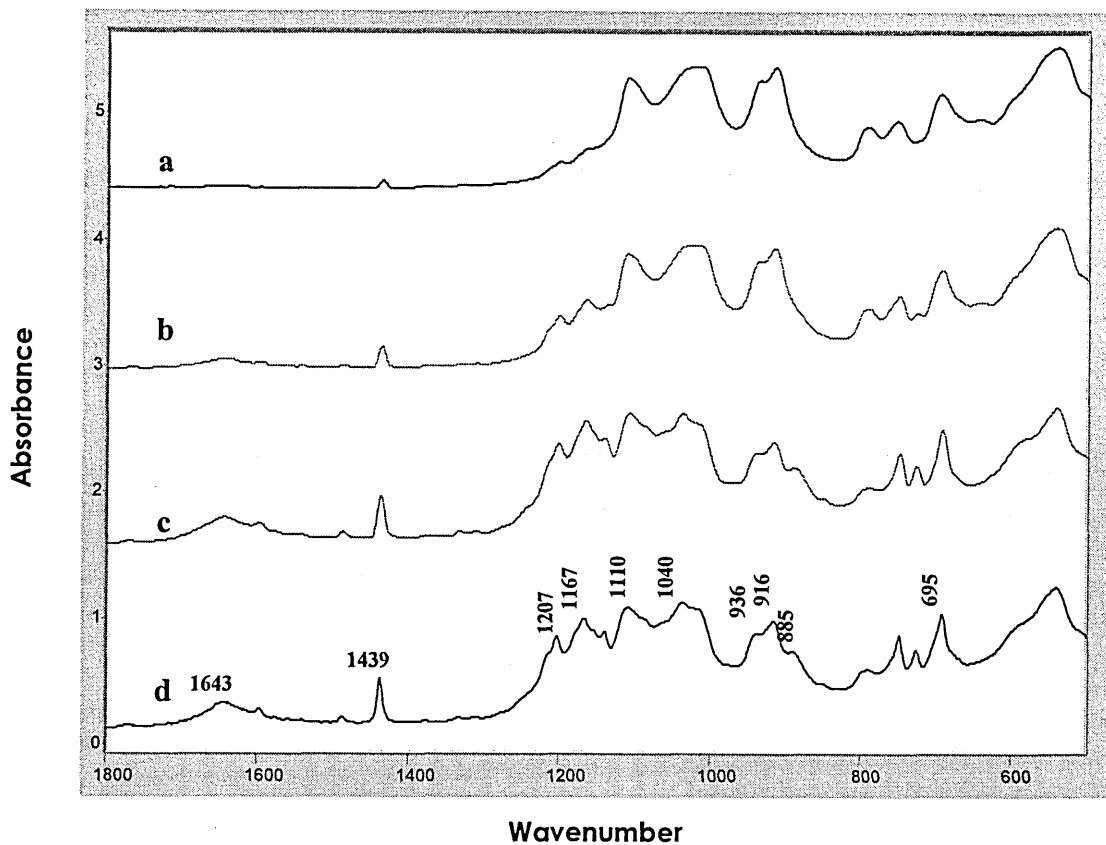
287

Figure 6.7 DRIFTS spectra (1800 - 500 cm⁻¹) of the KPPA intercalate after refluxing for (a) 3, (b) 9, (c) 15 and (d) 28 days.
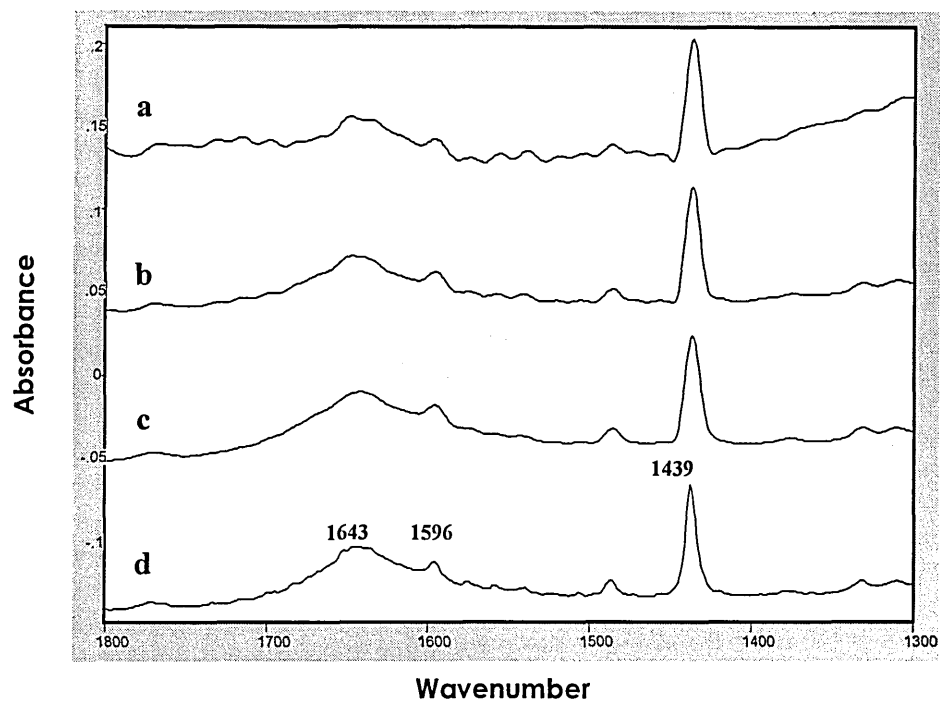

Figure 6.8 DRIFTS spectra (1800 - 1300 cm⁻¹) of the KPPA intercalate after refluxing for (a) 3, (b) 9, (c) 15 and (d) 28 days.

hydroxyls on the gibbsite sheet. In this region, there was also a broad contribution from hydrogen bonded OH in the region 2500-3700 cm^{-1}, which increased with reflux duration. A band at 3056 cm^{-1} and a corresponding shoulder at 3076 cm^{-1} were assigned to the C-H stretching vibrations of the phenyl ring, along with other bands at 1591 and 1487 cm^{-1} (fig. 6.8). Phenyl ring bands at 749 and 693 cm^{-1} could not be discerned because they overlapped with kaolin bands.

There was some uncertainty regarding the band at 1207 cm^{-1} because the ν(P=O) stretch occurs at 1220 cm^{-1} in PPA. This was also true of the 1140 cm^{-1} ν(P-O) stretching band which was downshifted (by 26 cm^{-1}) and appeared at 1167 cm^{-1}. The other ν(P-O) bands at 1068, 1040 and 990 cm^{-1} were obscured by the Si-O bands at 1100, 936 and 916 cm^{-1} assigned to the inner sheet and inner surface hydroxyls, respectively. However, there was a third contribution in this region near 885 cm^{-1}. The inner sheet hydroxyl was considered to be relatively inaccessible although its perturbation via interaction with adsorbed hydrazine
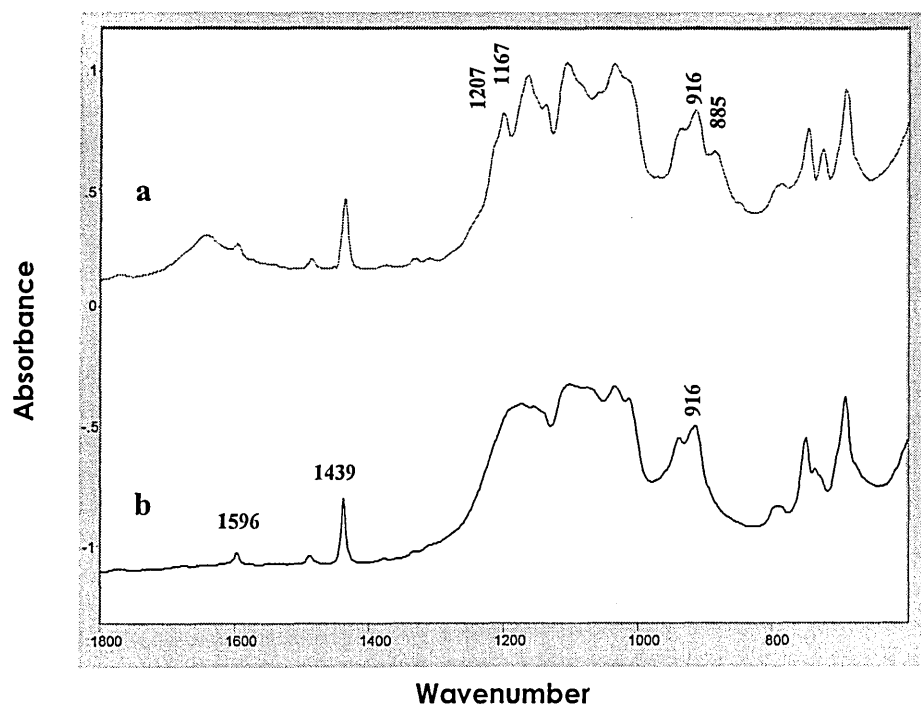

Figure 6.9   DRIFTS spectra of the 15-day reflux KPPA intercalate (a) after refluxing and (b) after heating at 150 °C / 2 h.

has been reported [6-19] which may suggest that the 885 cm^{-1} band represents a significant downward shift in the 936 cm^{-1} band.

A broad band at 1643 cm^{-1} was assigned to hydrogen bonded water and the P-C stretch of the PPA intercalant was shown as a prominent band at 1439 cm^{-1}, the intensity of both these bands increased with reflux duration.   The spectra recorded after increasing the reflux duration showed that an increasing quantity of water and PPA had been adsorbed, by the intensity of the bands at 1643 cm^{-1} and 1493 cm^{-1} having increased relative to the band at 916 cm^{-1} (fig. 6.7 and 6.8).

After heating the 15-day reflux product at 150 °C for two hours (fig. 6.9), the bands at 3457 and 1642 cm^{-1} were removed.   The band at 1207 cm^{-1} merged with a band at 1167 cm^{-1} and the band at 885 cm^{-1} had completely disappeared leaving the bands at 937 and 916 cm^{-1}.   In addition, a broad band attributed to hydrogen bonded OH (~3400 cm^{-1}) was significantly reduced, whereas the bands for the P-C stretch (1437 cm^{-1}) and the phenyl ring vibrations (3056, 1596, 1487 cm^{-1}) were not significantly affected by the increased temperature. This was taken as evidence of the strength of the bonding between PPA and the kaolin surface.

6.2.4 ^{31}P MAS NMR Analysis

The intensity per unit weight increased as the period of the reflux increased, this indicated a quantitative increase in the concentration of PPA that was binding at the kaolin surface. This intensity reached a maximum after refluxing for 15 days, after which time further refluxing appeared to remove PPA from the kaolin surface. Scrutiny of the corresponding XRD data (fig. 6.2) appeared to support this interpretation.

The ^{31}P MAS NMR spectrum of pure PPA exhibited a single resonance at +21.2 ppm (fig. 6.10 a), which correlated well to the literature value of +21 ppm [6-20]. The spectra for the

kaolin-phenylphosphonic acid reflux products was, however, more complex. The spectra for all the refluxed samples exhibited three peaks at +1.2, -3.7 and -7.3 ppm (fig. 6.10 b). The intensity ratio of the three peaks did not vary with reflux time, indicating that the first and last PPA molecules to be intercalated were all in the same environment.
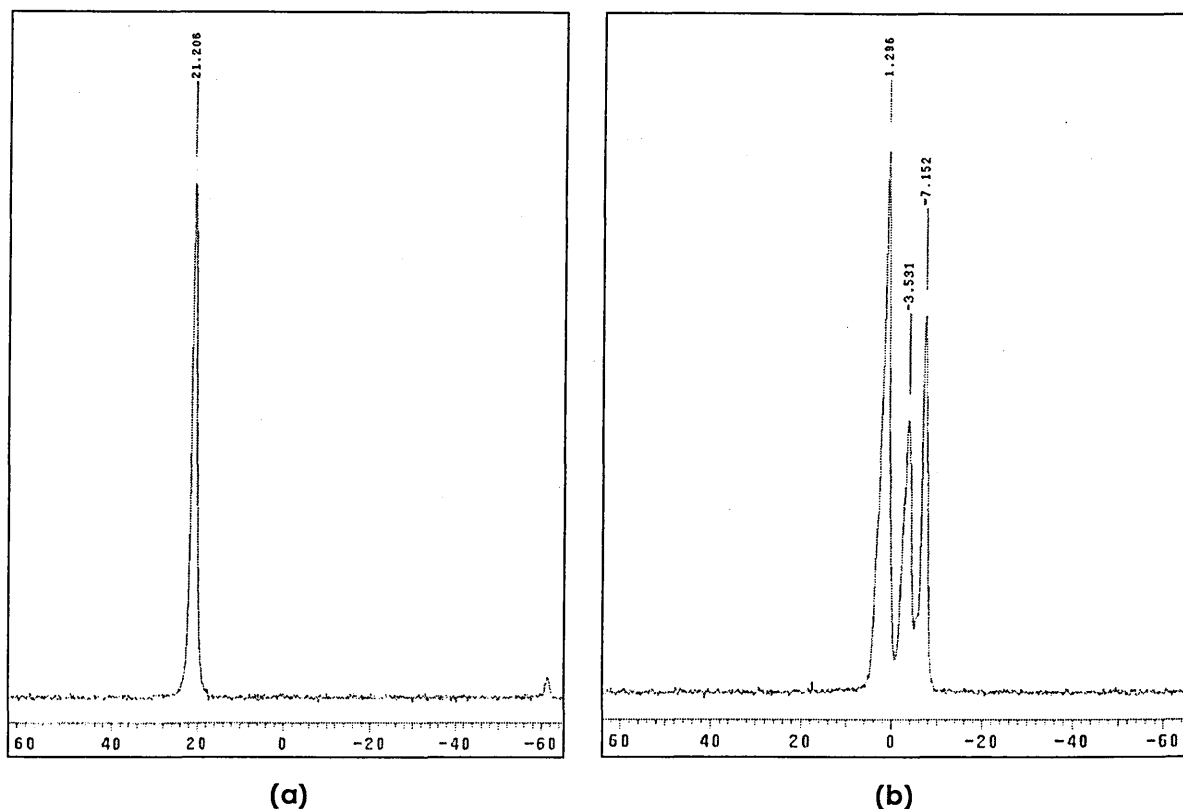

(a)   (b)

Figure 6.10   **³¹P MAS NMR of (a) PPA resonance and (b) KPPA-15 day reflux chemical shifts.**

The lack of a resonance at +21.2 ppm meant that there was no unreacted PPA in the reflux products and no trace of the coupling of two phosphorous systems, which would have a resonance at +5 ppm [6-21, 6-22]. It was difficult to determine what the nature of the three different resonances were, if they were wholly due to bonding of the PPA to the kaolin surface or mixed with coupling within the galleries (i.e. between PPA molecules). The other resonances were, therefore, representative of chemically altered PPA existing in a range of non-equivalent states within the unit cell. These were believed to be due to PPA binding to the surface hydroxyls of kaolin in three distinct ways, outlined in fig. 6.11. One shift may represent phosphonic acid groups trigonally hydrogen bonded to surface hydroxyls.

291

Whereas, the other two shifts may represent the phosphonic acid groups forming covalent bonds through one or two Al-O-P linkages to the surface.
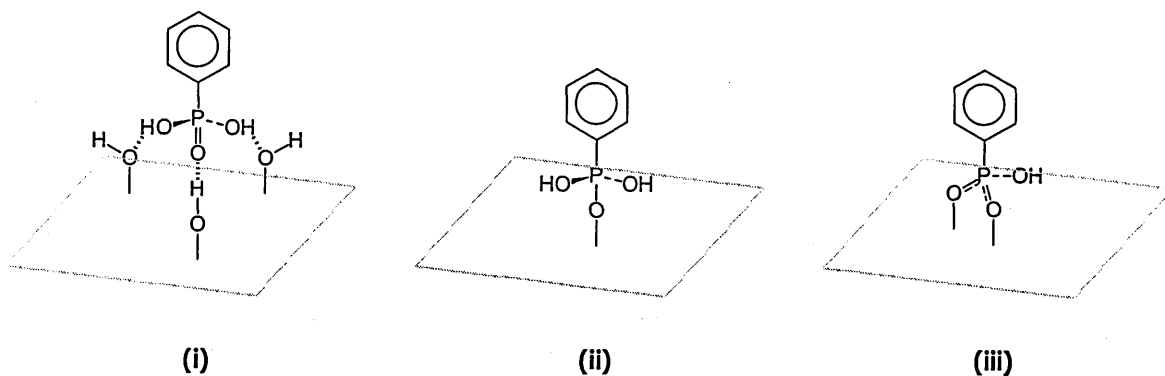

(i)   (ii)   (iii)

Figure 6.11 **Schematic representations of three proposed bonding orientations of PPA at the kaolin surface.**

The intensity per unit weight increases as the period of reflux increases, indicating a quantitative increase in the concentration of PPA binding at the surface. Reaching a maximum at 15 days after which time further refluxing appears to be removing PPA from the kaolin surface, this appears to be confirmed by the XRD data for the 6 samples.

KPPA-15 day reflux, chemical shifts (ppm)		
(a) air dried	**(b) 150 °C / 2 hr**	**(c) sample (b) rehydrated**
+1.25	+1.40	+1.40
-3.68	-3.43	-1.21
-7.30	-7.05	-5.64
		-7.85

Table 6.1 **Comparison of the chemical shifts observed after drying and rehydrating KPPA-15 day reflux samples.**

When samples of the 15-day reflux products were heated at 150 °C for two hours, only slight variations were observed in the ^{31}P NMR shifts (see table 6.1b). This could indicate a lack of water in the interlayer after refluxing, which removes the possibility of water bridges being formed between phosphonic acid groups. However, when the same samples were hydrated at elevated humidity and transferred under an inert atmosphere, the peaks changed from the three previously observed positions, to two doublets (see table 6.1 c, fig.

6.12). The interactions between the water molecules and the phosphonic acid groups appears to alter their bonding states considerably, most significantly the peak at -3.7 ppm was no longer present.
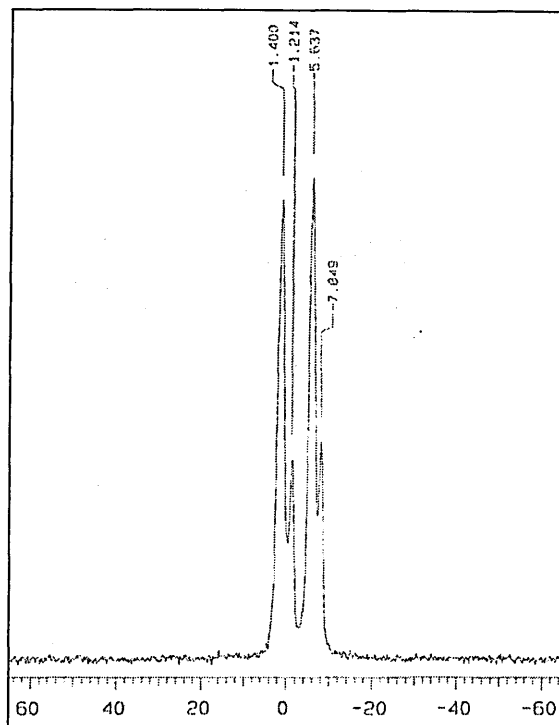

Figure 6.12 ^{31}P MAS NMR chemical shifts of hydrated KPPA-15 day reflux.

6.2.5   PS-KPPA Nanocomposite Preparation

The formation of nanocomposites from KPPA dispersed in a PS host matrix was unsuccessful when attempted using both *in-situ* polymerisation and melt blending processes. There was no evidence of any PS entering the expanded kaolin structure of samples prepared using KPPA samples refluxed for between 15 - 28 days. As a result of this lack of PS migration, agglomerates of KPPA were formed which resulted in there being no KPPA dispersal to transfer any thermal stability to the host matrix.

6.3   Discussion / Conclusion

The expansion of the interlayer spacing by 8.4 Å was consistent with the phenyl ring of PPA being oriented at a high angle to the kaolin basal surface. PPA intercalated the kaolin

crystal structure to form an expanded phase that exhibited remarkable thermal stability. The intercalation by reflux from a water-acetone mixture slowed beyond 15-days, with reference to PPA and water uptake, however, intercalated matter did increase in concentration as shown by TGA / DTG (fig. 6.5 and 6.6).

DRIFTS spectra showed that the KPPA complexes had retained water as well as PPA and that by heating these samples, this weakly hydrogen bonded water could be lost. ^{31}P MAS NMR of all the KPPA samples showed three peaks (at +1.2, -3.7 and -7.3 ppm) which were representative of PPA existing in three non-equivalent bonding states at the kaolin surface. The evolution of the weakly hydrogen bonded water appeared to significantly alter the nature of the bonding, most notably the disappearance of a shift at -3.7 ppm, which may have indicated the presence of PPA in a hydrogen bonded state after refluxing.

The inability to form nanocomposites through the union of KPPA and PS may have been due to an incompatibility of the production processes for the materials (i.e. solvent intercalation may produce a more intimate mixture). Other changes which could be made, may be to change the polymer host matrix or to possibly functionalise the intercalant species to increase the compatibility of the gallery environment.

The high thermal stability of these hybrid materials was evident from these studies. The use of covalently bound intercalants in nanocomposite manufacture warrants further investigation.

Chapter 6 - References

[6-1]   Giese, R.F., in *Hydrous Phyllosilicates*, ed. Bailey S.W., Mineralogical Society of America, Washington, DC, 29, 1988.

[6-2]   Bish, D.L., *Clays Clay Miner.*, 1993, **41**, 738.

[6-3]   Cruz, M., Jacobs, H. & Fripiat, J.J., *Proc. Int. Clay Conf.*, 1973, 35.

[6-4]   Giese, R.F., *Clays Clay Miner.*, 1978, **26**, 31.

[6-5]   Giese, R.F., *Bull. Miner.*, 1982, **105**, 417.

[6-6]   Johnstone, C.J., Sposito, G., Spocian, D.F. and Birge, R.R., *J. Phys. Chem.*, 1984, **88**, 5859.

[6-7]   Frost, R.L., Kristof, J., Paroz, G.N. and Kloprogge, J.T., *J. Phys. Chem.*, 1998, **102**, 8519.

[6-8]   Olejnik, S., Posner, A.M. and Quirk, J.T., *Clays Clay Miner.*, 1974, **19**, 83.

[6-9]   Frost, R.L., Kristof, J., Horvath, E. and Kloprogge, J.T., *Spectrochim. Acta, Part A*, 2000, **56**, 1711.

[6-10]   Frost, R.L., Kristof, J., Kloprogge, J.T. and Horvath, E., *Clays Clay Miner.*, 1999, **47**, 732.

[6-11]   Johnstone, C.J., Bish, D.L., Eckert, J. and Brown, L.A., *J. Phys. Chem.*, 2000, **104**, 8080.

[6-12]   Sugahara, Y., Satokawa, S., Yoshioka, K-I., Kurado, K. and Kato, C., *Clays Clay Miner.*, 1989, **37**, 143.

[6-13]   Makoto, M., *Clays Clay Miner.*, 1999, **47**, 793.

[6-14]   Komori, Y., Sugahara, Y. and Kurado, K., *Appl. Clay Sci.*, 1999, **15**, 241.

[6-15]   Guimaras, J.L., Peralta-Zamora, P. & Wypych, W.J., *J. Colloid Interface Sci.*, 1998, **206**, 281.

[6-16]   Range, K.J., Range, A. and Weiss A., 'Experimental Classification of Kaolin and Halloysite Minerals', in Proceedings of the International Clay Conference, Tokyo, Japan, ed. Heller, L., Israel University Press, Jerusalem; *Proc. Int. Clay Conf.*, 1969, **1**, 3.

[6-17]   Bailey, S.W., in Proceedings of the International Clay Conference, Strasbourg, France, ed. Farmer V.C. and Tardy, Y.; *Sci. Geol. Mem.*, 1989, **86**, 89.

[6-18]   Breen, C., D'Mello, N. and Yarwood, J., *J. Mater. Chem.*, 2002, **12**, 273.

[6-19]   Johnston, C.T. and Stone D.A., *Clays Clay Miner.*, 1990, **38**, 121.

[6-20]   Harris, R.K. and Merwin L.H., *J. Chem. Soc., Faraday Trans.*, 1989, **85**, 1409.

[6-21]   Fyfe, C.A. and Wasylishen R.E., in *Solid State Chemistry* Part 1. Techniques, eds. Cheetham, A.K. and Day, P., Oxford Science Publishers, Oxford, UK, 1988.

[6-22]   Carlino, S., Hudson, M.J., Waqif Husain, S. and Knowles, J.A., *Solid State Ionics*, 1996, **84**, 117.

7

Conclusions, Further and Future Work

7.1　Conclusions

7.1.1　Characterisation and Thermal Stability of Organoclays

In studies of the thermal stability of n-alkylammonium and n-alkyltrimethylammonium surfactants exchanged with structurally different MMT clays, various differences were shown with regard to the desorption of the respective organic content. TGA/DTG showed that alkyl chains with increasing lengths released organic compounds at varying stages, which were signified by weight losses within the 200-450 °C range. These stages appeared to be related to the increasing length of the alkyl chain in the clay gallery. For n-alkylammonium surfactants these stages of desorption were shown to increase in number and shift to higher temperatures as C_n was increased. Whilst for n-alkyltrimethylammonium surfactants the increasing number of desorption stages were shown to shift to increase the concentration of compounds desorbed at temperatures between 200-300 °C.

The desorption of the fragmented alkylammonium surfactants at higher temperatures (i.e. >380 °C) from iron containing SWa-1 (43 %) than SAz-1 (36 %) organoclays may be evidence of a radical trapping mechanism, which has been reported as offering a possible additive advantage in flame retardant polymers.

A large number aromatic species were shown to be desorbed at lower temperatures from the $C_n = 16$ (CTAB) organoclays, which could have implications for processing of polymer-clay nanocomposites (particularly by melt processing).

7.1.2　Polystyrene-Clay Nanocomposites (PSCNs)

7.1.2.1　Analysis of the Thermal Stability PSCNs

It has been shown that by dispersing 1 wt% of various alkyltrimethylammonium exchanged MMT clays in styrene monomer and then submitting these materials to a high temperature, short duration curing procedure led to the production of exfoliated polystyrene-clay nanocomposites (PSCNs). The preparation method was shown to be effective at

producing exfoliated nanocomposites, up to 1 wt% of the various organoclays using AIBN and BPO as initiators. The MCBP-C_n PSCNs remained exfoliated up to 5 wt% , they also showed higher thermal stability when compared with the commercial products, which XRD results showed to remain stacked at organoclay loadings > 1 wt%.

These materials were analysed by TGA and XRD to characterise any increase in thermal stability and the dispersal of clay platelets within the material. From a comparison of different types of free-radical initiators, it was demonstrated that by using AIBN as the initiator, the greatest increase in thermal stability was achieved. The relative effectiveness of the different initiators for the production of the most thermally stable PSCNs was AIBN > BPO > SPS > APS >>AIBA. This was thought to be due to the less bulky and more reactive AIBN being intercalated more easily, leading to intimate polymerisation within the galleries.

From a comparison of 0.5, 1.0 and 2.0 wt% initiator concentrations, 0.5 wt% was shown to be the concentration that was most effective at producing higher thermal stability in PSCNs. 0.5 wt% of initiator and concentrations above and below this may have been better amounts to use for this study; however, the results obtained in this thesis still give a strong indication of the effect of changing associated PSCN variables.

It has been demonstrated that lower organic modifier concentrations in combination with less bulky organocations (i.e. single linear alkyl chain) showed higher T_{max} values. The relative effectiveness of these various organoclays for the production of more thermally stable PSCNs was MCBP-C_n > C15A > C20A >> C10A. A possible reason for the lower efficacy of the commercially available organoclays may have been the congestion of the MMT galleries with alkyl chains, which may lead to them being relatively inflexible and reduced the migration of monomer into the gallery spaces.

A one-pot method for the production of PSCNs, by the *in-situ* polymerisation of PS in the presence of decanamide (an uncharged surfactant) and Na-MMT has been shown to be successful.

XRD and TGA analysis of these PSCN have shown the necessity for a balance between the concentrations of alkylamide and Na-MMT to optimise the d-spacing ($\geq$ 38.4 Å) and T_{max} (shifted +15-20 °C). An imbalance was shown to lead to the presence of agglomerated clay platelets which decreased the thermal stability of the PSCN matrix.

The one-pot synthesis of PSCNs incorporating NVF molecules, has to date been less successful. Attempts to produce PSCNs from pre-formulated NVF-MMT organoclays resulted in MMT remaining stacked in the PS matrix. The lack of dispersion was attributed to space-filling NVF and water making the MMT gallery congested and hindering the penetration of styrene monomer. XRD and TG analysis identified the slight expansion of the MMT galleries by NVF and the presence of two states within the galleries. These states were thought to be (i) NVF directly associated with Na$^+$ cations, held thermally stable until 260 °C and (ii) interstitial space-filling NVF, held thermally stable until 130 °C.

The removal of space-filling NVF and water led to a uniform dispersal of the NVF-MMT organoclay throughout a PS matrix. This dispersal shifted the T_{max} > +20 °C. However, the d_{001} = 25.7 Å shown by the corresponding PSCNs indicated that the concentration of PS within the galleries was limited. It was thought that polymerisation through the galleries was predominantly between NVF molecules. These were bonded at the gallery edges to the PS matrix and homogeneously dispersed as the PS chain growth propagated.

The one-pot synthesis of foamtaine scab (FS)-MMT PSCNs has so-far been unsuccessful. The MMT galleries in FS-MMT organoclays were shown to be expanded by 10.6 Å, to 22.3 Å.

These organoclays showed that the amphoteric surfactant had a relatively high thermal stability (i.e. T_{max} = 320 °C) which showed promise for its application within various processing methods and polymeric systems. However, in attempts to produce PSCNs the organoclay failed to disperse. This could have been due to the high molecular weight of the surfactant, the variety of charge carried by the surfactant or the relatively high thermal stability of FS in the MMT galleries, which was much higher than the production process used.

7.1.3 Associated Studies on Unsaturated Polyester-Clay Nanocomposites (UPCNs)

TG analysis of the UPCN samples showed a slight positive shift of T_{max}, from 360 °C for standard resins to 375 °C for the UPCNs (~15 °C). The increased thermal stability offered by the S-MMT was more effective under air than under a nitrogen atmosphere, which may have been evidence of the formation of a char layer.

The XRD traces showed that no exfoliation had occurred in the UPCN, but that the silane modified MMT (S-MMT) was well dispersed. This was believed to have been due to an unsuccessful silane treatment process at Scott-Bader.

Solvent resistance tests showed that the UPCNs were more resistant to water and ethanol than the standard resins. In all cases the SB post-cured materials were the most resistant to solvent diffusion, which was attributed to a higher degree of cross-linking. Dimensional stability tests on the resins and UPCN materials were conducted and the dimensions were recorded after heating to 250 °C, 300 °C and 320 °C. The UPCNs were shown to have approximately 2.5 % less dimensional loss than the corresponding resins.

ESEM topographical analysis showed an increase in the surface roughness of the UPCN relative to the UPR at increased temperature. The samples' surfaces became rougher and more stable to the radiation emitted by the microscope after exposure to higher

temperatures. AFM tapping mode analysis provided roughness analysis data which showed the smoothing effect of higher temperatures on UPR and the increase in surface roughness in the UPCN (~5x). Also, phase imaging showed that S-MMT had not been uniformly dispersed in the UPCNs. This was signified by an abundance of UPR in topographically low regions and an abundance of a crystalline clay phase in topographically high regions of the materials surface after heating.

ATR-FTIR analysis of the UPR and UPCNs, showed that the S-MMT had a good synergistic effect on the overall material. Under both post-cures, the addition of the organoclay reduced the decrease in intensity of a band at 1070 cm^{-1} (ν_{ring}(C-H)) and slightly reduced the increase in intensity of the band arising between 1778 cm^{-1} (ν(C=O), high frequency carbonyl). This was thought to be evidence that the well-dispersed clay agglomerates reduced the formation of combustion products, this was either done by thermally stabilising the polyester structure through formation of a char layer or by slowing the mass transit of thermally degraded by-products from the polyester structure by acting as a tortuous path to diffusion.

7.1.4 Kaolin-Phenylphosphonic Acid (KPPA)

The XRD analysis of kaolin intercalated with phenylphosphonic acid showed the interlayer to be expanded by 8.4 Å; this was consistent with the phenyl ring of PPA being oriented at a high angle to the kaolin basal surface. TG analysis of the PPA intercalated in the kaolin crystal structure to form an expanded phase that exhibited remarkable thermal stability. The intercalation by reflux from a water-acetone mixture slowed beyond 15-days, however, intercalated matter did increase in concentration as shown by TGA / DTG (fig. 6.5 and 6.6).

DRIFTS analysis showed that the KPPA complexes had retained water as well as PPA and that by heating these samples, this H-bonded water could be lost. ^{31}P MAS NMR of all the KPPA samples showed three peaks at +1.2, -3.7 and -7.3 ppm which represented PPA

existing in three non-equivalent bonding states at the kaolin surface. The evolution of hydrogen bonded water appeared to alter the nature of the bonding, shown most notably by the disappearance of a shift at -3.7 ppm, which may have indicated the presence of PPA in a hydrogen bonded state after refluxing.

The inability to form nanocomposites through the union of KPPA and PS was thought to be due to the incompatibility of the production processes for the materials. The very high thermal stability of the hybrid materials shown in this study indicated that the use of covalently bound intercalate in nanocomposite manufacture warrants further investigation.

7.2 Further Work

7.2.1 ATR-FTIR Study of PSCN Reaction Kinetics

The main regions that have been studied, so far, are the disappearance of C-H st. – 951-841 cm^{-1} and the appearance of C-H bend – 2955-2837 cm^{-1}.
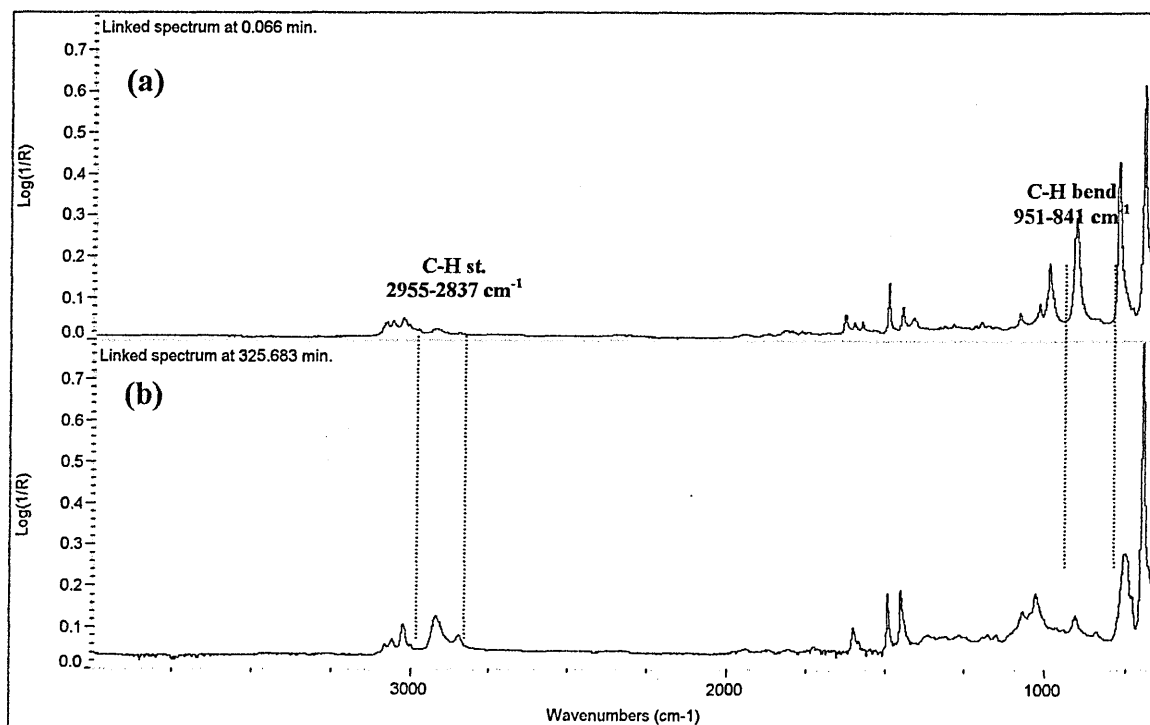

Figure 7.1   ATR-FTIR spectra of (a) styrene / 1wt% C15A and (b) polystyrene/1wt% C15A.
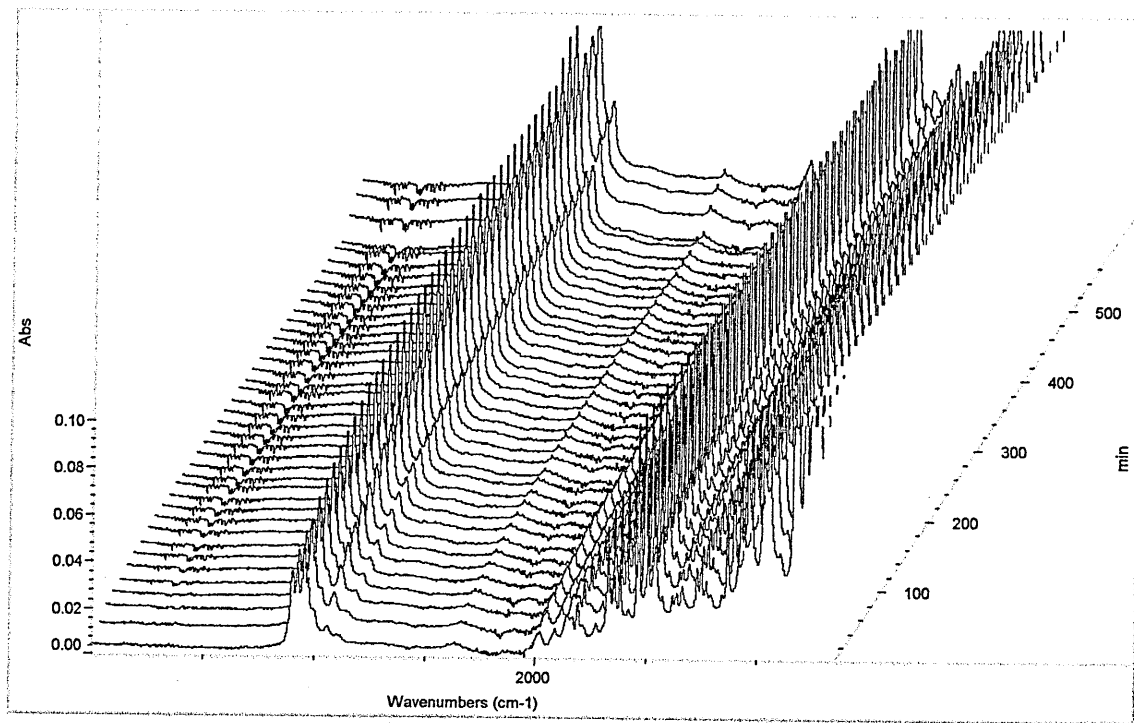
Figure 7.2   Styrene/1 wt% BPO Initiator, cured at 80 °C. Spectra taken every 15 mins, for 500 mins total.
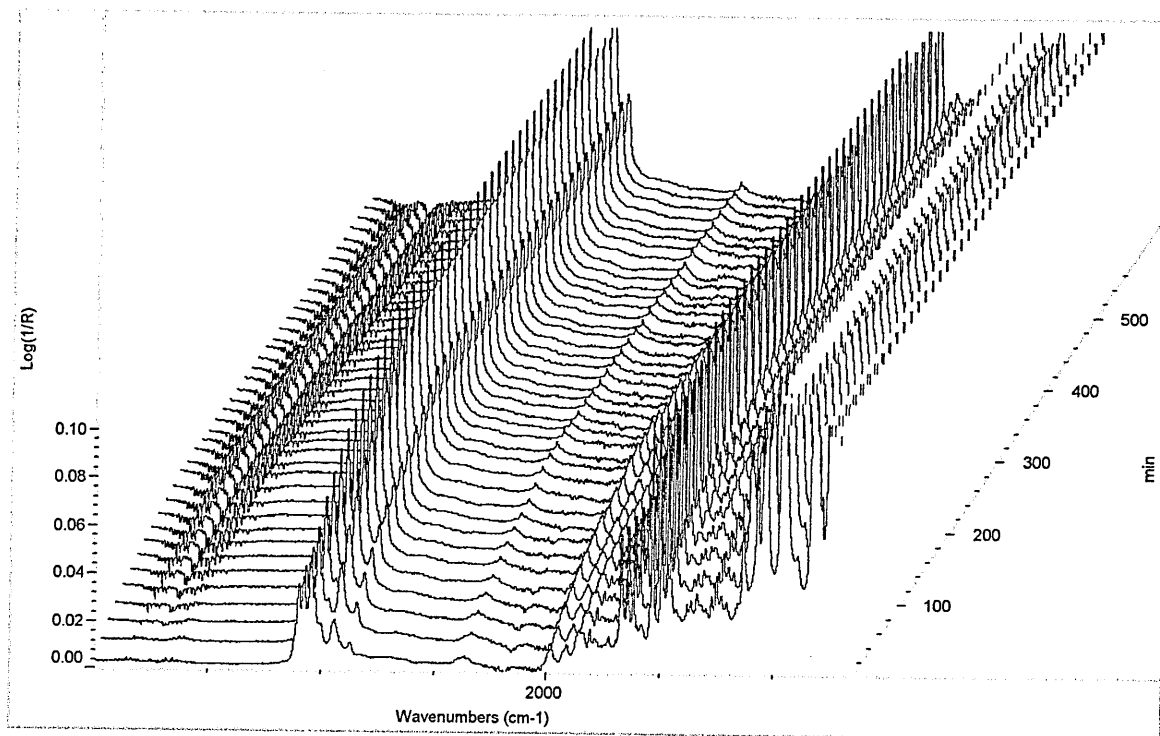

Figure 7.3   Styrene/1 wt% BPO Initiator/1 wt% C15A, cured at 80 °C. Spectra take every 15 mins for 500 mins total.
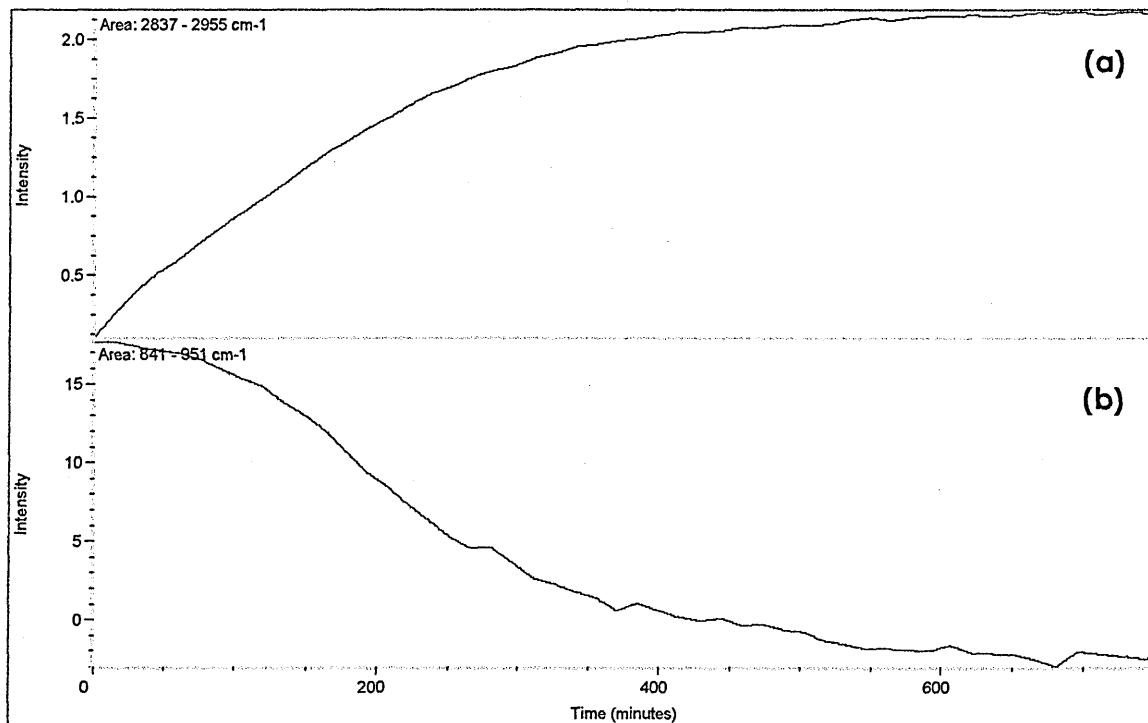
303

Figure 7.4 Integrated series peaks for styrene/1 wt% BPO sample, (a) appearance C-H st. 2955-2837 cm^{-1}, (b) disappearance C-H bend 951-841 cm^{-1}.
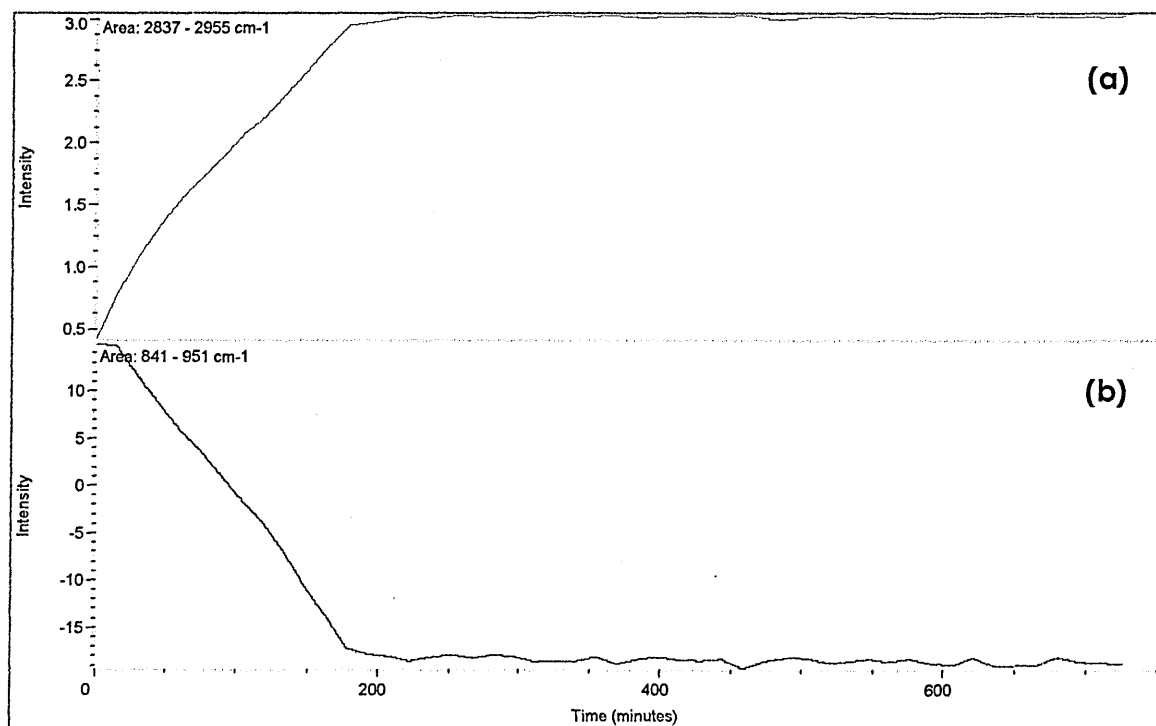

Figure 7.5 Integrated series peaks for styrene/1 wt% BPO/1 wt% C15A, (a) appearance C-H st. 2955-2837 cm^{-1}, (b) disappearance C-H bend 951-841 cm^{-1}.

304

In studies conducted to follow changes to the IR spectra during the cure of virgin polymers and PSCNs, there appeared to be a distinct increase in the rate of polymerisation of styrene brought about by the presence of the organoclay. One possibility is that ionic polymerisation of the styrene by the aluminosilicate surfaces markedly increases the polymerisation process.

In recently conducted studies to follow the polymerisation rate of various samples compared to virgin PS (comparative sequential IR spectra are shown in fig. 7.2/7.3). The plots of integrated peak area (fig. 7.4/7.5) for the primary regions of interest showed that polymerisation reached completion for the PSCN formulation in approximately 200 minutes, whereas virgin PS took >600 minutes to reach the same degree of polymerisation in the absence of an organoclay. The exact nature of this catalysis is uncertain, but it has been shown that at low concentrations C15A can be intimately dispersed within a PS matrix, and the clay brings the styrene monomers into contact with metal ions and hydroxyl groups. These initial investigations could form the basis of a wider kinetic study of PCNs.

7.2.2   GPC Analysis of Selected PSCNs

The analysis of only a small selection of samples by gel permeation chromatography (GPC) has been conducted to date (table 7.1).

Sample	Description
1	Polystyrene - Aldrich Standard (Av. MW 120,000)
2	Polystyrene/BPO (1wt% Initiated)
3	Polystyrene/Na-MCBP-CTAB (1 wt%)
4	Polystyrene/Na-MCBP-TTAB (1 wt%)
5	Polystyrene/Na-MCBP-DTAB (1 wt%)
6	Polystyrene/Na-MCBP-OTAB (1 wt%)
7	Polystyrene/Decanamide (1 wt%)/Na-MMT (1 wt%)
8	Polystyrene/C10A (1 wt%)

Table 7.1   Description of samples analysed by GPC.

The aim was to distinguish what effect, if any, that different organoclays had over the MW of different PSCN samples.

Sample	M$_n$	M$_w$	PDI
1	58273	121395	2.083
2	67240	117939	1.754
3	14492	57385	2.271
4	16563	38134	2.113
5	18046	30113	1.818
6	25269	37890	2.614

Table 7.2   Comparison of M$_w$ for samples 1-6.

The M$_n$, M$_w$ and PDI data suggested that as the length of the alkyl chain increased the M$_w$ and PDI increased. The reasons for the increase in M$_w$ and PDI are unclear, but may represent an increase in the concentration of monomer and initiator within the clay galleries. These first results also support results reported in ch.4, with the increased chain length offering greater thermal stability.

The GPC results for PSCNs formulated using a C10A organoclay and by an OPS method incorporating decanamide and Na-MMT are shown in table 7.3.

Sample	M$_n$	M$_w$	PDI
7	16929	112999	6.675
8	19593	114829	5.861

Table 7.3   Comparison of M$_w$ for samples 1-6.

Due to the nature of the OPS material (i.e. sample 7, table 7.3), the results of this self-assembling system were expected to be unpredictably varied, due to the differences in alkylamide interaction throughout the sample. The PSCN formulated with C10A (i.e. sample 8, table 7.3) also showed high M$_w$ and PDI, this result, especially the PDI may be a

strong indication as to why the thermal stability of other samples made with C10A was so poor. The mid-range PDI could be indicative of a polymer system in flux, with a high degree of heterogeneity, due to monomer being excluded by the organoclay.

This samples would need to be repeated and the series extended to encompass other factors like change of organocation, initiator and their loading.

7.3 Future Work

The work in this thesis could be expanded upon in a number of ways:

a. By conducting a direct comparison of all the N-alkylammonium and N-alkyltrimethylammonium surfactants used in this thesis (i.e. thermal stability of organoclays) with all the different clay species. This may be investigated further by exchanging a selection of the samples on organoclays with different exchange cations.

b. The effect of iron content on the thermal desorption of compatibilising agents could be investigated further by graduating the content of iron in the aluminosilicate and monitoring the effect on T_{max}.

c. By conducting a comparison between the PSCNs generated in this thesis and samples generated by other processing methods (i.e. melt polymerisation) it would be possible to determine what industrial advantages may be gained from *in-situ* polymerisation of PSCNs; time did not permit this comparison to be completed.

d. Further investigation of the novel techniques for OPS and PSCN production (especially incorporating decanamide and vinylformamide) would undoubtedly expand upon the promising initial results.

e. Expansion and completion of the kinetic study of PSCN curing.

f. The UPCNs may be significantly improved through greater quality control of the silane modified MMT and an increased styrene swelling duration for the organoclay species.

g. Further NMR studies of the KPPA samples produced in this thesis described in chapter 6. The further use of ^{31}P MAS NMR and also analysis by ^{29}Si MAS NMR may confirm the bonding states present at the kaolin gallery.

8
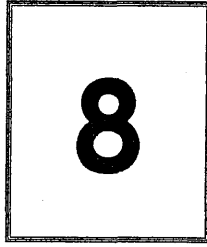
Associated Work

Materials Research Day.
Location: Sheffield Hallam University. Date: 16th January 2001.
Poster: *Thermal Analysis of Alkylammonium Exchanged MMT.*

Mineralogical Society, Clay Minerals Group Autumn Meeting.
Location: University of Huddersfield. Date: 17th October 2001.

Materials Research Day.
Location: Sheffield Hallam University. Date: 17th January 2002.
Poster: *Thermal Characterisation of Polystyrene-Clay Nanocomposites.*

IRDG University Research Meeting.
Location: Strathclyde University. Date: 11th April 2002.

IRDG Christmas Meeting.
Location: King's College, London. Date: 18th December 2002.

Materials Research Day.
Location: Sheffield Hallam University. Date: 22nd January 2003.

Hybridnet Meeting.
Location: Sheffield Hallam University. Date: 15th April 2003.

IRDG University Research Meeting.
Location: UMIST, Manchester. Date: 15th October 2003.

8.2   Postgraduate Study

The following taught units were attended as an integral component of the research studies aspect of the degree:

Date	Location	Course	Duration
2001	Sheffield Hallam University	Vibrational Spectroscopy	8 hours
2001	Sheffield Hallam University	Polymers and Liquid Crystals	8 hours
2001	Sheffield Hallam University	X-ray Crystallography	8 hours
2001	Sheffield Hallam University	X-ray Fluorescence	8 hours
2001	Sheffield Hallam University	Topographical Analysis	8 hours
2001	Scott-Bader, Wellingbrough	Industrial Polymer Processes	4 days

1. TG-MS Studies of the Thermal Decomposition of Alkyltrimethylammonium Exchanged MMT: The Formation of Ring Compounds.
A. Cunningham, C. Breen, *in press*

2. The Effect of Organic Modifier and Initiator Properties on the Thermal Stability of Polystyrene-MMT nanocomposites.
A. Cunningham, C. Breen, *in press*

3. Intercalation of PPA into Kaolin and Halloysite, ^{31}P NMR and Related Studies.
C. Breen, A. Cunningham, *in press*